Title

Effects of Thermochemical Nonequilibrium on Hypersonic Boundary-Layer Instability in the Presence of Surface Ablation or Isolated Two-Dimensional Roughness

Author

Mortensen, Clifton

Publication Date

2015

Peer reviewed|Thesis/dissertation

University of California
Los Angeles

Effects of Thermochemical Nonequilibrium on Hypersonic Boundary-Layer Instability in the Presence of Surface Ablation or Isolated Two-Dimensional Roughness

A dissertation submitted in partial satisfaction
of the requirements for the degree
Doctor of Philosophy in Aerospace Engineering

by

Clifton Holden Mortensen

2015

Abstract of the Dissertation

Effects of Thermochemical Nonequilibrium on Hypersonic Boundary-Layer Instability in the Presence of Surface Ablation or Isolated Two-Dimensional Roughness

by

Clifton Holden Mortensen

Doctor of Philosophy in Aerospace Engineering

University of California, Los Angeles, 2015

Professor Xiaolin Zhong, Chair

The current understanding of the effects of thermochemical nonequilibrium on hypersonic boundary-layer instability still contains uncertainties, and there has been little research into the effects of surface ablation, or two-dimensional roughness, on hypersonic boundary-layer instability. The objective of this work is to study the effects of thermochemical nonequilibrium on hypersonic boundary-layer instability. More specifically, two separate nonequilibrium flow configurations are studied: 1) flows with graphite surface ablation, and 2) flows with isolated two-dimensional surface roughness. These two flow types are studied numerically and theoretically, using direct numerical simulation and linear stability theory, respectively.

To study surface ablation, a new high-order shock-fitting method with thermochemical nonequilibrium and finite-rate chemistry boundary conditions for graphite ablation is developed and validated. The method is suitable for direct numerical simulation of boundary-layer transition in a hypersonic real-gas flow with graphite ablation. The new method is validated by comparison with three computational data sets and one set of experimental data. Also, a thermochemical nonequilibrium linear stability theory solver with a gas phase model that includes

multiple carbon species, as well as a linearized surface graphite ablation model, is developed and validated. It is validated with previously published linear stability analysis and direct numerical simulation results. A high-order method for discretizing the linear stability equations is used which can easily include high-order boundary conditions. The developed codes are then used to study hypersonic boundary-layer instability for a 7 deg half angle blunt cone at Mach 15.99 and the Reentry F experiment at 100 kft. Multiple simulations are run with the same geometry and freestream conditions to help separate real gas, blowing, and carbon species effects on hypersonic boundary-layer instability. For the case at Mach 15.99, a directly simulated 525 kHz second-mode wave was found to be significantly unstable for the real-gas simulation, while in the ideal-gas simulations, no significant flow instability is seen. An N factor comparison also shows that real-gas effects significantly destabilize the flow when compared to an ideal gas. Blowing is destabilizing for the real gas simulation and has a negligible effect for the ideal gas simulation due to the different locations of instability onset. Notably, carbon species resulting from ablation are shown to slightly stabilize the flow for both cases. For the Reentry F flow conditions, inclusion of the ablating nose cone was shown to increase the region of second mode growth near the nose cone. Away from the nose cone, the second mode was relatively unaffected.

Experimental and numerical results have shown that two-dimensional surface roughness can stabilize a hypersonic boundary layer dominated by second-mode instability. It is sought to understand how this physical phenomenon extends from an airflow under a perfect gas assumption to that of a flow in thermochemical nonequilibrium. To these ends, a new high-order shock-fitting method that includes thermochemical nonequilibrium and a cut-cell method, to handle complex geometries unsuitable for structured body-fitted grids, is presented. The new method is designed specifically for direct numerical simulation of hypersonic boundary-layer transition in a hypersonic real-gas flow with arbitrary shaped sur-

face roughness. The new method is validated and shown to perform comparably to a high-order method with a body-fitted grid. For a Mach 10 flow over a flat plate, a two-dimensional roughness element was found to stabilize the second mode when placed downstream of the synchronization location. This result is consistent with previous results for perfect-gas flows. For a Mach 15 flow over a flat plate, a two-dimensional surface roughness element stabilizes the second-mode instability more effectively in a thermochemical nonequilibrium flow, than in a corresponding perfect gas flow.

The dissertation of Clifton Holden Mortensen is approved.

Jeffrey D. Eldredge

Adrienne Lavine

Joseph M. Teran

Xiaolin Zhong, Committee Chair

University of California, Los Angeles

2015

Table of Contents

List of Figures

List of Tables

Nomenclature

c_r	Phase velocity
c_s	Mass fraction of species s
$c_{v,rot,s}$	Species rotation heat capacity at constant volume, J/kg· K
$c_{v,s}$	Species translation-rotation heat capacity at constant volume, J/kg· K
$c_{v,tr,s}$	Species translation heat capacity at constant volume, J/kg· K
D	Diffusion coefficient, m^2/s
e	Specific total energy, J/kg
$e_{v,s}$	Species specific vibration energy, J/kg
e_v	Specific vibration energy, J/kg
f	Frequency, Hz
F_j	Inviscid flux vector
G_j	Viscous flux vector
h	Roughness height, m
h_o	Stagnation enthalpy, J/kg
h_s	Species enthalpy, J/kg
h_s^o	Species heat of formation, J/kg
k_T	Translation-rotation thermal conductivity, N/(K·s)
k_V	Vibration thermal conductivity, N/(K·s)

M	Mach number
$\dot{m}$	Mass flux per area, kg/(m^2· s)
M_s	Species molecular weight, kg/mol
N_s	Number density of species s, 1/m^3
nms	Number of molecular species
ns	Number of species
p	Pressure, N/m^2
$Q_{T-V,s}$	Species vibration energy transfer rate, J/(m^3·s)
R	Universal gas constant, 8.3143 J/(mol· K)
r	Sphere radius
s	Surface streamline, m
T	Translation-rotation temperature, K
t	Time, s
T_V	Vibration temperature, K
U	Vector of conserved flow variables
u_j	Velocity in jth direction, m/s
W	Source vector
X_s	Molar concentration of species s, mol/m^3

Subscripts

∞	Freestream

b	Blowing/suction slot
n	Wall normal
s	Species
w	Wall

Greek Symbols

α_r	Streamwise wavenumber, 1/m
-α_i	Growth rate, 1/m
β	Transverse wavenumber, 1/m
ΔZ	Perturbation amplitude of Z
ΔZ_r	Real part of Z perturbation
δ	Boundary layer thickness, m
δ_{ij}	Kronecker delta
μ	Viscosity, kg/(s·m)
Ω	Nondimensional circular frequency
ω	Circular frequency, rad/s
ω_s	Rate of species production, kg/(m^3·s)
ϕ_Z	Phase of Z, deg
ρ	Density, kg/m^3
σ	Stefan-Boltzmann constant, 5.670×10^{-8} W/(m^2·K^4)

Acknowledgments

Without the constant support of my family and friends throughout my life, I would not be where I am today. I'm grateful I had excellent examples of how to excel in life from both of my parents. I'm thankful that my wife saw some redeeming qualities in a frustrated and broke graduate student. I'm grateful for the guidance of my adviser along the long path of learning and discovery. I'm thankful to all the other faculty who have helped me along the way. Also, I've had wonderful friends at school who I've enjoyed learning from and learning with.

This research was supported in part by the AFOSR/NASA National Center for Hypersonic Research in Laminar-Turbulent Transition, the Department of Defense (DoD) through the National Defense Science & Engineering Graduate Fellowship (NDSEG) Program, and AFOSR Grant FA9550-15-1-0268. This work used the Extreme Science and Engineering Discovery Environment (XSEDE), which is supported by National Science Foundation grant number ACI-1053575. Also, this work was supported by a grant of computer time from the DOD High Performance Computing Modernization Program at the AFRL DSRC. The views and conclusions contained herein are those of the authors and should not be interpreted as necessarily representing the official policies or endorsements either expressed or implied, of the Air Force Office of Scientific Research or the U.S. Government.

Vita

B.S. in Mechanical Engineering, Brigham Young University

M.S. in Mechanical Engineering, Brigham Young University

M.S. in Aerospace Engineering, University of California, Los Angeles

CHAPTER 1

Introduction

The transition from laminar-to-turbulent flow in a bounded shear layer has been an often perplexing problem for fluid dynamicists. Some of the pioneering research on the transition process in an incompressible viscous flow for a bounded shear layer was performed by Tollmien [Tol29] and Schlichting [Sch33]. It resulted in the discovery of the famous T-S, or Tollmien-Schlichting, waves. These are instability waves of a viscous nature that propagate in the streamwise direction while growing exponentially and often leading to the transition of a wall-bounded flow from laminar to turbulent. This discovery has served as a basis for others who extended the ideas to more complex flows. Since then, unstable wave-like modes have been found for many other wall-bounded flows such as compressible and hypersonic boundary layers.

While it is possible to find analytically whether a boundary layer is stable or unstable, actually predicting the location of transition onset, as well as identifying the exact physical mechanisms that lead to transition in complex flows, has proven quite challenging. An instance of these complex flows is high-speed flows, a subset of which is planetary entry. In [BC06] it is noted that "[r]esearch priorities for planetary-entry gas dynamics address uncertainty reduction in prediction of...laminar to turbulent transition criteria and turbulent heating levels on blunt bodies, particularly under conditions of surface ablation."

Boundary-layer transition has a strong effect on the estimation of heating rates for vehicles in high-speed flows. A turbulent boundary layer has a much

higher heating rate than a corresponding laminar boundary layer. In turn, the heating rates impact the design of a vehicle's thermal protection system which has a strong impact on the overall weight and cost of the vehicle. Maintaining a laminar boundary layer over a vehicle surface could lead to a tremendous reduction in heat transferred to the vehicle's surface, thereby decreasing the cost of the vehicle. Clearly, the less expensive the aerospace vehicle the more attractive it is assuming the performance is not degraded.

Figure 1.1 gives a schematic of boundary-layer transition paths based on the environmental disturbance level. Path A details the transition path for hypersonic boundary layers over flat plates and sharp cones in a low disturbance environment. A low disturbance environment is similar to realistic flight conditions. Receptivity is the process by which environmental disturbances are converted to flow instabilities. Eigenmode growth for hypersonic boundary layers is growth of small amplitude wave-like disturbances and is dominated by second mode growth. In the second mode growth process, linear disturbances grow exponentially and their growth is generally the slowest part of the transition process. Schubauer and Skramstad [SS48] found the first experimental evidence of wave-like disturbances occurring in a low-speed flat-plate boundary layer during the transition process. Once instabilities have significantly amplified in the boundary layer, their interactions are no longer negligible. This results in mode interactions and parametric instabilities, which then leads to breakdown and finally turbulence. Path B is similar to Path A, but it also includes transient growth. Transient growth is algebraic growth of freestream disturbances which can lead to a larger initial amplitude for disturbances when they reach eigenmode growth. Paths C, D, and E all skip the eigenmode growth region. This can be for various reasons such as high amplitude freestream disturbances, or roughness on the body. In this work, the focus will be on modal instabilities that occur in the eigenmode growth process such as Mack's second mode.

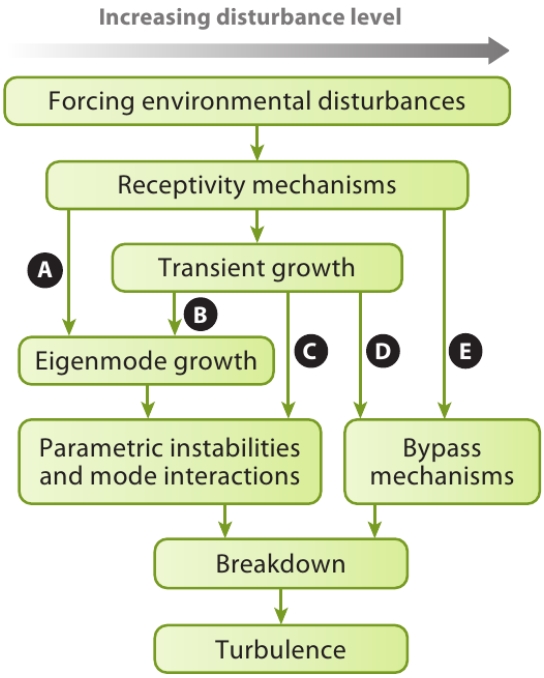

Figure 1.1: Paths to boundary-layer transition as a function of increasing disturbance level. Figure reproduced from Reshotko (2008) [Res08].

Laminar-turbulent transition in hypersonic boundary layers is a complex phenomena involving multiple factors such as freestream disturbances, receptivity, linear eigenmode growth, and multiple paths to transition. In this research, the physical phenomena associated with boundary-layer instability in thermochemical nonequilibrium flows is investigated. Specifically, two flow types will be investigated: 1) flows with surface ablation and 2) flows with isolated surface roughness. When ablation is accounted for in hypersonic boundary-layer transition, there are added difficulties such as shape change, ablation induced roughness, gas influx at the surface, thermochemical nonequilibrium, introduction of new chemical species from surface reactions, and the reactions of those species with the freestream gas. Surface roughness adds complexities to a flow such as recirculation regions, flow separation, and shock/boundary layer interaction. Also, there can be a significant increase in the complexity of the simulation when accounting for surface roughness, especially distributed surface roughness.

1.1 Linear Stability Theory

Numerical modeling of transition phenomena plays an important role in studying hypersonic boundary-layer transition as it can be extremely difficult to replicate exact flight conditions in wind tunnels. One method for modeling transition is linear stability theory (LST) which is an analytical tool used to test the stability of boundary layers to wave-like disturbances.

Significant research on the linear stability of compressible boundary layers has been performed by Mack [Mac84]. Mack found that the major instability waves for hypersonic boundary layers with a perfect gas assumption are the first and second Mack modes. Following researchers have implemented numerical codes using linear stability theory to compute the most unstable frequencies for a variety of flow conditions and gas models. Malik [Mal90] implemented multiple numerical methods for linear stability of perfect gas hypersonic boundary layer flows. Malik dropped the α^2 terms to compute the eigenvalue spectrum (global method) and then retained the α^2 term and used an iterative method to refine the eigenvalue (local method).

Thermochemical nonequilibrium flows can also be analytically analyzed using LST. Stuckert and Reed [SR94] used nonequilibrium LST to study the shock layer of a sharp cone with a 10 deg half angle at Mach 25 where the base flow was computed using the parabolized Navier-Stokes equations. They found that the second Mack mode is shifted to lower frequencies compared to perfect gas calculations. They attribute this to an increase in the size of the region of relative supersonic flow. In Stuckert's dissertation [Stu91], a formulation for the five-species chemical nonequilibrium and thermal equilibrium linear stability equations is given. Hudson [Hud96] outlined the linear stability equations for a five-species thermochemical nonequilibrium flow. Thermal nonequilibrium is accounted for using a two temperature model. The base flow for the stability calculations is computed

from the Navier-Stokes equations using a modified Steger-Warming flux splitting approach. It was found that for a Mach 10 and Mach 15 flow, the oblique first mode was destabilized due to chemical nonequilibrium. For the second mode, chemical nonequilibrium did not have a significant effect on spatial amplification rates. The mean flow temperatures were not high enough for significant dissociating of chemical species, which could explain why insignificant nonequilibrium effects were found.

Johnson et al. [JSC98] used nonequilibrium LST to study laminar-turbulent transition in hypersonic boundary layers using a five-species air model, or a CO_2 model. Their test cases were chosen to compare to experimental results and to study the effects of freestream total enthalpy and chemical composition on boundary-layer transition. They found that dissociation of air species is destabilizing to the second mode and stabilizing to the first mode. Also, as freestream total enthalpy increased, the transition onset location increased. The freestream total enthalpies tested for air were in the range of 3.35–13.5 MJ/kg.

1.2 Linear Parabolized Stability Equations

The linear parabolized stability equations (LPSE) are similar to LST but with fewer required assumptions for solution. One difference is the flow is *not* assumed to be parallel, i.e., the flow can change in the downstream direction. The solution procedure for the two methods is similar, but a shape function is required to march the LPSE solution downstream.

Chang et al. [CVM97] used LPSE to study hypersonic boundary layers with chemical nonequilibrium and thermal equilibrium. For a Mach 10 flat plate adiabatic boundary layer, chemical reactions were found to have a destabilizing effect on Mack's second mode. Using an e^N transition prediction method, they found that the transition location for a Mach 20 flow over a 6 deg wedge was 14 ft.,

24 ft., and 39 ft. for the equilibrium, nonequilibrium and perfect gas models, respectively. This is a large difference in transition prediction based on the flow assumptions which shows the need for the use of a nonequilibrium gas model for certain hypersonic flows. Chang points out that it is "very important to account for the chemistry effect in future transition prediction for hypersonic vehicles."

In [Mal03], another study that utilized LPSE with chemistry effects was performed. It analyzed two cases where laminar to turbulent transition was observed in free flight. Chemistry effects were found to be destabilizing in both cases, but the marked difference between chemical equilibrium and chemical nonequilibrium seen in [CVM97] was not seen in [Mal03]. Rather, the difference between computed N factors at the transition location was small i.e. 9.8 for chemical equilibrium and 9.5 for chemical nonequilibrium. Also, Malik notes that for the two free flight cases analyzed, the transition Reynolds number based on streamwise distance and the edge Mach numbers were significantly different but still resulted in similar N factors at the measured transition location. This helps to verify that the e^N method of transition prediction is valid for hypersonic flows with chemical nonequilibrium.

Johnson [Joh00, JC05] also used LPSE to study hypersonic boundary layers in chemical nonequilibrium while also including thermal nonequilibrium. Thermal nonequilibrium is accounted for using the Park two-temperature model. Johnson noted that the presence of chemical reactions and translation-vibration energy exchange in the boundary layer becomes increasingly important as the freestream enthalpy is increased. Also, exothermic reactions were shown to have a destabilizing effect. Similar to previous researchers, Johnson found that the e^N method gives a consistent method to estimate boundary layer transition where linear modal disturbances, such as the second mode, are dominant.

1.3 Direct Numerical Simulation

A complementary approach to LST and LPSE for studying hypersonic boundary layers in thermochemical nonequilibrium, is direct numerical simulation (DNS). In DNS, flow disturbances are simulated from the full Navier-Stokes equations without dropping any terms. Figure 1.2 is a schematic of a common DNS simulation. First, a mean flow laminar profile is computed, and then a disturbance is imposed in the freestream. This disturbance crosses the bow shock and excites three types of waves: fast acoustic, slow acoustic, and entropy/vorticity. The interaction of these waves and the flowfield is complex and can generate modal instability waves in the boundary layer, such as Mack's first and second modes. DNS mean flow profiles can also be used by LST to compute boundary layer instability information such as the most unstable frequency ranges and corresponding amplification rates.

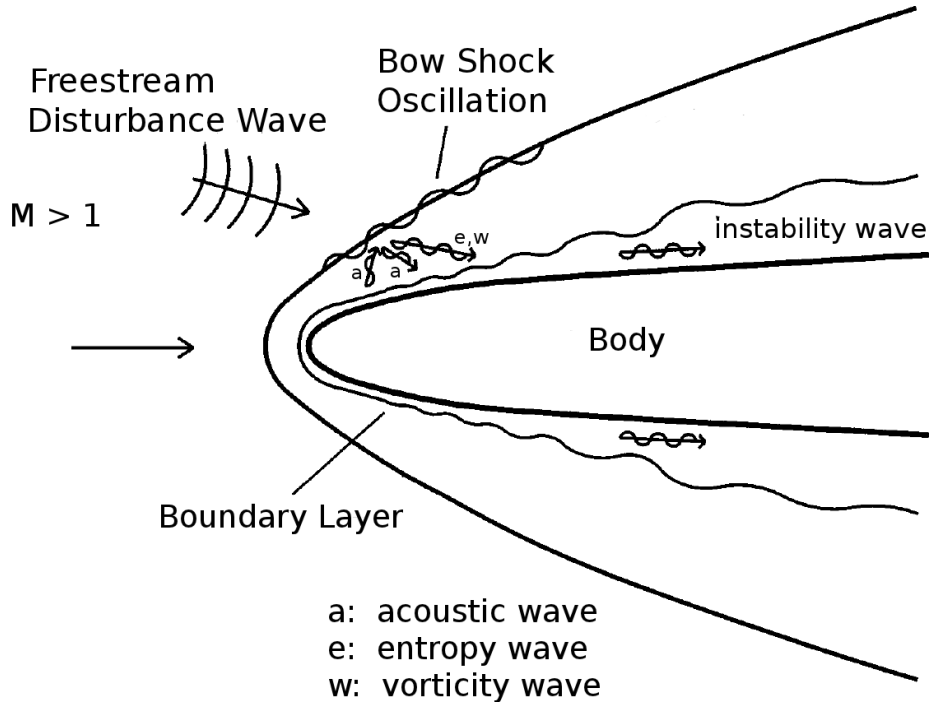

Figure 1.2: A schematic of the disturbance field for freestream waves over a hypersonic body. Figure reproduced from Zhong [Zho98].

Zhong [Zho98] developed a high-order finite-difference shock-fitting method for direct numerical simulation of hypersonic boundary layers. The method includes a set of upwind high-order finite-difference schemes with low dissipation so small amplitude disturbances can be numerically simulated. Recall that small amplitude disturbances are commonly seen in realistic flight conditions and are the starting point for eigenmode growth. The shock is treated as a boundary condition using Rankine-Hugoniot relations. Disturbances can then be imposed on the shock and their behavior simulated as they cross the shock.

Ma and Zhong [MZ03a, MZ03c, MZ05] used DNS and LST to study the receptivity of a perfect gas Mach 4.5 flow over a flat plate. The boundary layer was perturbed with freestream fast acoustic, slow acoustic and entropy waves. The results show that the receptivity of the flat plate boundary layer to freestream fast acoustic waves leads to the excitation of both Mack modes and a family of stable modes. The receptivity of slow acoustic freestream waves is several times stronger than that of fast acoustic freestream waves. Good agreement was obtained between DNS and LST behind the shock for wave angles and amplitudes.

Ma and Zhong [MZ04] studied the receptivity of freestream disturbances of a Mach 10 nonequilibrium oxygen flow over a flat plate. They found that in a Mach 10 oxygen flow, the unstable region for nonequilibrium flow is longer than for perfect gas. This leads to a significant real gas destabilizing effect on the second-mode waves. However, they did not consider thermal nonequilibrium or any gas/surface interaction. Prakash et al. [PPW11] studied receptivity of freestream disturbances with a thermochemical nonequilibrium shock-fitting method. Parsons et al. [PZK10] studied the receptivity effects of thermochemical nonequilibrium on blunt cones using a fifth-order DNS and a five-species air model. They found that freestream fast acoustic waves had higher pressure perturbation amplitudes for a flow with thermochemical nonequilibrium than a perfect gas. Also, they found that the maximum perturbation amplitude moved nearer to the blunt nose.

Stemmer [Ste06, Ste09] studied instabilities in high Mach number flows where high temperature gas effects are present using DNS. He uses a hybrid ENO/finite difference method with high-order accuracy and thermochemical nonequilibrium. Boundary layer profiles for a Mach 20 case show that significant dissociation of air species is present, as well as significant thermal nonequilibrium. Flow disturbances are introduced at the wall in the form of pressure disturbances. The nonequilibrium flow is compared to perfect gas flow and is found to have similar amplitudes for the linear disturbances.

1.4 Carbon Ablation

Thermal protection systems are commonly used to protect hypersonic vehicles from the harsh aerothermal environment they operate in [Ung67]. Often a TPS is ablating, such as those made using graphite or phenolic impregnated carbon ablator (PICA). Examples include ablative heat shields for hypersonic entry vehicles, throat liners inside rocket engines, and nosetips or fins for thermal protection of hypersonic missiles such as the nose cone for the Reentry F flight vehicle [CRH71, JSW72]. The design of these thermal protection systems is of major concern to the vehicle designer who must ensure the structural integrity of the vehicle throughout its flight envelope. For example, the Passive Nosetip Technology (PANT) [Woo75] program was designed to evaluate carbon based nosetips for entry vehicles. They highlighted some of the design difficulties encountered when carbon nosetips are used for thermal protection which included laminar-turbulent transition. Also, [Lin08] highlighted some design concerns for entry vehicles due to uncertainty in hypersonic boundary-layer transition on a cone frustum which include vehicle aerodynamics and impact dispersion.

The design of thermal protection systems is an iterative process requiring the evaluation of many configurations in order to determine the optimal. Experimen-

tal testing of the various designs can be done in the laboratory or by flight tests. However, the laboratory simulation of all required hypersonic flow conditions may not be possible. Likewise, flight tests are expensive and time consuming. Thus, numerical simulations today are assuming an increasingly important role as a cost-effective complement to laboratory and flight test research.

The flight of the Reentry F vehicle is important to the hypersonic transition community as actual in-flight measurements of boundary-layer transition at high Mach numbers were obtained and are available for analysis. Hypersonic free flight transition measurements are not common and are highly valuable for understanding actual in-flight transition. Some of the free flight transition data available for cones have ablating nose cones such as the Reentry F and Sherman and Nakamura [SN70] cases. Therefore, to gain the most insight from these valuable measurements, it is important to understand to what degree the ablating nose cone affects the transition location.

1.4.1 Numerical Methods for Carbon Ablation Prediction

Practical methods for ablation prediction employ various levels of simplification, ranging from empirical engineering correlation and approximate semi-empirical integral methods, to very detailed full Navier-Stokes simulation methods that model the nonequilibrium chemically reacting fluid dynamics coupled to in-depth heat conduction material models [Kee94, ZTW04, CM05a, CM05b, LSO94, Pot95]. Surface chemistry models are commonly used to couple the ablating material calculations with gas phase Navier-Stokes simulations. They can give a numerical estimate of mass addition rates from the ablative surface to the freestream, as well as what chemical constituents the ablator injects into the freestream. For carbon based ablators, they are frequently based on the most common surface reactions such as sublimation, oxidation, and nitridation.

Some common surface chemistry models for carbon ablators are that of Zhluktov and Abe [ZA99] and Park [Par05, Par76]. Zhluktov and Abe developed a kinetic model for air-carbon surface interactions based on the Langmuir approach to the kinetics of catalytic reactions. They take into account twelve coupled surface reactions. Three of the surface reactions are sublimation of C, C_2, and C_3 and a nitridation reaction is not included. They tested their surface chemistry model with the viscous shock layer equations which are obtained from reducing the Navier-Stokes equations.

Over the years, Park has investigated in detail many surface reactions for carbon based ablators. Park [Par76] determined the reaction probabilities for oxidation due to atomic oxygen and diatomic oxygen which are still commonly used. Park [Par05] combined various surface reactions into a model to calculate the stagnation point heating rate for the Stardust entry vehicle using a 1D viscous shock layer method with no material calculations within the carbon ablator.

Keenan [Kee94], and Keenan and Candler [KC93, KC94] coupled a finite volume thermochemical nonequilibrium computational fluid dynamics (CFD) code to a 2D heat equation solver that computes the temperature distribution within the ablator. Their research concentrated on steady graphite ablation without pyrolysis gas injection or surface recession. The solid/fluid computations were coupled through a surface energy balance, a surface mass balance for each species and a total mass balance.

A CFD code with thermochemical nonequilibrium was used in [CM05a] and [CM05b] to compare multiple surface chemistry models for graphite and carbon-phenolic ablation. Four surface chemistry models were compared: Zhluktov and Abe [ZA99], Park [Par83, Par05, Par93] with and without the nitridation reaction, and chemical equilibrium. It was found for the graphite ablation case, that the Park model with the nitridation reaction predicted the highest amount of mass blowing at the surface, while the Zhluktov and Abe model predicted the lowest.

Also, the chemical equilibrium model predicted the largest surface heat flux while both Park models predicted the lowest surface heat flux.

1.4.2 Ablation Induced Roughness and Shape Change

During the process of ablation, surface material is removed to reduce the energy transferred from the flow to the vehicle. Material removal from the surface is not constant over the length of the surface due to varying surface temperatures and pressures resulting in a changing surface shape. Shape change of an ablating nosetip can change the aerodynamic characteristics and flight stability of its vehicle. Shape change of ablating materials has been studied in the PANT program [Woo75]. The PANT program has shown that a major uncertainty in calculating the shape change of an ablative nosetip was associated with predicting the transition location, as mass flux rates are much higher when the boundary layer is turbulent. As the surface changes shape, the boundary layer profile will change and the instability characteristics of the boundary layer will also likely change. For the cases simulated in this work, $c_r \gg \dot{S}_{\max}$ where $\dot{S}_{\max}$ is the maximum surface recession rate. Since the phase velocity of the second mode instability is much larger than the surface recession rate, it is likely that the effect of surface recession on modal instability for the tested cases is small.

Along with shape change, an ablating surface will also create distributed surface roughness which is similar to a sandpaper type roughness. This is termed ablation induced roughness. Roughness can also be incurred in flight by particles impinging on the surface. This roughening may significantly alter the transition process such as leading to bypass transition where eigenmode growth is completely bypassed. Currently, there is substantial uncertainty concerning the effects of surface roughness on hypersonic boundary-layer transition. In [Sch08], the effects of roughness on hypersonic boundary-layer transition are reviewed where it is noted that that the characterization of ablation induced surface roughness in flight has

significant uncertainty. Also, it is noted that an understanding of the instabilities that lead to transition for a smooth wall are needed to understand the experimental results of roughened surfaces which tend to move the location of transition forward when compared to smooth surfaces.

With this in mind, this research will use a simplified pseudo-ablation approach where surface recession and roughness are neglected to provide a more tractable problem and hopefully increase the understanding of ablation on boundary-layer instability.

1.5 Ablation Effects on Boundary-Layer Instability

The research to find how surface ablation affects flow instability has been mostly experimental due to the significant challenges in correctly simulating an ablating flow. Also, much of the numerical and theoretical research focuses on how blowing affects instability in a hypersonic flow due to the relative ease of treatment when compared to an ablating flow. Here, both experimental and numerical research of hypersonic flow instability with surface ablation is reviewed.

1.5.1 Experimental Research

A review of experimental research to study ablation and blowing effects on hypersonic boundary layer stability was performed by Schneider [Sch10]. Experimental research has shown, in general, that blowing moves transition upstream and a larger mass addition causes a larger effect. He pointed out that blowing near the nosetip is thought to have a particularly significant effect on transition. This is important for ablation because the maximum surface mass flux for a zero degree angle-of-attack blunt vehicle occurs at the stagnation point or nose.

The PANT [Woo75] program performed a series of research tests on carbon ablation. Of these tests some were performed to study nosetip shape change and

transition for graphite ablation in a high enthalpy arcjet gas stream [SFP74]. Three carbon materials: ATJ-S graphite, a carbon/carbon material, and a carbon phenolic material, were tested. Boundary layer transition locations were inferred from overhead images taken of the graphite surface.

Kaattari [Kaa78] studied mass addition effects on boundary layer transition and heat transfer for Mach 7.32 flows over blunt bodies. The blowing profiles are different than blowing profiles obtained due to ablation. The blowing parameter—ratio of freestream mass flux to surface mass flux—was varied from 0.0 to 0.5 and the gas blown was air. For the hemispherical model at unit Reynolds number 2.3×10^6 /m when the blowing parameter was 0.01, transition began on the model. As the blowing parameter increased, transition continued to move forward. This shows that blowing can effect boundary layer transition even when the mass addition is only 1% of the freestream. For each of the cases simulated in this work, the maximum surface mass flux is commonly around 1% of the freestream mass flux.

1.5.2 Numerical Research

Currently there has been a limited amount of numerical research on how ablation and surface chemistry models affect hypersonic boundary-layer transition. Johnson et al. [JGC09] used linear stability analysis to analyze non-reacting and reacting hypersonic boundary layers with blowing and suction. For a non-reacting gas mixture of a Mach 4.5 flow over a flat plate, it was found that suction was stabilizing to the second mode and blowing was destabilizing. This data was similar to results first found by Malik [Mal89]. Johnson also found that, for a five-species air reacting boundary layer, the transition location would move forward with increasing total enthalpy assuming that transition occurred where the N-factor was equal to 5.5.

Ghaffari et al. [GMI10] performed a linear stability analysis of a hypersonic perfect gas flat plate boundary layer with wall blowing. They found that, as blowing increases, the maximum amplification rate of the disturbance instability grows and moves to lower frequencies. Li et al. [LCC11] studied boundary layer instability mechanisms for hypersonic perfect gas flows over slender cones and blunt capsules at zero angle of attack and an angle of attack of 16 deg. They found that for the slender cone, out-gassing is moderately stabilizing to the second mode. For the blunt capsule, out-gassing is destabilizing to the first mode.

A deficiency of previous research is that blowing profiles have been rather artificial, i.e., they are set from a similarity solution or at random. This can make the tested blowing profiles quite different than realistic blowing profiles. Also, other effects due to surface ablation such as injection of surface species into the meanflow has been neglected. The current work seeks to remedy these deficiencies by using a realistic blowing profile computed from a surface chemistry model and by blowing a realistic gas composition computed from a surface chemistry model, rather than simply blowing air.

1.6 Roughness Effects on Boundary-Layer Instability

Surface roughness has served primarily to promote early boundary-layer transition in a hypersonic flow when compared to a smooth surface, or, to not adversely affect transition significantly [Sch08]. However, recent direct numerical simulation results from [DWZ13, FWZ13, FWZ14, FWZ15] have shown that judiciously placed two-dimensional roughness elements can actually stabilize a hypersonic boundary layer and delay transition onset. Following these findings, experiments were performed in [FWH15] which showed that, indeed, similar to the direct numerical simulation results, two dimensional roughness elements can delay the onset of transition in a physical air flow. The fact that the numerical and experimental

evidence is consistent brings the idea that perhaps a passive control strategy may be implemented in flight, using finite height roughness, to stabilize a hypersonic boundary layer.

The potential delay of transition in a hypersonic boundary layer by two-dimensional roughness elements, as shown in [DWZ13, FWZ13, FWZ14, FWZ15, FWH15], comes from the second mode being the most dominant instability mode. It was shown that a two-dimensional roughness element, that is less than the boundary-layer thickness, when placed after the synchronization point of mode S and mode F, can lead to a suppression, or stabilization, of the second mode. When the same roughness element is placed upstream of the synchronization point, the second mode is destabilized, i.e., the second-mode instability growth is higher. Therefore, the location of the roughness element is critical to achieving a delay in transition.

Before the numerical findings that judiciously placed roughness elements could delay transition, there were experimental results that showed an unexplained delay in the onset of turbulence. For example, a Mach 6.0 boundary layer on a flat plate was experimentally tested in [HS64] with and without surface roughness. The surface roughness tested was not two dimensional, rather, it was a row of spheres that mimicked a two-dimensional roughness element. For the tested cases, when the height of the surface roughness tested was less than the height of the boundary layer, there was a delay in the onset of transition. Also, the required roughness height to trip the boundary layer flow to turbulence was two times the height of the boundary layer. Similarly, in [Fuj06] there was an experimentally measured delay in transition for a hypersonic boundary layer. In this instance, the freestream Mach was 7.1 and the geometry was a 5 deg half angle sharp cone. The roughness was two dimensional in this case, but was a wavy wall roughness, rather than an isolated hump. However, the two-dimensional wavy wall roughness still produced a delay in transition onset when placed far upstream of the breakdown region.

It is quite possible that the mechanism leading to the delay in transition seen in these experimental results is similar to the mechanism explained in [FWZ14]. That is, the transition delay in these experimental cases is similar to an isolated two-dimensional roughness damping the dominant second mode instabilities that have their synchronization locations upstream of the location of the roughness element.

Further experimental work was performed in [TZC15] to help confirm and understand the damping effects of two-dimensional roughness. An experimental test was run for a Mach 6 flat-plate boundary layer with two-dimensional surface roughness. Multiple heights for roughness elements were experimentally tested to find the effects on second-mode instability. The experimental findings showed growth in the flow disturbance upstream of the roughness element and then damping of the second mode downstream of the roughness. Also, a taller roughness was more effective at damping the second mode instability. These results are consistent with the numerical findings.

Another passive control concept, designed to suppress second mode instability through modification of an unperturbed surface, is the wavy wall concept. This concept of a two-dimensional wavy wall damping second-mode instability was tested experimentally and numerically in [BCM13]. It was found, similar to the isolated roughness case, that a high frequency band in the second mode region was damped, while a lower frequency band was slightly amplified. This idea to suppress the second-mode instability, seems to be physically similar to the distributed two-dimensional roughness concept in [FWZ15] in the limit of zero spacing between roughness elements. However, the authors of [BCM13] link the suppression of the second mode to a modification of the meanflow, rather than to the relative location of the synchronization location and the roughness element, as in [FWZ15].

1.7 Motivation

For future ablative and nonablative hypersonic vehicles, it is key to accurately predict boundary-layer transition. As it is extremely difficult to replicate exact flight conditions experimentally, numerical simulations and analytical modeling of disturbance waves is used to better understand the physics of the transition process. There has been much progress in the understanding of hypersonic boundary-layer instability with a perfect gas assumption, however, understanding of hypersonic boundary-layer instability with thermal and chemical nonequilibrium still contains significant uncertainties. For realistic hypersonic flight conditions, real-gas effects are significant and cannot be neglected for an accurate understanding of the flow physics.

Two distinct issues that affect hypersonic boundary-layer instability in thermochemical nonequilibrium flows will be addressed in this work: 1) surface ablation and 2) surface roughness. The effects of surface ablation on hypersonic boundary-layer instability is an open research problem. This open problem contains a few more specific research problems: What are the effects of ablation induced roughness? What are the effects of ablation induced outgassing? What are the effects of surface chemistry? In this research, the specific problems addressed are how does ablation induced outgassing and surface chemistry affect hypersonic boundary-layer instability. In order to study these effects, it will be necessary to study real-gas effects as the surface chemistry model necessitates that the flow react with the surface, and thus, the flow cannot be modeled as a perfect gas.

It could be argued that, for a complete understanding of ablation effects on boundary-layer transition, ablation induced roughness must be included as roughness effects are thought to have a strong effect on boundary-layer transition. The numerical treatment of roughness adds significant computational cost and complexity to any DNS simulation. Also, the effects of roughness is an open research

problem in itself. As a first step in studying ablation effects, the focus will be placed on ablation induced outgassing and surface chemistry. While this may not simulate graphite ablation exactly, it does yield a good starting point to understand how ablation affects boundary-layer transition.

The study of the effects of surface roughness on hypersonic boundary-layer instability will be confined to analyzing isolated roughness elements that are two-dimensional. This is done to extend the previous research findings that showed how isolated two-dimensional roughness elements in a hypersonic flow can efficiently damp second-mode instability. These previous findings will be extended from a perfect gas assumption to that of a gas in thermochemical nonequilibrium.

In order to study these research problems, two approaches are used: theoretical analysis using linear stability theory and numerical analysis using direct numerical simulation. While LST and DNS have previously been used to study thermochemical nonequilibrium flows, there is currently no research in the open literature, that the author is aware of, that has coupled LST or DNS with a surface chemistry model to study ablation effects on boundary-layer transition. Also, there has been no research the author is aware of, using LST or DNS, to study second-mode instability in a thermochemical nonequilibrium flow with two-dimensional surface roughness.

It should be noted that, it would be possible to combine the methods used here to treat surface ablation and roughness. The combination of these two methods with a roughened surface, similar to that of ablation induced outgassing, could potentially simulate surface ablation more realistically. However, the combination of these two methods would not be trivial—such as determining the in-flight distributed roughness profile and using a grid with fine enough resolution to capture flow features from three-dimensional roughness that can be on the order of hundreds of micrometers—and is beyond the scope of the current work.

1.8 Objectives

The main research objectives are as follows:

1. Develop and validate a shock-fitting thermochemical nonequilibrium finite-difference research code with a surface chemistry model for graphite ablation suitable for direct numerical simulation of flowfield disturbances

2. Develop and validate an axisymmetric linear stability theory code with thermochemical nonequilibrium and ablation boundary conditions

3. Develop and validate a cut-cell method included into the thermochemical nonequilibrium shock-fitting research code

4. Study the effects of outgassing, which is induced by graphite ablation, on hypersonic boundary-layer instability and transition in a real-gas flow using developed direct numerical simulation and linear stability theory codes

   (a) Study effects on a zero angle-of-attack blunt cone (Figure 1.3) where transition is likely to be second-mode dominated

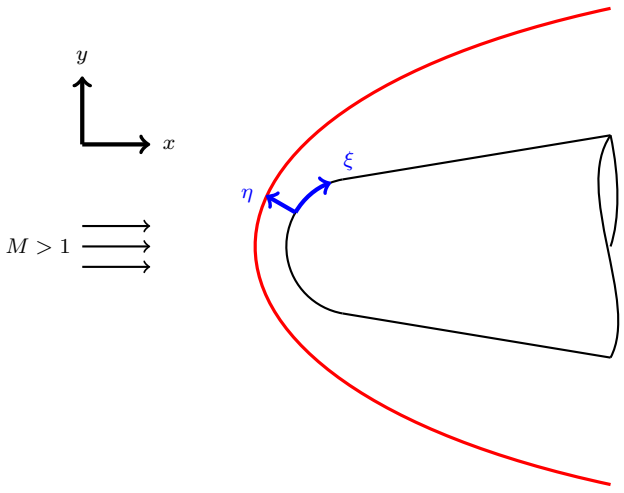

Figure 1.3: Blunt cone with Cartesian and body-fitted coordinates for DNS and LST, respectively. The shock is colored red.

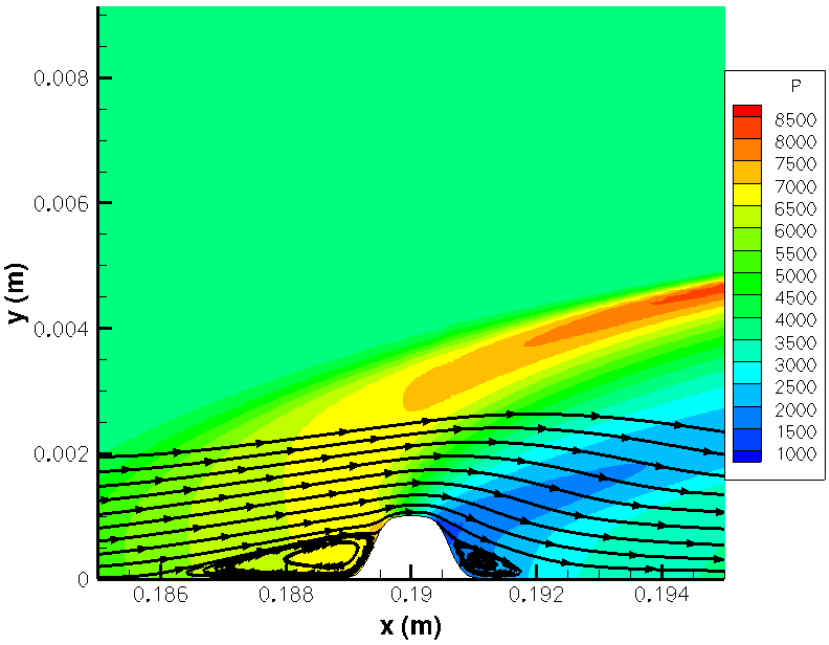

Figure 1.4: Pressure field near roughness with streamlines where $h/\delta = 20\%$

5. Study effects of isolated surface roughness elements (Fig. 1.4) on hypersonic boundary-layer instability and transition in a real-gas flow over a flat plate using developed direct numerical simulation and linear stability theory codes

With these research objectives, it is expected that a research contribution would be one of the first laminar-turbulent DNSs of a high Mach number ablating flow. There have been many fluid simulations of surface ablation and some fully turbulent DNSs of channel flow with ablation that are low Reynolds number [CN10]. However, as far as the author is aware, there have not been any high Reynolds number laminar-turbulent DNSs with surface ablation. Along these same lines, as far as the author is aware, there have not been any methods that couple an ablating surface model with a method to analyze boundary layer instability such as LST. Also, one of the first laminar-turbulent DNSs of thermochemical nonequilibrium flow over two-dimensional finite height surface roughness is presented here.

The thesis will start with an overview of the governing equations in Ch. 2, which includes the thermochemical nonequilibrium model and the surface chemistry model used. Next, the numerical methods for DNS, LST, and cut-cell will be given in Ch. 3. Chapters 4, 5, and 6 will show the validation cases for the DNS, LST, and cut-cell numerical methods, respectively. The results, showing the effects of ablation induced outgassing on transition, will be given in Chs. 7 and 8. The results, showing the effects of two-dimensional roughness on a thermochemical nonequilibrium flow, will be given in Chs. 9 and 10. Following that, the thesis will end with a summary of findings and some suggestions for future work in Ch. 11.

CHAPTER 2

Governing Equations and Models

The governing equations for thermochemical nonequilibrium are formulated for a two-temperature model with the rotational energy mode assumed to be fully excited and eleven non-ionizing species with finite-rate chemistry. Two temperatures are used to represent translation-rotation energy and vibration energy. The eleven species model (N_2, O_2, NO, C_3, CO_2, C_2, CO, CN, N, O, C) is used to simulate air, surface reactions, and reactions of air with ablation products. The conservative three-dimensional Navier-Stokes equations consist of eleven species mass conservation equations, three momentum conservation equations, the vibration energy conservation equation and the total energy conservation equation. Written in vector form the governing equations are

$$\frac{\partial U}{\partial t} + \frac{\partial F_j}{\partial x_j} + \frac{\partial G_j}{\partial x_j} = W \tag{2.1}$$

where U is the state vector of conserved quantities and W is the source terms defined by

$$U = \begin{bmatrix} \rho_1 \\ \vdots \\ \rho_{ns} \\ \rho u_1 \\ \rho u_2 \\ \rho u_3 \\ \rho e \\ \rho e_v \end{bmatrix}, \quad W = \begin{bmatrix} \omega_1 \\ \vdots \\ \omega_{ns} \\ 0 \\ 0 \\ 0 \\ 0 \\ \sum_{s=1}^{nms} (Q_{T-V,s} + \omega_s e_{v,s}) \end{bmatrix}.$$

F_j and G_j are the inviscid and viscous fluxes respectively and are defined by

$$F_j = \begin{bmatrix} \rho_1 u_j \\ \vdots \\ \rho_{ns} u_j \\ \rho u_1 u_j + p\delta_{1j} \\ \rho u_2 u_j + p\delta_{2j} \\ \rho u_3 u_j + p\delta_{3j} \\ (\rho e + p)\, u_j \\ \rho e_v u_j \end{bmatrix}, \qquad G_j = \begin{bmatrix} \rho_1 v_{1j} \\ \vdots \\ \rho_{ns} v_{nsj} \\ \tau_{1j} \\ \tau_{2j} \\ \tau_{3j} \\ -u_i \tau_{ij} - k_T \frac{\partial T}{\partial x_j} - k_V \frac{\partial T_V}{\partial x_j} + \sum_{s=1}^{nms} \rho_s h_s v_{sj} \\ -k_V \frac{\partial T_V}{\partial x_j} + \sum_{s=1}^{nms} \rho_s e_{v,s} v_{sj} \end{bmatrix}$$

where v_{sj} is the species diffusion velocity and $\tau_{ij} = \mu\left(\frac{\partial u_i}{\partial x_j} + \frac{\partial u_j}{\partial x_i}\right) - \frac{2}{3}\mu\frac{\partial u_k}{\partial x_k}\delta_{ij}$ is the viscous stress. The total energy per unit volume, ρe, is defined by

$$\rho e = \sum_{s=1}^{ns} \rho_s c_{v,s} T + \rho e_v + \frac{1}{2}\rho u_i u_i + \sum_{s=1}^{ns} \rho_s h_s^{\circ} \tag{2.2}$$

where h_s° is the heat of formation of species s, $e_{v,s}$ is the species specific vibration energy, and $c_{v,s}$ is the species translation-rotation specific heat at constant volume defined as

$$c_{v,s} = \begin{cases} \frac{5}{2}\frac{R}{M_s}, & s = 1, 2, \ldots, nms \\ \frac{3}{2}\frac{R}{M_s}, & s = nms+1, \ldots, ns. \end{cases} \tag{2.3}$$

The vibration energy per unit volume, ρe_v, is defined as

$$\rho e_v = \sum_{s=1}^{nms} \rho_s e_{v,s} = \sum_{s=1}^{nms} \rho_s \left(\sum_{m=1}^{nmod} \frac{g_{s,m} R}{M_s} \frac{\theta_{v,s,m}}{\exp\left(\theta_{v,s,m}/T_V\right) - 1} \right) \tag{2.4}$$

where *nmod* refers to the number of vibrational modes for each of the polyatomic molecules, $\theta_{v,s,m}$ refers to the characteristic temperature of each vibrational mode, and $g_{s,m}$ is the degeneracy of each vibrational mode. For the diatomic species there is only one vibrational mode and the degeneracy is unity. For C_3 and CO_2 there are three vibrational modes where two modes have a degeneracy of unity and one has a degeneracy of two. The characteristic vibration temperatures and their

degeneracies were taken from Park [Par90] for N_2, O_2 and NO, from Dolton et al. [DMG68] for C_3, and from McBride [MHE63] for CO_2, C_2, CO, and CN.

To model chemical nonequilibrium, eight dissociation reactions and sixteen exchange reactions are used. The dissociation reactions take the form

$$R_c = \sum_{s=1}^{ns} \left(-k_{f,c,s} \frac{\rho_r}{M_r} \frac{\rho_s}{M_s} + k_{b,c,s} \frac{\rho_{p_1}}{M_{p_1}} \frac{\rho_{p_2}}{M_{p_2}} \frac{\rho_s}{M_s} \right) \tag{2.5}$$

where c is the specific chemical reaction, r is the reactant, p_1 and p_2 are the products, and s is the collision partner. Each reaction is governed by a forward and backward reaction rate determined by Eqs. (2.7) and (2.8), respectively. Each of the dissociation reactions are given in Table A.1, along with their corresponding forward reaction rate constants in Arrhenius form. The exchange reactions take the form

$$R_c = \sum_{s=1}^{ns} \left(-k_{f,c} \frac{\rho_{r_1}}{M_{r_1}} \frac{\rho_{r_2}}{M_{r_2}} + k_{b,c} \frac{\rho_{p_1}}{M_{p_1}} \frac{\rho_{p_2}}{M_{p_2}} \right) \tag{2.6}$$

where r_1 and r_2 are the reactants and p_1 and p_2 are the products. Each of the exchange reactions, with corresponding forward reaction rate constants, are given in Table A.2. All forward reaction rate constants are taken from [Par85, PHJ91, BL92]. T_a is the defining temperature for the reaction and is defined as $T_a = \sqrt{T T_V}$ for reactions 1–3 and as $T_a = T$ for all other reactions. When computing the backward reaction rate for all reactions, $T_a = T$.

$$k_f = C_f T_a^{\eta} \exp\left(-\theta_d / T_a\right) \tag{2.7}$$

$$k_b = k_f / K_{eq} \tag{2.8}$$

The equilibrium coefficient, K_{eq}, is computed in two different ways. A curve fit from Park [Par90] is employed for reactions 1–3 and 9–10 as in Eq. (2.9). The equilibrium coefficients for the remaining reactions are computed from the Gibbs Free energy. Curve fits to the Gibbs Free energy are obtained from McBride et al. [MHE63] as in Eqs. (2.10) and (2.11) respectively where Δn is the stoichio-

metric coefficients of the products minus the reactants.

$$K_{eq} = A_0 \exp\left(\frac{A_1}{Z} + A_2 + A_3 \ln(Z) + A_4 Z + A_5 Z^2\right), \quad Z = \frac{10000}{T} \tag{2.9}$$

$$\frac{G^o}{RT} = a_1(1 - \ln T) - \frac{a_2}{2}T - \frac{a_3}{6}T^2 - \frac{a_4}{12}T^3 - \frac{a_5}{20}T^4 + \frac{a_6}{T} - a_7 \tag{2.10}$$

$$K_{eq} = \exp\left(-\frac{G^o}{RT}\right)(R_u T)^{-\Delta n} \tag{2.11}$$

With the forward and backward rates defined, the chemical production source terms for each species may be found from

$$\omega_{N_2} = M_{N_2}(R_1 + R_9 + R_{15} + R_{24}) \tag{2.12}$$

$$\omega_{O_2} = M_{O_2}(R_2 + R_{10} + R_{11} - R_{13} - R_{22} + R_{24}) \tag{2.13}$$

$$\omega_{NO} = M_{NO}(R_3 - R_9 + R_{10} - R_{12} - R_{19} + R_{23} - 2R_{24}) \tag{2.14}$$

$$\omega_{C_3} = M_{C_3}(R_4 + R_{17} - R_{21}) \tag{2.15}$$

$$\omega_{CO_2} = M_{CO_2}(R_5 + R_{13} - R_{20} - R_{23}) \tag{2.16}$$

$$\omega_{C_2} = M_{C_2}(-R_4 + R_6 - R_{14} - R_{16} - 2R_{17} + R_{21} - R_{22}) \tag{2.17}$$

$$\begin{aligned}\omega_{CO} = M_{CO}(&-R_5 + R_7 + R_{11} - R_{13} + R_{14} + R_{18} \\ &+R_{19} + 2R_{20} + R_{21} + 2R_{22} + R_{23})\end{aligned} \tag{2.18}$$

$$\omega_{CN} = M_{CN}(R_8 + R_{12} - R_{15} + R_{16} - R_{18}) \tag{2.19}$$

$$\omega_N = M_N(-2R_1 - R_3 - R_8 - R_9 - R_{10} - R_{15} - R_{16} + R_{18} + R_{19} - R_{23}) \tag{2.20}$$

$$\begin{aligned}\omega_O = M_O(&-2R_2 - R_3 - R_5 - R_7 + R_9 + R_{10} \\ &+R_{11} + R_{12} + R_{13} - R_{14} - R_{18} - R_{21})\end{aligned} \tag{2.21}$$

$$\begin{aligned}\omega_C = M_C(&-R_4 - 2R_6 - R_7 - R_8 - R_{11} - R_{12} \\ &+R_{14} + R_{15} + R_{16} + R_{17} - R_{19} - R_{20}).\end{aligned} \tag{2.22}$$

To calculate the source term in the vibration energy equation which represents the exchange of energy between the translation-rotation and vibration energies,

the Landau-Teller expression is used

$$Q_{T-V,s} = \rho_s \frac{e_{v,s}(T) - e_{v,s}(T_V)}{< \tau_s > + \tau_{cs}} \tag{2.23}$$

where $< \tau_s >$ is the Landau-Teller vibration relaxation time given by Lee [Lee85] defined as

$$< \tau_s >= \frac{\sum_{r=1}^{ns} X_r}{\sum_{r=1}^{ns} X_r / \tau_{sr}} \tag{2.24}$$

and τ_{sr} is obtained from Millikan and White [MW63] using

$$\tau_{sr} = \frac{1}{p} \exp\left[A_{sr}\left(T^{-1/3} - 0.015\mu_{sr}^{1/4}\right) - 18.42\right], \; p \text{ in atm} \tag{2.25}$$

$$A_{sr} = 1.16 \times 10^{-3} \mu_{sr}^{1/2} \theta_{v,s}^{4/3} \tag{2.26}$$

$$\mu_{sr} = \frac{M_s M_r}{M_s + M_r} \cdot 1000. \tag{2.27}$$

Here $\theta_{v,s}$ is the characteristic temperature corresponding to the energy level of the first excited vibrational mode. τ_{cs} is from Park [Par90] to more accurately model the relaxation time in areas of high temperatures occurring just downstream of the bow shock.

$$\tau_{cs} = 1/C_s \sigma_v N_s \tag{2.28}$$

$$C_s = \sqrt{8RT/\pi M_s} \tag{2.29}$$

$$\sigma_v = 10^{-21} (50000/T)^2 \tag{2.30}$$

The viscosity of each species is computed using a Blottner curve fit shown in Eq. (2.31). The coefficients are obtained from Blottner [BJE71], Gupta [GLS90], and Candler [Can90] and are shown in Table A.3. The mixture viscosity is then found using each species viscosity from a mixing rule obtained from Wilke [Wil50] as shown in Eqs. (2.32)–(2.34).

$$\mu_s = 0.1 \exp\left[\left(A_s^\mu \ln(T) + B_s^\mu\right) \ln(T) + C_s^\mu\right] \tag{2.31}$$

$$\mu = \sum_{s=1}^{ns} \frac{X_s \mu_s}{\phi_s} \tag{2.32}$$

$$X_s = \frac{c_s}{M_s} \tag{2.33}$$

$$\phi_s = \frac{\sum_{r=1}^{ns} X_r \left[1 + \left(\frac{M_s}{M_r}\right)^{1/4}\right]^2}{\left[8\left(1 + \frac{M_s}{M_r}\right)\right]^{1/2}} \tag{2.34}$$

The translation-rotation and vibration heat conductivities for each species are calculated from Eqs. (2.35) and (2.36) where $c_{v,tr,s} = \frac{3}{2}\frac{R}{M_s}$. $c_{v,rot,s} = \frac{R}{M_s}$ and $c_{v,vib,s} = \frac{\partial e_{vs}}{\partial T_V}$ for molecules and are zero elsewise. The total heat conductivities for each energy mode are combined similar to the viscosity using Eqs. (2.37) and (2.38). The diffusion velocity is calculated using Fick's law (Eq. (2.39)) and a constant Schmidt number (Eq. (2.40)) which yields acceptable results for species with similar molecular weights.

$$k_{T,s} = \mu_s \left(\frac{5}{2} c_{v,tr,s} + c_{v,rot,s}\right) \tag{2.35}$$

$$k_{V,s} = \mu_s c_{v,vib,s} \tag{2.36}$$

$$k_T = \sum_{s=1}^{ns} \frac{X_s k_{T,s}}{\phi_s} \tag{2.37}$$

$$k_V = \sum_{s=1}^{ns} \frac{X_s k_{V,s}}{\phi_s} \tag{2.38}$$

$$\rho_s v_{sj} = -\rho D_s \frac{\partial c_s}{\partial x_j} \tag{2.39}$$

$$Sc = \frac{\mu}{\rho D} = 0.5 \tag{2.40}$$

2.1 Surface Chemistry Model and Boundary Conditions

A surface chemistry model is required to couple the ablating graphitic surface with the flow. The surface chemistry model accounts for reactions occurring at

the graphite surface between the solid surface carbon and freestream gaseous species. Six surface reactions are taken into account: the first two reactions allow for surface removal of material through oxidation, the third reaction accounts for surface recombination of atomic oxygen, and the last three are due to sublimation of C, C_2, and C_3. C_3 is commonly included in most graphite ablation models as sublimation of graphite produces mostly C_3 with smaller amounts of C, C_2, and heavier carbon species.

Nitridation is not included here as there is still significant uncertainty in the nitridation coefficient. There has been recent experimental work to determine the nitridation coefficient in [SFA08] and [PB06]. Likely the nitridation coefficient is small leading to a minimal impact on the simulation when nitridation is excluded. Recent results have also shown that the nitrogen atom recombination reaction occurring at the surface of hot graphite is very fast [AAB13, DM11]. For the tested cases, the nitrogen atom concentration at the surface is only significant near the stagnation point which is away from the flow instability studied. However, it would likely need to be included when studying instabilities when the meanflow had a high concentration of atomic nitrogen near the surface.

The reactions and reaction probabilities for oxidation and recombination of atomic oxygen are obtained from Park [Par76] yielding

$$(\mathrm{C}) + \mathrm{O}_2 \rightarrow \mathrm{CO} + \mathrm{O} \tag{2.41}$$

$$(\mathrm{C}) + \mathrm{O} \rightarrow \mathrm{CO} \tag{2.42}$$

$$(\mathrm{C}) + \mathrm{O} + \mathrm{O} \rightarrow (\mathrm{C}) + \mathrm{O}_2. \tag{2.43}$$

The oxidation rates are based on kinetic theory giving

$$k_m = \alpha_m \sqrt{\frac{RT_w}{2\pi M_s}} \tag{2.44}$$

where T_w is the wall temperature and α_m is the reaction probability for each reaction in Eqs. (2.41)–(2.43), respectively. The reaction probabilities are obtained

experimentally yielding

$$\alpha_1 = \frac{1.43 \times 10^{-3} + 0.01 \exp\left(-1450/T_w\right)}{1 + 2 \times 10^{-4} \exp\left(13000/T_w\right)} \tag{2.45}$$

$$\alpha_2 = 0.63 \exp\left(-1160/T_w\right) \tag{2.46}$$

$$\alpha_3 = 0.63 \exp\left(-1160/T_w\right). \tag{2.47}$$

From which the associated surface species mass flux may be found from

$$\dot{m}_{O_2} = -\rho_{O_2} k_1 + \rho_O k_3 \tag{2.48}$$

$$\dot{m}_{CO} = \frac{M_{CO}}{M_{O_2}} \rho_{O_2} k_1 + \frac{M_{CO}}{M_O} \rho_O k_2 \tag{2.49}$$

$$\dot{m}_O = \frac{M_O}{M_{O_2}} \rho_{O_2} k_1 - \rho_O k_2 - \rho_O k_3. \tag{2.50}$$

There are three reactions for sublimation

$$(C) \rightarrow C \tag{2.51}$$

$$(C) \rightarrow C_2 \tag{2.52}$$

$$(C) \rightarrow C_3 \tag{2.53}$$

and for each reaction the mass flux is obtained from the Knudsen-Langmuir equation [Bak77]

$$\dot{m}_s = \alpha_s \left(p_{v,s} - p_s\right) \sqrt{\frac{M_s}{2\pi R T_w}} \tag{2.54}$$

where α_s is experimentally determined for each carbon species. The vapor pressure of the three carbon species is given by

$$p_{v,s} = \exp\left(\frac{P_s}{T_w} + Q_s\right) \quad p \text{ in atm} \tag{2.55}$$

where Table A.4 gives the reaction probabilities obtained from [PM68] and vapor pressure coefficients obtained from [DMG68] for each sublimation reaction.

Boundary conditions are needed to couple the surface chemistry model with the gas model, as well as set wall conditions for both temperatures and pressure. At the surface, a surface energy balance is solved to find temperature, and a surface

mass balance is solved to find the mass fraction of each species. A schematic of the various types of energy transfer occurring at the ablator surface is given in Fig. 2.1. This energy balance is applicable to a non-pyrolyzing ablator, such as graphite, in a quasi-stationary state. It results in

$$q_{\text{conv}} + q_{\text{diff}} + q_{\text{rad in}} = q_{\text{rad out}} + (\rho v)_w h_w + q_{\text{cond}} - \dot{m} h_{sol}. \tag{2.56}$$

Notice that the term q_{cond} requires knowledge of the temperature distribution inside of the solid to be calculated precisely. A simplified surface energy balance, similar to [ZA99], is used to avoid a complicated flow/solid coupling and allowing the focus of the simulation to stay on boundary-layer instability. The conduction of energy into the solid for quasi-stationary ablation can be roughly approximated as $q_{\text{cond}} = \dot{m} c_p T_w$ where c_p is the specific heat of the graphite ablator. Recalling that by definition $h_{sol} = c_p T_w$, and neglecting radiation from the fluid to the wall, the final energy balance yields

$$k_T \frac{\partial T}{\partial n} + k_V \frac{\partial T_V}{\partial n} + \sum_{s=1}^{ns} \rho h_s D_s \frac{\partial c_s}{\partial n} = \sigma \epsilon T^4 + \dot{m} \sum_{s=1}^{ns} c_s h_{s,o} \tag{2.57}$$

where

$$h_{s,o} = \left(c_{v,s} + \frac{R}{M_s} \right) T + e_{v,s} + h_s^o + \frac{1}{2} \left(u_1^2 + u_2^2 + u_3^2 \right) \tag{2.58}$$

and all values and derivatives are taken at the wall. For the carbon surface, $\epsilon = 0.9$ and σ is the Stefan-Boltzmann constant. Each derivative is taken normal to the surface where n represents the direction normal to the surface. Derivatives of 5th-order Lagrange polynomials are used to compute the normal derivatives at the surface.

The surface mass balance for each species is

$$\rho_s u_n - \rho D \frac{\partial c_s}{\partial n} = \dot{m}_s. \tag{2.59}$$

where each value and derivative is taken at the wall. The total mass balance found from summing Eq. (2.59) is

$$\rho u_n = \dot{m} \tag{2.60}$$

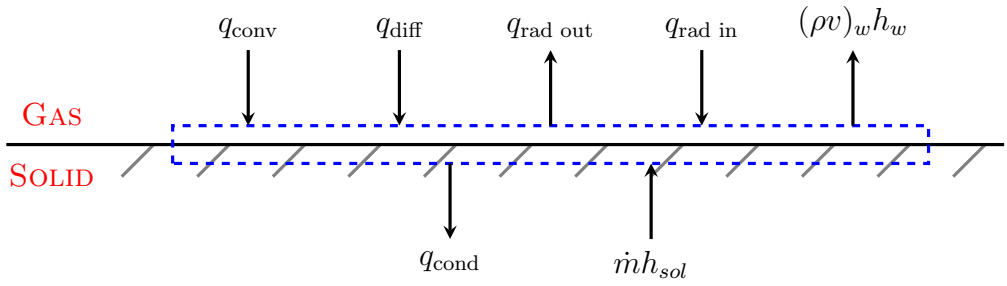

Figure 2.1: General energy transfer in surface control volume.

where the total mass flux is found from the sum of each species mass flux as

$$\dot{m} = \sum_{s=1}^{ns} \dot{m}_s. \tag{2.61}$$

Lastly, a condition for pressure is required at the surface. It is common to assume that $\frac{\partial p}{\partial n} = 0$ from the wall normal momentum equation for a wall with no slip. A finite velocity is obtained normal to the surface due to surface chemical reactions in ablation simulations making $\frac{\partial p}{\partial n} = 0$ invalid. Instead, the one-dimensional subsonic inlet conditions may be used as in [Kee94]. It is also common to use pressure extrapolation at the surface which is valid for a wall with no slip and a surface with a non-zero surface normal velocity. In the present work, 5th-order pressure extrapolation employing Lagrange polynomials is used instead of the one-dimensional subsonic inlet approach as extrapolation allows the high-order solution procedure for the interior points to set the wall pressure.

A Lagrange polynomial, which is used in this work for pressure extrapolation, is defined as

$$f(x) = \sum_{i=1}^{N} P_i f_i \tag{2.62}$$

where

$$P_i = \prod_{\substack{j=1 \\ j \neq i}}^{N} \frac{(x - x_j)}{(x_i - x_j)}. \tag{2.63}$$

Only a single dimensional extrapolation is performed because the simulation grid is assumed to be normal to the surface. Similarly, each of the derivatives in

Eqs. (2.57) and (2.59) is found by taking the derivative of a Lagrange polynomial which yields

$$\left.\frac{\partial f}{\partial x}\right|_{x_p} = \sum_{i=1}^{N} A_i f_i \tag{2.64}$$

where

$$A_i = \frac{\sum\limits_{\substack{j=1 \\ j\neq i}}^{N} \left[\prod\limits_{\substack{k=1 \\ k\neq i \\ k\neq j}}^{N} (x - x_k) \right]}{\prod\limits_{\substack{j=1 \\ j\neq i}}^{N} (x_p - x_j)}. \tag{2.65}$$

2.2 Five-Species Gas Model

It should be noted that, in Chs. 9 and 10, a five-species gas model is used instead of an eleven-species model. The five-species model (N_2, O_2, NO, N, and O) only simulates air. This is done when there is no ablation because it is much more computationally efficient to drop all the equations and terms resulting from ablation. Specifically, anything with carbon is dropped, because carbon is only created at the surface and is not present in the freestream for the simulated conditions. The boundary conditions at the surface are different for the five-species model and are given separately for each case. However, the remaining portion of the gas model that relates to five-species air remains unchanged.

CHAPTER 3

Numerical Methods

In this chapter, the high-order numerical methods will be covered for DNS, LST, and the cut-cell method. One section will be devoted to each method.

3.1 DNS Numerical Method

A high-order shock-fitting method developed for perfect-gas flow by Zhong [Zho98] has been extended for use on thermochemical nonequilibrium flows to compute the flowfield between the shock and the body. For shock-fitting computations the shock location is not known *a priori* so its position is solved along with the flowfield. Since the shock position is not stationary the grid used to compute the flowfield is a function of time. This leads to the coordinate transformation

$$\begin{cases} \xi = \xi(x,y,z) \\ \eta = \eta(x,y,z,t) \\ \zeta = \zeta(x,y,z) \\ \tau = t \end{cases} \Longleftrightarrow \begin{cases} x = x(\xi,\eta,\zeta,\tau) \\ y = y(\xi,\eta,\zeta,\tau) \\ z = z(\xi,\eta,\zeta,\tau) \\ t = \tau \end{cases} \tag{3.1}$$

where η is normal to the body, ξ is in the streamwise direction, ζ is in the transverse direction, $\zeta_t = 0$ and $\xi_t = 0$. The governing equation can then be transformed into computational space as

$$\frac{1}{J}\frac{\partial U}{\partial \tau} + \frac{\partial E'}{\partial \xi} + \frac{\partial F'}{\partial \eta} + \frac{\partial G'}{\partial \zeta} + \frac{\partial E'_v}{\partial \xi} + \frac{\partial F'_v}{\partial \eta} + \frac{\partial G'_v}{\partial \zeta} + U\frac{\partial (1/J)}{\partial \tau} = \frac{W}{J} \tag{3.2}$$

where J is the Jacobian of the coordinate transformation and

$$E' = \frac{F_1\xi_x + F_2\xi_y + F_3\xi_z}{J} \tag{3.3}$$

$$F' = \frac{F_1\eta_x + F_2\eta_y + F_3\eta_z}{J} \tag{3.4}$$

$$G' = \frac{F_1\zeta_x + F_2\zeta_y + F_3\zeta_z}{J} \tag{3.5}$$

$$E'_v = \frac{G_1\xi_x + G_2\xi_y + G_3\xi_z}{J} \tag{3.6}$$

$$F'_v = \frac{G_1\eta_x + G_2\eta_y + G_3\eta_z}{J} \tag{3.7}$$

$$G'_v = \frac{G_1\zeta_x + G_2\zeta_y + G_3\zeta_z}{J}. \tag{3.8}$$

A Lax-Friedrichs flux splitting approach is used to split the inviscid flux terms into positive and negative parts yielding

$$F' = F'_+ + F'_- \tag{3.9}$$

where

$$F'_+ = \frac{1}{2}\left(F' + \lambda U\right) \tag{3.10}$$

$$F'_- = \frac{1}{2}\left(F' - \lambda U\right) \tag{3.11}$$

and where λ is a positive parameter chosen to be larger than the local maximum eigenvalues of F_j. For example,

$$\lambda = \frac{|\nabla\eta|}{J}\left(\sqrt{(\epsilon c)^2 + u'^2} + c\right) \tag{3.12}$$

where u' is the transformed velocity in the η direction, $\epsilon = 0.05$, and c is the speed of sound.

A seven point stencil is then used to discretize the spatial derivatives

$$\frac{df_i}{dx} = \frac{1}{hb_i}\sum_{k=-3}^{3}\alpha_{i+k}f_{i+k} - \frac{\alpha}{6!b_i}h^5\left(\frac{\partial f^6}{\partial^6 x}\right) \tag{3.13}$$

where

$$a_{i\pm3} = \pm\,1 + \frac{1}{12}\alpha, \qquad a_{i\pm2} = \mp\,9 - \frac{1}{2}\alpha \tag{3.14}$$

$$a_{i\pm1} = \pm\,45 + \frac{5}{4}\alpha, \qquad a_i = -\,\frac{5}{3}\alpha \tag{3.15}$$

$$b_i = 60 \tag{3.16}$$

and where $\alpha < 0$ is a fifth order upwind explicit scheme and $\alpha = 0$ reduces to a sixth order central scheme. The upwinded inviscid terms, such as $\frac{\partial F'_{\pm}}{\partial \eta}$, use $\alpha = -6$ and the downwinded inviscid terms use $\alpha = 6$. Choosing $\alpha = \pm 6$ yields a low dissipation fifth order upwinded difference. The viscous terms are discretized using $\alpha = 0$. Second order derivatives are computed by applying the first order derivative operator twice.

Once the derivative operators are discretized, the method of lines approach is used to advance the solution in time. This approach starts with

$$\frac{\partial U}{\partial \tau} = L\left(U, \tau\right) \tag{3.17}$$

where $L\left(U, \tau\right)$ is obtained from discretizing the derivatives in Eq. (3.2) and applying boundary conditions. Multiple time advancement schemes were used to advance the solution in time. The time advancement scheme used for a particular case was chosen based on the flow conditions.

The first and most basic scheme implemented here is Explicit Euler. This scheme results in

$$U^{n+1} = U^n + \Delta\tau L\left(U^n\right) \tag{3.18}$$

where U^n is at time τ_0 and U^{n+1} is at time $\tau_0 + \Delta\tau$. This scheme, at times, resulted in excessively small time steps brought about by the stiffness from the source terms. This was most evident directly downstream of the bow shock near the nose of a blunt body where the energy modes and chemical reactions changed rapidly. Away from the nose region, this scheme had adequate performance.

The second scheme is an explicit third-order Runge-Kutta scheme described in [Wil80]. This scheme is designed to minimize memory usage. It is mathematically defined as

$$U^{n+1} = U^n + \frac{1}{6}k_1 + \frac{3}{10}k_2 + \frac{8}{15}k_3 \tag{3.19}$$

where

$$k_1 = \Delta\tau L\left(U^n, \tau_0\right) \tag{3.20}$$

$$k_2 = \Delta\tau L\left(U^n + \frac{1}{3}k_1, \tau_0 + \frac{1}{3}\Delta\tau\right) \tag{3.21}$$

$$k_3 = \Delta\tau L\left(U^n - \frac{3}{16}k_1 + \frac{15}{16}k_2, \tau_0 + \frac{3}{4}\Delta\tau\right). \tag{3.22}$$

This scheme also had the same problems as explicit Euler when dealing with the stiffness of the thermochemical nonequilibrium equations. However, it has significantly less temporal error than explicit Euler.

The last scheme used is a semi-implicit scheme where the fluxes are treated explicitly and the source term is treated implicitly. The equation to be solved is rewritten as

$$\frac{\partial U}{\partial \tau} - L\left(U, \tau\right) - W\left(U\right) = 0 \tag{3.23}$$

which separates the source term so it may be treated separately. A first-order forward discretization is used for $\frac{\partial U}{\partial \tau}$ and a trapezoidal method is used for the source term resulting in

$$U^{n+1} - \frac{\Delta\tau}{2}W\left(U^{n+1}\right) - U^n - \Delta\tau L\left(U^n, \tau_0\right) - \frac{\Delta\tau}{2}W\left(U^n\right) = 0. \tag{3.24}$$

This is a non-linear equation that must be solved iteratively. However, note that the source terms are not coupled across grid points making this a point implicit scheme. Therefore, the non-linear system to be solved is local to each grid point making it trivially parallelizable on any multi-processor machine.

The nonlinear Newton's method is used to solve the system of equations. The starting point to apply the non-linear Newton method to this system of equations

is to define

$$Q = U^{n+1} - \frac{\Delta\tau}{2} W\left(U^{n+1}\right) - U^n - \Delta\tau L\left(U^n\right) - \frac{\Delta\tau}{2} W\left(U^n\right) = 0 \tag{3.25}$$

and note that a truncation of the Taylor series expansion gives

$$\frac{\partial Q}{\partial U^{n+1}} \Delta U = -Q \tag{3.26}$$

where

$$\Delta U = U^{n+1} - U^n. \tag{3.27}$$

Taking the partial derivative $\partial Q / \partial U^{n+1}$ and substituting in for Q results in the system of equations

$$\left(I - \frac{\Delta\tau}{2} \frac{\partial W\left(U^{n+1}\right)}{\partial U^{n+1}}\right) \Delta U = -U^{n+1} + \frac{\Delta\tau}{2} W\left(U^{n+1}\right) + R^n \tag{3.28}$$

where I is the identity operator and

$$R^n = U^n + \Delta\tau L\left(U^n, \tau_0\right) + \frac{\Delta\tau}{2} W\left(U^n\right). \tag{3.29}$$

The steps of the nonlinear Newton's method is then to solve Eq. (3.28) for ΔU, update U^{n+1} using Eq. (3.27), and repeat until some convergence criteria is met. Commonly this solution procedure required two to four steps before converging to machine epsilon on a 64 bit machine with double precision variables.

The semi-implicit method was implemented to deal with the stiffness introduced by the source terms. Specifically, in the nose region of some blunt cones tested there was difficulty in getting a smooth and converged solution at the first few points downstream of the bow shock. This semi-implicit treatment did help to alleviate the time restraint caused by the stiffness and smooth out the solution in regions with large stiffness. However, in regions downstream of the nose where the source terms introduced less stiffness, the extra computational costs of this method were not justified by a substantial decrease in the time step.

3.1.1 Shock-Fitting Formulation

In the current shock-fitting formulation, the shock is located at

$$\eta\left(x,y,z,t\right)=\eta_{\max}=\text{constant} \tag{3.30}$$

and is treated as a computational boundary. The grid points at $\eta_{\max}$ are assumed to be immediately downstream of the shock. In the freestream, the flow is assumed to be in thermal equilibrium and the chemical composition of the flow is fixed. The shock is assumed to be infinitely thin resulting in no relaxation as the flow crosses the shock. There is no relaxation because the relaxation rates are finite. This leads to the chemical composition remaining constant across the shock, as well as the vibration temperature. The relaxation zone is entirely downstream of the shock since neither process has any time to relax across the shock.

Under these assumptions, the Rankine-Hugoniot jump conditions are

$$p_s=p_\infty\left[1+\frac{2\gamma}{\gamma+1}\left(M_{n,\infty}^2-1\right)\right] \tag{3.31}$$

$$\rho_s=\rho_\infty\left[1+\frac{\left(\gamma+1\right)M_{n,\infty}^2}{\left(\gamma-1\right)M_{n,\infty}^2+2}\right] \tag{3.32}$$

$$u_{n,s}=v_n+\frac{\rho_\infty}{\rho_s}\left(u_{n,\infty}-v_n\right) \tag{3.33}$$

$$\mathbf{u}_{t,s}=\mathbf{u}_{t,\infty}=\mathbf{u}_\infty-u_{n,\infty}\mathbf{n} \tag{3.34}$$

$$\mathbf{u}_s=\mathbf{u}_{t,\infty}+u_{n,s}\mathbf{n}=\mathbf{u}_\infty+\left(u_{n,s}-u_{n,\infty}\right)\mathbf{n} \tag{3.35}$$

$$c_s=c_\infty \tag{3.36}$$

$$T_{V,s}=T_{V,\infty} \tag{3.37}$$

where the subscripts ∞ and s denote the freestream and the region immediately downstream of the shock, respectively. Here, $M_{n,\infty}$ is the normal component of the freestream Mach number relative to the shock, $\mathbf{u}$ is the velocity vector, u_n is the normal velocity component, and $\mathbf{u}_t$ are the tangential velocity components. To use the Rankine-Hugoniot jump conditions, the grid velocity (v_n) is required.

The definition of the grid velocity may be obtained from the normal vector to the shock front which is

$$\mathbf{n} = \frac{\eta_x \,\hat{i} + \eta_y \,\hat{j} + \eta_z \,\hat{k}}{|\nabla \eta|}. \tag{3.38}$$

From this, the velocity of the shock front along $\mathbf{n}$ is found to be

$$v_n = \frac{-\eta_t}{|\nabla \eta|}. \tag{3.39}$$

To determine the grid velocity, information from inside the flow domain is required. To obtain this information, the Rankine-Hugoniot relations may be rewritten as

$$F'_s = F'_\infty \tag{3.40}$$

where the inviscid flux term F' is defined as

$$F' = \frac{F_1\eta_x + F_2\eta_y + F_3\eta_z + U\eta_t}{J}. \tag{3.41}$$

Substituting the definition of F' into Eq. (3.40) and moving all terms to the left-hand-side it is found that

$$(F_s - F_\infty) \cdot \mathbf{a} + (U_s - U_\infty)\, b = 0 \tag{3.42}$$

where

$$\mathbf{a} = \left(\frac{\eta_x}{J}\right)_s \hat{i} + \left(\frac{\eta_y}{J}\right)_s \hat{j} + \left(\frac{\eta_z}{J}\right)_s \hat{k} \tag{3.43}$$

$$b = \left(\frac{\eta_t}{J}\right)_s. \tag{3.44}$$

To put Eq. (3.42) in a form that is suitable for time integration, a temporal derivative must be taken which results in

$$\underbrace{\frac{\partial F_s}{\partial \tau} \cdot \mathbf{a} + \frac{\partial U_s}{\partial \tau} b}_{\substack{\text{unsteadiness} \\ \text{downstream of shock}}} - \underbrace{\left(\frac{\partial F_\infty}{\partial \tau} \cdot \mathbf{a} + \frac{\partial U_\infty}{\partial \tau} b\right)}_{\substack{\text{freestsream} \\ \text{unsteadiness}}} + \underbrace{(F_s - F_\infty) \cdot \frac{\partial \mathbf{a}}{\partial \tau} + (U_s - U_\infty)\, \frac{\partial b}{\partial \tau}}_{\text{shock movement}} = 0 \tag{3.45}$$

where terms arise that account for unsteadiness in flow variables upstream and downstream of the shock, as well as shock movement during the simulation. Note that for a steady meanflow simulation the terms that account for freestream unsteadiness are set to zero. However, when introducing perturbations in the freestream for an unsteady DNS, these terms are non-zero.

Now the partials of the inviscid flux vector need to be put in terms of the conserved variables. This may be done through the chain rule yielding

$$-\left(U_s - U_\infty\right)\frac{\partial b}{\partial \tau} = B'_s\frac{\partial U_s}{\partial \tau} - B'_\infty\frac{\partial U_\infty}{\partial \tau} + \left(F_s - F_\infty\right)\cdot\frac{\partial \mathbf{a}}{\partial \tau} \tag{3.46}$$

where

$$B'_s = \frac{\partial F'}{\partial U}. \tag{3.47}$$

The Jacobian matrix, B'_s, has the eigenvalues

$$\frac{|\nabla\eta|}{J}\left(u_n - v_n\right)_s, \ldots, \frac{|\nabla\eta|}{J}\left(u_n - v_n\right)_s, \frac{|\nabla\eta|}{J}\left(u_n - v_n - c\right)_s, \frac{|\nabla\eta|}{J}\left(u_n - v_n + c\right)_s \tag{3.48}$$

where c is the speed of sound. The eigenvalue corresponding to the characteristic field that approaches the shock from downstream is $\frac{|\nabla\eta|}{J}\left(u_n - v_n + c\right)_s$. The left eigenvector associated with this eigenvalue is

$$\mathbf{l} = \frac{1}{c^2}\begin{bmatrix} (\gamma-1)\left(\frac{1}{2}\mathbf{u}\cdot\mathbf{u} - h_r^0 - c_{v,r}T\right) - cu_n + RT/M_r \\ cn_x - (\gamma-1)\,u \\ cn_y - (\gamma-1)\,v \\ cn_z - (\gamma-1)\,w \\ \gamma - 1 \\ -(\gamma-1) \end{bmatrix}_s. \tag{3.49}$$

The left eigenvector behind the shock satisfies the relation

$$\mathbf{l}\cdot B'_s = \frac{|\nabla\eta|}{J}\left(u_n - v_n + c\right)_s\mathbf{l}. \tag{3.50}$$

Multiplying both sides of Eq. (3.46) by the left eigenvector and then using Eq. (3.50), the final relation for the shock velocity is obtained where

$$\frac{\partial b}{\partial \tau} = \frac{-1}{\mathbf{l}\cdot(U_s - U_\infty)} \left[\frac{|\nabla\eta|}{J}\left(u_n - v_n + c\right)_s \mathbf{l}\cdot\frac{\partial U_s}{\partial \tau} - (\mathbf{l}\cdot B'_\infty)\frac{\partial U_\infty}{\partial \tau} + \mathbf{l}\cdot(F_s - F_\infty)\cdot\frac{\partial \mathbf{a}}{\partial \tau}\right]. \quad (3.51)$$

Notice that this equation depends on $\partial\mathbf{a}/\partial\tau$. Therefore, two equations need to be integrated in time to obtain the grid velocity: $\partial\mathbf{a}/\partial\tau$ and $\partial b/\partial\tau$. These equations are integrated along with the flow solution in the computational domain with the procedures described in Sec. 3.1 to solve for the grid velocity. Once the grid velocity is known, the Rankine-Hugoniot jump conditions may be used to set the solution at $\eta_{\max}$.

3.1.2 Surface Chemistry Model Iterative Solution Method

The set of equations that defines the surface chemistry model described in Sec. 2.1 is nonlinear, and requires an iterative solution at every wall grid point. Also, there are surface-normal derivatives in the equations that can couple the boundary points together. Fortunately, the physical grid used here is always in the surface-normal direction, so there is no coupling of the solution between grid points. In other words, an iterative method is required to solve the surface chemistry equations at each surface grid point, and this solution is independent of the solution at other surface grid points.

The iterative method used for solution of the equations is the nonlinear Newton's method. For the solution procedure, it is convenient to express the equations of the surface chemistry model as

$$F_i(\mathbf{x}) = 0, \quad i = 1, 2, \ldots, ns+1 \quad (3.52)$$

for

$$\mathbf{x} = (\rho_1, \rho_2, \ldots, \rho_{ns}, T) \quad (3.53)$$

where

$$F_i(\mathbf{x}) = c_i\dot{m} - \rho D_i \frac{\partial c_i}{\partial n} - \dot{m}_i, \quad i = 1, 2, \ldots, ns-1 \tag{3.54}$$

$$F_{ns}(\mathbf{x}) = p - \sum_{s=1}^{ns} \rho_s \frac{R}{M_s} T \tag{3.55}$$

$$F_{ns+1}(\mathbf{x}) = k\frac{\partial T}{\partial n} + k_V \frac{\partial T_V}{\partial n} + \rho \sum_{s=1}^{ns} h_s D_s \frac{\partial c_s}{\partial n} - \sigma\epsilon T^4 - \dot{m} \sum_{s=1}^{ns} c_s h_{s,o}. \tag{3.56}$$

Notice that only $ns-1$ species mass balance equations are required to reach a solution. It doesn't matter which of the equations are dropped. Dropping any of the species mass balance equations (Eq. (2.59)) will give the same result.

A first-order truncation and rearrangment of the Taylor series of F_i gives

$$-F_i(\mathbf{x}) = \frac{\partial F_i}{\partial x_j}\delta x_j \tag{3.57}$$

where the individual elements of the Jacobian $(\frac{\partial F_i}{\partial x_j})$ are given in Appendix A and

$$\delta x_j = x_j^{n+1} - x_j^n. \tag{3.58}$$

The steps to solution are then to use the old values to solve Eq. (3.57) for δx_j. Then, x_j^{n+1} is computed and the procedure is repeated, after setting $x_j^n = x_j^{n+1}$. The iteration is stopped when $\delta x_j / x_j \leq 1 \times 10^{-10}$. This method generally required two iterations to converge and reliably converged, assuming a good initial guess was known.

3.2 High-Order LST Numerical Method

Once meanflow solutions have been obtained from a suitable meanflow solver, such as the one given in [MZ14], it is possible to analyze flow instability using linear stability analysis. For the linear stability analysis, a body-fitted orthogonal curvilinear coordinate system is used for axisymmetric bodies where x is in the streamwise direction, y is in the wall-normal direction, z is in the transverse direction, and the origin is located on the body surface. Curvature in the streamwise

and transverse directions is included similar to [MS91]. Elemental lengths are defined as $h_1\,dx$, dy, and $h_3\,dz$ where

$$h_1 = 1 + \kappa y \tag{3.59}$$

$$h_3 = r_b + y\ cos\,(\theta) \tag{3.60}$$

and where κ is the streamwise curvature, r_b is the local radius of the body, and θ is the local half angle of the body. The coordinate system for a flat plate is recovered by setting h_1 and h_3 to unity. For a straight cone, only h_3 is required and h_1 is set to unity.

The derivation of the thermochemical nonequilibrium LST equations follows the work of [Hud96] excepting the species velocity terms which are substituted into the governing equations before linearization similar to [KUT12]. The LST equations are derived from the non-conservative form of the governing equations where the instantaneous flow is comprised of a mean and fluctuating component $q = \bar{q} + q'$. Here, q represents any flow variable such as velocity, density, temperature, etc. The instantaneous flow is then substituted into the governing equations where the steady flow is assumed to satisfy the governing equations and is subtracted out. The meanflow is assumed to be a function of the wall-normal coordinate y only, i.e., $\bar{q}(x, y, z) \approx \bar{q}(y)$ and the flow disturbances are assumed to be small, i.e., linear. The perturbations are then assumed to be in the form of a normal mode described by

$$q'\,(x, y, z) = \hat{q}\,(y) \exp\left[i\,(\alpha x + \beta z - \omega t)\right] \tag{3.61}$$

where ω is the circular frequency of the mode and α and β are the wave numbers. Commonly, ω and β are assumed to be real and the wave number α is assumed to be complex which means the modes grow in space rather than time. If ω is complex and α and β are real then the modes grow in time rather than space. A negative imaginary part of the wave number α results in disturbance growth while a positive value results in disturbance decay. If $\alpha_i = 0$ then there is no growth or

decay of the disturbance which is termed a neutral disturbance. For comparison to DNS, the spatial stability approach is used, i.e., α is complex which results in the dispersion relation $\alpha = \Omega(\omega, \beta)$.

Substituting in the normal mode form for the perturbations reduces the problem to a coupled set of ns+5 ordinary differential equations

$$\left(\mathbf{A}\frac{d^2}{dy^2} + \mathbf{B}\frac{d}{dy} + \mathbf{C}\right)\vec{\phi} = \vec{0} \tag{3.62}$$

where $\vec{\phi} = \{\hat{\rho}_1, \hat{\rho}_2, ..., \hat{\rho}_{ns}, \hat{u}, \hat{v}, \hat{w}, \hat{T}, \hat{T}_V\}^T$ and $\mathbf{A}$, $\mathbf{B}$, and $\mathbf{C}$ are complex square matrices of size ns+5. This is now a boundary value problem where the derivative operators can be discretized and the equations solved numerically.

For hypersonic compressible boundary layers, it is important to have high grid resolution near the generalized inflection point [Mac84]. Two different grid types were used. The first grid is used to cluster grid points around the inflection point only and has been used by previous researchers [HCC97]. It is defined so that

$$y = \frac{a\eta}{b - \eta} \tag{3.63}$$

where

$$a = \frac{y_{\max} y_i}{(y_{\max} - 2y_i)} \tag{3.64}$$

$$b = 1 + \frac{a}{y_{\max}} \tag{3.65}$$

and $y_{\max}$ is the outer domain boundary near the shock, y_i is the location of the generalized inflection point, and η runs from zero to one. For hypersonic boundary layers, the generalized inflection point moves toward the boundary layer edge so y_i may be placed near the boundary layer edge. If grid metrics are required, they can be computed directly from Eq. (3.63).

The second grid uses two different functions to cluster points around the inflection point and near the wall. It will be called the cosine-exponential grid. For some boundary layers analyzed in this research, there was a sharp increase

in the eigenfunctions near the wall for the temperatures and densities that was not captured correctly with the grid that only clustered points near the inflection point. The cosine-exponential grid was much more effective for boundary layers with strong changes in the eigenfunctions near the wall. The cosine-exponential grid is defined so that

$$y = y_i \left(1 - \cos\left(\pi\eta\right)\right)/2, \qquad 0 \leq y \leq y_i \tag{3.66}$$

$$y = y_i + \frac{a\eta}{b - \eta}, \qquad y > y_i \tag{3.67}$$

where

$$a = \left(y_{\max} - y_i\right) s \tag{3.68}$$

$$b = \frac{1 + a}{y_{\max} - y_i} \tag{3.69}$$

and s is a stretching parameter that stretches towards y_i for $s < 1$ and away for $s > 1$. Here, $s = 0.5$ was used. Similar to the previous grid, $y_{\max}$ is the outer domain boundary near the shock, y_i is the location of the generalized inflection point, and η runs from zero to one.

With the grid defined, it is now possible to discretize the derivative operators. In [Mal90] there is an excellent overview of numerical methods suitable for stability calculations of hypersonic flows which include finite difference, compact difference, and spectral formulations. A fourth order central difference scheme has been used by previous researchers [Hud96, Cha04] to good effect. Here, a different approach than what has previously been used for hypersonic stability calculations is taken. The first and second derivative operators in the wall-normal direction are discretized by taking derivatives of Lagrange polynomials in physical space. If x_p is the grid point where a first derivative is required then

$$\left.\frac{\partial f}{\partial x}\right|_{x_p} = \sum_{i=1}^{N} A_i f_i \tag{3.70}$$

where

$$A_i = \frac{\sum_{\substack{j=1 \\ j\neq i}}^{N} \prod_{\substack{k=1 \\ k\neq i \\ k\neq j}}^{N} (x_p - x_k)}{\prod_{\substack{m=1 \\ m\neq i}}^{N} (x_i - x_m)} \tag{3.71}$$

and N is the total number of points in the stencil. Similarly, for a second derivative at x_p

$$\left.\frac{\partial^2 f}{\partial x^2}\right|_{x_p} = \sum_{i=1}^{N} B_i f_i \tag{3.72}$$

where

$$B_i = \frac{\sum_{\substack{\ell=1 \\ \ell\neq i}}^{N} \sum_{\substack{j=1 \\ j\neq i \\ j\neq \ell}}^{N} \prod_{\substack{k=1 \\ k\neq i \\ k\neq j \\ k\neq \ell}}^{N} (x_p - x_k)}{\prod_{\substack{m=1 \\ m\neq i}}^{N} (x_i - x_m)}. \tag{3.73}$$

For the interior points, a centered stencil is used thus requiring an odd number of points. An even number of points may be used which would require an offset stencil. For grid points near the boundary, an offset stencil is used where the number of points in the stencil is maintained. It should be noted that the largest source of numerical error from approximating the derivatives in this fashion will come from the second derivative approximation. To decrease this error, more points may be used in the second derivative stencil than the first derivative stencil, but here an equal number of points are used for each derivative approximation. These derivative operators are applied in physical space rather than computational space to avoid Runge's phenomena where spurious oscillations can occur for a one-sided stencil with a high order of approximation. Also, in areas of low grid density, this method is susceptible to odd-even decoupling of the solution. If the derivative operators of Eqs. (3.70) and (3.72) are applied to a centered stencil in computational space, the standard central finite difference coefficients are obtained. In other words, the fourth order method used by previous researchers for interior

points can be obtained from the current method using a five point stencil in computational space.

There are a couple advantages to approximating the derivatives in this fashion. Once the subroutines for computing the coefficients are set up, it is trivial to change the number of points used to approximate the derivatives. This makes it easy to switch from low to high order or *vice versa* without making any changes to the code as the order of the method is dependent upon the number of points chosen for the derivative stencils. Since the derivatives are taken in physical space rather than computational space, grid metrics are not required. Although it is not used here, this allows an arbitrary placement of grid points within the computational domain. Also, the formulation for derivatives at the boundary can use the same derivative approximations which easily integrates high-order boundary conditions into the code. As one of the main focal points in the current work for developing a thermochemical nonequilibrium LST code is to include gas/surface interactions, wall-normal derivatives are quite important making this technique a good fit.

After discretization, nonlinearities exist in α, so the global method suggested in [Mal90] is used to compute the eigenvalue spectrum with $\alpha^2 = 0$. This method computes the eigenvalues from a generalized eigenvalue problem $\tilde{A}\vec{\phi} = \alpha\tilde{B}\vec{\phi}$ where the LAPACK [ABB99] subroutine ZGGEV is used to obtain a solution. It is possible to avoid the computationally intensive global method and obtain an initial guess for α from a nearby streamwise location, similar frequency, or a DNS simulation *assuming* the unsteady DNS results are available.

Once an initial guess for α is obtained, the local method is used where α^2 is no longer dropped. This results in

$$\bar{A}\phi = \bar{B} \tag{3.74}$$

where $\bar{A}$ is obtained from discretizing Eq. (3.62). Notice that for the conditions given, $\bar{B} = 0$. To avoid a trivially zero solution, $\bar{B}$ should ideally be non-zero.

This can be done by replacing one of the boundary conditions by a free parameter and iterating α until this free parameter approaches zero. When it nears zero, the solution of Eq. (3.74) approaches the solution of the homogeneous problem, and the correct ϕ and α have been computed.

Newton's method is used to iterate α, and drive the free parameter to zero. For Newton's method, the update step is

$$\alpha^{n+1} = \alpha^n - \frac{u(0)}{\frac{\partial u(0)}{\partial \alpha}} \tag{3.75}$$

where $u(0)$ is the free parameter used in place of the boundary condition for the wall-tangent velocity. By taking a derivative of Eq. (3.74) with respect to α and rearranging, it is found that

$$\bar{A}\frac{\partial \phi}{\partial \alpha} = -\frac{\partial \bar{A}}{\partial \alpha}\phi \tag{3.76}$$

where the solution will yield $\frac{\partial u(0)}{\partial \alpha}$ which is required to update α. One might think the addition of solving another linear system of the same size would add significant computational cost, making the secant method an attractive alternative. However, the solution of Eqs. (3.74) and (3.76) have the same LU decomposition of the matrix $\bar{A}$, assuming that LU factorization is used to solve the system of equations. This dramatically decreases the computational cost. For the cases tested here, it was found that the slight increase in computation for Newton's method was outweighed by the faster convergence and more reliable convergence of Newton's method over the secant method. For solution of the system of equations using LU factorization, the LAPACK subroutine ZGESV is used.

3.2.1 LST Boundary Conditions

Boundary conditions are required in the freestream and at the wall for LST. In the freestream, all perturbations are zero except the wall-normal velocity perturbation which is found from the mass conservation equation similar to [Stu91]. The freestream boundary conditions are set near $0.98H_s$ where H_s is the height of the

shock measured from the wall. It is possible to linearize the Rankine-Hugoniot jump conditions at the shock which would be required for a mode with an eigenfunction that oscillates in the freestream such as the unstable supersonic modes shown in [CVM97]. However, the unstable second mode studied here has a decaying eigenfunction in the freestream where the current boundary conditions used are suitable.

The boundary conditions at the wall are slightly more complicated. There are $ns+5$ independent variables in the stability calculations, therefore $ns+5$ conditions are required at the wall. The approach taken here is to linearize all of the equations used to set the wall boundary conditions in the mean flow simulation. The linearization procedure is consistent with the linearization of the interior flow. Of these $ns+5$ conditions, the simplest are the no slip in the wall tangent directions resulting in $\hat{u_1} = \hat{u_3} = 0$. The surface energy balance in Eq. (2.57) can be linearized resulting in

$$\frac{dT}{dy}k' + k\frac{\partial T'}{\partial y} + \frac{dT_V}{dy}k'_V + k_V\frac{\partial T'_V}{\partial y} + \rho\sum_{s=1}^{ns} h_s D_s \frac{\partial c'_s}{\partial y} + \rho\sum_{s=1}^{ns} h_s \frac{\partial c_s}{\partial y} D'_s + \rho\sum_{s=1}^{ns} D_s \frac{\partial c_s}{\partial y} h'_s + \left(\sum_{s=1}^{ns} h_s D_s \frac{\partial c_s}{\partial y}\right)\rho' - 4\sigma\epsilon T^3 T' - \dot{m}\sum_{s=1}^{ns} c_s h'_{s,o} - \dot{m}\sum_{s=1}^{ns} h_{s,o} c'_s - \left(\sum_{s=1}^{ns} c_s h_{s,o}\right)\dot{m}' = 0 \tag{3.77}$$

where the perturbation of the diffusion coefficients and the species mass flux terms are dependent on the specific gas model and surface chemistry model used. They can be found from a first order Taylor series expansion. Note that the overbars have been dropped from the steady terms for simplicity and y denotes the wall-normal coordinate. As there are $ns+5$ independent variables, it is required to put Eq. (3.77) in terms of these independent variables. Then the normal mode form for the perturbations may be substituted for the equation to be suitable as a boundary condition. For the gas model and surface chemistry model given here,

this results in

$$\frac{dT}{dy}\left(\sum_{r=1}^{ns}\frac{\partial k}{\partial \rho_r}\hat{\rho}_r+\frac{\partial k}{\partial T}\hat{T}\right)+k\frac{\partial \hat{T}}{\partial y}+\frac{dT_V}{dy}\left(\sum_{r=1}^{ns}\frac{\partial k_V}{\partial \rho_r}\hat{\rho}_r+\frac{\partial k_V}{\partial T}\hat{T}+\frac{\partial k_V}{\partial T_V}\hat{T}_V\right)$$
$$+k_V\frac{\partial \hat{T}_V}{\partial y}+\rho\sum_{s=1}^{ns}h_sD_s\frac{\partial}{\partial y}\left(\frac{\hat{\rho}_s}{\rho}-\frac{c_s}{\rho}\sum_{r=1}^{ns}\hat{\rho}_r\right)+\rho\sum_{s=1}^{ns}h_s\frac{\partial c_s}{\partial y}\left(\sum_{r=1}^{ns}\frac{\partial D_s}{\partial \rho_r}\hat{\rho}_r+\frac{\partial D_s}{\partial T}\hat{T}\right)$$
$$+\rho\sum_{s=1}^{ns}D_s\frac{\partial c_s}{\partial y}\left[\left(c_{v,s}+\frac{R}{M_s}\right)\hat{T}+\frac{\partial e_{v,s}}{\partial T_V}\hat{T}_V\right]+\left(\sum_{s=1}^{ns}h_sD_s\frac{\partial c_s}{\partial y}\right)\sum_{r=1}^{ns}\hat{\rho}_r-4\sigma\epsilon T^3\hat{T}$$
$$-\dot{m}\sum_{s=1}^{ns}c_s\left[\left(c_{v,s}+\frac{R}{M_s}\right)\hat{T}+\frac{\partial e_{v,s}}{\partial T_V}\hat{T}_V+\frac{\dot{m}}{\rho}\hat{v}\right]-\frac{\dot{m}}{\rho}\sum_{s=1}^{ns}h_{s,o}\left(\hat{\rho}_s-c_s\sum_{r=1}^{ns}\hat{\rho}_r\right)$$
$$-\sum_{n=1}^{ns}c_nh_{n,o}\left[\sum_{r=1}^{ns}\sum_{s=1}^{ns}\frac{\partial \dot{m}_s}{\partial \rho_r}\hat{\rho}_r+\sum_{s=1}^{ns}\frac{\partial \dot{m}_s}{\partial T}\hat{T}\right]=0 \quad (3.78)$$

where all values and derivatives are defined at the wall. To this point the derivation of the linearized surface energy balance has made no assumptions about parallel flow, so it is still applicable to non-parallel methods. Recall from Eq. (2.60) that $\dot{m}=\rho u_n$ which requires any terms containing $\dot{m}$ to be set to zero to enforce the parallel flow assumption. Also, note that this equation is in essence imposing an upper bound on the temperature perturbation at the wall. Mack [Mac84] notes that "for almost any frequency, it is not possible for the wall to do other than to remain at its mean temperature" which would require that $\hat{T}=0$. For ablative flows, the exact boundary between wall and fluid is a little less sharp. There may be melting of the surface material and/or pyrolosis gas injection that are not present for a standard non-porous, wall-bounded flow. Taking these physical mechanisms into account, it is quite possible for $\hat{T}\neq 0$. In reality, $\hat{T}$ at the surface may lie between these two extremes so it is useful to see how each boundary condition influences instabilities. Both of these cases are tested in Sec. 7.3. For either case of temperature perturbation, the wall is assumed to be in thermal equilibrium resulting in $\hat{T}_V=\hat{T}$.

Conditions on each species density perturbation are required at the wall. Eq. (2.59) gives the condition on the species density at the wall for the mean-

flow simulation. A linearization of this equation yields

$$\rho_s v' + \frac{\dot{m}}{\rho}\rho_s' - \rho D_s \frac{\partial}{\partial y}\left(\frac{\rho_s'}{\rho} - \frac{c_s}{\rho}\sum_{r=1}^{ns}\rho_r'\right) - \rho\frac{\partial c_s}{\partial y}D_s' - D_s\frac{\partial c_s}{\partial y}\sum_{r=1}^{ns}\rho_r' - \dot{m}_s' = 0 \quad (3.79)$$

where once again the overbars denoting steady conditions have been dropped for simplicity and $\dot{m}_s'$ is the species mass flux perturbation related to the specific gas/surface interaction model. Substituting in the normal mode for each independent perturbation gives ns wall conditions in the form

$$\rho_s \hat{v} + \frac{\dot{m}}{\rho}\hat{\rho}_s - \rho D_s \frac{\partial}{\partial y}\left(\frac{\hat{\rho}_s}{\rho} - \frac{c_s}{\rho}\sum_{r=1}^{ns}\hat{\rho}_r\right) - \rho\frac{\partial c_s}{\partial y}\left(\sum_{r=1}^{ns}\frac{\partial D_s}{\partial \rho_r}\hat{\rho}_r + \frac{\partial D_s}{\partial T}\hat{T}\right)$$
$$- D_s\frac{\partial c_s}{\partial y}\sum_{r=1}^{ns}\hat{\rho}_r - \sum_{r=1}^{ns}\frac{\partial \dot{m}_s}{\partial \rho_r}\hat{\rho}_r - \frac{\partial \dot{m}_s}{\partial T}\hat{T} = 0. \quad (3.80)$$

Once again note that the parallel flow assumption has not been made yet. To make the parallel flow assumption simply drop the terms with $\dot{m}$. Note that the equation can be further simplified if $\hat{T} = 0$ by dropping all $\hat{T}$ terms.

With the species surface mass balance linearized, recall that a total mass balance was used to set the wall-normal velocity (Eq. (2.60)) in the meanflow simulation. Further recall that this condition is found from a linear combination for each species surface mass balance. Therefore, a linearization of this equation will result in no new information at the boundary. For the boundary to be adequately constrained another equation is required. In the meanflow simulation, pressure extrapolation is used to account for the incoming characteristic at the wall. Linearizing the pressure extrapolation condition and substituting in the normal modes results in

$$\left(\sum_{s=1}^{ns}\rho_s\frac{R}{M_s}\hat{T}\right)_1 + \left(\sum_{s=1}^{ns}\frac{R}{M_s}T\hat{\rho}_s\right)_1 - \sum_{j=2}^{N}\gamma_j\left(\sum_{s=1}^{ns}\rho_s\frac{R}{M_s}\hat{T} + \sum_{s=1}^{ns}\frac{R}{M_s}T\hat{\rho}_s\right)_j = 0 \quad (3.81)$$

where the subscript 1 denotes the grid point at the wall, N is the number of points used, and γ_j are the weights for extrapolation. This accounts for the last required boundary condition and is used in place of a $\hat{v}$ equation. It is also

possible to linearize the total mass flux equation and substitute the linearized pressure extrapolation condition for one of the linearized surface mass balance equations. Both methods were tested and the differences between the two were negligible.

3.3 Cut-Cell Numerical Method

The cut-cell method follows that of [DWZ10] and the finite-difference stencils used in the cut-cell method follow that of [Gre14]. A schematic of the cut-cell grid is shown in Fig. 3.1. The curvilinear grid is only body-fitted to the body which causes the roughness element at the surface of the body to intersect the grid. The curvilinear grid, along with the roughness element, is then transformed from physical space into computational space using the coordinate transform given in Eq. (3.1). Note that the top of both domains is bounded by the shock and the bottom by the body.

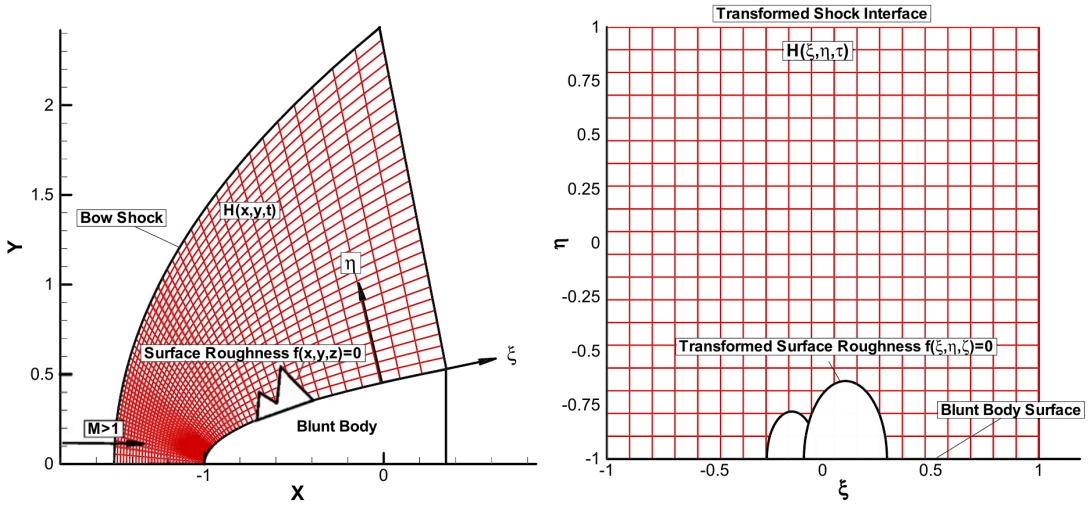

(a) (b)

Figure 3.1: Cut-cell grid in (a) the physical domain and (b) the computational domain from [DWZ10].

The first step in the cut-cell method is to locate the intersection of the irregular surface with the computational grid lines. Once this intersection is found, it is trivial to locate the same intersection in physical coordinates. The edge of the irregular surface may be defined as $\Gamma(x, y, z) = \gamma(\xi, \eta, \zeta) = 0$. This could be either some spline function used to fit a collection of points, or in the case of surface roughness, an elliptic or hyperbolic-tangent profile. Usually, the function Γ is known and it needs to be changed, through some mapping from physical to computational space, to a function of the computational coordinates.

Once in computational space, the function γ may intersect either the ξ, η, or ζ grid lines. For two-dimensional roughness, only the ξ and η grid lines need be considered. If the roughness function γ crosses an η grid line, then ξ is known and η must be found. Newton's method is used to solve for η and η is updated using

$$\eta^{n+1} = \eta^n - \frac{\gamma(\xi, \eta^n)}{d\gamma(\xi, \eta^n)/d\eta} \tag{3.82}$$

where the superscript n corresponds to the working step in Newton's method. The same method was used if the roughness intersected a ξ grid line. It was found that Newton's method was sensitive to the initial guess and could jump to nearby solutions if the initial guess was not close enough. To rectify this, the midpoint method was used to get the initial guess close enough that Newton's method could reliably converge on the proper solution. Since the physical grid is a function of time (see Eq. (3.1)), the intersection of the irregular surface and the computational grid changes with time. Therefore, the points where the irregular surface crosses the computational grid need to be found at every iteration.

Once the intersection of the irregular surface and the grid have been found, a point classification scheme is required to determine how a given point will be treated. Four different types of grid points are used: regular points, dropped points, irregular points, and boundary points. Figure 3.2 shows a schematic of point classification in the eta direction. Each of the four point types are shown

along with the location of the body overlapping the stencil. Regular points are points in the computational domain where the standard finite difference stencil, given in Eq. (3.13), is used. That is, there is no infringement of the roughness element onto any of the points used in the standard stencil. The standard stencil here is a centered seven point stencil so three points that are not boundary points are needed to either side of the point for it to be regular. This is shown in Fig. 3.2 where η_5 is the first point away from the body that meets this requirement.

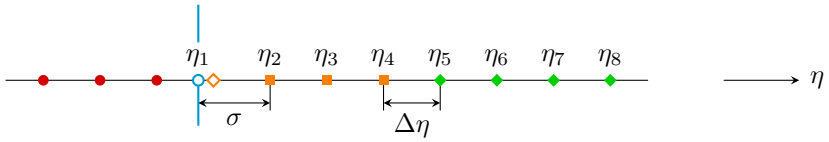

Figure 3.2: Point classification of η grid line for; regular points ◆, irregular points ■, boundary points ○, dropped points in all directions ●, and dropped points in the η direction only ◇. The body is denoted by —.

There are two types of dropped points. The first type of dropped points are points contained inside of the roughness element. They are denoted by ● in Fig. 3.2. They are not used for any numerical calculations. The second type is points that are deemed too close to boundary points. Locating these dropped points is done in each direction by determining σ which is the distance from the point to the body in computational space along a grid line. If σ is less than some predefined value, then the point is too close to the body and it is dropped, in that direction, from the finite-difference stencil. Note that, a point may be a dropped point in one grid direction and not in another. A reason for dropping points with a small σ is the time step requirement for stability can be severely limited if σ is excessively small. Here, $\sigma = 0.5$ is used in each grid direction and was found to perform satisfactorily. This choice of σ is made with the implicit assumption that the distance between two points in computational space in any grid direction is unity.

Boundary points are defined as any intersection of a grid line with the roughness element. They are not a part of the original Cartesian grid. At these points, extrapolation of interior flow variables, or their derivatives in the wall-normal direction, may be required as boundary conditions. A second-degree least-squares polynomial is used for extrapolation and to compute wall-normal derivatives. The polynomial is

$$f(x,y) = c_1 + c_2\Delta x + c_3\Delta y + c_4\Delta x^2 + c_5\Delta x\Delta y + c_6\Delta y^2 \tag{3.83}$$

where

$$\Delta x = x - x_{bp}, \quad \Delta y = y - y_{bp} \tag{3.84}$$

and where f is the interpolated variable, the coefficients $c_1, c_2, \ldots, c_6$ are found using a least-squares approximation, and the subscript bp refers to the physical location of the boundary point. The closest twenty one points by index were used to determine the coefficients. This same method was used in [Gre14] where it was found that a least-squares polynomial was more stable than a two-dimensional polynomial interpolation without a least-squares approximation.

Irregular points are points near the roughness element where the standard finite difference grid stencil cannot be used due to an overlap of the stencil with the body. These are points η_2, η_3, and η_4 in Fig. 3.2. Offset stencils, computed from derivatives of Lagrange polynomials, with a non-uniform spacing are used for the irregular points. Here, third-order and fourth-order offset stencils are used for inviscid terms while fourth-order and fifth-order offset stencils are used for the viscous terms. Following the schematic of Fig. 3.2, a derivative of the upwind flux for the jth irregular point in computational space is

$$\frac{\partial F_j'^{+}}{\partial \eta} = \frac{1}{\Delta\eta}\sum_{k=1}^{6} a_{j,k}^{+} F_{j,k}'^{+}. \tag{3.85}$$

The coefficients $a_{j,k}^{+}$ for the inviscid flux terms are given in Table D.1 along with the corresponding downwind coefficients. These coefficients are upwind biased.

Similarly to Eq. (3.85), the viscous flux may be found and the corresponding coefficients are given in Table D.2. It was shown in [Gre14] that a solution procedure using the coefficients in Tables D.1 and D.2 along with a fifth-order interior scheme resulted in a fourth-order method.

CHAPTER 4

DNS Validation

Three validation cases are computed with the shock-fitting code using the eleven species gas model and the surface chemistry model. Two cases are compared to simulations in [Kee94] and one case is compared to a simulation from [CM05a] that has corresponding experimental data. Recall that [Kee94] has served as a starting point for the gas model and surface chemistry model. It should be noted that [Kee94] and [CM05a] use shock-capturing methods where a shock-fitting method is used in this work.

4.1 Comparison to the $M_\infty = 15.99$ Simulation of PANT Case 1

The first test case freestream conditions come from experimental tests on graphite from the Passive Nosetip Technology (PANT) program [Woo75] and is called PANT Case 1. The experimental facility used to conduct these tests is the Arnold Engineering Development Center Aeroballistic Range G. The freestream conditions are given in Table 4.1. The geometry is a sphere cylinder with a nose radius of 0.635 cm. The grid shown in Figure 4.1, was chosen similar to [Kee94] using 32 points on the surface and 91 points in the surface normal direction. However, the shock-fitting method uses a two sided stretching in the wall normal direction to accurately capture relaxation processes just downstream of the shock whereas [Kee94] uses a one sided boundary layer stretching. In the shock-fitting code there

is no computation of the temperature within the graphite ablative material but [Kee94] does compute the temperature within the ablator. For a more reasonable comparison, a curve fit of [Kee94]'s simulated surface temperature was used to set the two surface temperatures rather than using the surface energy balance. Only the sphere region has been computed for comparison as this is the region where ablation effects are the most pronounced.

Table 4.1: Freestream conditions for PANT case 1.

Parameter	Value
M_∞	15.99
ρ_∞ [kg/m^3]	2.4093×10^{-2}
P_∞ [N/m^2]	2026.0
C_{N_2}	0.7635
C_{O_2}	0.2365

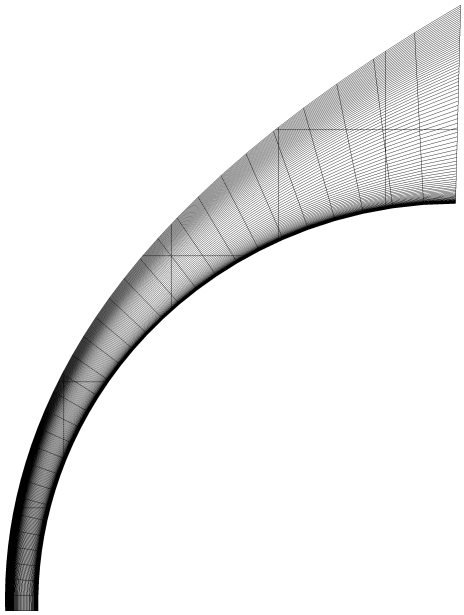

Figure 4.1: Computational grid for PANT case 1.

Figure 4.2 shows computed contours for PANT case 1. The two temperatures are clearly not in equilibrium for this case. The maximum value of translation-rotation temperature is reached directly downstream of the normal shock at $y = 0$. The vibration temperature is assumed frozen across the shock so the maximum is not reached behind the shock. The maximum vibration temperature is reached as it tries to equilibrate with the translation-rotation temperature as flow moves downstream.

Pressure attains a maximum at the stagnation point and then decreases downstream. For a blunt body at zero angle-of-attack pressure reaches a maximum on the body at the stagnation point. For this case there is a velocity normal to the wall attributable to ablation induced outgassing. This moves the stagnation point away from the body and thus pressure reaches a maximum slightly away from the body. For this case the Mach numbers downstream of the shock are subsonic to supersonic. Mack's first mode is generally more unstable for edge Mach numbers below 4.5 so for this blunt body flow transition would be first mode dominated.

Contours of oxygen (O_2) and atomic oxygen (O) are given to show the reacting behavior of the flow. Near the shock the mass fraction of oxygen is 0.22 and due to the high temperatures it dissociates into 2O and reacts with other air molecules as the flow moves downstream. Near the wall oxygen is almost completely dissociated but there is not a large amount of atomic oxygen. This is because the oxygen is reacting with the graphite surface to form CO.

Figure 4.3 gives a comparison of the stagnation line translation-rotation temperature and vibration temperature where $n = 0$ corresponds to the sphere stagnation point. In this and each following figure n represents the direction normal to the surface. In each figure of this section the solid lines represent the shock-fitting computation and the dashed lines represent validation data. A large discrepancy in the computed temperatures can be seen near the shock at approximately $n = 0.054$ cm. This is most likely due to the different computational methods

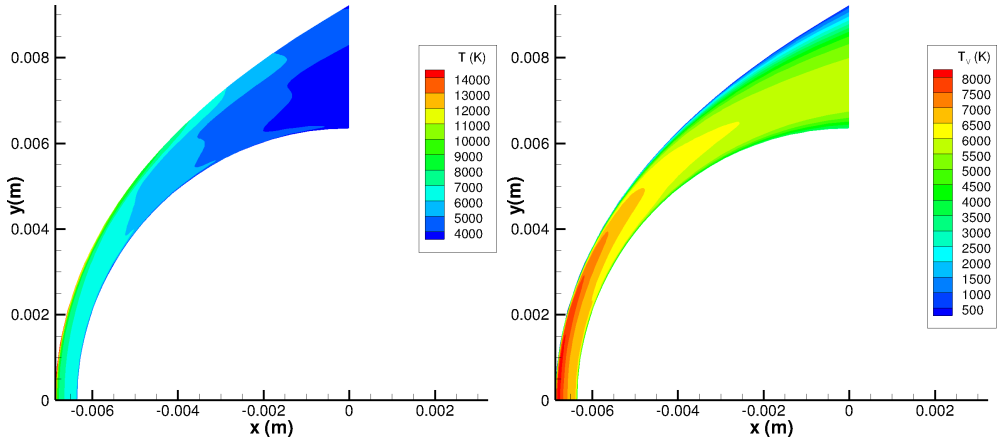

(a) Translation-rotation temperature

(b) Vibration temperature

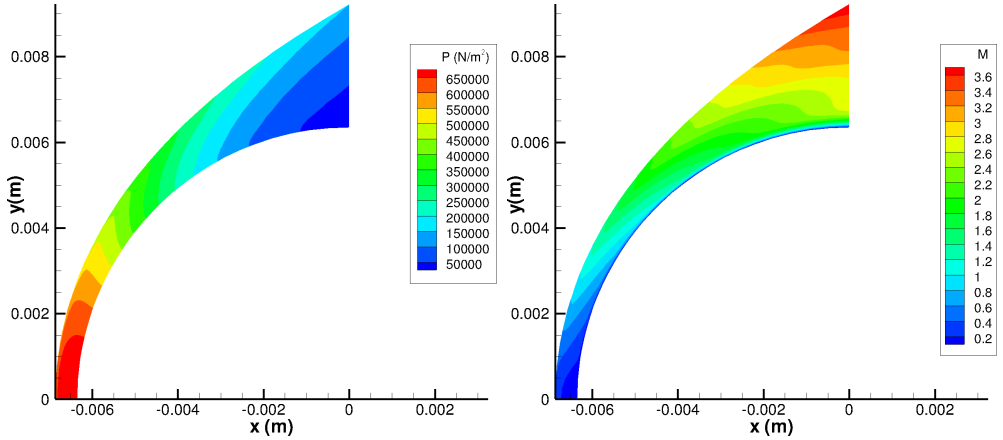

(c) Pressure

(d) Mach number

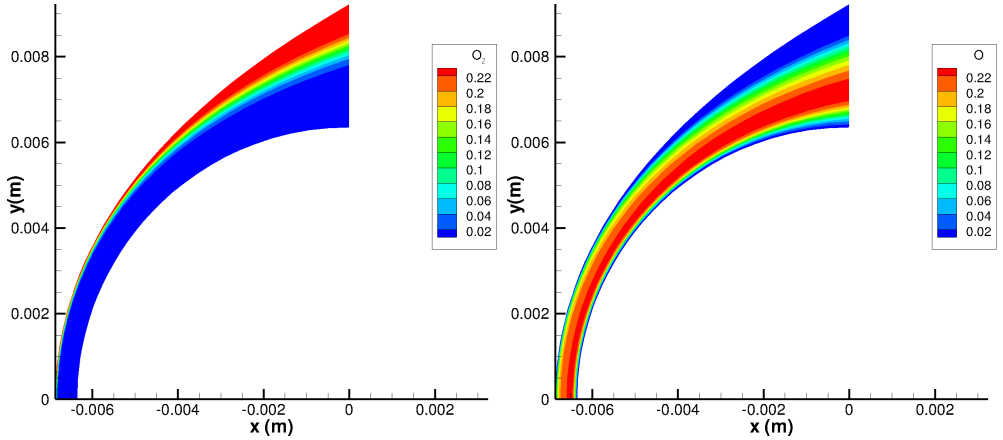

(e) Oxygen mass fraction

(f) Atomic oxygen mass fraction

Figure 4.2: Contours of selected values for PANT case 1.

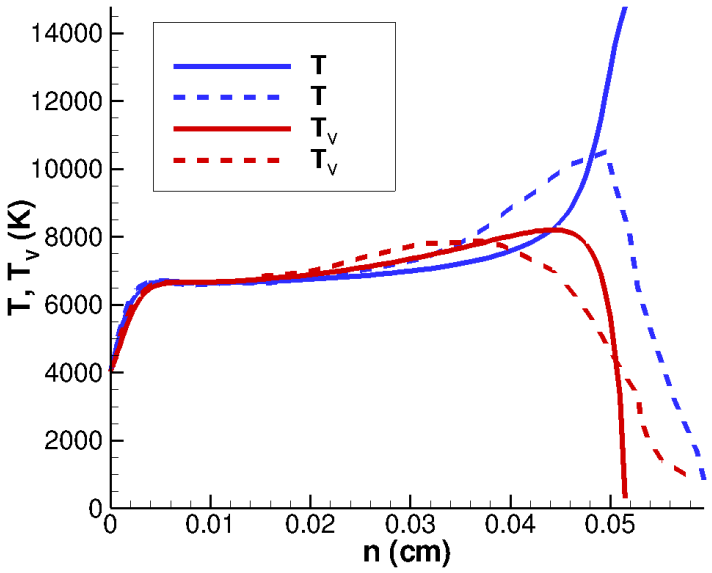

Figure 4.3: Translation-rotation temperature and vibration temperature comparison on the stagnation line. Dashed lines from [Kee94] and solid lines from current simulation.

used and the different grid stretching in the wall normal direction. The shock-fitting method used in this paper uses Rankine-Hugoniot relations to compute the temperature behind the shock whereas shock-capturing methods capture the shock and are commonly more diffusive near the shock. Similar results from Prakash et al. [PPW11, PPW10] also show a discrepancy in computed temperatures behind a shock for thermochemical nonequilibrium flow between a shock-fitting method and a shock-capturing method.

The shock standoff distance on the stagnation line for the shock-fitting method is 0.0515 cm. It is difficult to tell exactly where the shock lies for the shock capturing method. The shock is located at 0.050 cm for the shock capturing method assuming the shock lies at the maximum of translation-rotation temperature. This yields a 3% relative difference between the two methods which is adequate. There is a discrepancy in the temperature equilibration location for the shock-fitting

method ($n \approx 0.045$ cm) and the shock capturing method ($n \approx 0.035$ cm). For the shock-fitting method, the distance between the shock and the equilibration point is less. For the shock-fitting method, there is a much larger difference between the translation-rotation temperature and the vibration temperature behind the shock. This makes the vibration temperature increase quicker than the shock capturing method thus moving the equilibration point nearer to the shock. Physically the shock thickness will be thin when the continuum approximation is valid as it is here. The equilibration point of the shock-fitting method may be physically more accurate as the shock is approximated as a line for a 2D calculation and the shock capturing method smears the shock over multiple grid points. This means that for the shock-fitting method the vibration temperature is exactly its freestream value after the shock because it has not had time to relax whereas for the shock capturing method the vibration temperature rises across the shock due to shock smearing.

A comparison of contour lines for the entire computational domain of vibration temperature and $1 - T_V/T$ is given in Fig. 4.4. Only the lines that were clearly distinguishable from [Kee94] are used for comparison. The discrepancy between the two methods is the most pronounced near the shock similar to the discrepancy in stagnation line temperatures. Near the body there is a good agreement between the two methods. The simulated T in the computational domain will be in good agreement with [Kee94] as T_V and $1 - T_V/T$ are in good agreement.

A comparison of the stagnation line mass fractions and the mass fractions at the sphere exit are given in Fig. 4.5 to ensure the gas phase reactions are implemented correctly. For both subfigures, the comparison between the mass fractions shows only small discrepancies towards the surface ($n \approx 0$) where the computed temperatures between the two methods are similar. N_2 dissociates faster near the shock for the shock-fitting method due to higher simulated temperatures resulting in a slight discrepancy. As the flow moves toward the body the temperature

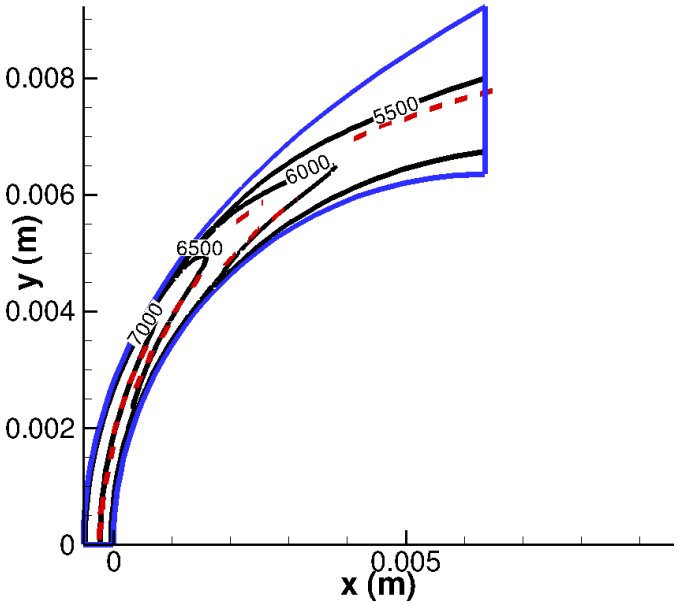

(a)

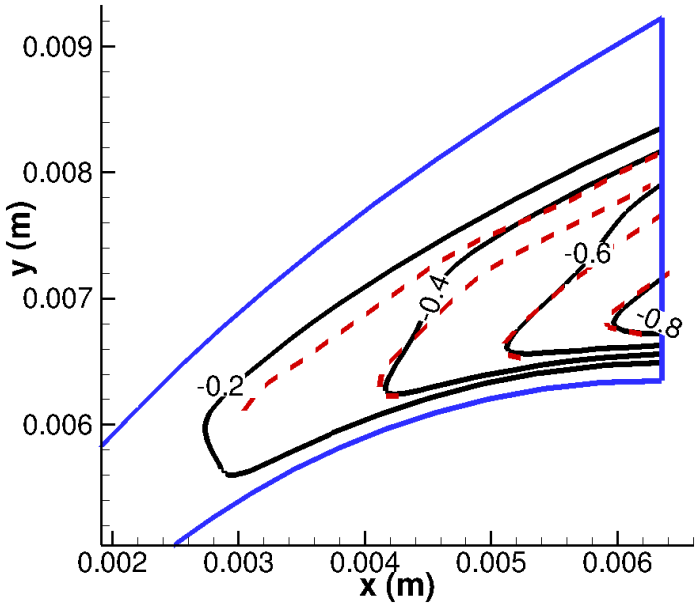

(b)

Figure 4.4: Comparison of (a) T_V contours and (b) $1 - T/T_V$ contours where the dashed red lines are from [Kee94] and the black lines are from the current simulation.

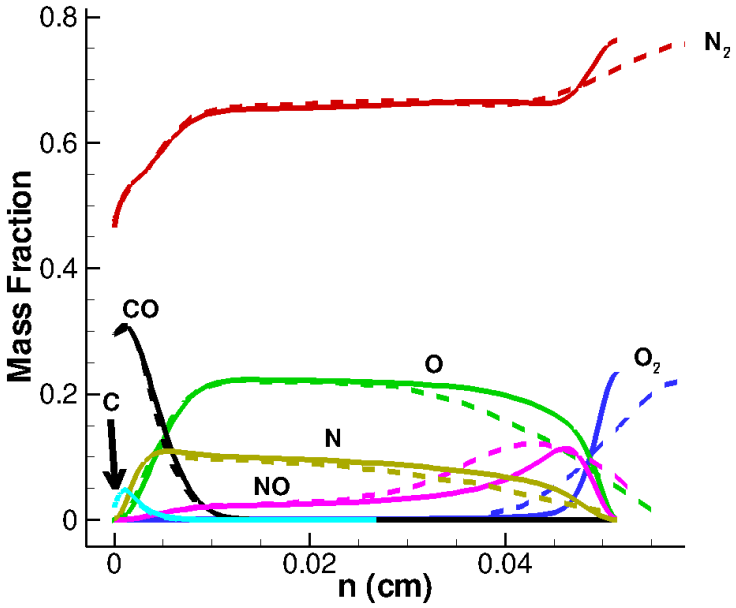

(a)

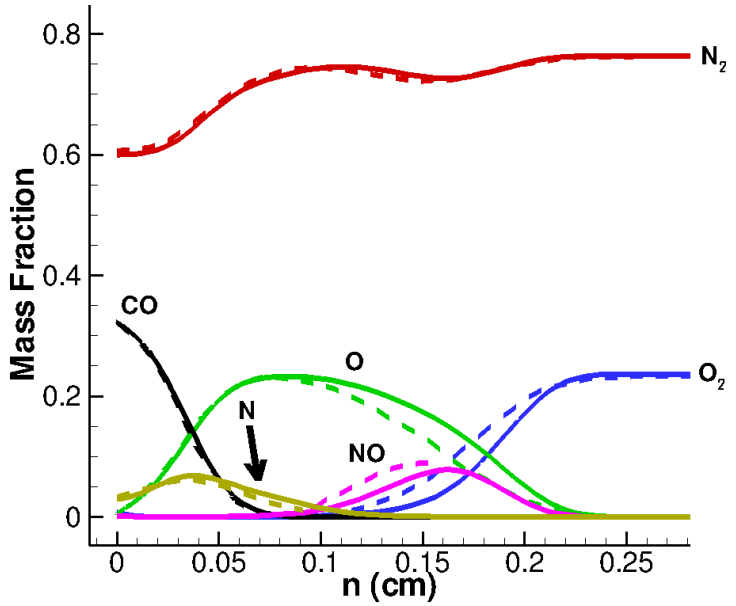

(b)

Figure 4.5: Comparison of (a) mass fractions on the stagnation line, and (b) mass fractions at the sphere exit. Dashed lines from [Kee94] and solid lines from current simulation.

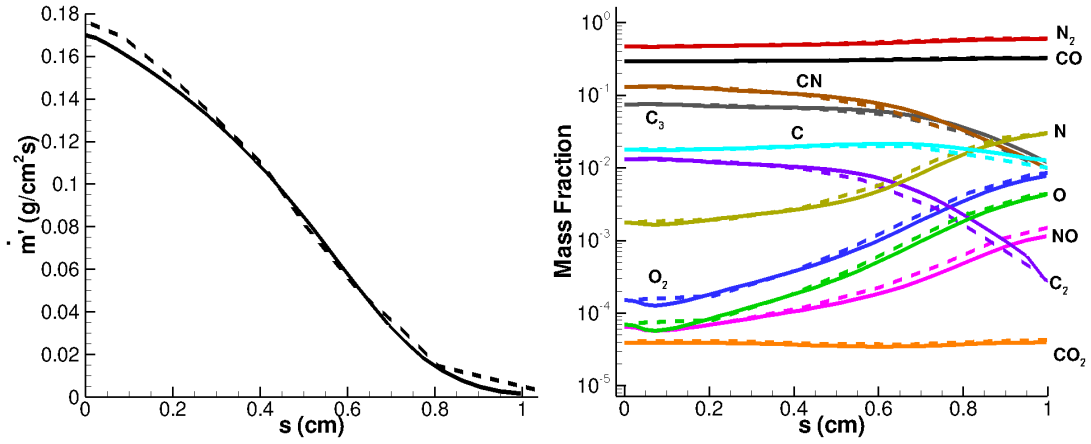

(a) Surface mass flux

(b) Surface mass fractions

Figure 4.6: Comparison of surface values to [Kee94] where s is measured on the surface streamline and $s = 0$ corresponds to the stagnation point. Dashed lines from [Kee94] and solid lines from current simulation.

discrepancy is smaller and the mass fraction of N_2 compares well. Near the shock there are discrepancies in the mass fractions of O_2, O, and NO due to a higher temperature computed by the shock-fitting method. This causes higher reaction rates and faster dissociation of O_2.

A comparison of the surface chemistry model was obtained by comparing the total surface mass flux, $\dot{m}'$, and the surface mass fraction of each species shown in Fig. 4.6. The surface streamline is s and is measured starting from the stagnation point. It should be noted that [Kee94]'s data was digitized from a plot where the scale was small leading to the jumpiness in the data of Fig. 4.6(a) which was not in the original plot. Good agreement is obtained for the surface mass flux. There is a 3% relative difference at the stagnation point in surface mass flux and the profiles of the two computations are similar. s $\approx$ 1 cm corresponds to the sphere exit and at this point the mass flux is close to zero so for this case most of the ablation occurs near the nose as expected. In Fig. 4.6(b) the surface mass fractions are compared. The comparison between each species is adequate.

4.2 Comparison to the $M_\infty = 15.99$ Simulation of PANT Case 2

A second case was compared with [Kee94] and is called PANT case 2. These flow conditions also come from the PANT program. Similar to PANT case 1, the geometry is a sphere and the grid has 32 points along the surface and 91 points in the surface-normal direction. A curve fit to the temperature profile obtain in [Kee94] is used for a more reasonable comparison of results. The freestream conditions for this case are given in Table 4.2.

Table 4.2: Freestream conditions for PANT case 2.

Parameter	Value
M_∞	15.99
ρ_∞ [kg/m^3]	2.4093×10^{-1}
P_∞ [N/m^2]	20260.0
C_{N_2}	0.7635
C_{O_2}	0.2365

Similar to PANT case 1, a comparison of contour lines for the entire computational domain of T_V and $1 - T_V/T$ are given in Fig. 4.7. Only the lines that were clearly distinguishable from [Kee94] are used for comparison. Assuming T_V and $1 - T_V/T$ compare well, T will also compare well. For this case, the two methods agree well throughout the entire domain. The discrepancies in temperature directly downstream of the shock are not as pronounced here as they are in PANT case 1. This is most likely due to the larger freestream density leading to a quicker equilibration of the two temperatures.

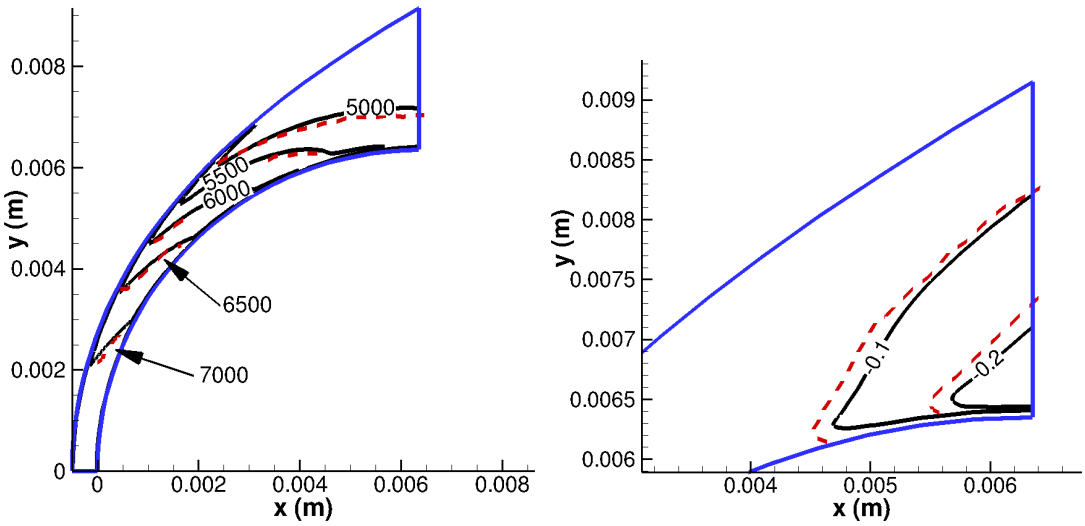

(a) (b)

Figure 4.7: Comparison of (a) T_V contours and (b) $1 - T/T_V$ contours where the dashed red lines are from [Kee94] and the black lines are from the current simulation.

The mass fractions at the sphere exit plane are compared in Fig. 4.8. Similar to PANT case 1, there is a good agreement near the wall and there is some difference near the shock due to a higher computed translation-rotation temperature for the shock-fitting method. In Fig. 4.8(b), a close up of the mass fractions at the sphere exit is given. Similar to PANT case 1, there is adequate agreement in all the species.

Figure 4.9 compares the surface mass flux. s is the surface streamline and is measured from the stagnation point. At the stagnation point there is a 7% relative difference between the two computations and the maximum relative difference is 17% at $s = 0.142$ cm. In [Kee94] it is noted that the maximum mass flux should occur at the stagnation point so the increase in mass flux after the stagnation point is not physical. Also, it is noted that the modified Steger-Warming scheme that is used in the shock-capturing method has some numerical issues near the

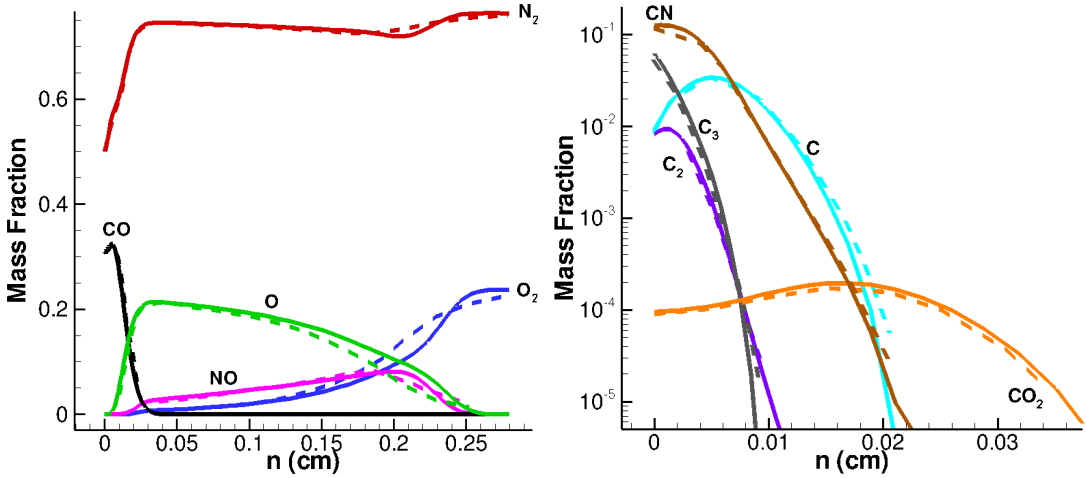

(a) (b)

Figure 4.8: Comparison of (a) mass fractions at the sphere exit and (b) a close up of the mass fractions at the sphere exit. Dashed lines from [Kee94] and solid lines from current simulation.

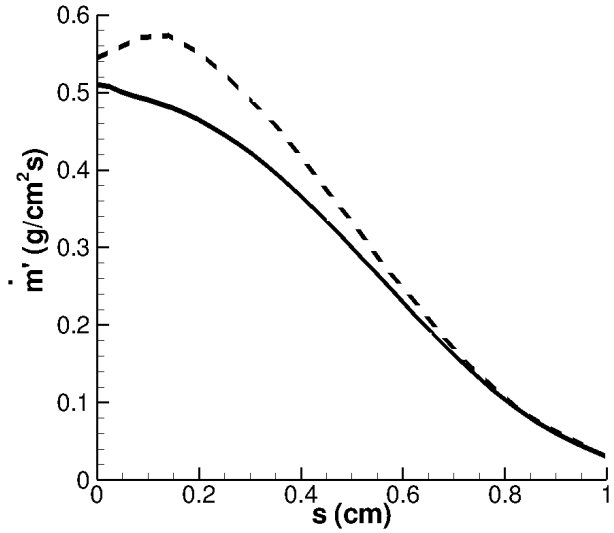

Figure 4.9: Comparison of surface mass flux where s is measured on the surface streamline and $s = 0$ corresponds to the stagnation point. Dashed line from [Kee94] and solid line from current simulation.

stagnation point. Taking these points into account, the decreasing mass flux with a maximum at the stagnation point seen in the shock-fitting method is physically more accurate.

Overall, the comparison between the results from the shock-fitting method and those in [Kee94] for PANT case 1 and 2 is good. The mass fractions for each of the gas species compares well throughout the domain and at the surface. This suggests that the gas phase reactions, as well as the surface boundary conditions, have been implemented correctly. Both the translation-rotation and vibration temperatures compare accurately for PANT case 2 while there is some discrepancy near the shock for PANT case 1. The discrepancies seen in PANT case 1 are suggestive of the different numerical methods used and different grid types used, rather than incorrect implementation.

4.3 Comparison to $M_\infty = 5.84$ Graphite Ablation Case

A third case was simulated to compare the gas model and surface chemistry model to simulations performed by Chen and Milos [CM05a] of a sphere cone geometry with graphite ablation. This test case was chosen to compare with computations as well as an experiment performed at the Interactive Heating Facilities at NASA Ames Research Center. A surface temperature was measured during this experiment so instead of computing the surface temperature from a surface energy balance a curve fit to the experimental data is used. In [CM05a], a different gas chemistry model than the model in the shock-fitting method is used and several surface chemistry models were tested. None of the surface chemistry models tested in [CM05a] matched the model presented here. The nose radius is $r = 1.905$ cm and the cone half angle is 10 deg. The grid has 42 points on the surface and 101 points in the surface normal direction. The freestream conditions are given in Table 4.3.

Table 4.3: Freestream conditions for $M_\infty = 5.84$ case.

Parameter	Value
M_∞	5.84
ρ_∞ [kg/m^3]	3.00×10^{-3}
P_∞ [N/m^2]	1671.36
C_{N_2}	0.6169
C_{NO}	0.0046
C_N	0.1212
C_O	0.2573

Figure 4.10 shows the comparison of the sphere surface mass blowing rates and the sphere surface pressure. The dashed lines represent digitized data from [CM05a], the symbols represent the experiment, and the solid line represents current computations. Four different types of surface chemistry models are used in [CM05a] for one set of freestream conditions. Park (Nitridation) represents a surface chemistry model from Park [Par83, Par05, Par93] containing oxidation, nitridation, and sublimation of C_3. Park (No Nitridation) represents the same model with the surface nitridation reaction turned off. A chemical equilibrium boundary condition represents that the gas phase and ablation boundary conditions are in equilibrium and the remaining surface chemistry model is a finite rate model proposed by Zhluktov and Abe [ZA99] which includes oxidation, sublimation, and recombination but no nitridation.

The ablation boundary conditions used in the shock-fitting code represent the two experimental data points the best out of all the models. In Fig. 4.10(a) near the stagnation point the current computations are almost identical to the experiment. This was not obtained by changing model parameters but rather the model

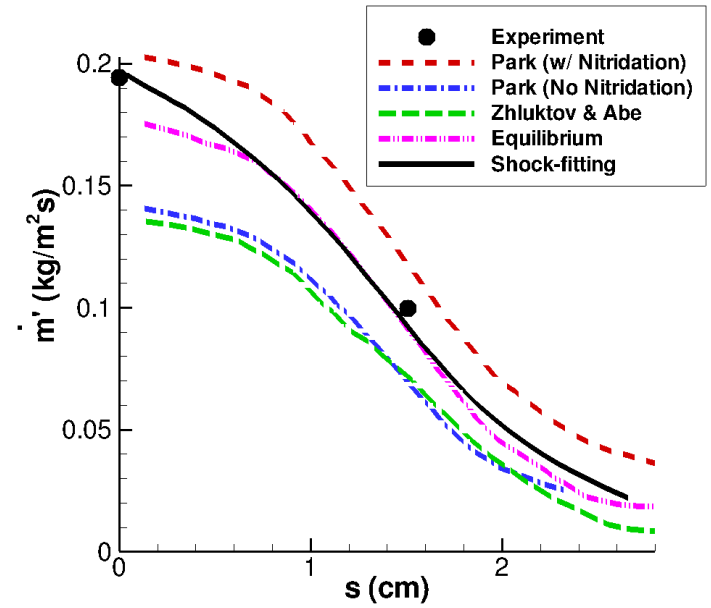

(a)

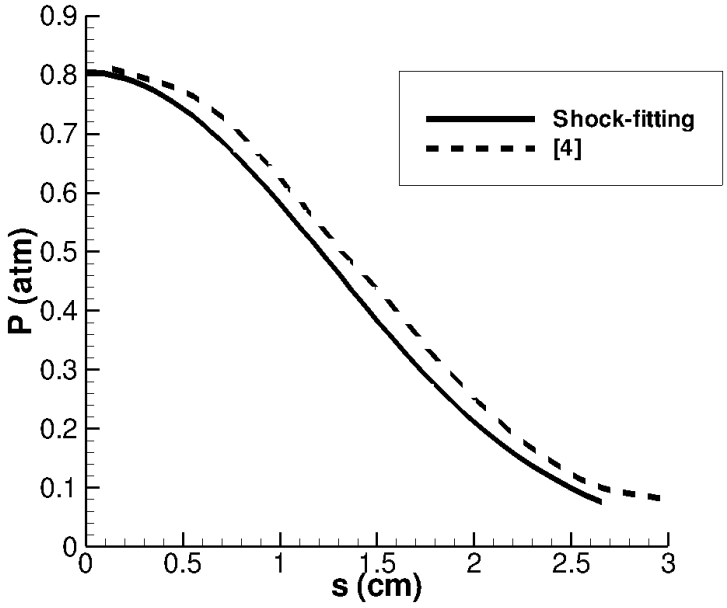

(b)

Figure 4.10: Comparison of (a) sphere surface mass blowing rates and (b) sphere surface pressure. Dashed lines from [CM05a] and solid lines from current simulation.

just happens to represent this particular data set quite accurately. The shock-fitting surface chemistry model is closest to the assumption of chemical equilibrium at the surface. The mass flux is less than the Park model with nitridation. The current surface chemistry model does not include nitridation but does include recombination of atomic oxygen and sublimation of C, and C_2 which is not included in Park with nitridation. Since sublimation of C and C_2 is small, the difference between the two models is mainly due to the added nitridation reaction as well as slight variations in the reaction probabilities. When the nitridation reaction is turned off the current surface chemistry model has a greater mass flux than Park. A comparison to the complex model of Zhluktov and Abe is not as straight forward. Zhluktov and Abe account for many more reactions and also account for active sites where chemical processes can take place. Near the stagnation point at the first available data point there is a 33% relative difference between Zhluktov and Abe and the current computations. The absolute difference between the models decreases along the surface streamline but the relative difference increases to 81% at $s = 2.66$ cm.

Figure 4.10(b) shows the sphere surface pressure profiles from the shock-fitting method and [CM05a] using the Park model with nitridation. The exact surface pressure boundary condition used in [CM05a] was not available while the pressure condition used in the shock-fitting code for this case is the 1D characteristic boundary condition for a subsonic inlet. The pressure obtained by the two methods shows a good agreement considering that the gas phase chemistry models are different as well as the surface chemistry model.

A comparison of the the species mass fraction along the stagnation line is given in Fig. 4.11. The solid lines represent the shock-fitting code and the symbols represent [CM05a] with the Park nitridation surface chemistry model. There is a good comparison for the standard air species. Near the wall, the mass fraction of O_2 increases significantly for the shock-fitting method while it decreases for

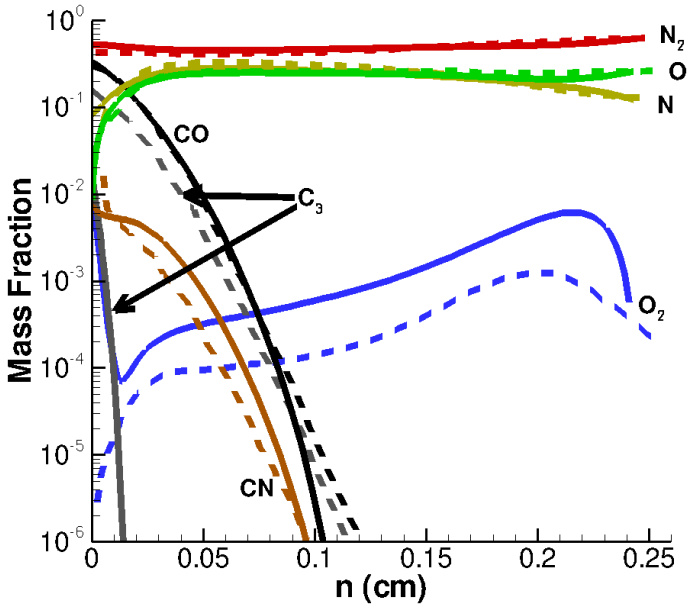

Figure 4.11: Comparison of species mass fraction along the stagnation line to [CM05a]. Dashed lines from [CM05a] and solid lines from current simulation.

[CM05a]. This is because the Park nitridation model does not include surface recombination of atomic oxygen while it is included in the shock-fitting surface chemistry model. The mass fraction for CN is higher at the wall for the Park nitridation model because nitridation is included while it is not in the shock-fitting model. There exists a significant difference in the mass fraction of C_3. In the shock-fitting code the mass fraction of C_3 decreases quickly along the stagnation streamline and reaches 10^{-5} at approximately 0.1 mm from the surface. For [CM05a], C_3 decreases but not as quickly and reaches 10^{-5} at approximately 1 mm from the surface. While part of this may be attributable to diffusion—[CM05a] uses $Le = 1$ while shock-fitting uses $Sc = 0.5$—most would be attributed to differences in the gas model. [CM05a] only includes dissociation of C_3 while the shock-fitting gas model includes dissociation of C_3 and two exchange reactions (reactions 17 and 21) involving C_3. These exchange reactions give two more pathways for C_3 to react and change chemical composition most likely leading to the difference between the two simulations.

For this case, the gas and surface models implemented in the shock-fitting method compare well with other gas and surface models implemented in validated research codes. This suggests that the models are consistent with other validated models. The surface mass flux for the shock-fitting method compares well with the limited experimental data, suggesting that the current model is adequately simulating graphite ablation for the experimentally tested conditions.

CHAPTER 5

LST Validation

To validate the LST code with the full linearized surface model boundary conditions, first, a comparison to established results is given for a 5 species (N_2, O_2, NO, N, and O) real-gas flow. Then, a comparison is given of the results from the LST code and results from a DNS simulation [MZ14].

5.1 5 Species Flat Plate Comparison for Mach 10 Flow

A comparison to [Hud96] of linear stability results for a real-gas flow with five chemical species over a Mach 10 flat plate was performed. The freestream conditions are given in Table 5.1. The meanflow conditions at the wall are no-slip, non-catalytic for each species, and adiabatic for both of the temperatures. The meanflow solution was computed with a different meanflow solver than [Hud96]. The governing equations used to obtain both results are the same, however, there are some minor differences in the gas model. One reaction has been added in the current simulation and the forward reaction rates and equilibrium coefficients differ.

A comparison of the amplification rate for the second mode is given in Fig. 5.1. The comparison is made 0.05 m downstream of the flat plate leading edge. The maximum amplification rate and the frequency of the maximum amplification rate for the second mode compare well. There is some difference between the two results between 575 and 650 kHz. However, this difference is minimal. Considering

Table 5.1: Freestream conditions for $M_\infty = 10$ flat plate case.

Parameter	Value
M_∞	10.0
ρ_∞ [kg/m^3]	5.68×10^{-2}
p_∞ [N/m^2]	4560
$c_{N_2,\infty}$	0.78
$c_{O_2,\infty}$	0.22

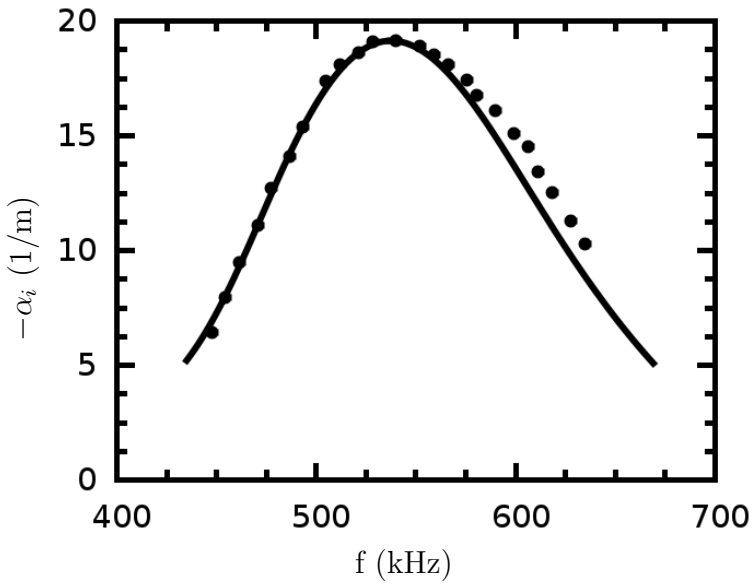

Figure 5.1: Comparison of the amplification rate with [Hud96]. • were extracted from [Hud96] and — is from current simulation.

the differences in the gas model and that different mean flow solvers were used to compute the meanflow, the comparison is quite good.

5.2 Grid Convergence Study

Before a code comparison can be performed to DNS results, a grid convergence study must be done to determine the required number of grid points for the LST grid. Three different grid densities were used with 100, 200, and 300 points respectively. A comparison for the amplification rate at multiple frequencies as well as the temperature perturbation amplitude for a 525 kHz second-mode wave is given in Figure 5.2. For the 200 grid point solution the percent relative error for the amplification rate is less than one percent for the majority of the unstable frequency range. The error increases near the edges of the frequency range because the amplification rate is near zero. There are only slight changes in the temperature perturbation amplitude between all three solutions. Two hundred grid points yields a grid converged solution for this streamwise location.

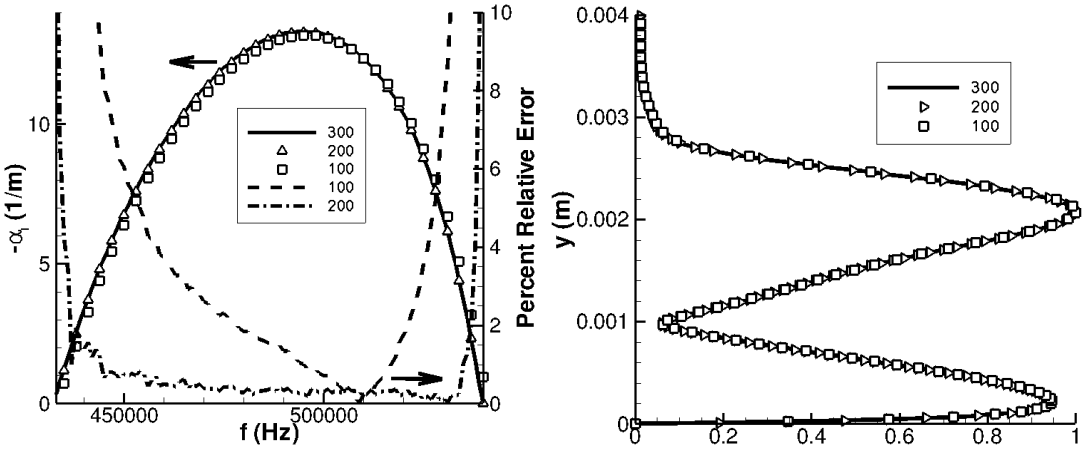

(a) (b) $|\hat{T}|/|\hat{T}|_{max}$

Figure 5.2: Comparison of (a) amplification rate and (b) temperature perturbation amplitude for three different grid densities.

5.3 LST Comparison to DNS

In the DNS simulation, fast acoustic waves in the freestream are imposed on the bow shock and then their behavior is simulated as they pass through the entire domain. This approach does not simulate the behavior of a single mode like LST but rather multiple modes can be present for each frequency. For the most consistent comparison, a streamwise location was selected where DNS results showed a clean exponential disturbance growth, i.e., no modulation. This was done because exponential growth is indicative of modal growth, and therefore a dominant boundary layer mode, rather than multiple competing modes. The streamwise location selected is s=0.564 m measured along the cone surface from the stagnation point.

Figure 5.3 shows the steady boundary layer profile computed by DNS. Here u and v represent the velocity components parallel to the wall and normal to the wall respectively. Significant thermal nonequilibrium is present in the boundary layer even though the wall boundary conditions for the simulation puts the two temperatures into thermal equilibrium. The no-slip condition is present for the u velocity component and wall-normal blowing is less than 1 m/s. The only significant carbon species in the boundary layer is CO which has a mass fraction of 0.123 at the wall and decreases quickly away from the wall. The temperatures are high enough for dissociation of oxygen to occur but not high enough for nitrogen to dissociate significantly.

Figure 5.4 gives a comparison of the perturbation amplitude and phase for a second-mode wave ($\beta = 0$) of translation-rotation temperature, vibration temperature, streamwise velocity, and densities of N_2, O_2, and CO. The LST eigenfunctions were computed using a fourth order stencil. For both temperatures, the comparison is quite good. Both the temperature and its gradient and phase near the wall compare well. The linearized surface energy equation which is used

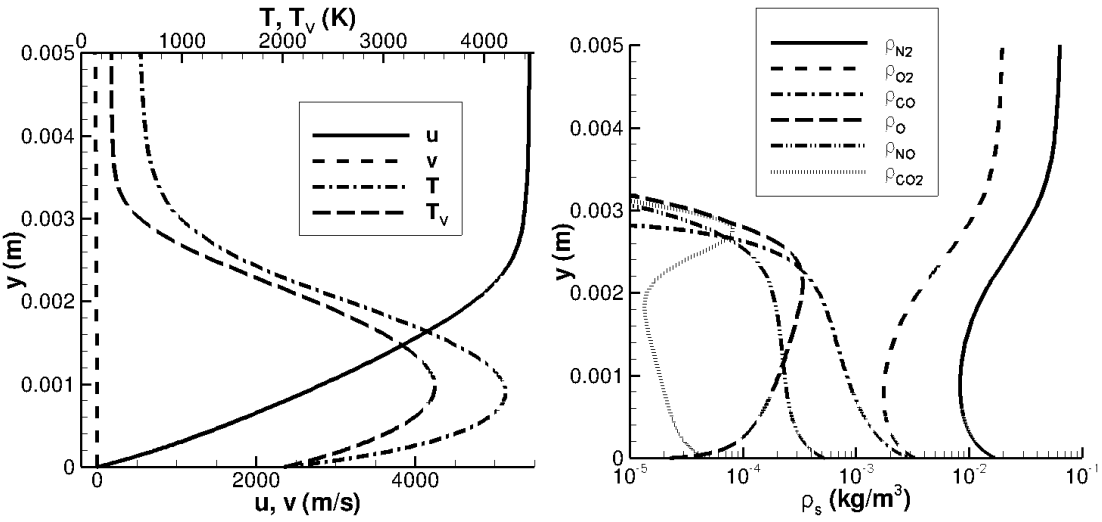

(a) (b)

Figure 5.3: Boundary layer profiles at s=0.564 m for (a) velocity and temperature, and (b) species density.

in conjunction with the other boundary conditions to set the translation-rotation temperature at the wall accurately compares with the DNS results. Similarly, each density perturbation and its near wall gradient and phase compares well with the DNS results near the wall showing that the linearized surface mass balances are implemented correctly.

At this streamwise location in the DNS simulation, there is a wave that has crossed the bow shock due to the fast acoustic forcing in the freestream. This wave experiences some resonant interactions near the nose before it propagates downstream. The effects of this wave are seen near the edge of the boundary layer ($y = 3.15 \times 10^{-3}$ m). This wave is not modal and is likely comprised of multiple waves in the continuous spectra. This causes some oscillatory behavior near the boundary layer edge that is seen in the DNS simulation but is not due to the second mode. Therefore, differences between the two simulation methods in the amplitude and phase near the boundary layer edge are most likely caused from this incoming wave.

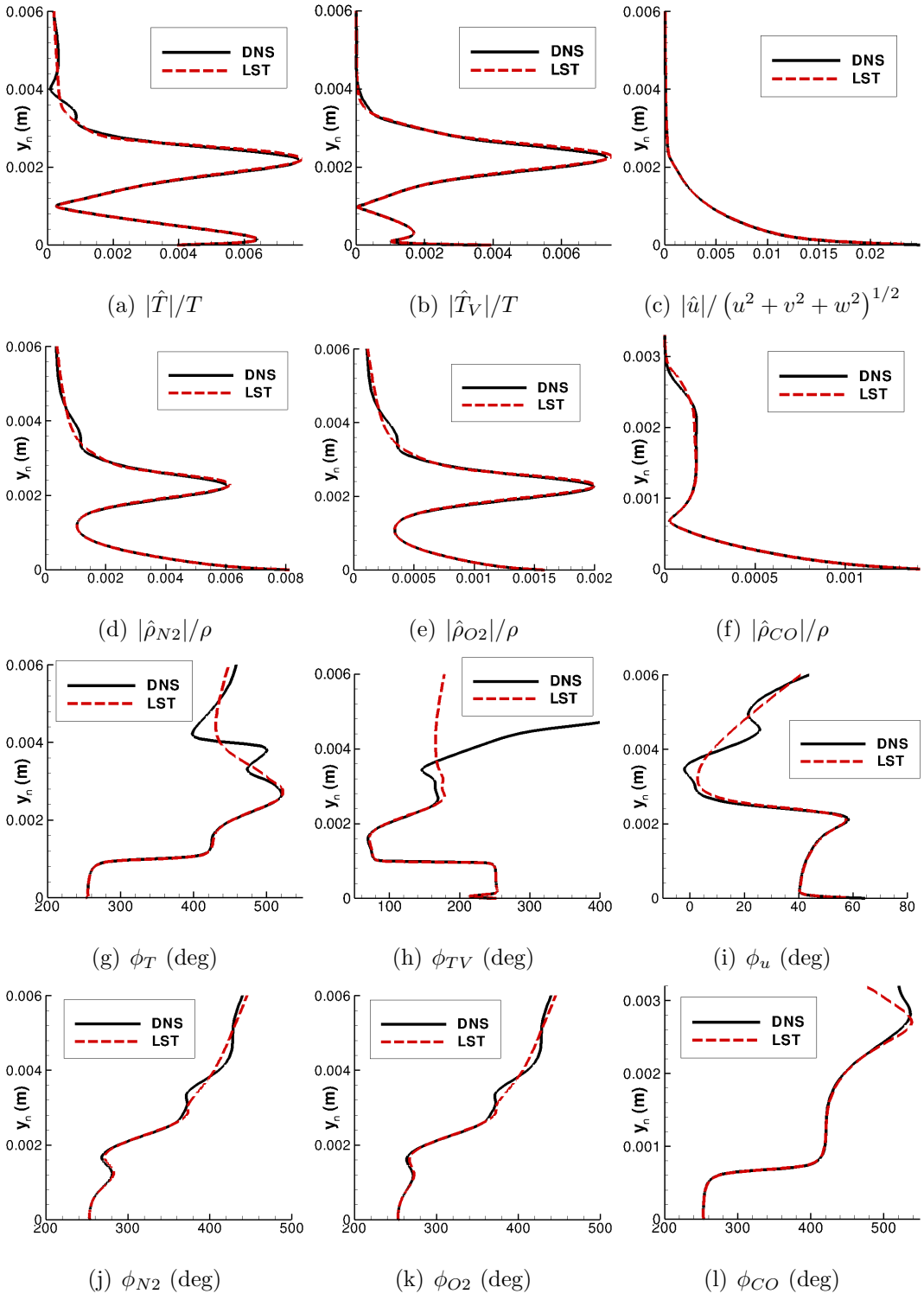

(a) $|\hat{T}|/T$ (b) $|\hat{T}_V|/T$ (c) $|\hat{u}|/\left(u^2+v^2+w^2\right)^{1/2}$

(d) $|\hat{\rho}_{N2}|/\rho$ (e) $|\hat{\rho}_{O2}|/\rho$ (f) $|\hat{\rho}_{CO}|/\rho$

(g) ϕ_T (deg) (h) ϕ_{TV} (deg) (i) ϕ_u (deg)

(j) ϕ_{N2} (deg) (k) ϕ_{O2} (deg) (l) ϕ_{CO} (deg)

Figure 5.4: Eigenfunction amplitude and phase comparison for a 525 kHz second-mode wave between DNS and LST at **s**=0.564 m for select variables.

It is also possible to compare the growth rate and wave number, i.e., the real and imaginary parts of alpha, obtained from LST to a DNS simulation. It is difficult to make a comparison at a single location, so multiple streamwise locations are used. Figure 5.5(a) shows the wave number comparison for a 525 kHz second-mode wave where s is the streamwise distance measured from the stagnation point. The oscillations seen in the DNS results are due to multiple wave modes present simultaneously in the boundary layer. The wave number computed from LST compares well with the DNS simulation. Upstream near $s = 0.2$ m, the 525 kHz is just becoming unstable in the DNS simulation so the second mode is not dominant yet. Moving downstream, the second mode starts to become dominant as witnessed by the lessening fluctuations and the comparison between the two is much better. A similar trend is seen in Figure 5.5(b) where a comparison of the growth rate is given. Upstream there are large fluctuations in growth rate that damp downstream. The LST predicted growth rate for the second mode lies near the center of the oscillations.

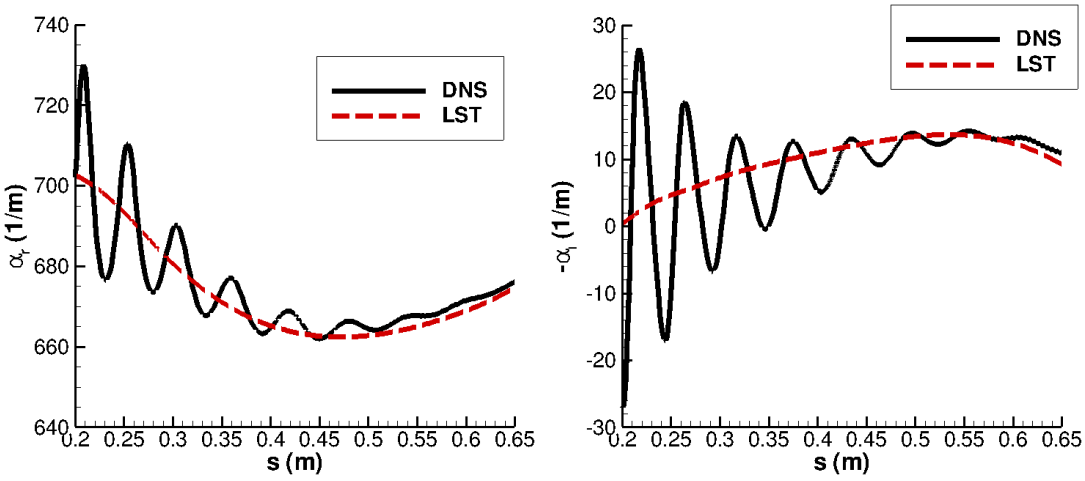

(a) (b)

Figure 5.5: LST comparison to DNS for the (a) wave number and (b) growth rate of a 525 kHz second-mode wave.

Overall, the comparison between these two significantly different methods is good. The eigenfunction obtained from LST accurately compares to DNS for the amplitude and phase of the individual flow variables. The comparison inside the boundary layer, where the second mode is dominant, is good. Also, when traversing the cone from downstream to upstream, the wave number and growth of the second mode compares well with DNS simulations. As direct numerical simulation and linear stability theory are two dramatically different methods to analyze linear instabilities in a boundary layer, the good agreement obtained between the methods shows that they have been implemented correctly.

5.4 Order of Error Estimate

As the derivative operators used to solve Eq. (3.62) are implemented in a non-standard fashion, an order of error estimate is given to show the approximate order of the error incurred. Three different schemes were tested. Scheme 1 and 2 use the approach described in Sec. 3.2 with a three point and five point stencil, respectively. In the previous research of [MZ13], a fourth order central approximation was used for interior derivatives, a second order central approximation was used one point away from the boundary, and a first order approximation was used at the boundaries. Each of these was taken using the standard centered finite difference stencil in computational space similar to [Hud96]. This will be called scheme 3.

Fig. 5.6 shows a plot of the error in the growth rate for the three schemes. The dashed lines represent ideal second and fourth order convergence rates useful for comparison. Scheme 1 has a convergence rate of 1.87 which is to be expected for a consistently three point stencil. Scheme 2 has a convergence rate of 3.98 which is also expected for a consistently five point stencil. Scheme 3 has a convergence rate of 2.39 which is lower than fourth order due to the lower order stencils used

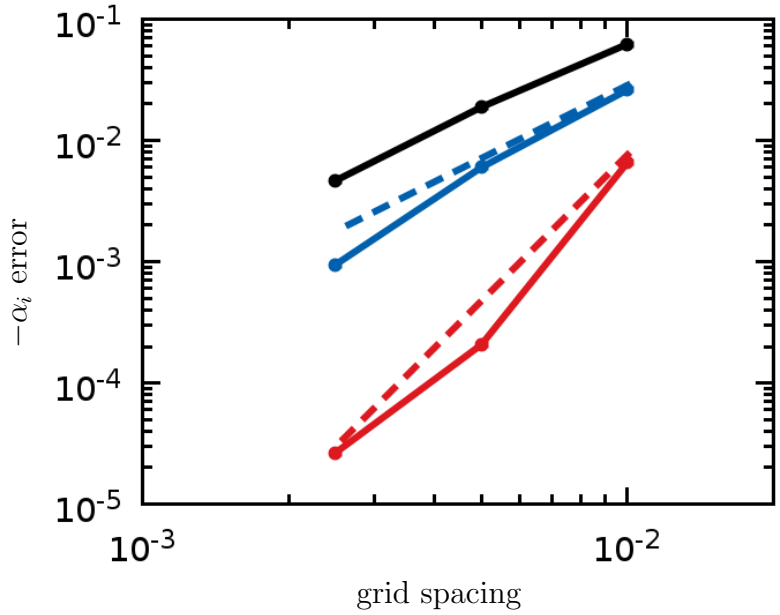

Figure 5.6: Rate of convergence for scheme 1 —, scheme 2 —, and scheme 3 —. Ideal second -- and fourth -- order convergence rates are plotted for comparison.

near the boundary. Of the schemes tested, the scheme that uses a consistently five point stencil, rather than switching to first order on the boundaries, gives the method with the rate of convergence nearest to four. The high-order numerical method proposed in Sec. 3.2 has rates of convergence consistent with the number of points used in the derivative stencil.

CHAPTER 6

Cut-Cell Method Validation

To validate the cut-cell method described in Sec. 3.3, two simulations with the same shock-fitting DNS code were run for a flat plate with a single roughness element. The freestream parameters for the case are given in Table 5.1. Both simulations were run with the same flow parameters and the same roughness element. One simulation used the previously validated curvilinear DNS code with a grid that was body-fitted to the flat plate as well as the roughness. The other simulation used the exact same code except that the grid is only fitted to the flat plate and the roughness element is treated using the cut-cell method. Using these two different simulation techniques makes it so that the main difference between the two simulations is the treatment of the roughness element, thus, testing the implemented cut-cell code.

A hyperbolic tangent is used for the roughness shape. This shape was chosen because a body-fitted grid may be used and there is a simple analytic form to model the roughness height. Also, the derivatives of the roughness height are continuous which are then used to directly compute the grid metrics for the body-fitted solution. The equation for the roughness height is

$$h(x) = \frac{k}{2}\left[\tanh\left(S_r\left(x - x_c\right) + L_r\right) - \tanh\left(S_r\left(x - x_c\right) - L_r\right)\right] \tag{6.1}$$

where k is the roughness height at the center line, x_c is the center of the roughness, S_r is a shape parameter, and L_r affects the roughness width. For this test case: $k = 5 \times 10^{-4}$ m, $x_c = 0.39$ m, $S_r = 3210$, and $L_r = 1926$. These parameters were found to have a negligible effect on the stability of the shock-fitting numerical method

when a body-fitted grid was used. This resulted in a more precise comparison between the body-fitted and cut-cell simulations.

The two separate grids for the body-fitted and cut-cell cases are shown in Fig. 6.1. Only half of the wall-normal points are shown for clarity. Note that the grid for the body-fitted method is more dense near the roughness element when compared to the cut-cell grid. This is due to the wall-normal stretching function that starts at the edge of the roughness element for the body-fitted grid and starts at the flat plate for the cut-cell grid. For this shape, the body-fitted grid is more efficient, but not all roughness shapes can be treated using a body-fitted grid such as an elliptical roughness element which is simulated in ch. 9.

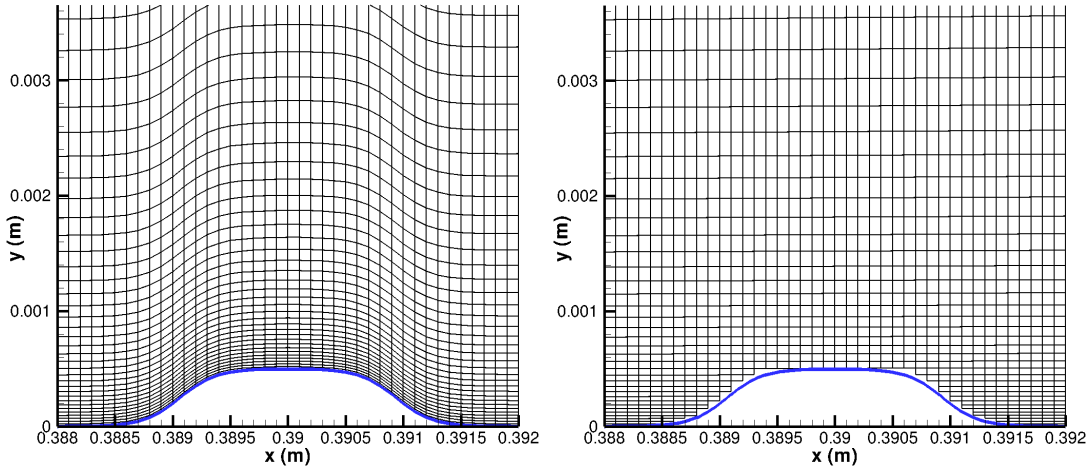

(a) (b)

Figure 6.1: Comparison of (a) body-fitted and (b) cut-cell grids near the roughness element. Half of the wall-normal points are shown.

Both methods were run to solution convergence and then a comparison was performed. A wall-normal velocity contour comparison along with a pressure comparison is given in Figure 6.2. The solid lines are from the body-fitted solution and the dashed lines are from the cut-cell solution. The roughness height is approximately 7.5% of the velocity boundary-layer thickness with no roughness at $x = 0.39$ m. The roughness height was chosen so that there would be no shocks

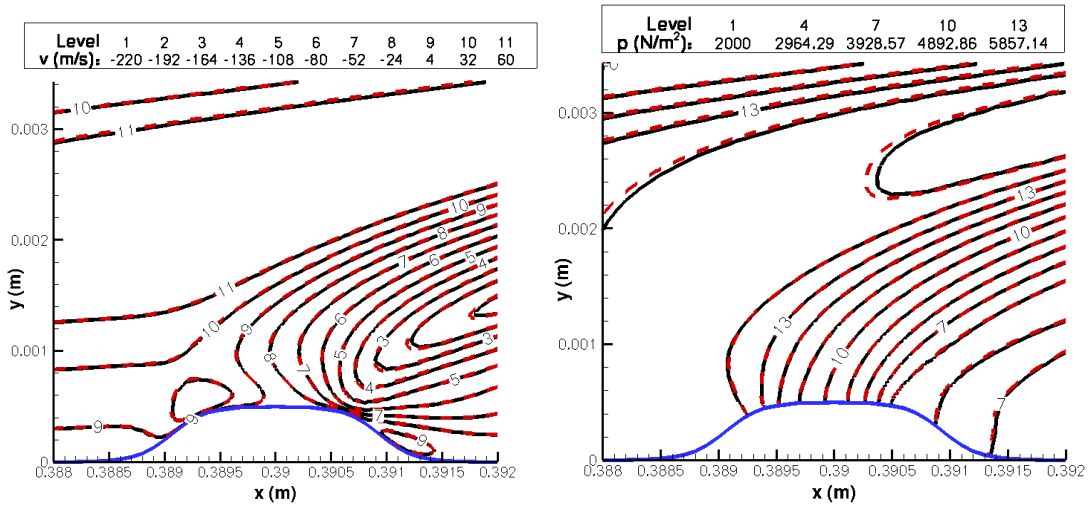

(a) (b)

Figure 6.2: Comparison between the body-fitted and cut-cell solution (a) wall-normal velocity and (b) pressure contours. Body Fitted — and Cut Cell —.

inside the domain as the current implementation of the high-order DNS code only handles shock waves as a boundary of the computational domain. There is little to no visible difference between the two methods near the roughness element. There is some difference in pressure near $y = 0.002$ m which is most likely due to the different grid spacing at this location. Overall, the comparison between the two methods is quite good.

Along with contour plots, wall-normal slices were also compared. Fig. 6.3 shows wall-tangent velocity and temperature profiles at three different streamwise locations. The profiles are located at the center of the roughness ($x = 0.39$ m), the upstream curved portion of the roughness ($x = 0.389$ m), and the downstream curved portion of the roughness ($x = 0.391$ m). The cut-cell solution was interpolated to the body-fitted grid for the comparison. The solutions between the two methods show no visible differences for each of the profiles. The integrated velocity profiles over the boundary layer showed a 0.25%, 0.16%, and 0.16% difference between the two methods. A percent difference between the two solutions

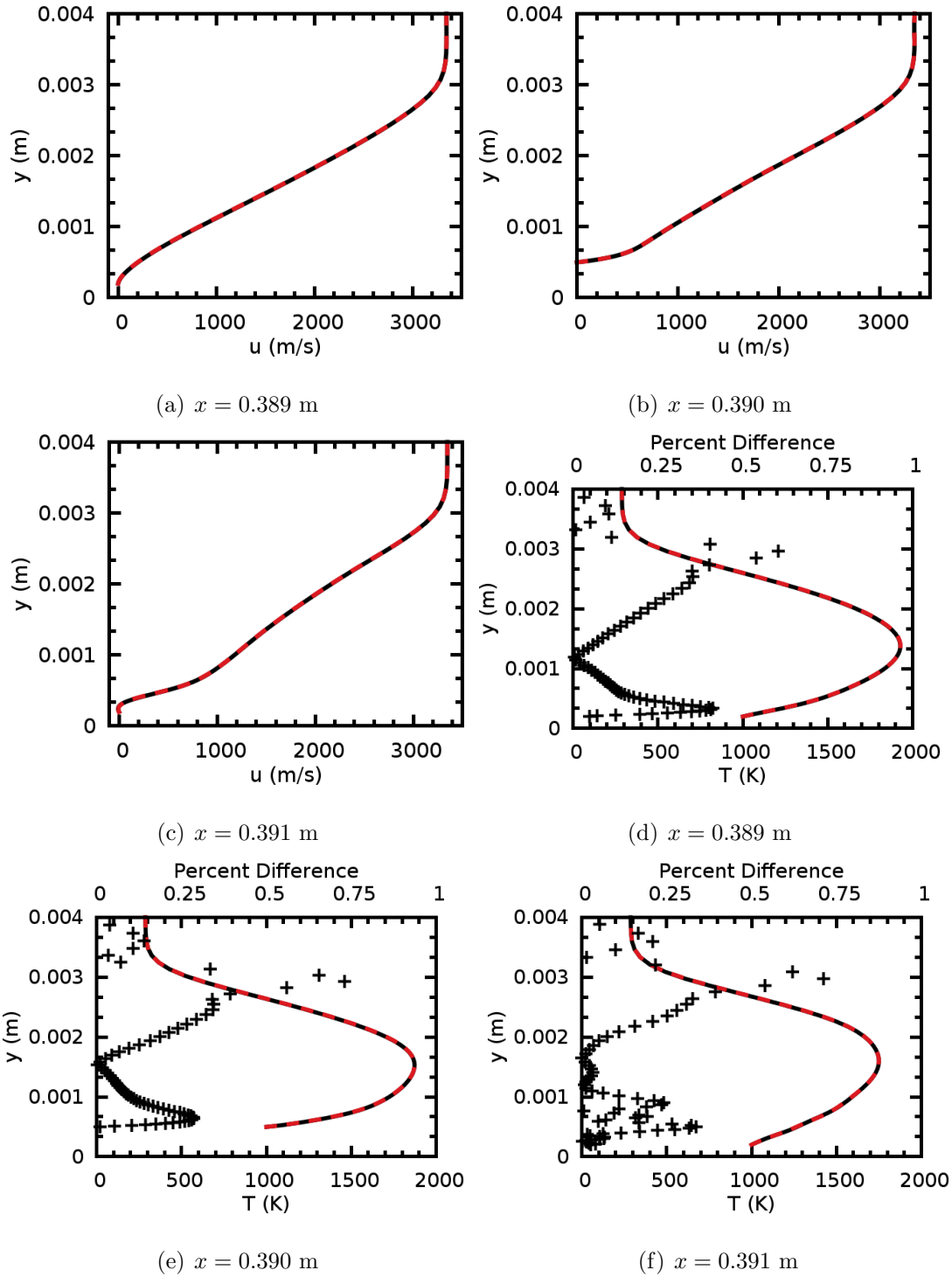

(a) $x = 0.389$ m

(b) $x = 0.390$ m

(c) $x = 0.391$ m

(d) $x = 0.389$ m

(e) $x = 0.390$ m

(f) $x = 0.391$ m

Figure 6.3: Body-fitted and cut-cell solution comparison for (a-c) wall-tangent velocity profiles and (d-f) temperature profiles at select streamwise locations. Body Fitted —, Cut Cell - -, and Percent Difference +.

is given for temperature in Figs. 6.3(d)–6.3(f). The largest percent difference is located near the edge of the boundary layer and is less than 1%. These results coincide with [Gre14] where solutions between body-fitted and cut-cell methods for a hyperbolic tangent roughness also showed no visible differences.

Overall, the comparison between the body-fitted and the cut-cell solutions is quite good. There is little noticeable difference in wall-normal velocity and pressure contours. The percent difference in temperature profiles at three locations on the roughness is less than 1% for each profile. The cut-cell method accurately compares to the body-fitted method. This information shows that the cut-cell method has been implemented correctly.

CHAPTER 7

DNS and LST Analysis of $M_\infty = 15.99$ Blunt Cone

After validating the numerical and theoretical tools used to analyze hypersonic boundary-layer instability in the presence of graphite ablation, direct numerical simulations and linear stability analysis are performed using the new high-order methods to study hypersonic boundary-layer receptivity and instability with real-gas effects and graphite ablation effects over a blunt cone.

A DNS is composed of two distinct simulation results: 1) the simulation of the steady laminar base flow, and 2) the simulation of freestream disturbances imposed on the steady base flow. Figure 7.1 shows the simulated domain for this case, where the shock is colored black and the wall and the outlet are blue. The steady base flow is laminar, with no turbulence model, and must be extremely numerically convergent or small amplitude waves will be overcome by numerical noise. Once the base flow is converged within predefined tolerances, linear (i.e., small amplitude) non-interacting freestream fast-acoustic waves are imposed on the steady laminar base flow in the freestream. As the freestream waves cross the shock and enter the boundary layer, the receptivity process has begun. Receptivity links the linear freestream waves with the initial conditions of disturbance amplitude, frequency, phase, etc., for the breakdown of laminar flow. Boundary-layer receptivity to freestream disturbances has been reviewed in [SRK02] and more recently covered in [Fed11] as part of the hypersonic boundary-layer transition process. After receptivity in a low disturbance environment, modal growth

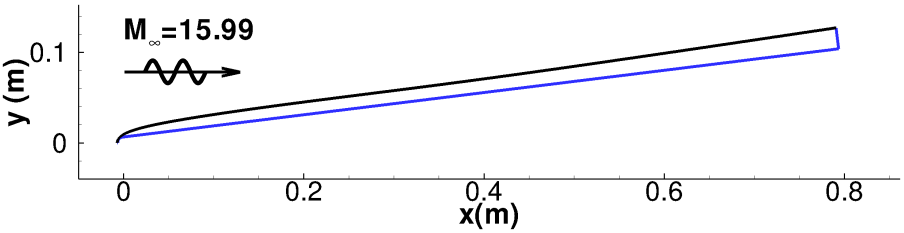

Figure 7.1: Simulation domain for 7 deg half-angle blunt cone. The shock is black, and the wall and outlet are blue.

occurs where the second mode is commonly the dominant mode for flat plates and sharp cones at a zero angle of attack. The second mode originates after the synchronization location from either mode S or mode F, which are termed for their similar phase speeds to slow and fast-acoustic waves, respectively, as they separate from the continuous spectrum. Eigenmode growth provides initial conditions to nonlinear breakdown, making it essential to understand eigenmode growth as well as receptivity to accurately predict transition.

The receptivity and eigenmode growth process in a low freestream disturbance environment for flat plates and cones has been studied extensively for perfect gas flows, but there is a limited amount of information and some uncertainty as to how a real gas affects these processes. In [ZW12] there is a review of the current progress of DNS on hypersonic boundary-layer receptivity, instability, and transition. It is noted that there is a small amount of DNS research into real-gas flows and there is a need for progress in this area. The purpose of these simulations is to further understand real-gas effects and ablative effects on the second mode.

7.1 Steady-State Solutions of $M_\infty = 15.99$ Blunt Cone

In this research, one of the goals is to assess real-gas and ablation effects, which are in the form of surface chemistry, on hypersonic boundary-layer receptivity and

instability. To do this, five distinct steady simulations were run. Each of these steady simulations has the same geometry and the same freestream conditions. The geometry is a sphere cone with a nose radius of 0.00635 m and a cone half angle of 7 deg. The freestream conditions are the same as the the first DNS validation case, named PANT case 1, and are listed in Table 4.1. The cone axis is aligned with the freestream flow, yielding an angle of attack equal to zero. The laminar flow over a cone at zero angle of attack is axisymmetric. Thus, only a two dimensional axisymmetric flowfield is simulated where the transverse direction is treated by Fourier collocation. The freestream unit Reynolds number and stagnation enthalpy are $Re_u = 7.3 \times 10^6$ /m and $h_{o,\infty} = 15.3$ MJ/kg, respectively. This is a high enthalpy case where thermochemical nonequilibrium effects are significant and still present well downstream of the nose.

Each of the five meanflow cases are listed in Table 7.1. Case 1a and 1b have the same meanflow profile which is computed by the eleven species thermochemical nonequilibrium model with ablation boundary conditions. The surface temperature profile computed from case 1 is used to set the wall temperature for cases 2–5. Case 2 is a 5-species air thermochemical nonequilibrium simulation with surface blowing. The 5-species air gas model is the exact same as the N_2, O_2, NO, N, O components in the eleven species model. The imposed surface blowing has the same mass flux as case 1, but standard freestream air is blown instead of carbon products. Case 3 is the same as case 2 except there is no blowing at the surface. Also, the surface recombination of atomic oxygen (Eq. (2.43)) is retained for both cases 2 and 3. Cases 4 and 5 are both ideal-gas cases which use the same nonequilibrium code with the source terms turned off, the vibration energy held constant, and the mass fractions held to their freestream values. This is done so the viscosity, thermal conductivity, etc. are calculated the exact same way for each of the five meanflow cases. Case 4 has the same mass flux profile as case 1 and case 2, while case 5 has no blowing.

Table 7.1: Types of steady simulations.

Case Number	Gas Type	ns	Blowing	LST BCs
1a	Real Gas	11	Ablation	full linearized ablation
1b	Real Gas	11	Ablation	$\hat{T}_w = 0$
2	Real Gas	5	Yes	$\hat{T}_w = 0$
3	Real Gas	5	No	$\hat{T}_w = 0$
4	Ideal Gas	2	Yes	$\hat{T}_w = 0$
5	Ideal Gas	2	No	$\hat{T}_w = 0$

A grid convergence study was performed for case 1a to ensure that the computational grid was sufficient to capture the meanflow as well as the unsteady flowfield disturbances. The grid density in the streamwise direction was chosen to adequately resolve the highest imposed perturbation frequency (525 kHz). There are 3155 grid points in the streamwise direction. The grid in the wall-normal direction was tested with 240, 480, and 720 points. The meanflow solution was computed for each case, and then unsteady simulations were run. Figure 7.2 shows the surface pressure perturbation for the highest imposed frequency using the three different grid densities. The maximum relative error between the 480 and 720 simulations is 2.3% at $s = 0.75$ m. Other variables at different locations were checked as well and showed similar relative errors. For lower frequencies, the relative error is less than the highest imposed frequency. The 480 wall-normal grid point solution is grid converged.

A steady-state contour plot of the translation-rotation temperature and the vibration temperature for case 1 is given in Fig. 7.3. It is difficult to clearly visualize the entire computational domain because of its shape, so only the nose region and start of the cone frustum are displayed for the sake of clarity. The translation-rotation temperature reaches its maximum value of 14,783 K directly

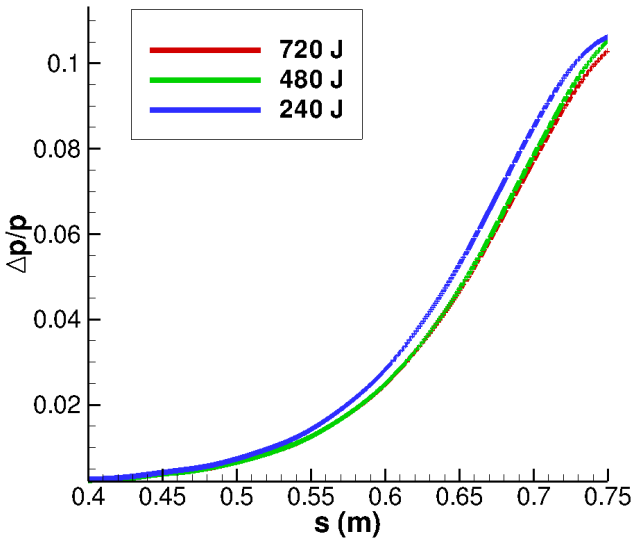

Figure 7.2: Grid convergence study with three different grid densities in the wall-normal direction for the 525 kHz surface pressure perturbation.

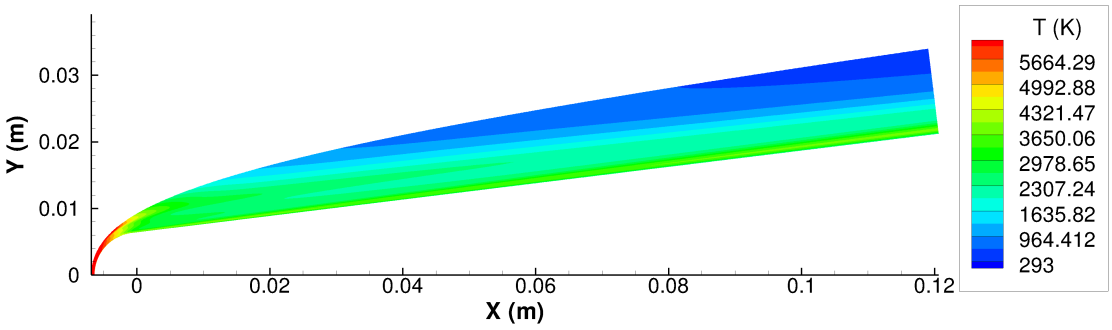

(a) Translation-rotation temperature

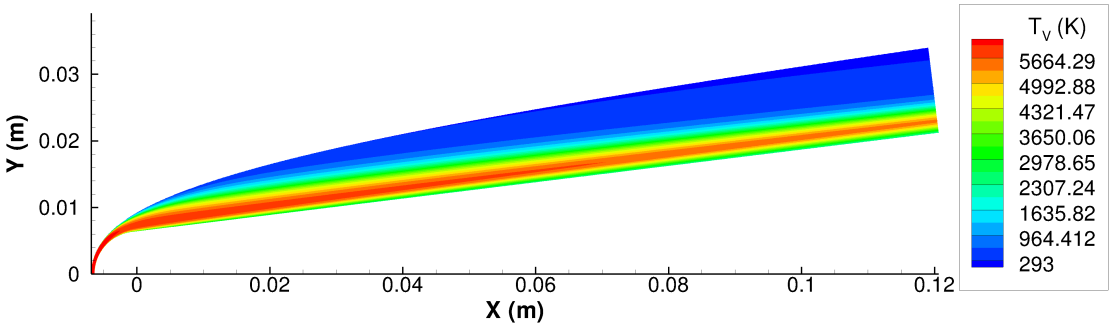

(b) Vibration temperature

Figure 7.3: Contour plots of T and T_V.

behind the normal shock at the stagnation line but then cools as the flow moves downstream. The vibration temperature reaches its maximum value of $8,198$ K at approximately $x = -0.68$ cm along the stagnation line. The shock angle decreases as the flow moves downstream resulting in lower temperatures directly downstream of the shock. On the cone frustum, the vibration temperature is higher than the translation-rotation temperature near the boundary-layer edge, indicating thermal nonequilibrium. In this region, the vibration temperature is relaxing towards the lower translation-rotation temperature.

Unlike many simulations of hypersonic boundary-layer receptivity, neither is the wall temperature constant nor the adiabatic condition ($\frac{\partial T}{\partial n} = 0$) enforced. Instead, for a flow where ablative effects are considered, a surface energy balance (Eq. (2.57)) may be solved which yields a varying temperature profile. The temperature profile for this flow is shown in Fig. 7.4(a). Recall that the surface is assumed to be in thermal equilibrium, meaning $T_V = T$ at the surface. The temperature has a maximum at the stagnation point and then drops rapidly as the flow expands. Surface temperature in hypersonic flows with ablation is important, as the wall temperature directly determines the reaction rate and probability for oxidation. It also plays a role in sublimation. In this case, as the wall temperature drops, the wall mass flux should drop as well. Note that the temperature of the wall is decreasing, which corresponds to wall cooling, which is stabilizing to first mode waves and destabilizing to second mode waves. Also note that, for 0.2 m$\geq$s$\geq$0.8 m, 0.14$\geq$T$_w$/T$_0$ $\geq$0.13, where T$_0$ is the stagnation temperature.

As temperature determines, to a large degree, surface mass loss due to ablation, the surface blowing profile should be similar to the surface temperature profile. To help visualize the blowing profile caused by chemical reactions at the surface, Fig. 7.4(b) shows the wall mass flux per area nondimensionalized by the freestream mass flux per area. This nondimensionalization is chosen because it is common in stability literature with wall blowing. As expected, the largest mass flux is at the

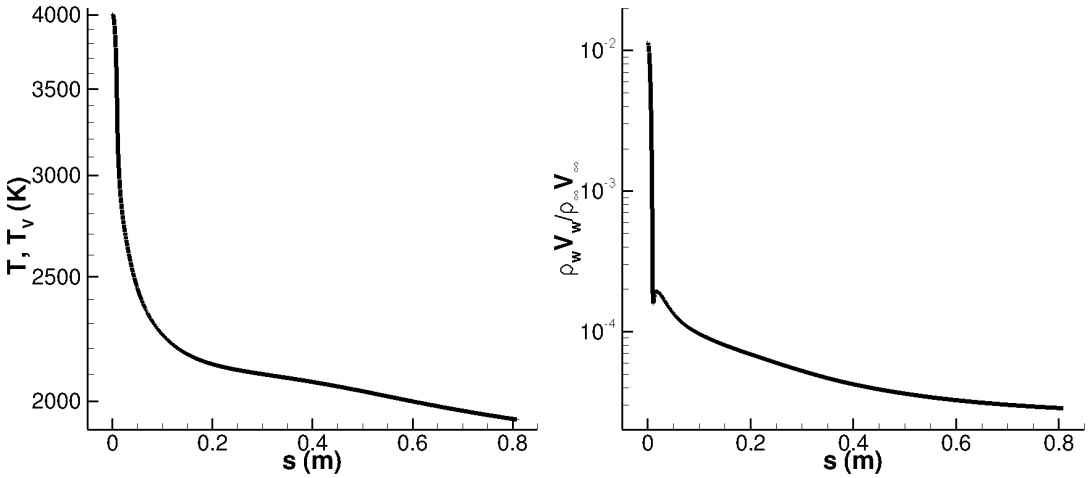

(a) (b)

Figure 7.4: Surface (a) temperature and (b) nondimensional mass flux. The surface is in thermal equilibrium.

stagnation point (approximately 1% of the freestream mass flux), corresponding to a maximum in wall temperature where the oxidation reactions as well as the sublimation reactions are all significant. Notice the surface mass flux drops nearly two orders of magnitude across the cone nose and remains roughly the same order of magnitude along the cone frustum, indicating that outgassing effects would likely be most significant upstream in the nose region. This rapid drop of wall mass flux also corresponds to a rapid decrease in sublimation, which is shown in Fig. 7.5. The fact that there is still wall blowing in the cone frustum is due to the oxidation reactions. The wiggle near the nose of the cone is located directly downstream of the beginning of the cone frustum. The discontinuity in the surface curvature is likely the cause for the wiggle, and the appearance of the wiggle is exaggerated by use of a logarithmic scale.

The surface mass flux is created by interaction of the graphite ablator and the surrounding flow. To help understand the chemical processes at the surface, Fig. 7.5 shows the mass fraction for each species at the surface. The species with

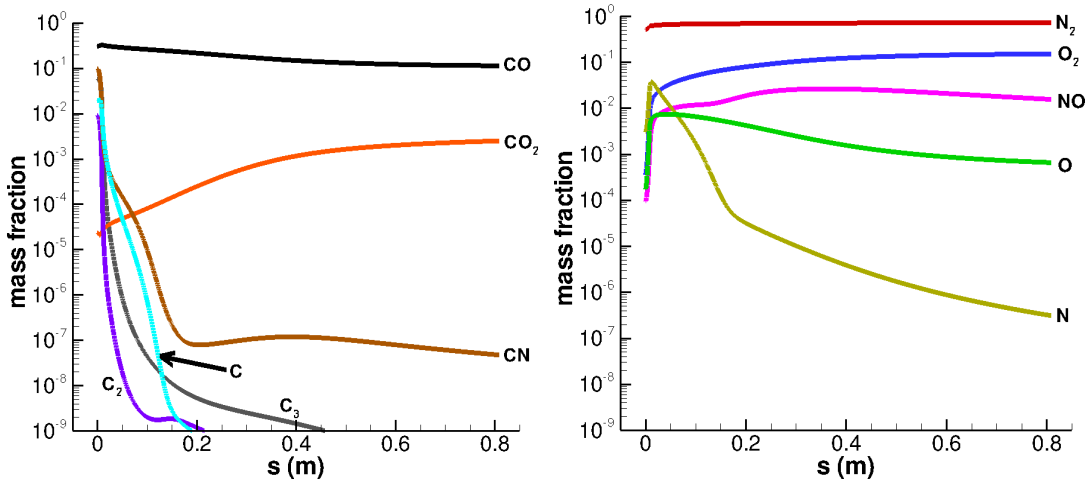

(a) (b)

Figure 7.5: Surface mass fraction for (a) carbon-containing species, and (b) air species.

the largest mass fraction at the surface is N_2, but it does not react with the surface. The next largest mass fraction is CO. Recall from Eqs. (2.41) and (2.42) that the carbon surface can react with O and O_2 to form CO. These two reactions are the dominate reactions for the entire length of the surface, i.e., they are responsible for the most mass loss due to ablation at the surface. Sublimation of C_3 (Eq. (2.51)) is an order of magnitude less than CO at the stagnation point. In the sphere region, it is the dominate sublimation product. There is a significant mass fraction of CN at the surface, even though a nitridation reaction is not taken into account in the surface chemistry model. CN at the surface is due to reactions of ablation products with N_2 and NO. For the entire length of the cone frustum, CO contains the most mass of the carbon containing species. This shows that CO is the species most likely to have the largest effect on boundary-layer receptivity and instability over the blunt cone.

To visualize the species mass concentrations in the surface-normal direction, a surface-normal plot is given in Fig. 7.6, which shows species mass fractions at

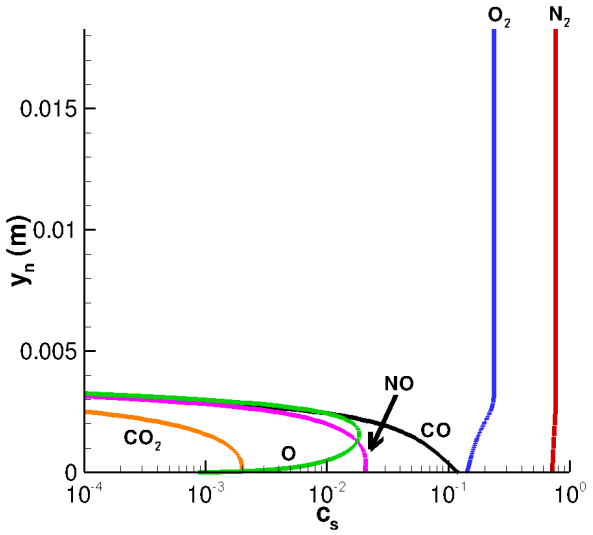

Figure 7.6: Species mass fraction in surface-normal direction for **s**=0.6 m.

s=0.6 m. Only flowfield species with a mass fraction above 10^{-4} are shown. The total enthalpy boundary-layer edge is at $y_n = 2.74 \times 10^{-3}$ m for this streamwise location. Outside of the boundary layer, the flowfield is mainly composed of N_2 and O_2. Inside the boundary layer, the temperature increases and chemical reactions become significant. Notice that, similar to Fig. 7.5(a), CO and CO_2 have the largest mass concentration of the carbon-containing species. At the boundary-layer edge, the mass concentration of CO is on the order of 10^{-2} and for CO_2 it is on the order of 10^{-4}. The critical layer for a hypersonic boundary layer approaches the boundary-layer edge for high-Mach-number flows such as the M_∞=15.99 flow simulated here. Large disturbance amplitudes for species densities are expected at the critical layer for second-mode instabilities. Since the largest carbon-containing species has less than 1% of the flow mass at the boundary-layer edge, it is likely that the effects of the carbon containing species are small, as they are mainly constrained to the near-surface region and not significantly present near the critical layer.

The mass concentration of CO and CO_2 for case 1 at multiple streamwise locations is shown in Fig. 7.7. They are shown because most of the mass from

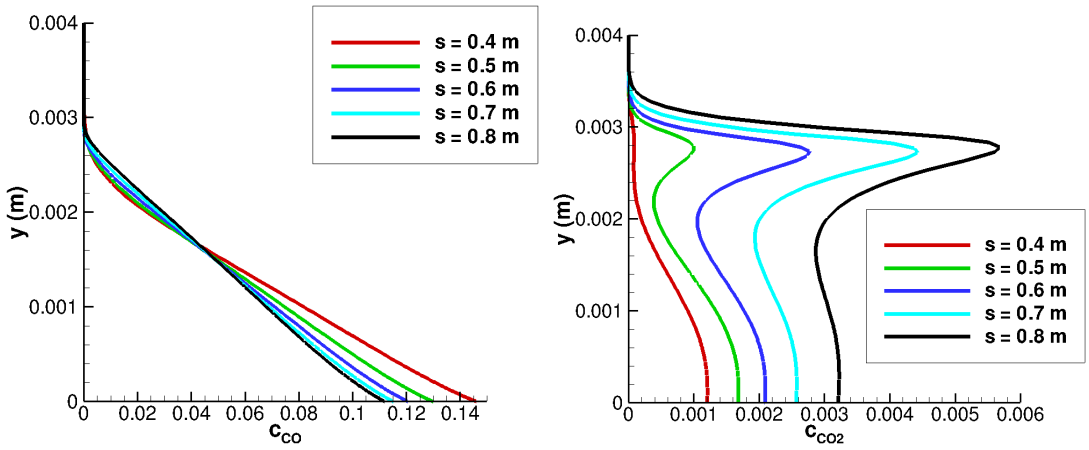

(a) (b)

Figure 7.7: Mass concentration of (a) CO and (b) CO_2 at multiple streamwise locations for case 1.

ablation is contained in CO which is being transferred to CO_2 as the flow moves downstream and cools. Likely, if carbon species are to have an effect on flow instability it will be through CO and CO_2. Recall from Eqs. (2.41) and (2.42) that CO is created at the surface through surface reactions and then can react with the freestream flow. However, CO_2 is formed solely through gas phase reactions. The largest mass concentration for CO is found at the surface and decreases in the downstream direction. As the flow moves downstream, some CO_2 is recombining which increases the mass concentration of CO_2 and decreases the mass concentration of CO. There is a peak in the mass fraction of CO_2 near $y = 0.003$ m which is near the boundary-layer edge. This peak is due to lower temperatures near the boundary-layer edge.

Figure 7.8 shows the height of the boundary layer for a portion of the cone frustum. The height of the boundary layer is the location where the total enthalpy is 99.5% of the total enthalpy immediately downstream of the bow shock in the wall-normal direction. Notice that, for a portion of the cone frustum, the boundary layer is decreasing in the downstream direction rather than increasing. At first

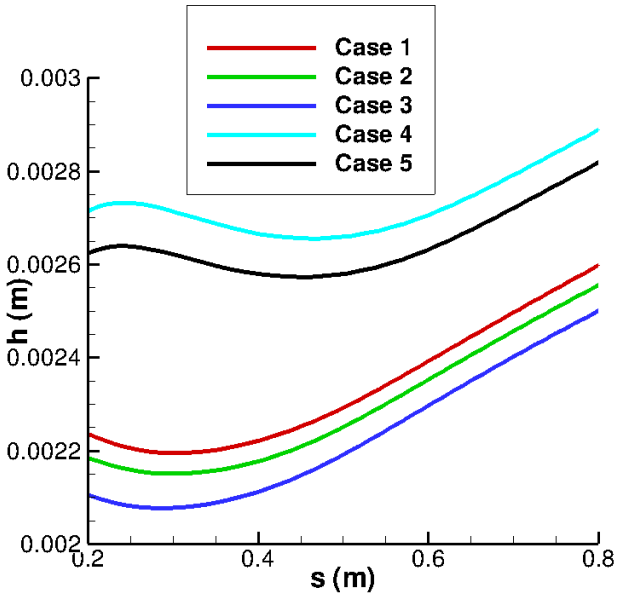

(a)

Figure 7.8: Meanflow (a) wall temperature and (b) total enthalpy boundary-layer thickness.

this may seem counterintuitive, as generally the boundary layer is continually increasing in the downstream direction. In this case, a favorable pressure gradient combined with a strong decrease in wall temperature that cools the boundary layer and contracts the flow, decreases the height of the boundary layer. Along with the boundary layer, a supersonic blunted cone will produce an entropy layer. At the end of the domain ($s = 0.8$ m), the entropy layer has almost been fully swallowed by the boundary layer.

It has been shown in previous experimental research that the height of the boundary layer is approximately half the wavelength of the dominant second mode [STD84]. The phase velocity of the dominant second mode can be roughly approximated as the boundary-layer edge velocity, leading to $c_r \approx const. \approx \omega/\alpha_r \approx 2fh$. This shows that as h decreases, f will increase, to maintain a constant c_r. With this piece of information, it is expected that perhaps some

lower frequencies will become unstable for cases 1–3 before higher frequencies near $s = 0.2$ m due to the decrease in boundary-layer height.

Before moving on to an unsteady analysis, a comparison of all five meanflow profiles is given for a single streamwise location ($s = 0.564$ m) in Fig. 7.9. There is only a small difference in the streamwise velocity profiles. The height of the velocity boundary layer is larger for cases 4 and 5, which is to be expected, as cases 4 and 5 are perfect gas. Similarly, the height of the temperature boundary layer is larger for the perfect gas cases. Since cases 4 and 5 have a greater boundary-layer height, it is expected that their unstable frequency range will be lower than cases 1–3. It is also possible to compare the species densities between all five cases noting that for perfect gas $\rho_{O2} = c_{O2,\infty}\rho$. At the wall, case 1 has less oxygen than the other cases. In case 1, ablation has introduced carbon products into the flow, and this far downstream most of the carbon is in the form of CO. This means that for each carbon atom in CO, an oxygen atom is needed, which will reduce the density of oxygen and atomic oxygen for case 1 when compared to the other cases. This behavior is not seen in case 2 or 3 as there are no carbon containing species. Near $y = 0.002$ m, case 1, 2, and 3 begin to have the same density of oxygen as CO has not diffused significantly beyond this wall-normal distance.

7.2 Boundary-Layer Receptivity for $\mathbf{M_\infty = 15.99}$ Blunt Cone

After simulating the steady base flows, unsteady simulations were performed for cases 1a, 4, and 5. It was assumed *a priori* that the dominant instability mode for the freestream conditions and geometry would be the second mode. The second mode is most unstable when its phase velocity is aligned with the freestream flow. Therefore, an unsteady two-dimensional axisymmetric simulation was performed to minimize the required computing resources.

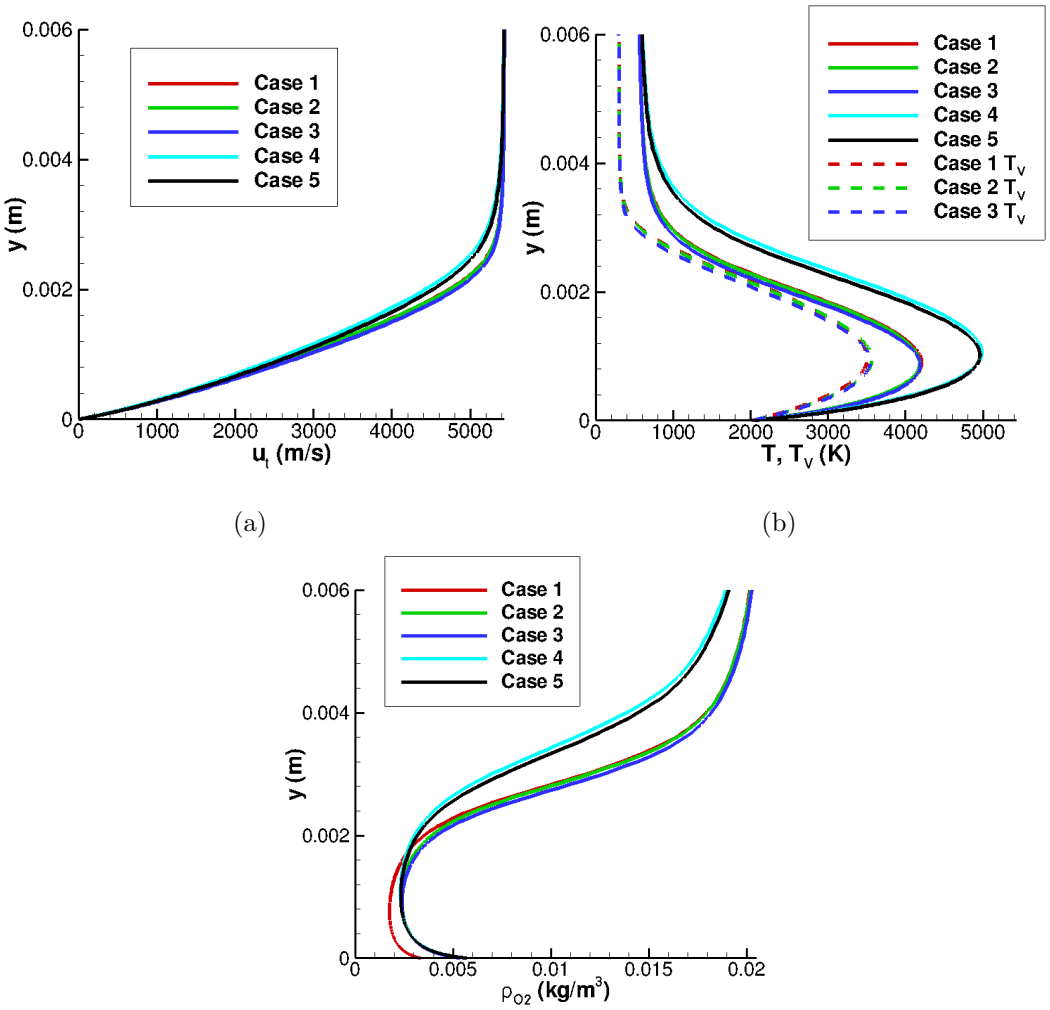

(a)

(b)

(c)

Figure 7.9: Meanflow profile comparison at s=0.564 m.

Freestream disturbances were imposed on the steady base flow to find how the boundary layer behaved in the presence of graphite ablation and thermochemical nonequilibrium. The freestream disturbances imposed were weak planar fast-acoustic waves in the freestream before reaching the shock at a zero incidence angle The freestream variables can be written as a summation of the meanflow and an oscillating perturbation as

$$\begin{bmatrix} \rho_{1,\infty} \\ \vdots \\ \rho_{ns,\infty} \\ u_{1,\infty} \\ p_\infty \end{bmatrix} = \begin{bmatrix} \bar{\rho}_{1,\infty} \\ \vdots \\ \bar{\rho}_{ns,\infty} \\ \bar{u}_{1,\infty} \\ \bar{p} \end{bmatrix} + \begin{bmatrix} \Delta\rho_{1,\infty} \\ \vdots \\ \Delta\rho_{ns,\infty} \\ \Delta u_{1,\infty} \\ \Delta p_\infty \end{bmatrix} \exp\left(i\left(k_{x,\infty}\left(x - \left(u_{1,\infty} + c_\infty\right)\right)t\right)\right) \quad (7.1)$$

where the disturbance amplitudes for fast-acoustic waves are defined by

$$\epsilon = \frac{\Delta p_\infty}{\gamma_\infty p_\infty} = \frac{\Delta\rho_\infty}{\rho_\infty} = \frac{\Delta u_{1,\infty}}{c_\infty}. \quad (7.2)$$

Here, γ_∞ is the ratio of specific heats in the freestream, c_∞ is the speed of sound in the freestream, and $\epsilon = 5 \times 10^{-4}$. Seven frequencies are imposed, starting with a base frequency of 75 kHz, where each frequency is a multiple of this base and the last frequency is 525 kHz. All frequencies are imposed simultaneously, and their phases are set randomly.

For each of the three unsteady cases, the simulation was run until the solution became periodic in time. After which, the simulation was run for one more full period in time and data were output for a temporal Fourier analysis. The Fourier analysis decomposed the flowfield disturbances back to the original seven imposed freestream frequencies, giving the amplitudes and phase angles of all saved variables for each frequency in the following form:

$$\phi'(x, y, t) = \Delta\phi(x, y) \exp\left[i\left(\psi(x, y) - 2\pi f t\right)\right], \quad (7.3)$$

where ϕ' is the perturbation of some variable, $\Delta\phi$ is the amplitude of that variable, ψ is the corresponding phase angle, and f represents a single dimensional

frequency. An instantaneous snapshot of the flowfield can be obtained from the real part of ϕ' when t is specified.

In a DNS, many boundary-layer modes are present in the boundary layer simultaneously. As one mode becomes dominant for a given frequency, it is possible to derive equations for the growth rate, wave number, and phase speed of this mode from Eq. (7.3), which yields

$$-\alpha_i = \frac{1}{\Delta\phi(f)} \frac{d}{ds} \Delta\phi(f) \tag{7.4}$$

$$\alpha_r = \frac{d}{ds} \psi(f) \tag{7.5}$$

$$c_r = \frac{2\pi f}{\alpha_r} \tag{7.6}$$

where s is the streamwise coordinate, $\Delta\phi(f)$ represents a variable amplitude at a given frequency, $\psi(f)$ represents the corresponding phase angle at the given frequency, and $\alpha_i < 0$ indicates instability. It is possible to compute α_i, α_r, and c_r using variables that peak at the critical layer for second mode disturbances. If this is done, interpolation may be required to trace the critical layer downstream. In this work, surface pressure is used as a second-mode pressure disturbance, has a maximum amplitude at the surface, and no interpolation is required. Previous researchers [MZ03b] have used surface pressure perturbations to compute α_i, α_r, and c_r from a DNS, which compared well with theoretical results.

An accurate comparison of growth rate, wave number, and phase velocity of an individual instability mode may be obtained between DNS and linear stability theory (LST) results when the particular boundary-layer instability mode is dominant, i.e., its magnitude is larger than magnitudes of other instability modes simultaneously present in the boundary layer. This is the case in many hypersonic boundary layers where the second mode grows exponentially and dominates other instability modes. If a dominant instability mode is not present, then wave modulation occurs due to multiple instability modes of similar magnitudes. In this work, an 11-species real-gas LST code with ablative boundary conditions that

accounts for transverse curvature is used for comparison to, and analysis of, DNS results. Also, ideal-gas LST results are used, which are obtained from a derivative of the real gas code, i.e., source terms are turned off and the vibration energy equation is neglected. Note that, second mode-growth is a maximum for $\beta = 0$, which represents a two-dimensional axisymmetric instability.

Before moving further, the unsteady DNS boundary conditions for each simulation need to be addressed. For each of the three cases, different unsteady wall boundary conditions are imposed. Each case uses pressure extrapolation to set the disturbance wall pressure. For case 1a, the surface mass balance as well as the surface energy balance are used as boundary conditions. This means that the wall-normal velocity will fluctuate as well as the wall temperature. For case 5, the no-slip condition is enforced on the disturbances and $T'_w = 0$. For case 4, the mass flux is forced to remain constant and $T'_w = 0$. When enforcing the mass flux to remain constant, the wall-normal velocity must fluctuate because density will fluctuate at the surface [recall Eq. (2.60)].

An unstable frequency range for the second mode at $s = 0.60$ m was computed using LST and is shown in Fig. 7.10. A positive growth rate $-\alpha_i$ indicates an unstable second mode, whereas a negative growth rate indicates a stable second mode. LST predicts for case 1a at this streamwise location that the second mode will be unstable between 430 and 547 kHz. The growth rates for the 450 and 525 kHz second modes are 12.4 and 8.6, respectively. The DNS shows that the 525 kHz second mode would be unstable and the 450 kHz second mode would be unstable as well, indicating an agreement between the two methods. A similar agreement was obtained upstream near $s = 0.30$ m for case 1a where the 525 kHz disturbance is unstable in the DNS and is predicted to be unstable by LST. Figure 7.10(b) shows the unstable frequency range predicted by LST for case 4. The unstable range is similar for both cases 4 and 5, so only one case is shown. LST predicts that, at this streamwise location, the second mode will be unstable

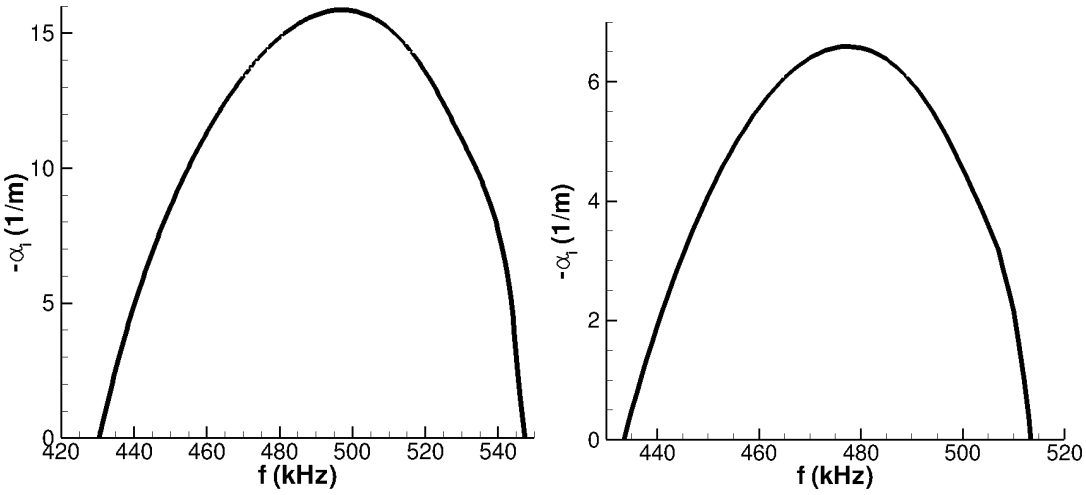

Figure 7.10: Unstable frequency range at $s = 0.60$ m obtained from LST.

between 434 and 513 kHz. Therefore, it is expected that, at $s = 0.60$ m, the imposed 525 kHz disturbance will be stable in both cases 4 and 5 and the 450 kHz disturbance will show some disturbance growth. Note that the LST results were not available at the time the DNS freestream forcing frequencies were chosen, so the forcing frequencies are not tailored to the LST predictions.

For a second-mode wave, it is well known that the maximum pressure perturbation occurs at the surface and the growth of the second mode is exponential. Figure 7.11 shows a plot of the real part of the 525 kHz pressure perturbation at the wall for case 1a and case 4. The real part of the pressure perturbation mimics the instantaneous flow. Case 5 is not shown, but its behavior is similar to case 4. For the pressure perturbation of case 1a, exponential growth is clearly visible, indicating a dominant second mode. There is no exponential growth for case 4; there is just modulation around a relatively constant amplitude. This modulation, or pumping, indicates that no dominant mode is present, but rather multiple competing modes are present. It is possible to separate multiple competing modes through multimode decomposition, as in [Tum03]. This is beyond the scope of the present work, as the focus here is on second-mode instability.

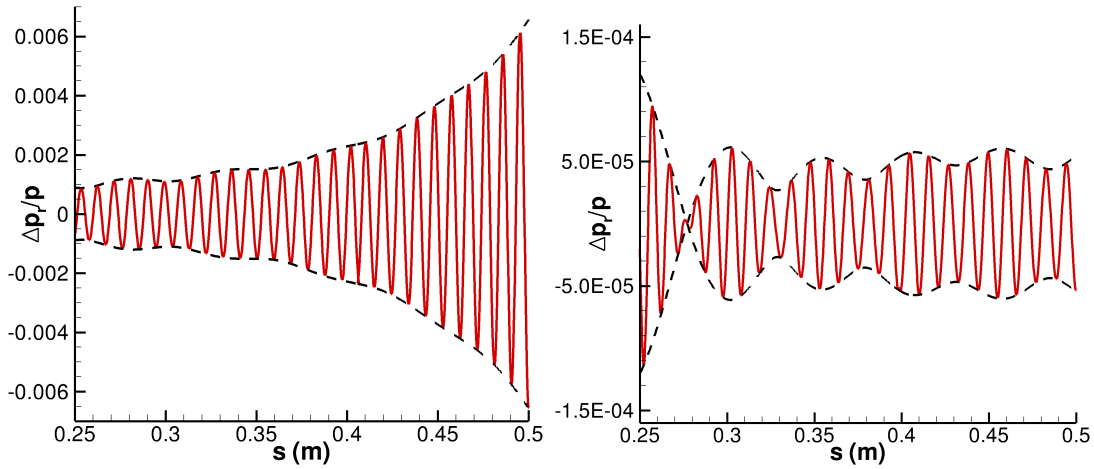

(a) Real Gas

(b) Ideal Gas Blowing

Figure 7.11: Instantaneous surface pressure for 525 kHz disturbance.

If there is a dominant boundary-layer mode in the DNS, it is possible to compare the growth rate, wave number, and phase speed to LST predictions of the dominant mode. A comparison of the growth rate for the 525 kHz disturbance is given in Fig. 7.12. Case 5 is not shown, but its behavior is similar to case 4. The oscillations in the DNS growth rates comes from multiple competing modes that are all present in the boundary layer simultaneously during the simulation where the LST growth rate is smooth because it is predicting only the second mode. For all three cases, growth can be seen near $s = 0$, which represents the stagnation location. This growth is most likely due to resonant interactions of the freestream fast-acoustic forcing waves with mode F. The real-gas DNS simulation shows second-mode growth starting near $s = 0.2$ m. The second mode amplitude grows exponentially, starting from $s = 0.2$ m, whereas other boundary-layer modes may be stable or decay exponentially. As the second mode grows exponentially, it becomes the dominant mode. This behavior can be seen as the oscillations in the DNS growth rate gradually dampen downstream of $s = 0.2$ m. Recall from Eq. (7.4) that the growth rate is computed from the DNS surface pressure perturbation amplitude. As the second-mode amplitude becomes much

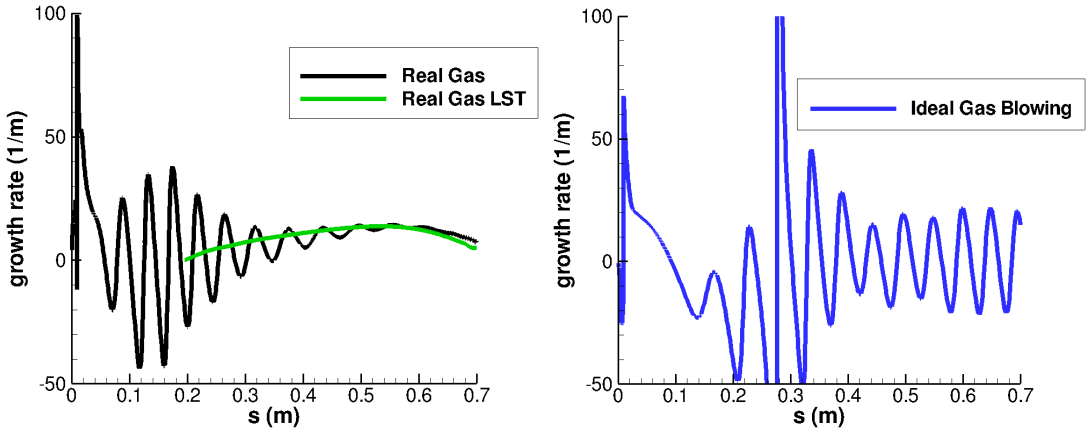

(a) Real Gas DNS and LST

(b) Ideal Gas Blowing DNS

Figure 7.12: Growth rate comparison for the 525 kHz disturbance.

larger than other modes in the boundary layer, the simulated growth rate from the DNS should be similar to LST predictions for the second mode. Similar growth rates between DNS and LST indicate that the modal growth from the DNS is indeed the second mode and that the second mode has become the dominant instability mode. For this complex DNS flowfield, the current comparison to LST is quite good. The two methods begin to diverge downstream ($s > 0.7$ m), where the DNS disturbance amplitudes are large enough that nonlinear behavior cannot be neglected. As LST assumes that disturbances are linear, some difference is to be expected. It should be noted that, with significant wall cooling and surface blowing, third and higher modes could possibly become unstable. For the simulated domain, no higher modes were found for the 525 kHz frequency although it is possible they may appear further downstream. Decreasing oscillations are not seen in case 4 because there is no dominant instability mode. For case 4, it is difficult to say if there is any growth because the growth rate is so strongly oscillatory.

The wave number and phase speed for the 525 kHz disturbance is shown for all three cases in Fig. 7.13. An LST comparison is given for case 1a, and the phase

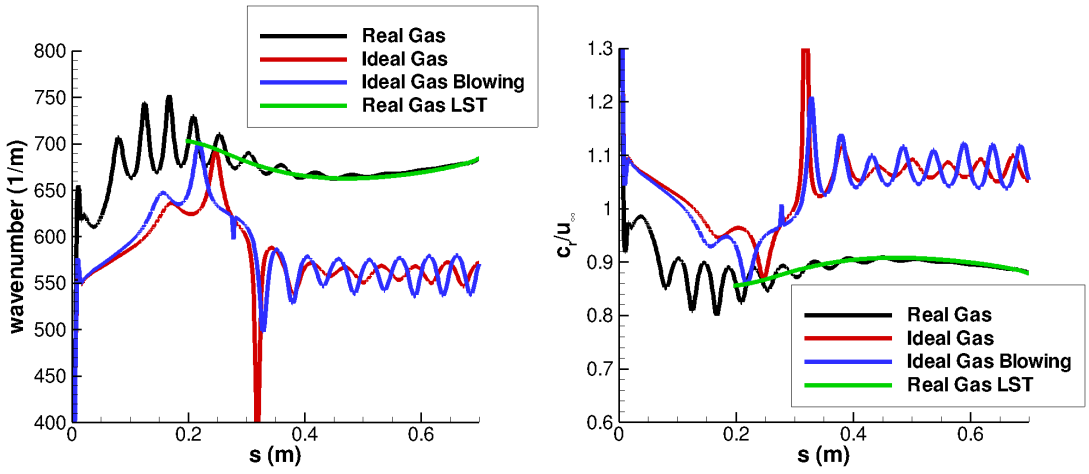

(a) (b)

Figure 7.13: Comparison of (a) wave number, and (b) phase velocity nondimensionalized by the freestream velocity for the 525 kHz disturbance.

speed is nondimensionalized by the freestream velocity. An LST comparison to cases 4 and 5 is not given, as there is no well-defined boundary-layer instability mode and the focus of this research is on real-gas effects. Once again, oscillations are seen in the DNS simulation that die out for case 1a as the flow moves downstream ($0.2 \geq s \geq 0.7$ m), indicating a dominating boundary-layer mode. For both the wave number and the phase speed, the LST and DNS results compare well, which increases the reliability of the results for both methods. Mode F and mode S are expected to be present simultaneously in the DNS. The phase speeds for mode F and mode S as they separate from the continuous spectrum are $c_r/u_e = 1 \pm 1/M_e$, respectively, where the subscript e represents boundary-layer edge conditions. M_e can be approximated as M_∞ for a flat plate with a weak shock. For a blunt body, such as the blunt cone simulated here, the edge conditions are not well defined due to a varying shock shape. Therefore, the flat plate conditions for the phase speeds of mode F and mode S (i.e., $c_r/u_e \approx 1 \pm 1/M_\infty$) may be used as a guide rather than a precise measurement. Tracing the phase velocity downstream from s=0 to $s \approx 0.2$ m for cases 4 and 5 shows the phase

velocity drop from 1.3 to below 0.9 as it likely approaches a synchronization point with mode S. After this synchronization point, the phase velocity then increases back to the fast-acoustic phase velocity. For case 1a, the phase velocity drops slightly below 0.9 and remains there for the length of the domain.

It is interesting to note that the boundary-layer wave for case 1a has a nondimensional phase speed near unity at the domain entrance, which is indicative of an entropy/vorticity wave where, for cases 4 and 5, the phase speed is around 1.1, indicating a fast-acoustic wave. Recall that freestream fast-acoustic waves were used in the freestream to perturb the steady base flow. Logically, it would seem that with fast-acoustic freestream forcing the incoming wave would be predominantly fast acoustic as well, but it is possible that real-gas effects or surface chemistry effects are exciting the entropy/vorticity wave stronger than the perfect-gas cases.

An instantaneous snapshot of the translation-rotation temperature and vibration temperature in the real-gas perturbed flowfield for the 525 kHz frequency disturbance is shown in Fig. 7.14. The instantaneous snapshot is obtained by setting $t = 0$ in Eq. (7.3) and taking the real part of the perturbed quantity. The 525 kHz frequency is shown because it is the most unstable frequency in the real gas simulation and second-mode behavior can clearly be seen. The top of the domain is the shock, and the bottom of the domain is the cone surface. Note that the scales for the subfigures are not the same due to exponential disturbance growth, so colors cannot be compared exactly between subfigures.

For the translation-rotation temperature contour plots, the second-mode wave can be seen in the oscillating colors near the wall and at the boundary-layer edge. This is due to a large perturbation near the boundary-layer edge and a large perturbation near the wall. The magnitude of the second-mode wave in Fig. 7.14(a) decreases slightly, indicating that the boundary-layer flow is stabilizing for this frequency component. For Figs. 7.14(b) and 7.14(c), the second-mode wave increases in magnitude in the downstream direction as it becomes dominant. The

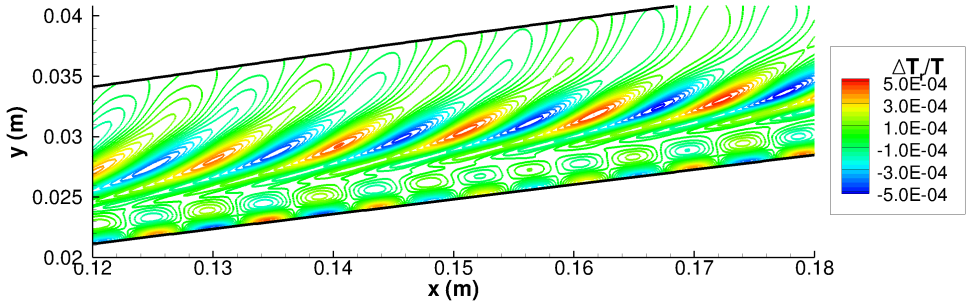

(a) Translation-rotation temperature (0.12 m $\leq x \leq$ 0.18 m)

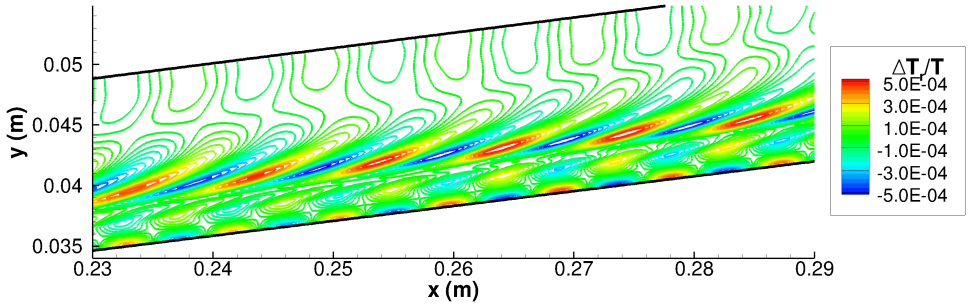

(b) Translation-rotation temperature (0.23 m $\leq x \leq$ 0.29 m)

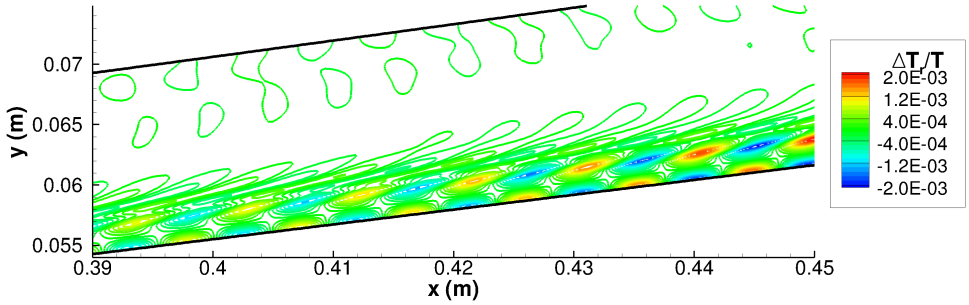

(c) Translation-rotation temperature (0.39 m $\leq x \leq$ 0.45 m)

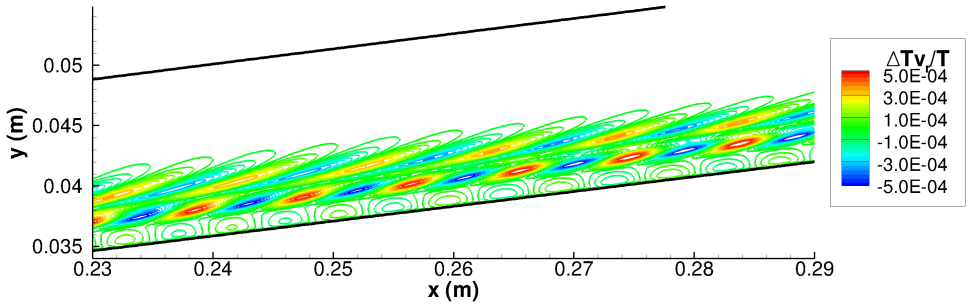

(d) Vibration temperature (0.23 m $\leq x \leq$ 0.29 m)

Figure 7.14: Instantaneous perturbation contour plots for the 525 kHz frequency disturbance.

increase in magnitude should be exponential as second-mode growth is exponential. Exponential growth is visible by comparing Figs. 7.14(b) and 7.14(c). Red and blue in Fig. 7.14(b) is on the order of 10^{-4}, whereas red and blue in Fig. 7.14(c) is on the order of 10^{-3}, indicating exponential growth of the second-mode wave. Above the second-mode wave are waves due to freestream forcing waves as they cross the shock in the nose region and then propagate downstream. These waves propagate downstream and toward the boundary layer with a relatively constant amplitude. Eventually, they move into the boundary layer and are dominated by the second mode. Just below the shock, waves can be seen that are a direct result of fast-acoustic freestream forcing waves propagating through the shock. There are also Mach waves that can be seen just outside of the boundary layer as the flow adjusts to disturbances.

Similar to the translation-rotation temperature, the second-mode wave can be seen in the vibration temperature contour plot with an increasing magnitude in the streamwise direction. The peak near the boundary-layer edge is much larger than the peak near the wall for vibration temperature. The perturbation just outside of the boundary layer is due to freestream forcing waves entering near the cone nose similar to translation-rotation temperature. For both temperatures, the maximum perturbation amplitude is the same order of magnitude.

The wave structure for oxygen and atomic oxygen is shown in an instantaneous snapshot for the 525 kHz disturbances given in Fig. 7.15. The second-mode wave is seen near the boundary-layer edge and is only slightly visible near the wall for oxygen. The amplitude of the second-mode wave increases in the downstream direction as the second mode becomes more dominant. For oxygen, the amplitude near the boundary-layer edge is larger than the amplitude near the wall. Freestream forcing waves are seen near the shock along with Mach waves. In the atomic oxygen contour plot, the temperature outside of the boundary layer is not large enough for any significant amount of atomic oxygen to exist, so there

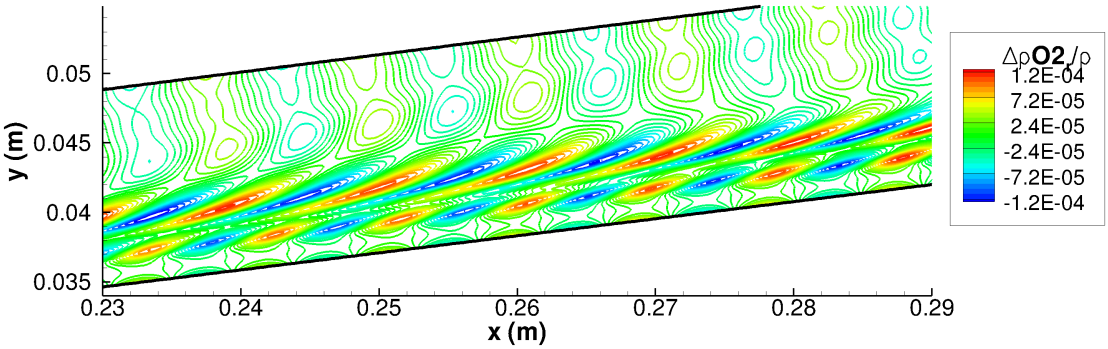

(a) Oxygen

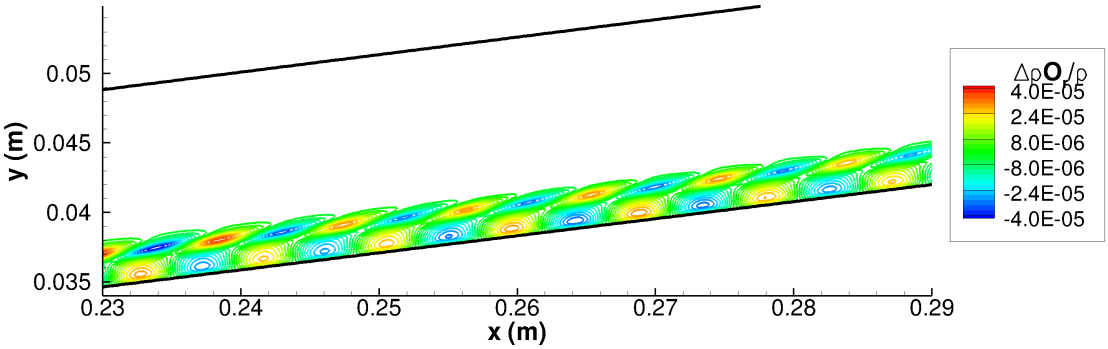

(b) Atomic oxygen

Figure 7.15: Instantaneous perturbation contour plots for the 525 kHz frequency disturbance.

are no freestream waves visible. The second-mode wave is clearly distinguishable for atomic oxygen. The magnitude of the second-mode wave is decreasing downstream for atomic oxygen because atomic oxygen is recombining to form oxygen, thus decreasing the density of atomic oxygen and its perturbation.

Since the unsteady flow is decomposed using a temporal Fourier transform, it is possible to plot the perturbation amplitudes to determine the growth or decay of each frequency component. Figure 7.16 gives a comparison of the wall-pressure perturbation amplitude of each frequency component for cases 1a, 4, and 5. For all three cases, initial disturbance growth can be seen near $s = 0$ as a result of resonant interactions between the forcing fast-acoustic waves and the fast-acoustic

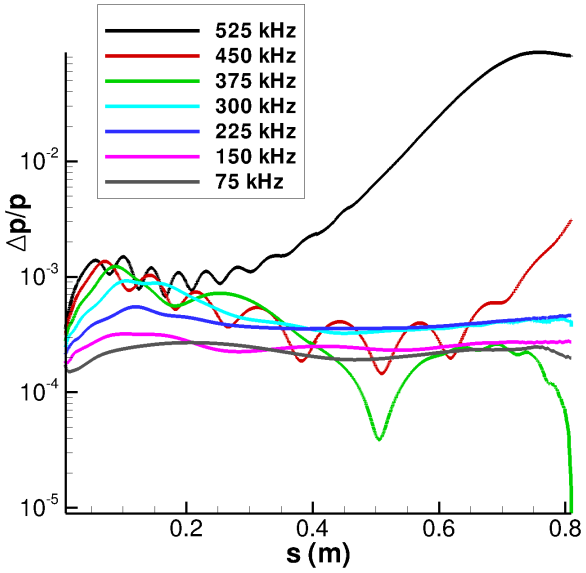

(a) Real Gas

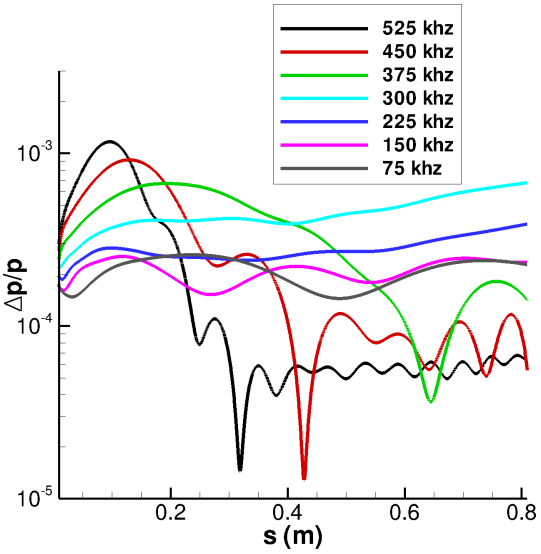

(b) Ideal Gas

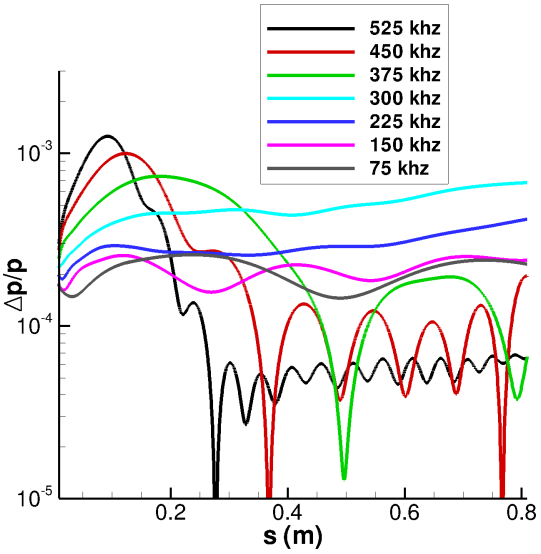

(c) Ideal Gas with Blowing

Figure 7.16: Pressure perturbation amplitude at the wall computed by DNS.

mode in the boundary layer. For case 1a, the most unstable frequency is 525 kHz and its exponential growth starts around x=0.2 m and is unstable almost to the end of the domain. This is a large unstable region of approximately 0.6 m. This growth is unstable second-mode growth. The 450 kHz disturbance becomes unstable near the end of the domain, but by this time, the disturbance flowfield has become nonlinear. It should be noted that the end of the domain (approximately x=0.7 m to x=0.8 m) for the real-gas simulation has surface pressure perturbation amplitudes above 1% of the freestream values. Meanflow distortion, or the zero frequency component obtained from the temporal Fourier transform, shows that velocity and pressure perturbation amplitudes at the surface near 10% of the steady base flow values at the domain exit. Also, temperature and density at the critical layer approach 1% of the freestream values at the domain exit. This significant mean flow distortion indicates that the flowfield has become nonlinear. It is possible to check for higher harmonics, which indicate flowfield nonlinearity, but the current grid is not well enough resolved to accurately capture those frequency components. As the flow becomes nonlinear, breakdown to turbulence follows, which requires a three-dimensional simulation to continue beyond $s \approx 0.8$ m.

Contrary to case 1a with a strong second-mode growth, cases 4 and 5 show only minor instability. For cases 4 and 5, the 525 and 450 kHz disturbances exhibit no visible exponential growth downstream of $s = 0.2$ m where exponential growth was seen for the real-gas simulation. There is only some slight instability shown for the 300 and 225 kHz disturbances downstream of $x = 0.4$ m, but the growth is much smaller than the second-mode growth seen in the real-gas simulation. It is conjectured that second-mode exponential growth will start for 300 and 225 kHz further downstream, as the unstable frequency range should decrease in the streamwise direction.

As this simulation (unlike previous DNSs of hypersonic boundary-layer instability in the open literature) accounts for graphite surface ablation, an indication

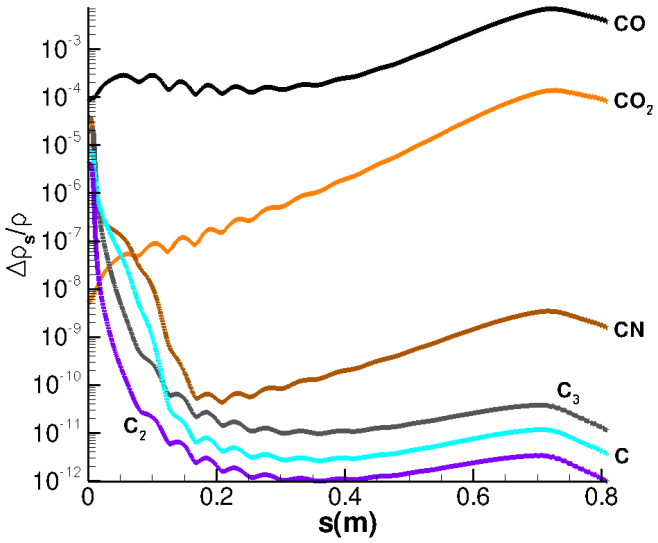

Figure 7.17: Perturbation of species density for each carbon species at 525 kHz. Perturbed quantities taken at the wall and obtained from DNS.

of which carbon-containing species plays the largest role in second-mode instability is sought. The perturbation amplitudes for each carbon species at the wall are shown in Fig. 7.17. As none of the carbon species significantly diffuse away from the surface (see Fig. 7.6), it is difficult to visualize their perturbations except to plot them along the surface. The two most significant species amplitudes are CO and CO_2. This follows the fact that CO and CO_2 are the two carbon species that have the most mass at the wall in the steady solution, as seen in Fig. 7.5. It is interesting to note that the initial growth due to resonant interactions of freestream fast acoustic waves and fast acoustic modes seen for Δp at 525 kHz is only seen slightly in the species densities of CO and CO_2 and is not seen in the other species. This could simply be due to the fact that the mass in these species is already decreasing so quickly at the wall (Fig. 7.5) that the resonant interactions have little effect.

In the second-mode growth region for the 525 kHz second mode (0.2 m$\leq$ s $\leq$0.7 m), the maximum amplitudes at a single streamwise location for these two species occur at the wall, where only a slight peak is seen away from the

wall. This is unlike N_2 and O_2 , where there is a high amplitude near the wall and a high amplitude near the boundary-layer edge as well. This is due to the fact that CO and CO_2 are not diffusing far from the wall and have no significant mass at the boundary-layer edge. As the development of the second mode strongly depends on steady flow properties near the critical layer, which moves toward the boundary-layer edge for hypersonic flows, it is possible that, in slender geometries with surface ablation where the second mode is the dominant instability mode, when blowing is small (as it is here), the effects of surface ablation on second-mode development are minimal. Note that this does not include possible ablation-induced surface roughness effects on second-mode development. Further simulations with and without surface ablation would be required to validate this argument.

7.3 Linear Stability Analysis of $M_\infty = 15.99$ Blunt Cone

LST is able to predict instability waves and their corresponding growth rates from steady boundary-layer profiles. The characteristics of an instability wave are strongly tied to the meanflow boundary-layer profile which is taken as an input for the linear stability analysis. It is possible to use a single meanflow boundary layer profile computed using one gas model and then change gas models in an LST code to predict how the characteristics of *only* instability waves will behave with changing models. This has been done to good effect by previous researchers [JSC98]. Since instability waves are tied so strongly to the meanflow profiles, to predict how different gas types, i.e. ideal gas and real gas, effect the entire process of hypersonic boundary layer transition, the meanflow as well as the computation of instability waves needs to be performed with each of the separate models. Similarly, both a meanflow and instability waves need to be computed to assess the overall effect of surface chemistry such as wall catalycity and surface

ablation on hypersonic boundary layer instability. By computing a meanflow and the corresponding instability waves with the different models, an accurate comparison of the gas effects on flow instability, rather than simply the instability waves, can be given.

LST gives information about what disturbance frequencies are unstable and the corresponding growth rates of those frequencies, but there is no information on the amplitude of the incoming disturbance. To estimate boundary-layer transition using LST, the e^N transition criterion is used which is defined as

$$e^N = \frac{A}{A_0} = \exp\left(-\int_{s_0}^{s} \alpha_i dx\right). \tag{7.7}$$

Here, A is the integrated disturbance amplitude, A_0 is the initial amplitude, s_0 is the location where the disturbance first becomes unstable, and α_i is the spatial amplification rate. The integration is performed for a constant frequency ω. Note that a negative imaginary part of the wave number α results in disturbance growth while a positive value results in disturbance decay. The N factor is specifically the exponent of e^N. In-flight transition N factors are commonly understood to be around 10. [Mal03] showed that 9.5 and 11.2 correlated with transition onset for two high Mach number flight tests. In ground test facilities the transition N factor is usually lower.

Before moving further, the LST wall boundary conditions for each of the meanflow cases needs to be covered briefly. The difference between cases 1a and 1b is the boundary conditions used in the stability computations. In case 1a, the full linearized surface model for graphite pseudo-ablation is used while in case 1b the linearized surface energy balance (Eq. (3.78)) is replaced with $\hat{T}_w = 0$. For cases 2–5, $\hat{T}_w = 0$ as the wall meanflow temperature is set from case 1. For cases 2 and 3, the corresponding surface mass balances are linearized to provide conditions for species perturbations at the wall. Note that this is the same as described previously in Sec. 3.2.1 but the mass flux terms where carbon species are produced are

dropped. For cases 4 and 5 the fluctuation of the composition is forced to zero, i.e., $c_s' = 0$.

Note that the same fourth order LST code was used for each of the cases. For cases 2 and 3, only changes to the boundary conditions were required. For cases 4 and 5, all species and their perturbations except N_2 and O_2 were forced to zero, the meanflow as well as the perturbation vibration temperature was forced to zero, source terms and their derivatives were forced to zero, and k_V and D_s with their derivatives were forced to zero. Also, the boundary conditions for cases 4 and 5 were changed.

Before creating an N factor plot, it is required to locate the second mode before tracing it either downstream or upstream. To aid in locating the second mode for various frequencies, a plot of the fast and slow modes, mode F and mode S respectively, is obtained at a single streamwise location ($s = 0.65$ m). Figure 7.18 shows the phase velocities, and growth rates, for the fast and slow modes for cases 1b, 2, and 4. Case 1a is similar to 1b, case 3 to 2, and case 5 to 4, which is why they are not shown. The fast mode appears near $c_r = 1 + 1/M_\infty = 1.063$ and the slow mode appears near $c_r = 1 - 1/M_\infty = 0.937$. The slow mode is the mode that turns into the second mode as the frequency increases for each case. This can be seen as $-\alpha_i$ becomes positive for the slow mode indicating exponential growth. Qualitatively, there is little difference between the three cases shown. The main qualitative difference is that the third mode, represented by the bump in growth rate near 1100 kHz for each case, follows the second mode for both cases 1b and 4. However, the third mode comes from the fast acoustic spectrum for case 4. Also, the third mode, while not unstable for any of the cases, is much more pronounced for the real gas cases, i.e., cases 1–3. The third mode is visible for case 4, but it is noticeably smaller.

After locating the second mode, it is possible to trace it upstream and downstream using LST to find the second-mode N factor. Figure 7.19 shows the N

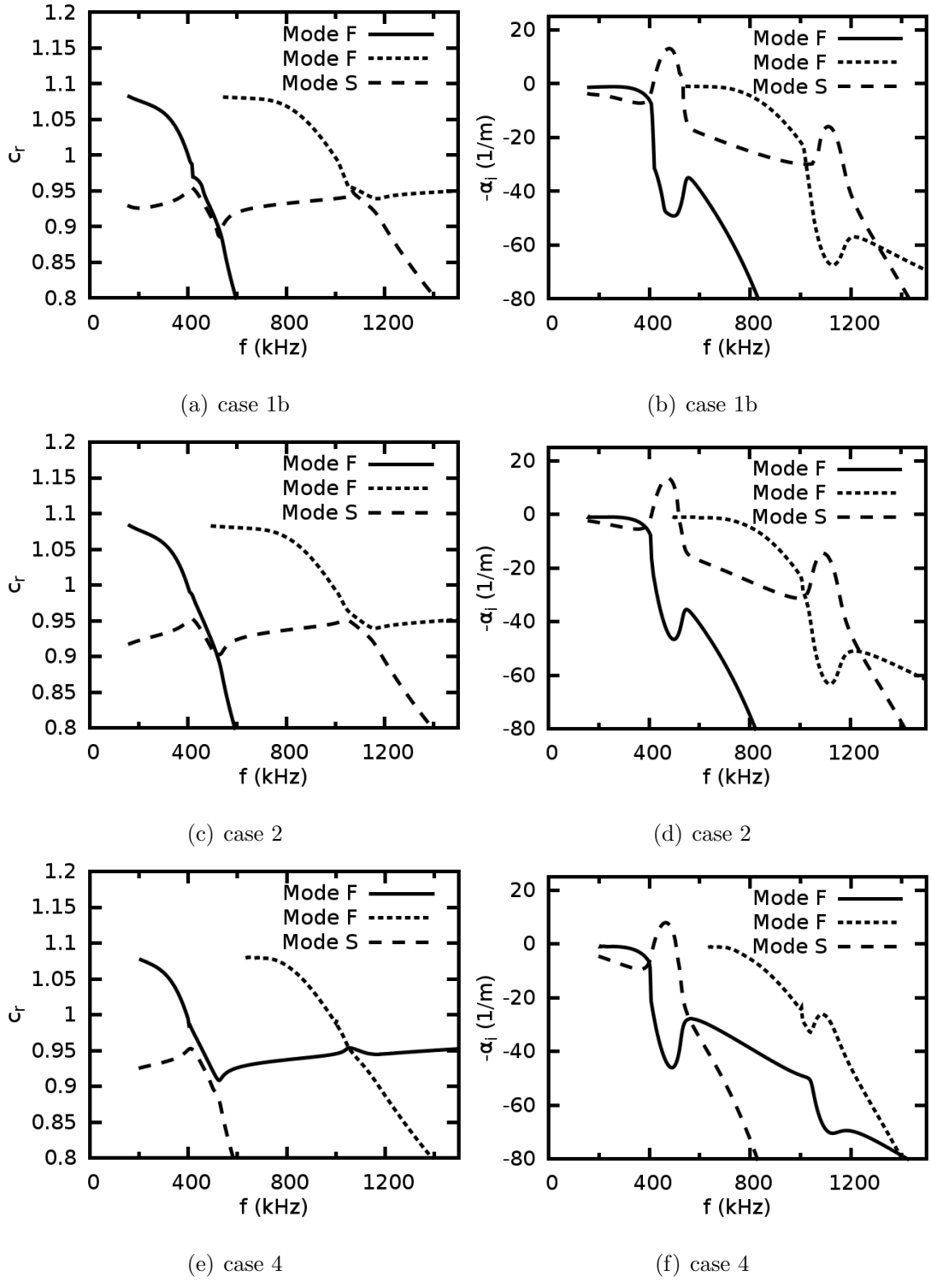

(a) case 1b

(b) case 1b

(c) case 2

(d) case 2

(e) case 4

(f) case 4

Figure 7.18: Fast and slow mode plot of (a) phase velocity and (b) growth rate.

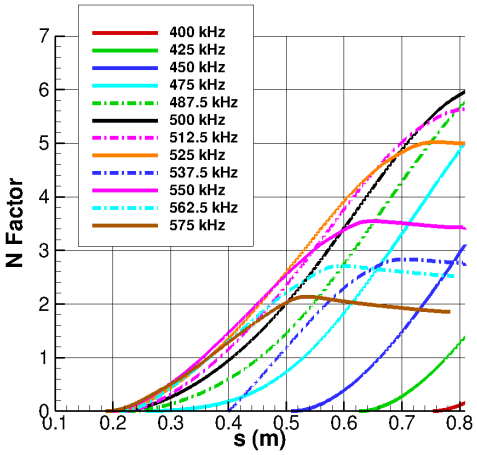

(a) case 1a

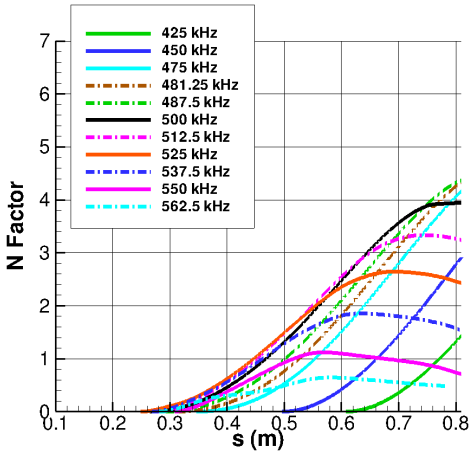

(b) case 1b

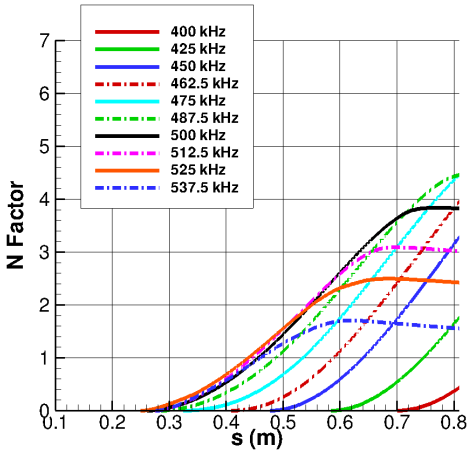

(c) case 2

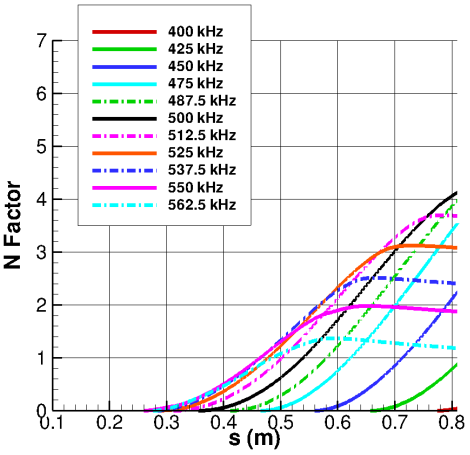

(d) case 3

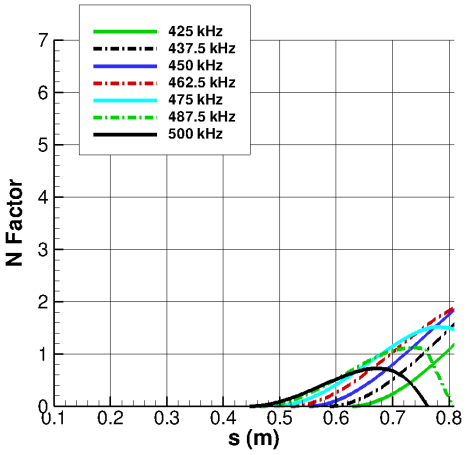

(e) case 4

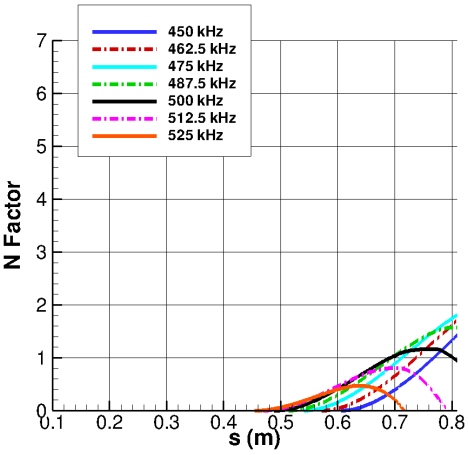

(f) case 5

Figure 7.19: N factor comparison.

factor plots for each of the six cases. The case with the largest N factor is case 1a where the N factor is 5.97 at the exit of the domain. This means that from the neutral point the disturbance has grown 391 times. The corresponding frequency for this maximum N factor of case 1a is 500 kHz. The second largest N factor is found from case 1b where N=4.37 and the corresponding frequency is 487.5 kHz. Recall that the only difference between cases 1a and 1b is the temperature perturbation boundary condition which is $\hat{T}_w = 0$ for case 1b. Comparing the N factors shows that the most amplified frequency for case 1a is nearly five times larger than the most amplified frequency for case 1b. Also, the frequency of the maximum second-mode N factor is shifted to a slightly lower frequency for case 1b. Hence, a change in only the temperature perturbation boundary condition can have a significant effect on a hypersonic boundary layer's second mode.

From Figs. 7.19(b) and 7.19(c) it is possible to note the differences that result due to changing the wall blowing from ablation to blowing air at the freestream mass concentration. Essentially this would be measuring the effect of carbon species due to ablation in the boundary layer as opposed to only 5-species air in the boundary layer. Recall from Fig. 7.9 that the difference in streamwise velocity and both temperatures for Case 1 and 2 is negligible, but there is some difference in the chemistry. For case 1b, the largest N factor is 4.37 at 487.5 kHz. For case 2, the maximum N factor is 4.46 at a frequency of 487.5 kHz. The difference between these two cases is small with case 2 slightly more unstable than case 1. The frequency for the most amplified disturbance is the same for both cases. Therefore, for this test case, the carbon species in the boundary layer slightly damp the second-mode instability. These results are consistent with [AH97], where it was found experimentally that a high enthalpy CO_2 flow transitioned later than corresponding N_2 or air flows at the same enthalpy.

To investigate these effects further, similar to [JSC98], the sign of the heat of formation was changed for CO_2 and CO in the instability calculations for case 1b,

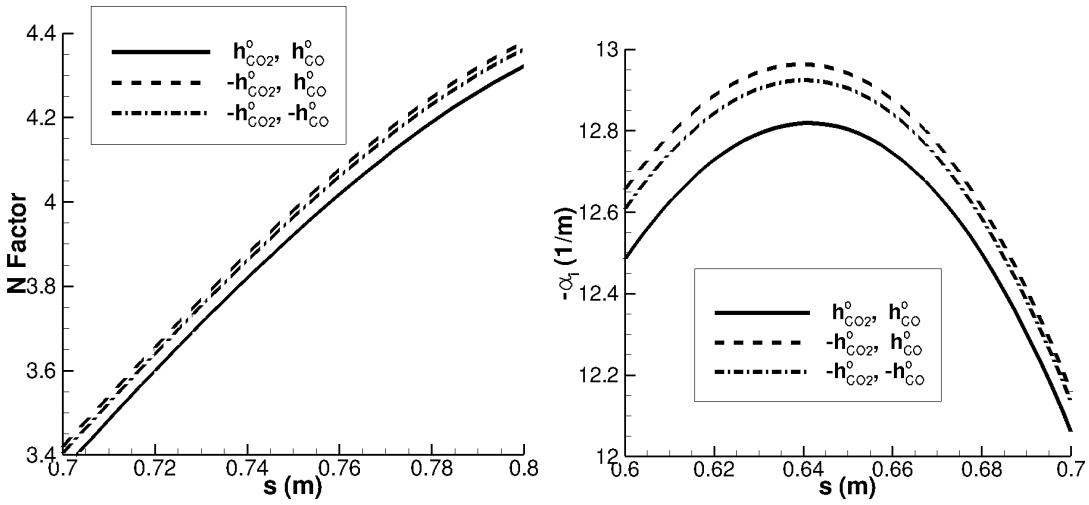

(a) (b)

Figure 7.20: N factor and growth rate comparison for varying CO_2 and CO heat of formation of the 487.5 kHz second mode.

while the meanflow remained the same. This effectively extracts heat from the flow, as compared to the nominal case, when CO_2 is produced, rather than adding heat. The results from this numerical experiment are shown in Fig. 7.20 for the frequency with the highest N factor in case 1b (487.5 kHz). Note that by switching the sign for the heat of formation, an increased N factor, or growth rate, means the effects are stabilizing when the sign of the heat of formation is not switched. Also note that, the only significant reaction including carbon species over the range shown is the recombination of CO_2 denoted by $CO + O + M \rightarrow CO_2 + M$.

When only the sign of CO_2 is switched, the N factor is increased due to an increased growth rate. The increase in growth rate is slight and remains around 1% to 3% over the length of the unstable second-mode range. When the sign of the heat of formation is switched for both CO_2 and CO, the N factor is still higher when compared to the nominal case. However, CO has the opposite effect of CO_2. It is slightly decreasing the growth rate when compared to the case that only switches the sign of CO_2. To summarize these findings, switching the sign

for the heat of formation of CO_2 measures the effect that production of CO_2, from CO and O, has on the flow instability. When the sign for the heat of formation of CO_2 is switched, it destabilizes the second mode. Therefore, when the sign is not switched, CO_2 stabilizes the second mode. This stabilizing effect is, however, quite slight for the given case which likely explains the slight decrease in N factor from case 1b to case 2.

It should be noted that it has been shown that the rate of CO+O recombination is slow and atomic oxygen recombination can be much faster [SCM00]. If this is the case, the flow may be composed of O_2 and CO which can exist stably under these conditions. This could possibly change the stabilizing effect shown here which is likely due to the recombination of CO and O. Further simulations with different reactions and reaction rates would be needed to further elucidate this issue. However, for the reactions and reaction rates used here, it is likely that as blowing increases, there will be more mass from carbon species in the boundary layer. Assuming that the same trend is followed, this will more strongly stabilize the boundary layer. Also, if the estimated ablation rates are low, it would be possible to predict transition in a second mode dominated graphite ablative flow by assuming the surface blowing to be composed of air rather than various carbon products.

It is also possible to isolate the effects of blowing on boundary-layer instability in a hypersonic real gas. Figures 7.19(c) and 7.19(d) show cases 2 and 3 where case 2 has blowing and case 3 does not. The largest N factor for case 2 is 4.46 at 487.5 kHz. The largest N factor for case 3 is 4.12 at 500 kHz which results in a decrease of the most amplified disturbance by 40%. Therefore, the boundary layer with blowing is destabilized compared to the boundary layer with no blowing. Note that the blowing profile is large upstream near the nose but small downstream of the nose. So it is conjectured that the strong blowing upstream has a larger effect than the near zero blowing downstream. Also, recall from Fig. 7.8 that

the boundary-layer thickness is slightly less for case 3 as compared to case 4. It is likely that the slight shift in frequency between these two cases is due to the slight difference in the thickness of the boundary-layer. The fact that the blowing is found to destabilize the second mode is consistent with previous research in [JGC09] for a reacting boundary layer.

Similarly, blowing effects on a hypersonic boundary layer with an ideal gas assumption can be seen by comparing Figs. 7.19(e) and 7.19(f). The maximum N factor for case 4 is 1.88 at a frequency of 462.5 kHz and the maximum N factor for case 5 is 1.81 at a frequency of 475 kHz. The difference between these two cases is minute showing that for the ideal gas boundary layer blowing has a negligible effect on boundary layer stability in this particular case.

Finally it is possible to isolate real gas effects by comparing case 2 with case 4 and case 3 with case 5 (Figs. 7.19(c) and 7.19(e) and Figs. 7.19(d) and 7.19(f), respectively). The difference in maximum N factor between cases 2 and 4 is 2.58 which results in a disturbance that is thirteen times larger for case 2. This is a significant difference. Here, the real gas causes the largest disturbance to grow an order of magnitude more than the ideal gas case. Note also that the neutral points for unstable frequencies have moved downstream for the ideal gas case when compared to the real gas case. This is to be expected as the height of the boundary layer is larger for the ideal gas case (recall Fig. 7.8). Similar results are seen by comparing cases 3 and 5. The difference in maximum N factor is 2.31 which gives a most amplified disturbance that is ten times larger for case 3. Also, the start of the unstable frequency range for each frequency has again shifted downstream. Therefore, in this particular case, real gas effects are destabilizing to the hypersonic boundary layer. Real gas effects in both comparisons result in a maximum disturbance at the domain exit that is one order of magnitude larger than the corresponding ideal gas case. Also, the neutral points shift downstream for the ideal gas cases.

As seen in Eq. (7.7), the N factor is obtained by integrating the growth rate in the streamwise direction. By examining the growth rates corresponding with each N factor, it can be found how the growth rate is influencing the N factor. A growth rate plot for each case is given in Fig. 7.21. Comparing cases 1a and 1b the growth rate for each frequency is overall larger for case 1a. Also, the range along the cone for the unstable frequencies is larger for case 1a, i.e., a frequency for case 1a is unstable over a larger length of the cone. Noting these differences, the difference in N factor between cases 1a and 1b is due to the larger growth rate and the larger range over which the frequencies are unstable.

Comparing cases 1b and 2, the growth rates for both cases, as well as the unstable ranges, are nearly the same. Looking specifically at the second mode at 487.5 kHz, the maximum growth rate is 12.82 at 0.64 m for case 1b and is 12.98 at 0.63 m for case 2. This is a relative difference of 1.2% between these cases. This difference makes sense as the maximum N factor of the two cases was nearly identical.

Comparing cases 2 and 3 it can be seen that the growth rate is nearly the same for both cases, therefore, the difference in N factor must be explained by a larger unstable range for case 2. Here, blowing is causing the unstable region to become larger for the most unstable frequencies in the domain.

The growth rates of cases 1a, 1b, 2, and 3, show that the highest frequency is not always the first unstable frequency. For example, notice Fig. 7.21(c) where the highest frequency included in the calculations is 537.5 kHz and it crosses from stable to unstable at $s = 0.276$ m. Upstream of $s = 0.276$ m, there are lower frequencies than 537.5 kHz, such as 525 kHz, that are already unstable. This behavior is most likely due to the decreasing boundary-layer thickness causing some higher frequencies to become unstable later. This behavior is not seen for either case 4 or case 5 as there are no significant second mode instabilities when the boundary-layer is decreasing.

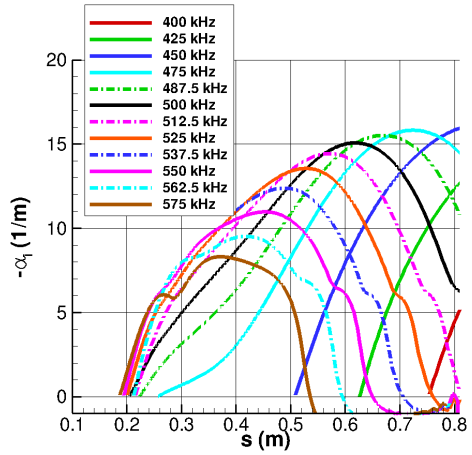

(a) case 1a

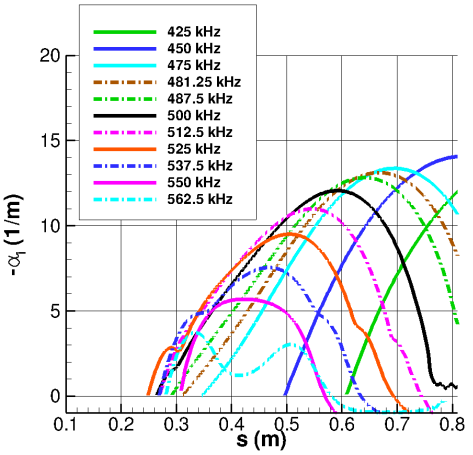

(b) case 1b

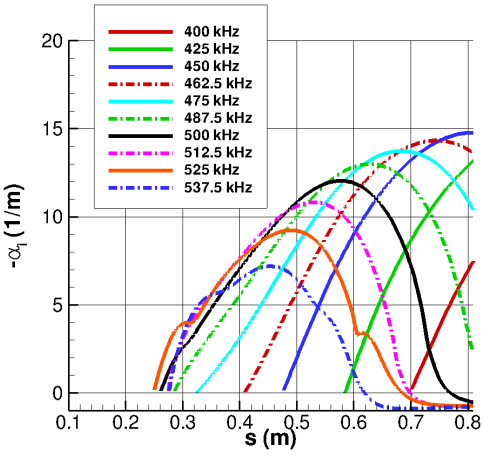

(c) case 2

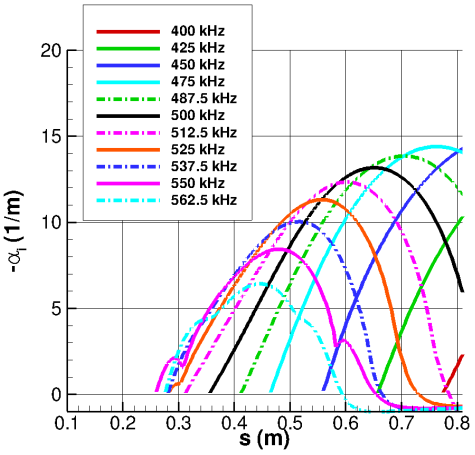

(d) case 3

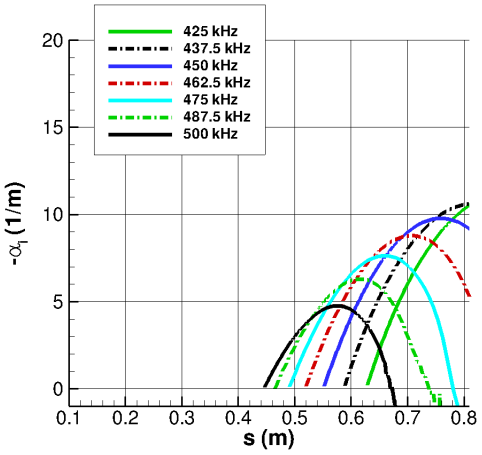

(e) case 4

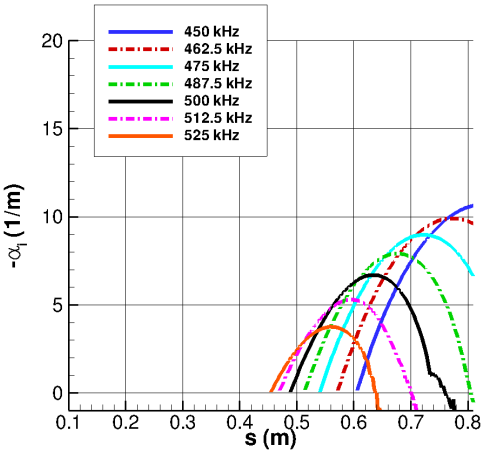

(f) case 5

Figure 7.21: Growth rate ($-\alpha_i$) comparison.

Again, it is possible to analyze real gas effects by comparing case 2 with case 4 and case 3 with case 5 (Figs. 7.21(c) and 7.21(e) and Figs. 7.21(d) and 7.21(f), respectively). Comparing cases 2 and 4, it can be seen that the growth rates for the real gas are larger than for the ideal gas. Also, the frequencies are unstable over a larger streamwise distance. Similarly, the growth rates for case 3 are much larger than for case 5 and the unstable range is larger for case 3. For this case, real gas effects increase the disturbance growth rate as well as increase the unstable range of the disturbance.

To analyze the effects of transverse curvature on the second mode only, the N factor was obtained using LST without the curvature terms for each case. Note that the meanflow is still computed with the transverse curvature effect and it is only in the instability waves where transverse curvature is neglected. Figure 7.22 shows the N factor comparison for case 1b with and without transverse curvature. The largest N factor computed with the transverse curvature terms neglected is 4.68 for the 487.5 kHz second mode. This results in a 37% amplification compared to case 1b where the transverse curvature terms are included. The frequency for the largest N factor is not changed. This trend is the same for each of the cases. For each case, excluding the transverse curvature terms results in a larger N factor, i.e. the second mode is destabilized, but the frequency remains the same. These results are consistent with previous instability calculations using a perfect gas [MS91] and a chemically reacting flow [CVM97].

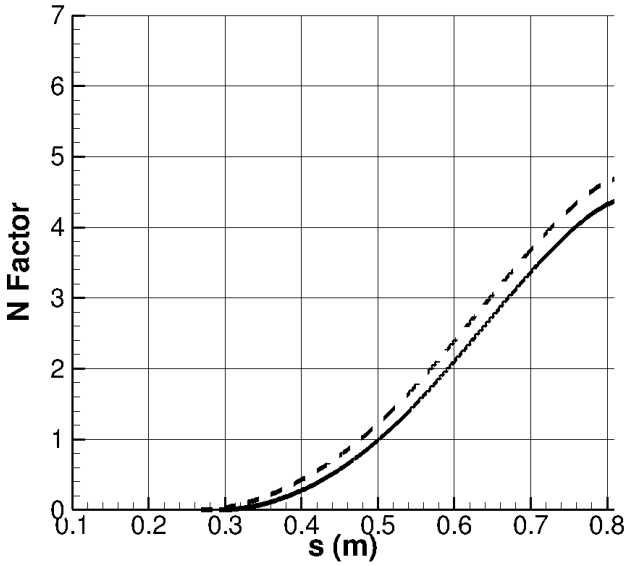

Figure 7.22: N factor comparison for case 1b of the most amplified frequency (487.5 kHz) with — and without - - transverse curvature.

CHAPTER 8

Linear Stability Analysis of the Reentry-F $M_\infty = 19.925$ Blunt Cone

This blunt cone case corresponds to a flight test, called Reentry F, designed to study the effects of a turbulent boundary layer on surface heating. High quality transition data is available from this experiment at multiple points along the flight trajectory. The vehicle geometry is a 5 deg cone with an ablating nose cone. This ablating nose cone is blunted and has a nominal nose radius of 2.54 mm [JSW72]. The vehicle geometry, along with the simulated shock location, is shown in Fig. 8.1. The freestream conditions simulated here are for the vehicle at 100 kft and are given in Table 8.1. The blunt-cone nose was composed of ATJ graphite from the nose tip to 0.22 m downstream along the cone axis. During the flight, the nose cone ablated and changed shape, thus, an estimate for the ablated nose tip radius at the given flight altitude is needed. The same estimated nose tip radius of 3.1×10^{-3} m from [Mal03] is used here. The remaining section of the straight cone had a beryllium surface. Surface temperature measurements are available along the beryllium portion of the cone [How71]. These conditions have been studied extensively by previous researchers [Mal03, JC05] where the most unstable frequencies and their N factors at transition onset were calculated for multiple gas models. However, their analysis neglected outgassing due to an ablating nose cone and carbon species in the freestream due to ablation which are accounted for in the current work.

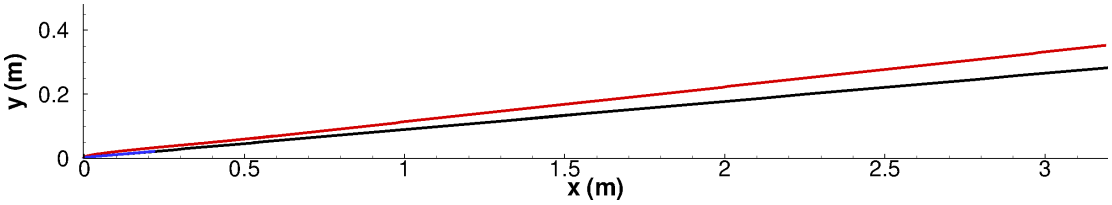

Figure 8.1: Physical domain of the Reentry-F simulation. The shock is red, the surface of the ablating nose cone is blue, and the surface of the remainder of the cone is black.

Table 8.1: Freestream conditions for the Reentry-F cases.

Parameter	Value
M_∞	19.925
ρ_∞ [kg/m^3]	0.01672
p_∞ [N/m^2]	1099.0
c_{N_2}	0.767
c_{O_2}	0.233

8.1 Steady-State Solutions of the Reentry-F $M_\infty = 19.925$ Blunt Cone

Two separate meanflow simulations were run. The first case, called case 6, is a five species thermochemical nonequilibrium simulation. This simulation is similar to the meanflow simulations run in [Mal03] and [JC05]. The surface temperature is set from experimental results downstream of the ablating nose and an estimate from [Mal03] is used for the nose temperature. Non-catalytic conditions at the surface are used for each species across the entire length of the vehicle. The second case, called case 7, is an eleven species thermochemical nonequilibrium

simulation. This simulation accounts for the ablating nose through inclusion of the surface chemistry model described in Sec. 2.1. Downstream of the ablating nose, the experimental wall temperature is used and a non-catalytic condition is enforced at the surface.

The grid used in cases 6 and 7 is a body conforming ijk grid. It has 1250 points in the streamwise direction, 481 points in the wall-normal direction, and 4 points in the transverse direction. Figure 8.2 shows an example of the grid for part of the physical domain on the nose cone for k=1. The streamwise points are clustered near the ablating nose cone to give more resolution in areas of high streamwise gradients near the nose. Also, there is grid clustering near the surface and near the shock.

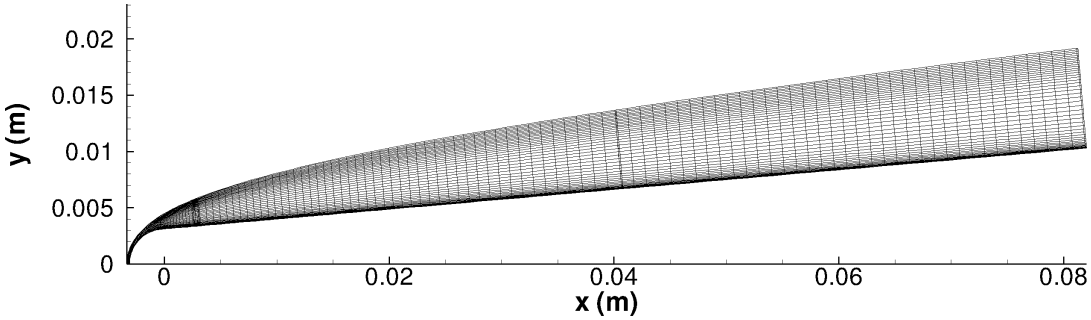

Figure 8.2: Part of the physical grid on the nose cone for case 6. Every 10 grid points are shown in each direction.

Figure 8.3 shows a comparison of the streamwise velocity between case 6, case 7, [Mal03], and [JC05]. Different computational grids were used for the different cases making the comparison at slightly different streamwise locations. However, the comparison between the cases is quite good. There are only slight differences between each of the cases. There is a difference between case 6 and case 7 but it is not visible in the plot. This shows that the inclusion of the ablating nose cone has only a slight effect on the meanflow profile of wall-tangent velocity at the domain outlet.

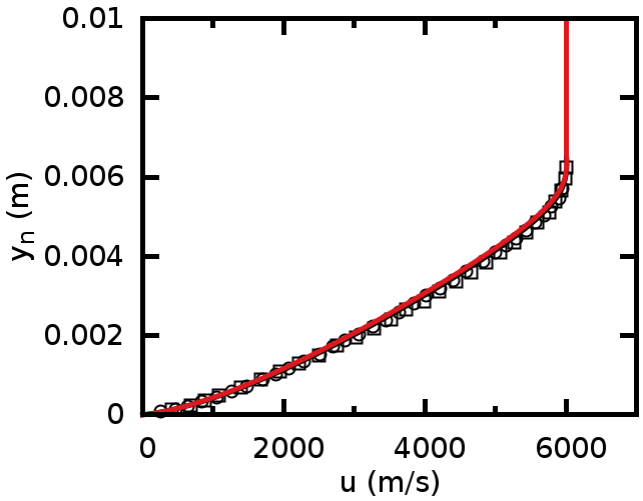

Figure 8.3: Comparison of streamwise velocity. Case 6 at s=3.21 m denoted by —, case 7 at s=3.21 m denoted by —, [Mal03] at s=3.24 m denoted by □, and [JC05] at s=3.26 denoted by ○.

The wall temperature for cases 6 and 7 is shown in Fig. 8.4(a). The wall temperature used in [Mal03] and [JC05] is the same as case 6. The maximum wall temperature at the stagnation point for both cases is nearly the same. The wall temperature for case 7 drops quicker than case 6 near the stagnation point and then almost levels off near $s = 0.22$ m which corresponds to the end of the ablating nose cone. After the ablating nose cone, case 7 is fit to the experimentally measured wall temperature and is the same as case 6 downstream of $s = 1.0$ m. The main difference between these two cases is the brief leveling off of the wall temperature before dropping again in case 7 which is not seen in case 6. Figure 8.4(b) shows the comparison of the computed wall heat flux between case 6, case 7, [Mal03], and [JC05]. This comparison also has corresponding experimental data. For [Mal03] and [JC05], there is a noticeable rise in heat flux downstream of the nose near $s = 0.1$ m that is only slightly present in case 6 and not present at all in case 7. It is likely that this rise in heat flux is due to the estimated wall temperature distribution and likely exacerbated by a lack of streamwise grid in this

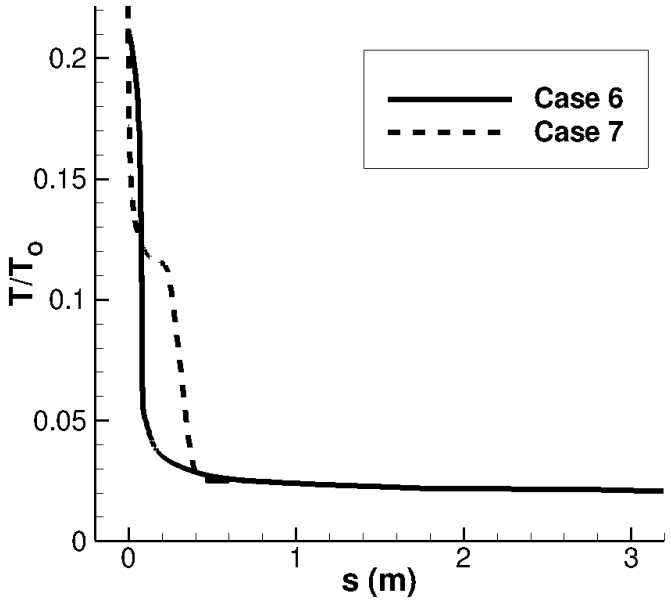

(a)

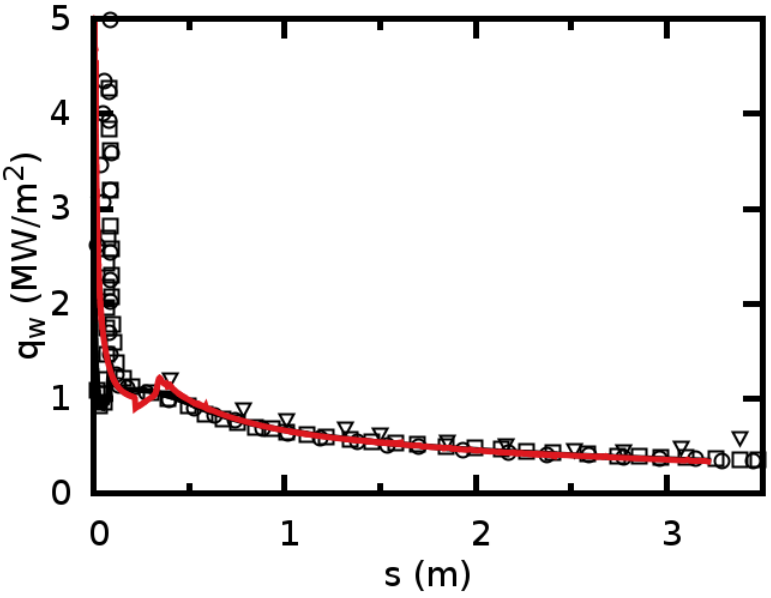

(b) Case 6 —, case 7 —, [Mal03] □, [JC05] ○, and experiment ▽

Figure 8.4: Comparison of (a) wall temperature and (b) heat flux.

area of rapid wall temperature decrease. The heat flux for case 7 is more natural. It is a maximum at the stagnation point and decreases downstream. There is a jump near $s = 0.22$ m due to the discontinuity in surface boundary conditions. After this discontinuity, the heat flux increases slightly due to recombination of species, especially CO_2, near the wall. This increase in heat flux more accurately matches the experimentally measured heat flux than the other cases. Downstream of $s = 1.0$ m, each of the cases heat fluxes lie on top of each other.

The translation-rotation temperature and the vibration temperature at several streamwise locations are shown in Fig. 8.5. Each profile has the same wall temperature except the station at x=0.22 m which is at the end of the nose cone. At this station, both temperatures are higher for case 7. Moving downstream starting from x=1.76 m, the translation-rotation temperature shows little variation between case 6 and 7. Each of the profiles for case 7 are shifted away from the wall due to a thickening of the boundary layer from blowing, but the shift is small. For the vibration temperature there is a larger difference. For case 6, the vibration temperature is consistently less which is most likely due to the existence of CO_2, as well as a thicker boundary layer, for case 7. From these meanflow results, it is likely that temperature effects on flow instability will be more pronounced upstream near the nose cone where the difference between the cases is the largest.

The surface mass flux nondimensionalized by the freestream mass flux is given in Fig. 8.6. The mass flux is a maximum at the stagnation point where it is 2% of the freestream mass flux. The most significant blowing occurs on the hemispherical nose tip. Downstream of the hemispherical nose tip on the straight portion of the cone, the mass flux is less than 0.1% of the freestream mass flux. It seems likely that any effects on flow instability due to blowing would stem from the higher mass flux on the nose tip rather than the lower mass flux on the straight portion of the nose cone.

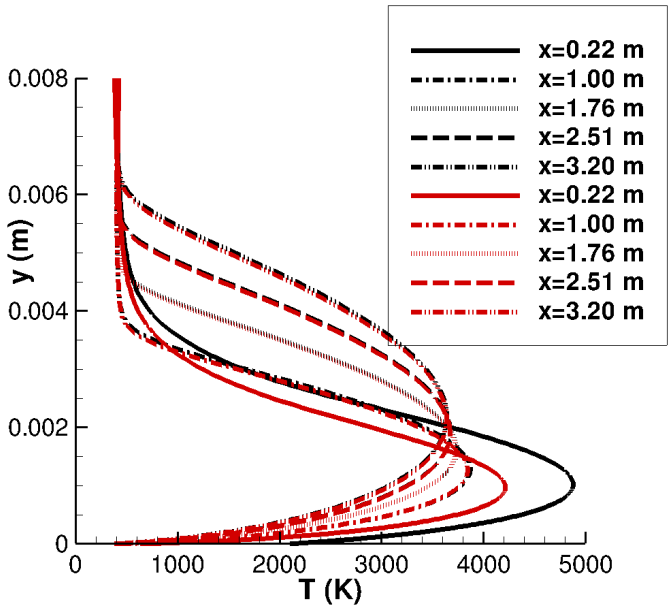

(a)

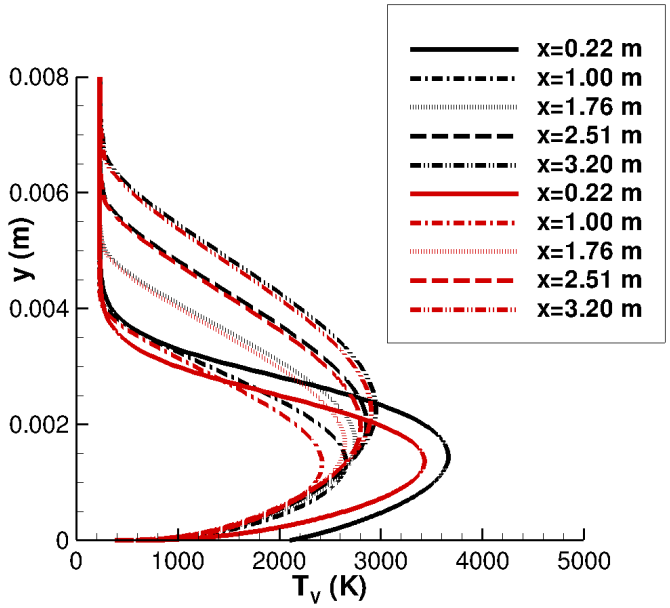

(b)

Figure 8.5: Wall-normal profiles for cases 6 (red) and 7 (black) of (a) the translation-rotation temperature and (b) the vibration temperature.

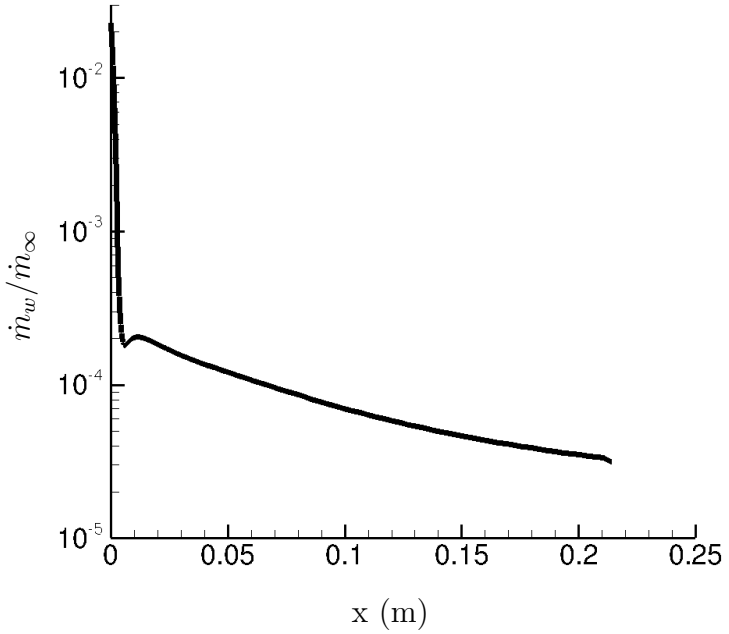

Figure 8.6: Surface mass flux for case 7.

The mass fractions of CO and CO_2 for case 7 are shown in Fig. 8.7. Of the gas species containing carbon, only CO and CO_2 are shown because they are the most massive. Each station is normal to the surface at a given location. The first location corresponds to the end of the ablating nose cone. At this station, carbon in the freestream is mainly in the form of CO and it makes up approximately 10% of the fluid mass near the surface. At x=0.50 m, CO accounts for roughly 1% of the mass near the center of the boundary layer. Downstream of x=1.00 m, the mass of CO has become less than 0.1% and continues to decrease downstream. On the other hand, CO_2 is less than 0.1% at the exit of the nose cone due to the high surface temperature. But increases rapidly to 5% of the mass at the wall at x=0.5 m. Then decreases gradually downstream. Downstream of x=0.50 m there is not a significant amount of carbon in any species except CO_2. Therefore, it is expected that CO_2 will impact flow instability more than CO near the experimentally measured transition location.

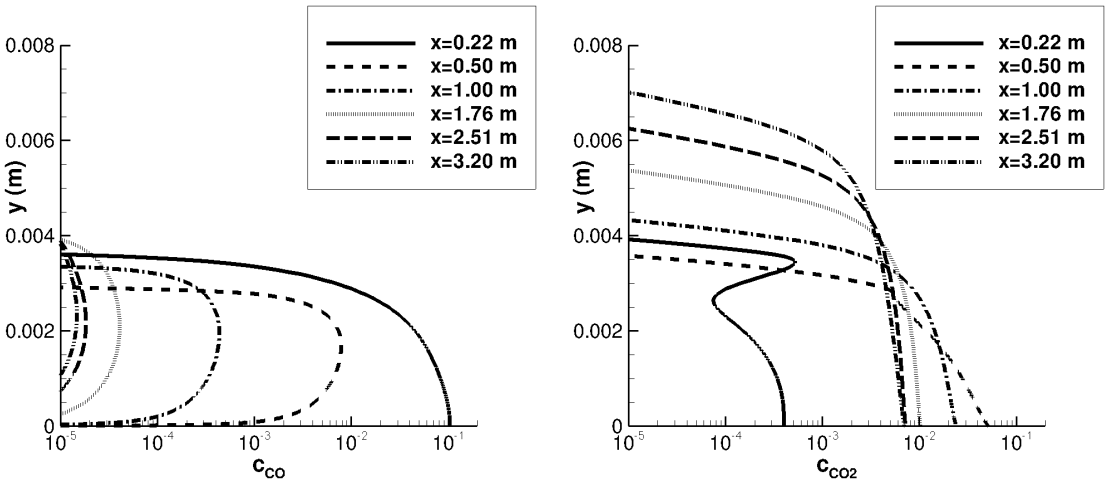

(a) (b)

Figure 8.7: Wall-normal profiles for case 7 of (a) c_{CO} and (b) $c_{\mathrm{CO_2}}$.

8.2 Instability Characteristics of Reentry-F $\mathbf{M_\infty = 19.925}$ Blunt Cone

N factor plots for both cases 6 and 7 are shown in Fig. 8.8. The location of transition onset, as indicated by the rise in the experimental heat flux, is s=2.9 m. This location is marked on the figures. The largest N factor at this streamwise location for case 6 is 7.8 at a frequency of 260 kHz. Compare this with the value of 8.1 at a frequency of 240 kHz obtained in [Mal03] using linear stability theory and a finite-rate chemistry model. Considering the differences in the model, the N factor at transition is quite close. In [JC05], an N factor of 8.7 at a frequency of 250 kHz was obtained using a similar thermochemical nonequilibrium model, but the parabolized stability equations were used rather than linear stability theory to compute the flow instability. With a similar gas model, one would expect the comparison of the N factor to be closer, however, N factors computed from PSE are generally larger than those computed using LST, so the difference is not unusual. Overall, the stability calculations agree reasonably well with previous stability calculations for the same geometry and flow conditions.

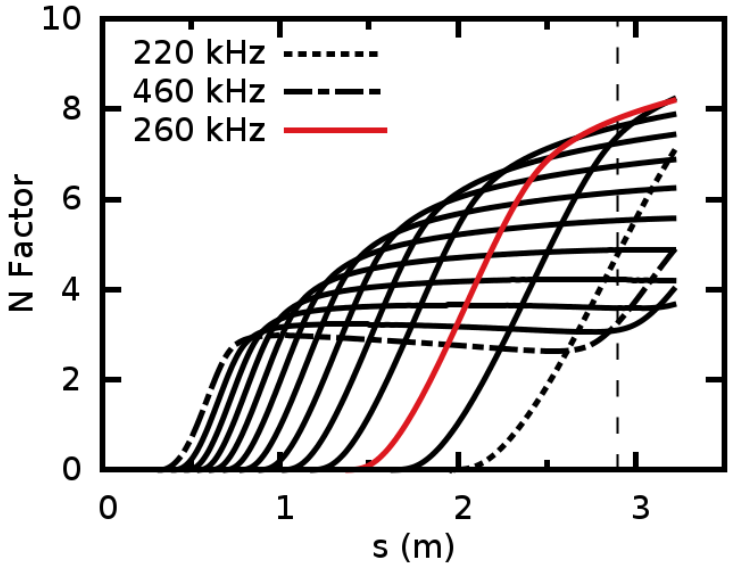

(a) case 6

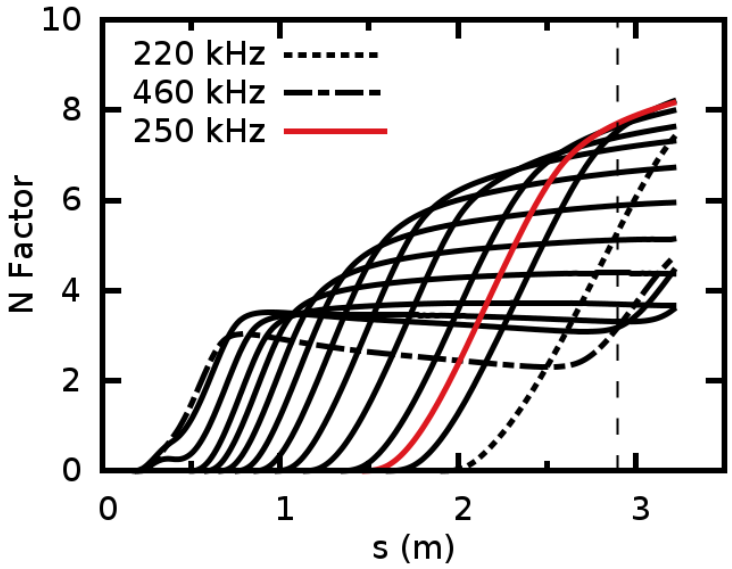

(b) case 7

Figure 8.8: N factor comparison.

The largest N factor at $s = 2.9$ m for case 7 is 7.7 at a frequency of 250 kHz. This is not a large difference from the N factor of 7.8 obtained in case 6 and may be near to the numerical noise of the simulation. However, this slight damping effect is consistent along the cone downstream of $s = 1.0$ m making it unlikely that it is significantly affected by numerical noise. Also, the frequency that leads to transition for case 7 is 10 kHz lower than that of case 6. This same stabilizing behavior was seen in Sec. 7.3 where the carbon chemistry obtained from ablation was shown to slightly stabilize the flow as compared to a simulation with only 5 species air.

Upstream of $s = 1.0$ m, the ablating nose cone has increased the N factor. The largest difference is 68% at $s = 0.8$ m. Here, the blowing effects are stronger than at $s = 2.9$ m as the location is closer to the nose cone. Recall from Fig. 7.21 that blowing effects over a M_∞=16 blunt cone were shown to destabilize the second mode. It is likely that this close to the nose cone, the blowing effects are destabilizing the second mode more than the carbon species are stabilizing the second mode. This results in a net increase in the most amplified second mode upstream of $s = 1.0$ m.

The growth rates for each of the frequencies used to create the N factor plots for cases 6 and 7 are shown in Fig. 8.9. For case 6, the largest amplitude occurs upstream for the higher frequencies shown, and then decreases downstream as the frequency decreases. However, the streamwise extent over which a frequency is unstable increases as the frequency decreases. Therefore, even if the maximum amplitude is lower, the unstable region is larger which leads to larger N factors for the lower frequencies. For case 7, the behavior is a little different. The start of instability for the 460 kHz second mode has moved upstream and the maximum amplitude has decreased. This leads to an overall amplification of the 460 kHz instability by 38%. So, even though the maximum amplitude decreases, the larger unstable range increases the N factor of the second mode for case 7. Downstream

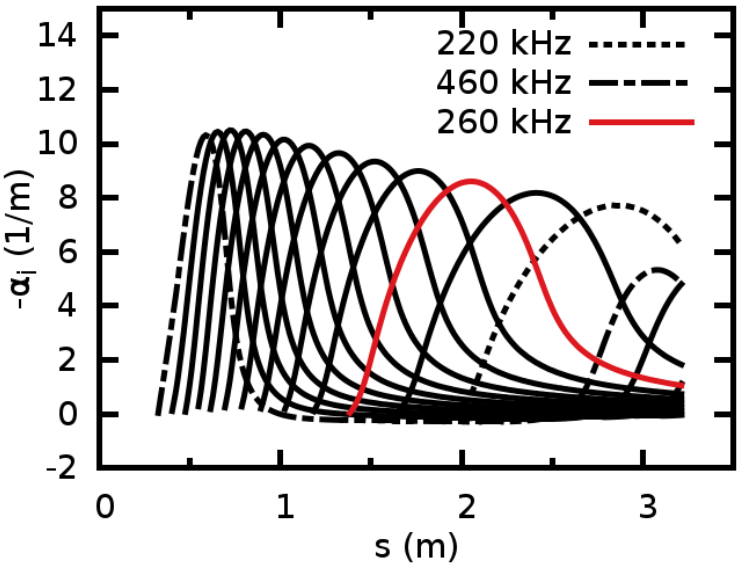

(a) case 6

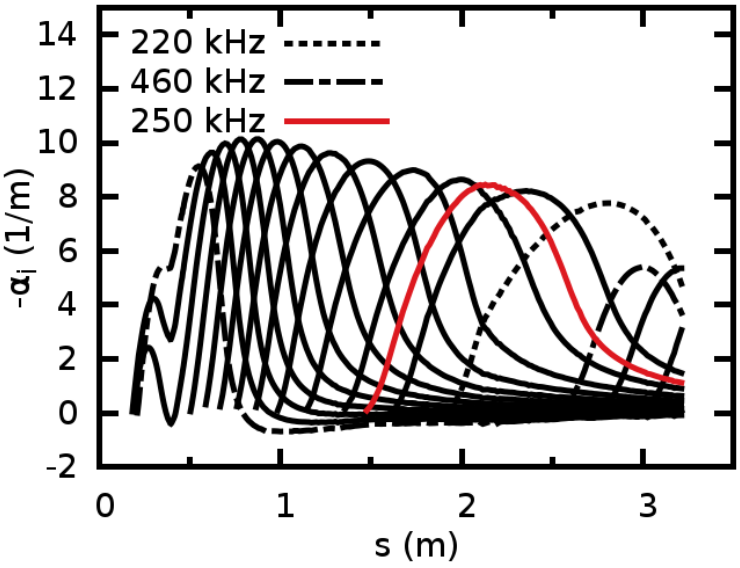

(b) case 7

Figure 8.9: Growth rate ($-\alpha_{\mathrm{i}}$) comparison.

of approximately $s = 0.6$ m, the differences in the growth rates between cases 6 and 7 is minimal.

Along with the growth rates, the phase velocities for each of the frequencies used to create the N factor plots for cases 6 and 7 are shown in Fig. 8.10. Downstream of $s = 0.6$ m, there are only slight differences between cases 6 and 7. However, upstream of $s = 0.6$ m for the frequency range 420–460 kHz, there is a marked difference in the phase velocity at which the second mode first becomes unstable. For case 6, when the 460 kHz second mode first becomes unstable, the phase velocity is near 0.96. However, for case 7, the phase velocity at which the 460 kHz second mode first becomes unstable is near 0.925. It seems that the nose cone effects are decreasing the phase velocity of the second mode instability at instability onset.

Figure 8.11 shows a comparison of the growth rate and phase velocity between case 6 and case 7 at a single frequency of 460 kHz. For case 6, there is clear second-mode instability denoted by a large positive growth rate and a change in the sign of the phase velocity slope near s=0.5 m. This change in phase velocity slope occurs near the synchronization location of the fast and the slow acoustic modes. There is also a clearly defined third mode unstable region denoted by a large positive growth rate and a change in the sign of the phase velocity slope near $s = 3.0$ m. This region of second mode growth, and then a later region of third mode growth, was also seen in [Mal03] and [JC05].

Comparing the second-mode growth region for cases 6 and 7, the maximum second-mode growth rate for case 7 is less than case 6. However, the maximum second-mode growth rate and location of initial instability growth has shifted upstream for case 7. This creates a larger region over which the second mode is unstable. Even though the maximum amplification has decreased, the increased extent over which the second mode is unstable results in a higher N factor for case 7. Also, there is a jog in the growth rate for case 7 near s=0.5 m which is likely

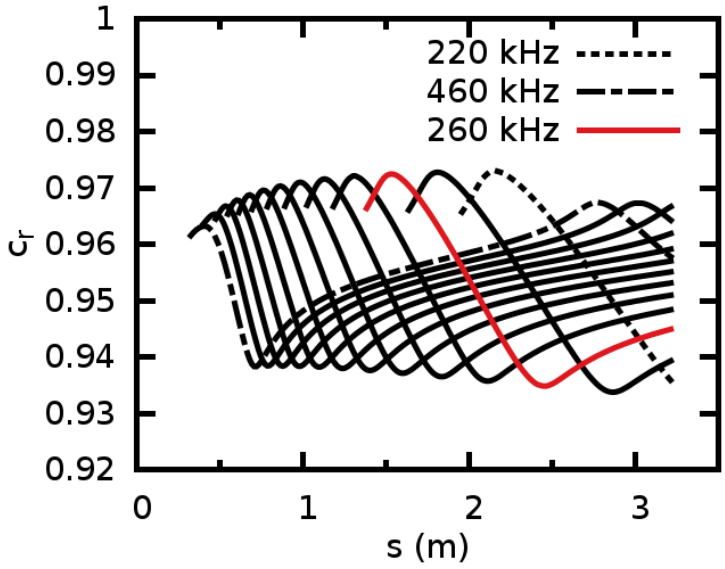

(a) case 6

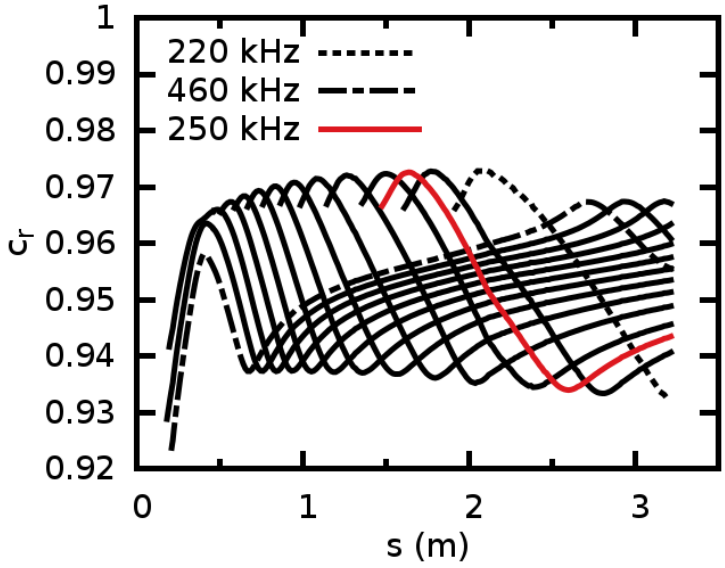

(b) case 7

Figure 8.10: Phase speed (c_r) comparison.

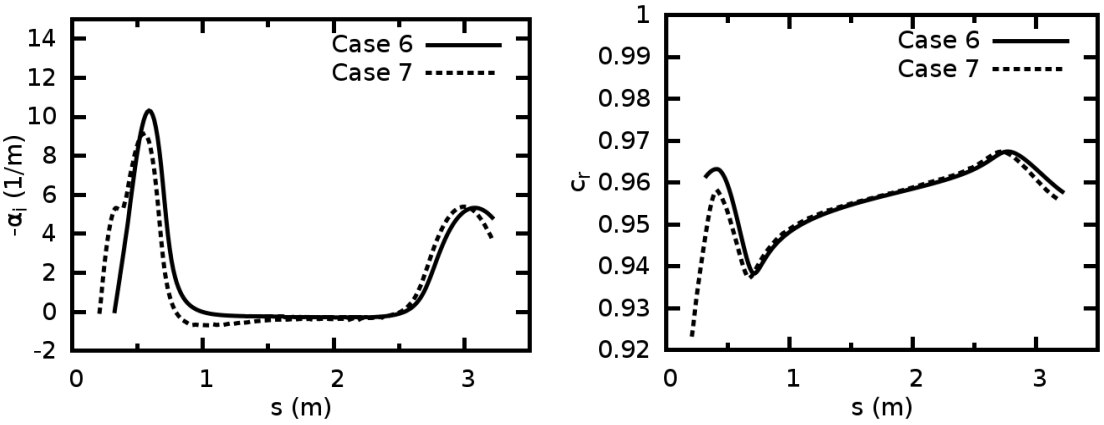

(a) (b)

Figure 8.11: 460 kHz frequency comparison.

due to the rapid change in temperature slope at the same streamwise location and not to a switch from first to second modes. The third mode is affected by a shift upstream while the maximum growth rate is unaffected.

To analyze the effects of carbon species on the second-mode instability wave at a frequency of 460 kHz, the sign for the heat of formation for CO_2 was switched in the linear stability analysis. The computed growth rates along the cone are shown in Fig. 8.12. When the sign for the heat of formation of CO_2 is switched, the resulting second-mode instability wave is destabilized. This means that, when the sign is not switched, the effects of CO_2 are to stabilize the instability wave. Recall from Fig. 8.7(b) that there is a large addition in the mass of CO_2 due to recombination in the range 0.22 m$\leq x \leq$0.5 m. It is this addition of mass due to recombination that is likely leading to this stabilizing effect. The same numerical experiment was run for CO where it was found that there was a stabilizing effect when the sign for the heat of formation was switched. Therefore, when the sign is not switched, the second mode would be destabilized. Each of these results are consistent with the results in Sec. 7.3 of a Mach 15.99 blunt cone with surface ablation. Downstream of $x = 0.6$ m where there is not significant recombination

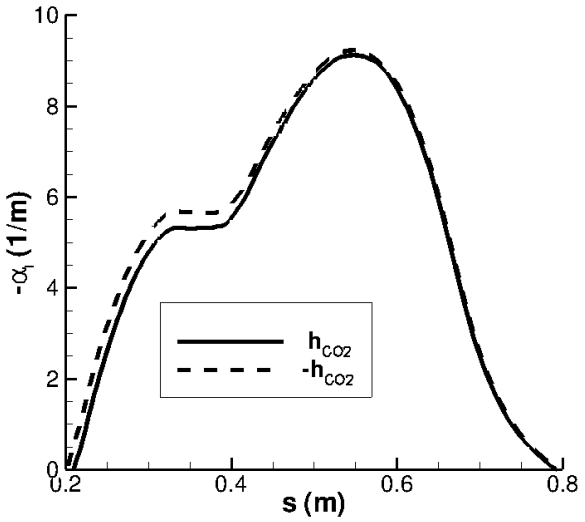

Figure 8.12: 460 kHz growth rate with sign of heat of formation of CO_2 switched.

of CO_2, switching the sign for the heat of formation of either CO or CO_2 results in a negligible difference.

Over the length of the cone simulated, the frequency 460 kHz has an unstable second mode region that spans part of the ablating nose cone, as well as an unstable third mode region that begins near the aft end of the cone. For this frequency, meanflow profiles are given at $s = 0.22$ m (downstream edge of the nose cone), $s = 0.50$ m, and $s = 3.00$ m. At each of these profiles, the unstable second, or third mode, eigenfunctions are shown. The figures for each of the meanflow profiles and wall-normal eigenfunctions are Figs. 8.13–8.21 where the wall-normal coordinate is scaled by the local boundary-layer thickness defined as 98.5% of the total enthalpy boundary layer.

In [Mac84], it was shown that the second and third modes had pressure eigenfunctions where the real part crossed the zero axis once and twice, respectively. The real part of the pressure eigenfunction crosses the zero axis once in Figs. 8.14(a) and 8.17(a), showing that the unstable mode is the second mode. The

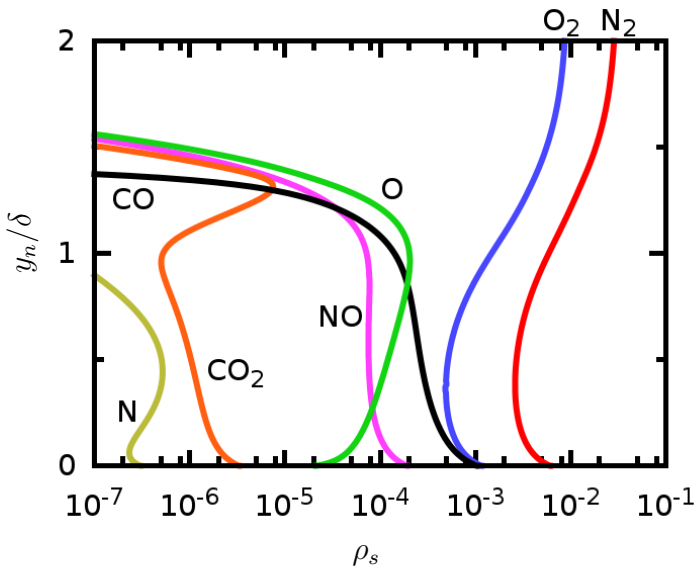

(a)

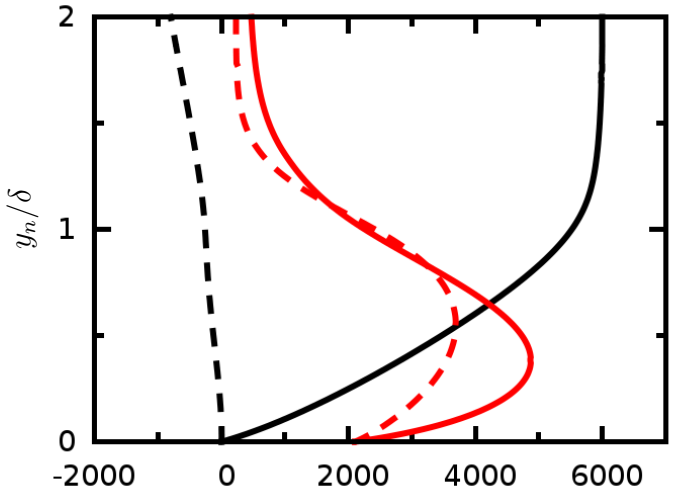

(b)

Figure 8.13: Meanflow profiles at $s = 0.22$ m for (a) species density and (b) u_t —, $10 \cdot u_n$ - -, T —, and T_V - -.

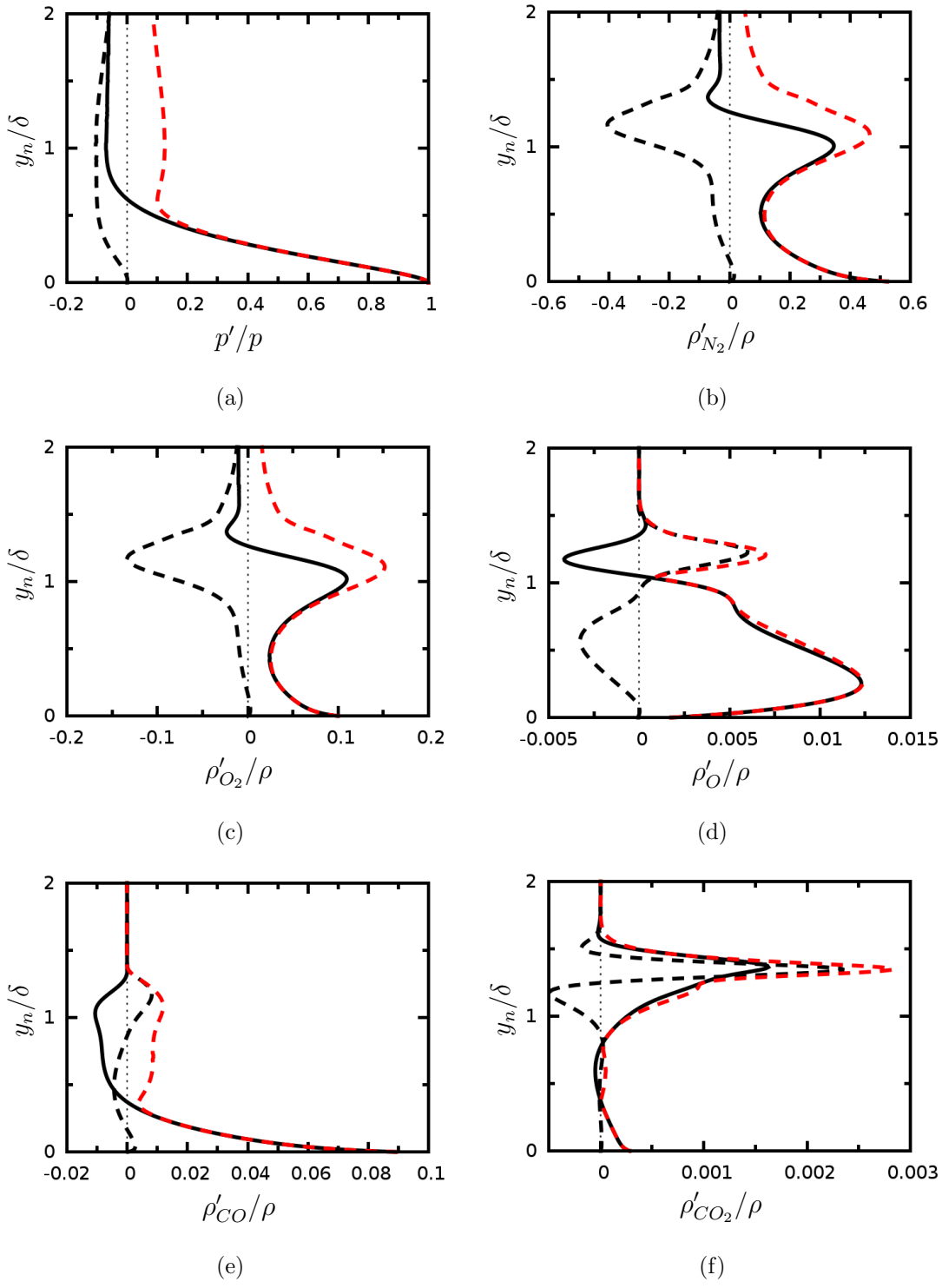

Figure 8.14: Eigenfunction obtained from LST for the 460 kHz 2nd mode at $s = 0.22$ m. Real component —, imaginary component - -, and amplitude - -.

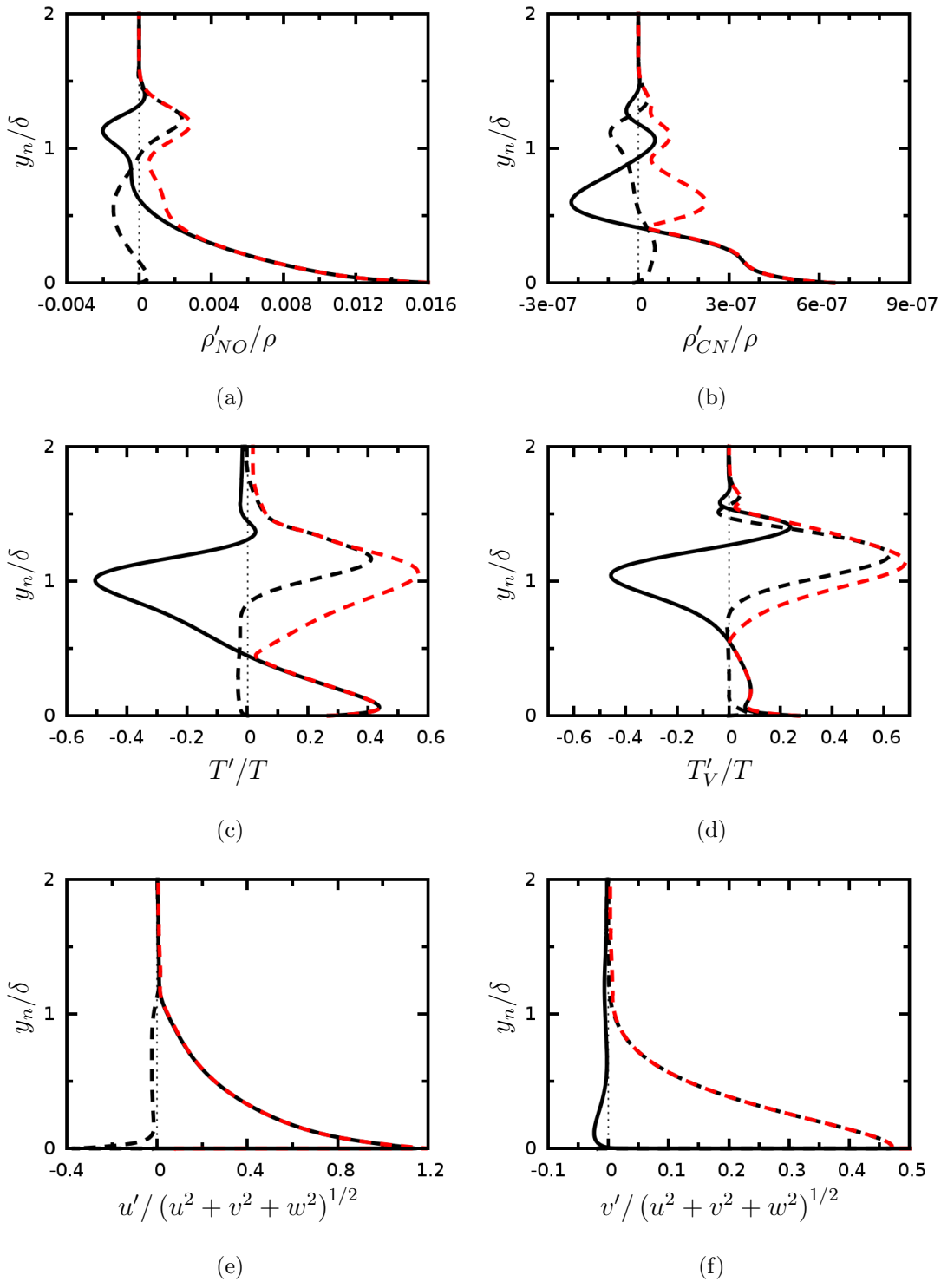

Figure 8.15: Eigenfunction for the 460 kHz 2nd mode at $s = 0.22$ m continued. Real component —, imaginary component - -, and amplitude - -.

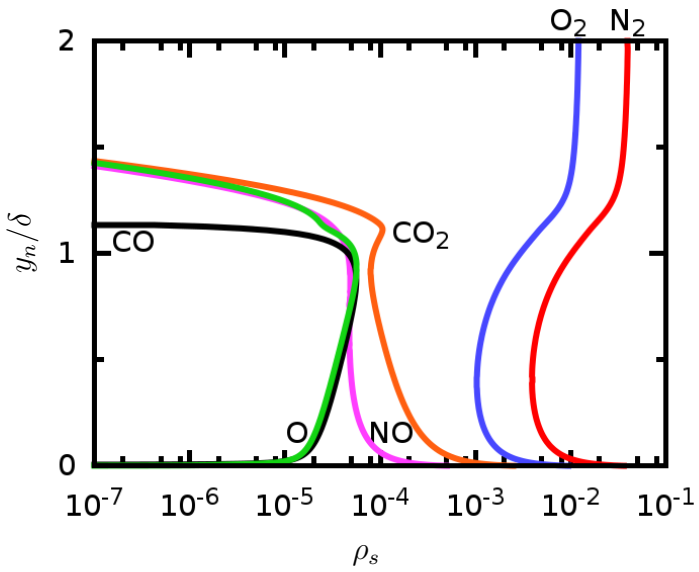

(a)

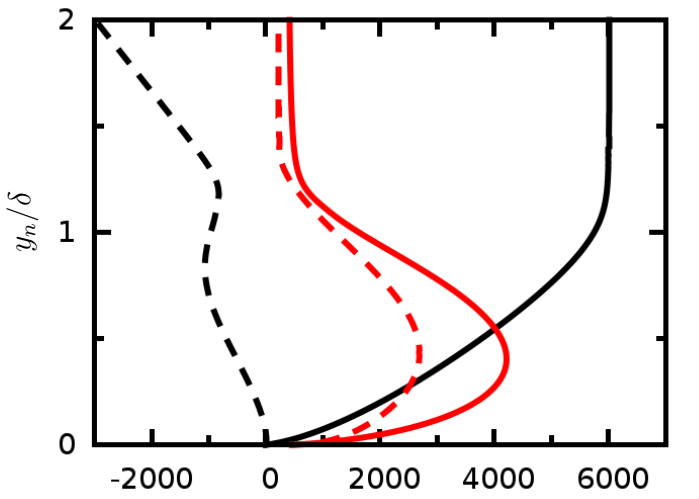

(b)

Figure 8.16: Meanflow profiles at $s = 0.50$ m for (a) species density and (b) u_t —, $100 \cdot u_n$ - -, T —, and T_V - -.

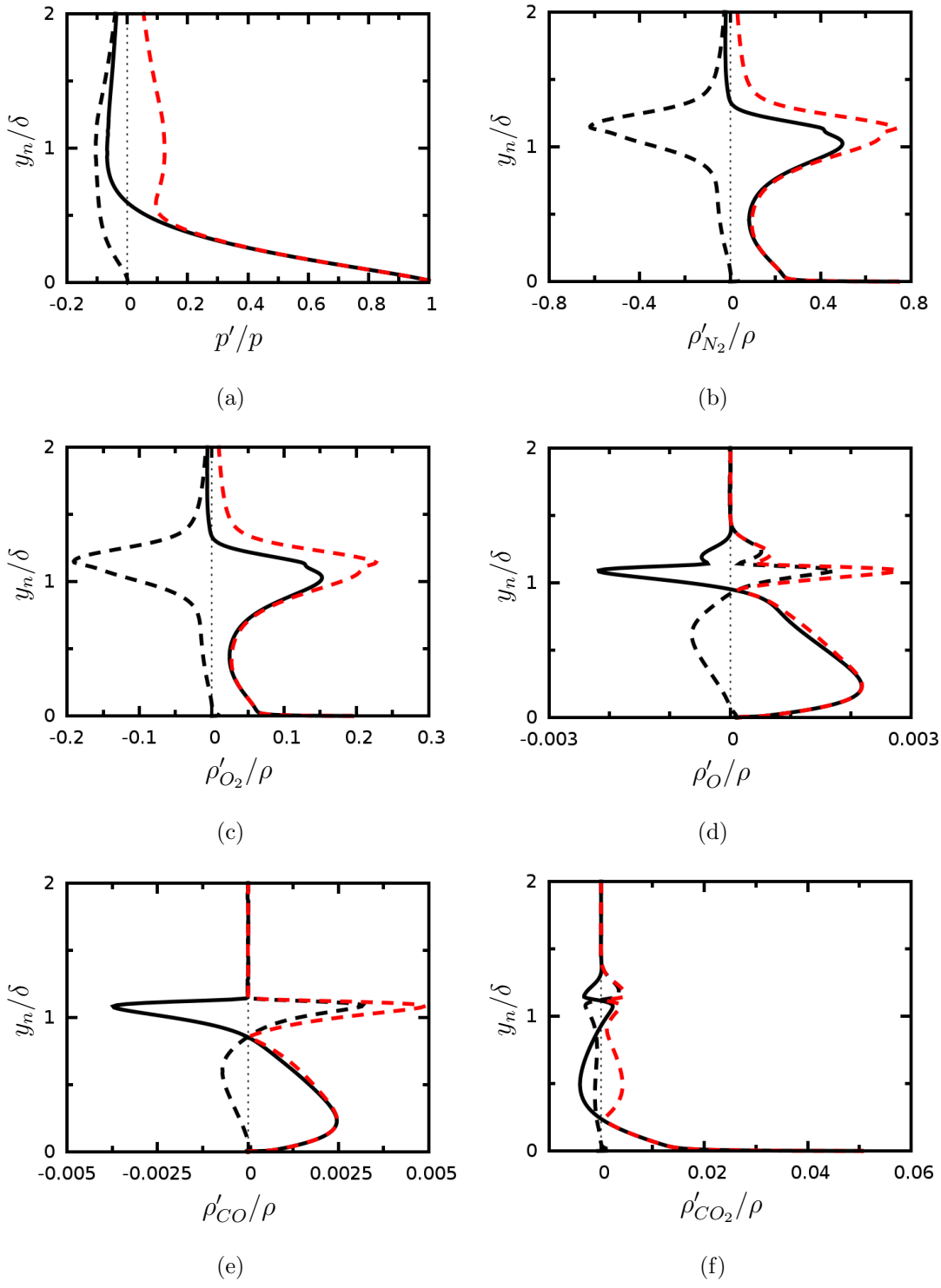

Figure 8.17: Eigenfunction obtained from LST for the 460 kHz 2nd mode at $s = 0.50$ m. Real component —, imaginary component - -, and amplitude - -.

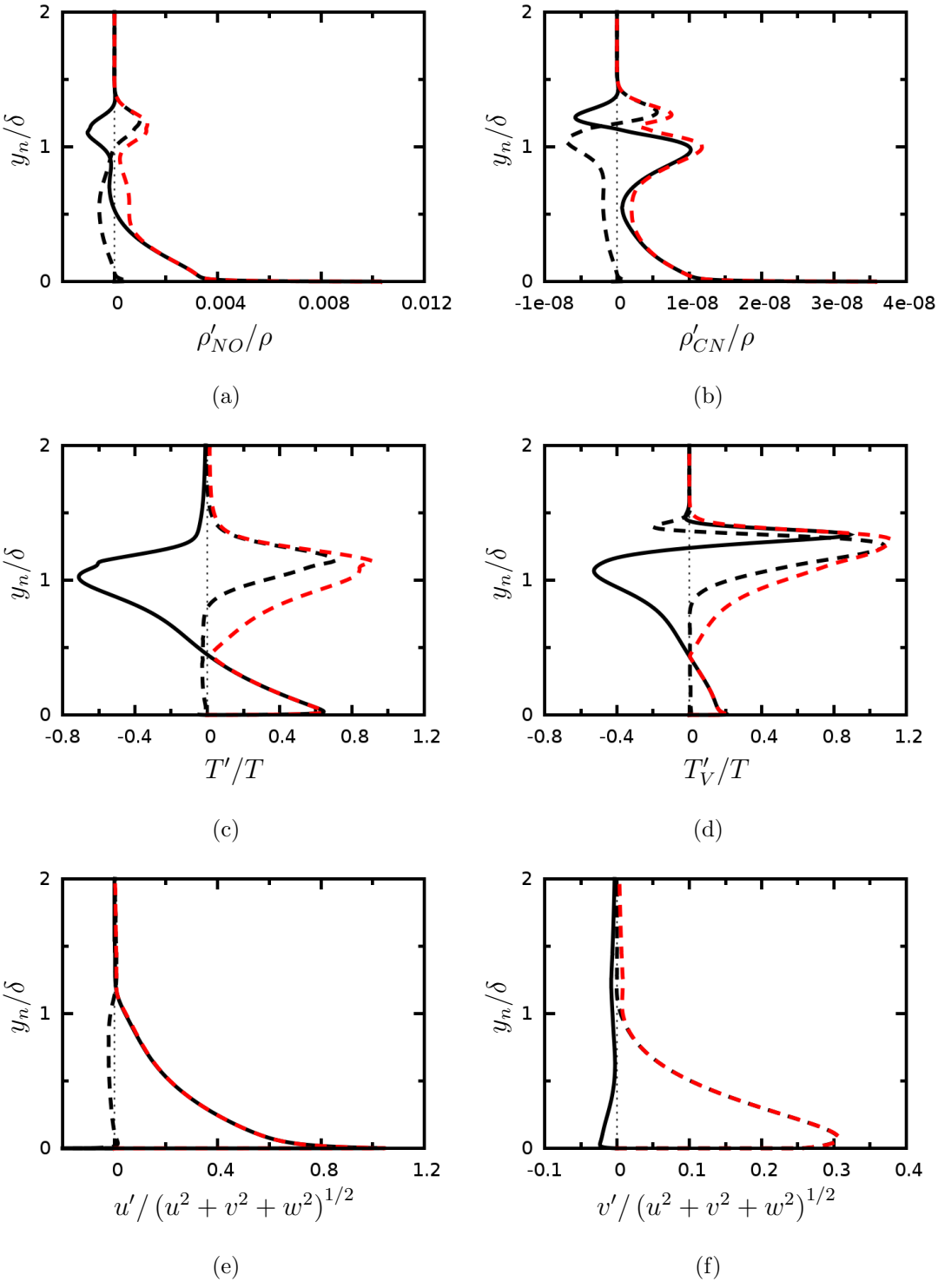

Figure 8.18: Eigenfunction for the 460 kHz 2nd mode at $s = 0.50$ m continued. Real component —, imaginary component - -, and amplitude - -.

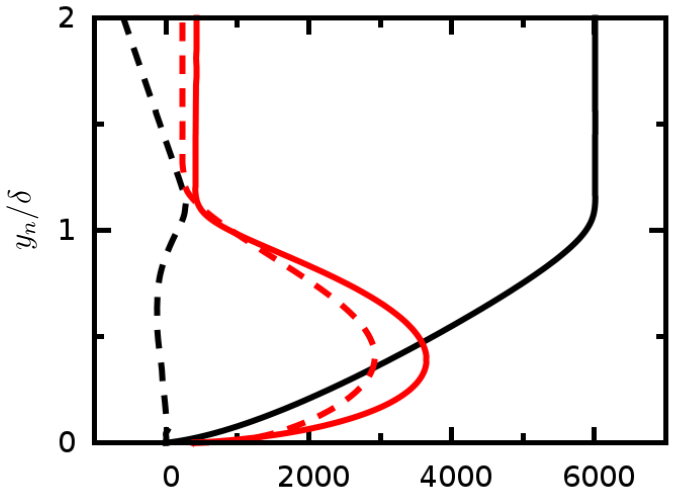

(a)

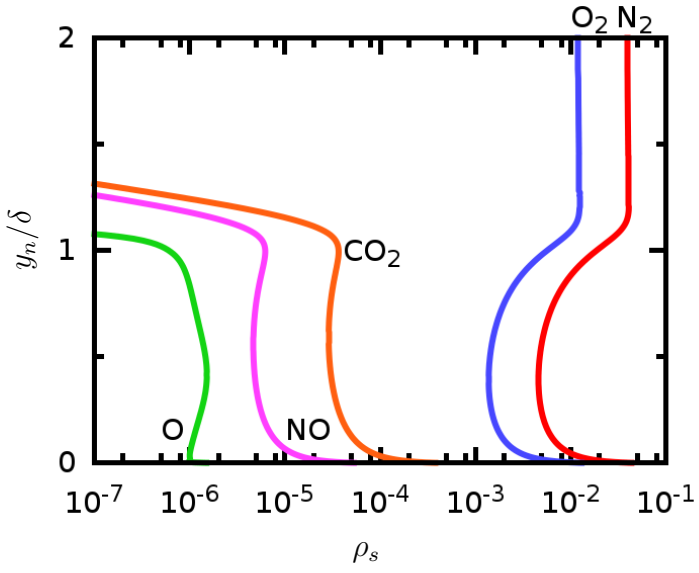

(b)

Figure 8.19: Meanflow profiles at $s = 3.00$ m for (a) species density and (b) u_t —, $100 \cdot u_n$ - -, T —, and T_V - -.

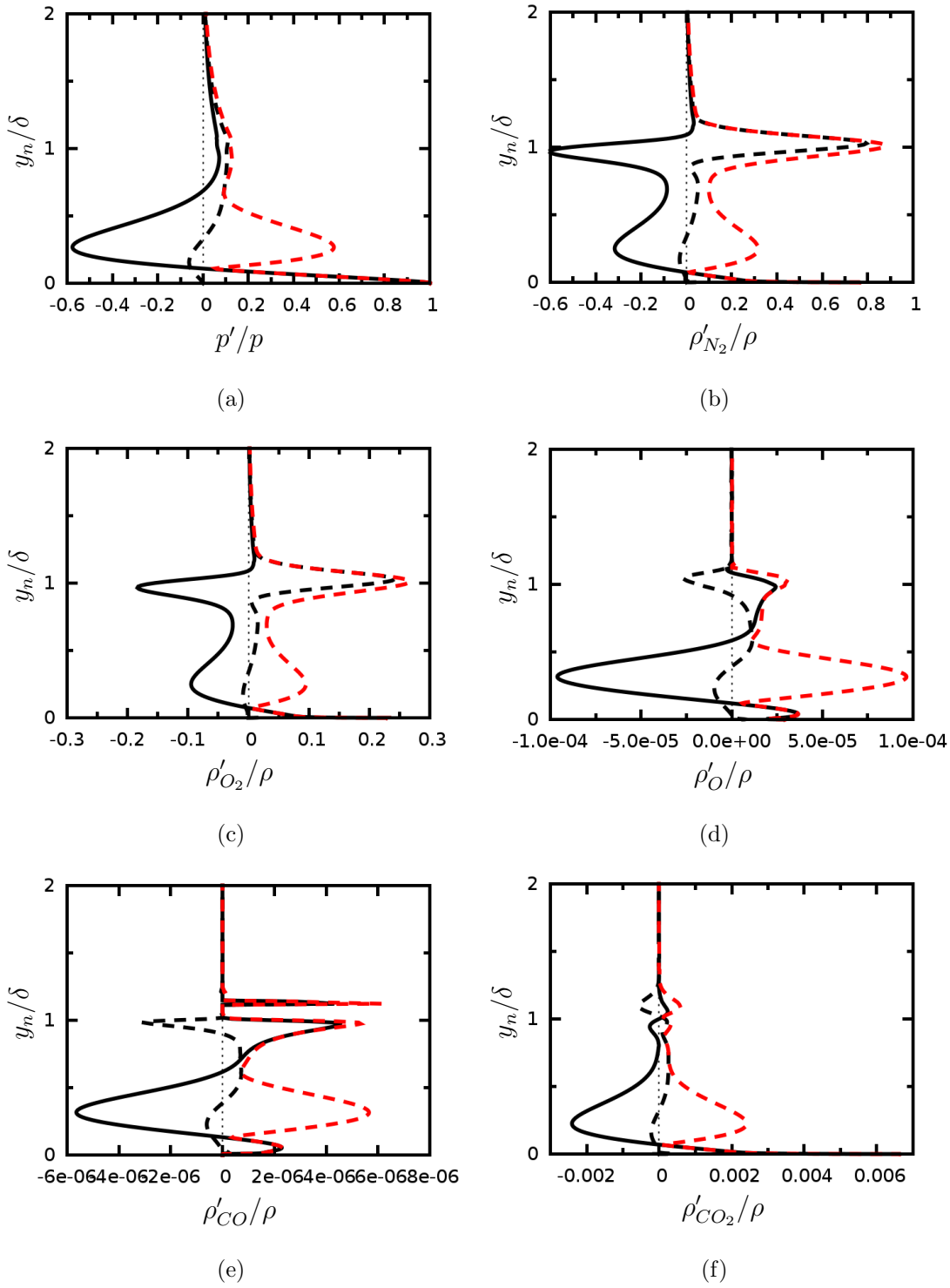

Figure 8.20: Eigenfunction obtained from LST for the 460 kHz 3rd mode at $s = 3.00$ m. Real component —, imaginary component - -, and amplitude - -.

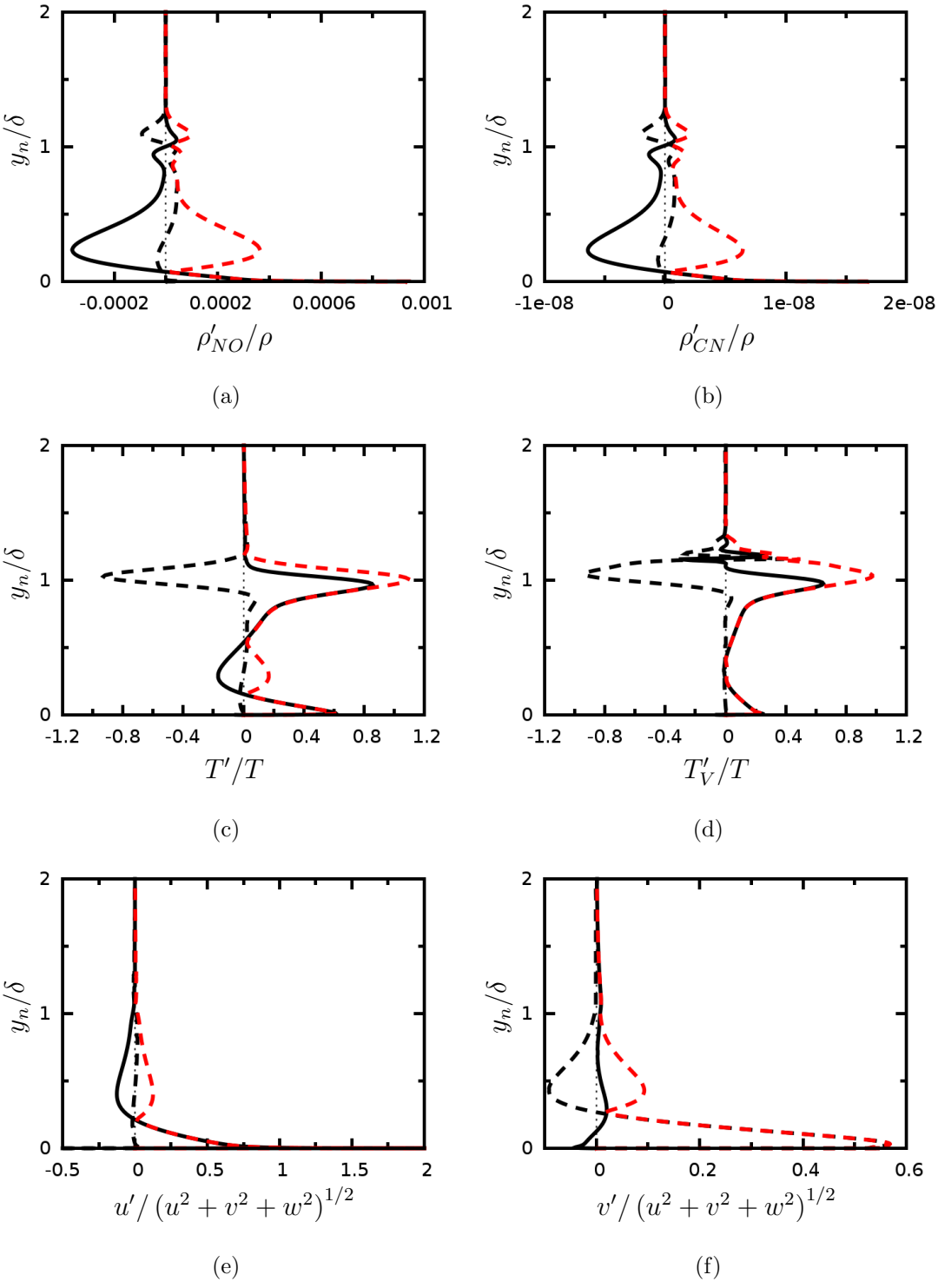

Figure 8.21: Eigenfunction for the 460 kHz 3rd mode at $s = 3.00$ m continued. Real component —, imaginary component - -, and amplitude - -.

real part of the pressure eigenfunction crosses the zero axis twice in Fig. 8.20(a), showing that the unstable mode is the third mode.

The comparison of growth rate and phase velocity for the 260 kHz instability between cases 6 and 7 is shown in Fig. 8.22 and has only slight differences. Only second mode instability is present for this frequency over the portion of the cone simulated. The unstable region begins near $s = 1.5$ m and is shifted slightly upstream for case 7. There is very little variation in shape between the cases for both growth rate and phase velocity. Essentially, both cases give the same result with case 7 shifted slightly upstream of case 6. This is likely due to the slight increase in boundary-layer thickness of case 7 due to the outgassing in the nose cone. This is why case 7 has a lower frequency for the largest N factor at $s = 2.9$ m.

The ablating nose cone extends 0.22 m downstream of the stagnation point. Over the downstream portion of the nose cone, there is some unstable growth of the second mode for frequencies near 410–470 kHz. Fig. 8.23 shows the second-mode N factor over the ablating nose cone for the meanflow of case 7. The difference between the figures is that the perturbation boundary condition at the surface used for the linear stability analysis has been changed. Similar to the results in Sec. 7.3, the temperature perturbation boundary condition from Eq. (3.78) destablizes the second mode compared to the case with $\hat{T}_w = 0$. The onset of instability is moved upstream and the most amplified frequency is 14% larger. However, the maximum N factor achieved on the nose cone is small for either case and does not directly affect the frequency that likely leads to transition.

It has been shown that including the ablative nose cone affects frequencies differently. For higher frequencies, whose second mode unstable regions are near the nose cone, such as the 460 kHz frequency, the location of initial instability growth is moved upstream and there is a slight damping of the second mode. The growth rate of the third mode is unaffected with a slight upstream shift. For lower

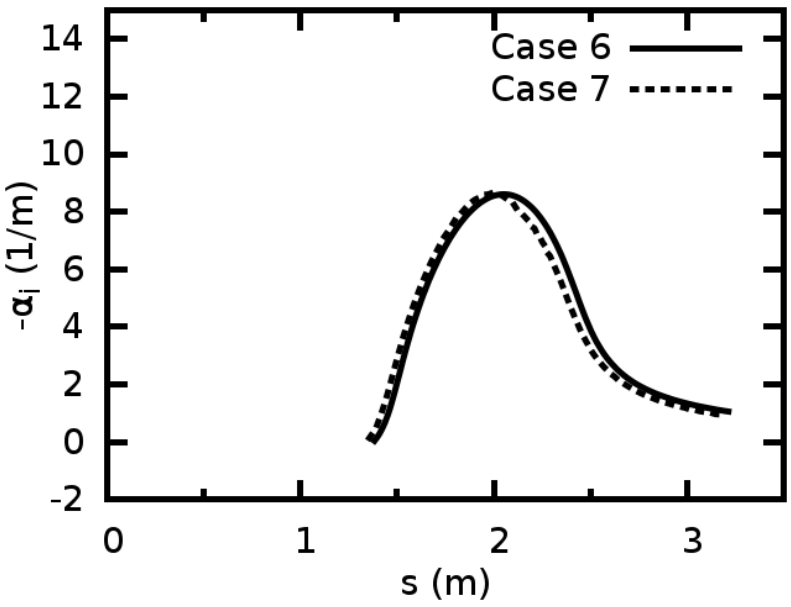

(a)

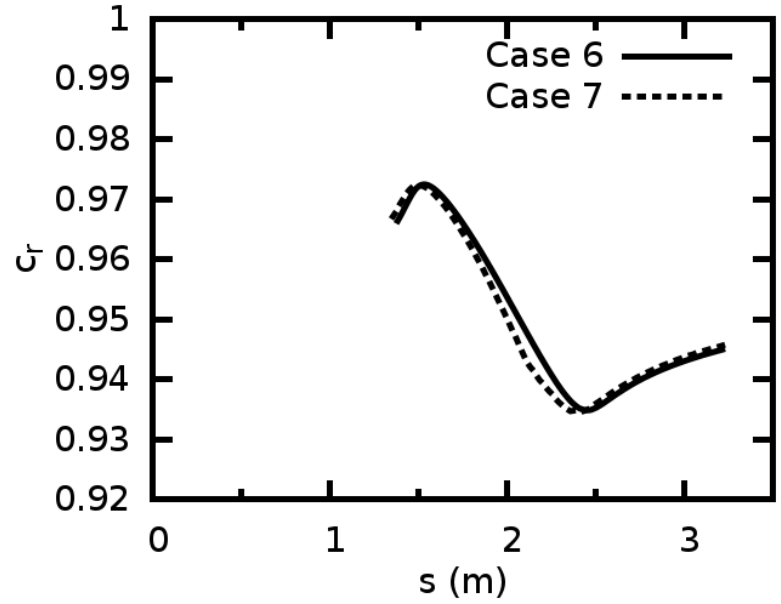

(b)

Figure 8.22: 260 kHz frequency comparison.

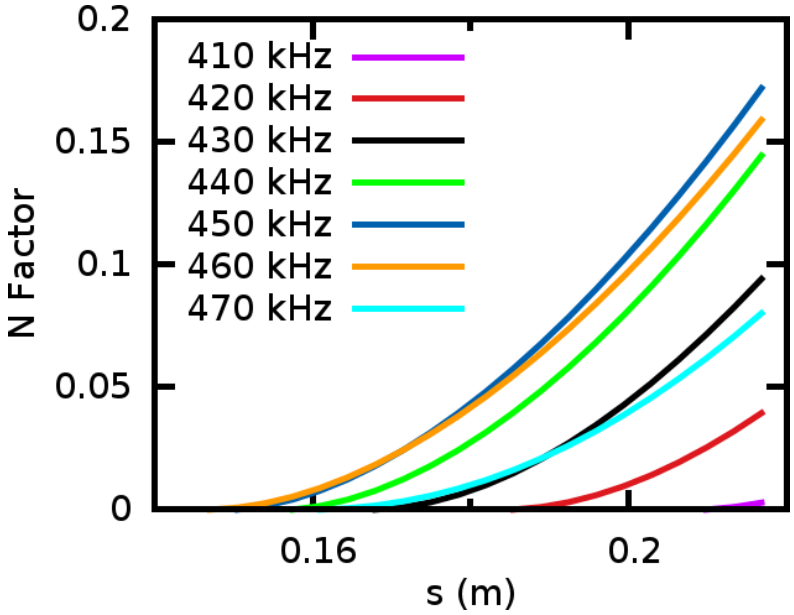

(a) $\hat{T}_w \neq 0$

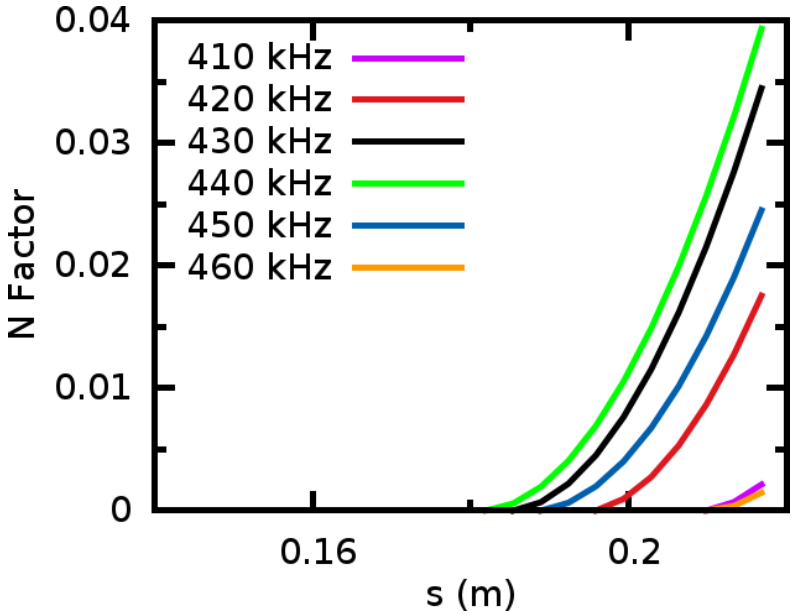

(b) $\hat{T}_w = 0$

Figure 8.23: N factor comparison on the nose cone.

frequencies, whose second mode unstable region is far downstream of the ablating nose cone, such as the 260 kHz frequency, the growth rate and phase velocity of the instability is the same except for a slight upstream shift. It is likely that this upstream shift is attributable to the increase in boundary-layer thickness caused by the ablating nose cone.

These findings indicate that including the effects of the ablating nose cone is stabilizing to the second mode instability when the second mode is far downstream of the nose. Near the nose cone, ablation induced outgassing effects cause an increase in the region of instability and a decrease in the maximum amplification rate which does result in a higher N factor. However, assuming that the transition location is far enough downstream of the ablating nose cone, the effects of the ablating nose cone are to slightly stabilize the second mode. It should be noted that a LST analysis, like the one performed here, does not include the receptivity process which is likely different when the ablating nose cone is included. This would result in different initial amplitudes to the eigenmode growth process for cases 6 and 7. However, N factor correlation, which is derived from an eigenmode analysis without including receptivity, has been shown to reliably correlate with transition onset. This correlation implies that transition is strongly affected by eigenmode growth and the effect that the ablating nose cone has on eigenmode growth, for the conditions tested, is small. Therefore, this small difference in N factors and frequencies that lead to transition seems to indicate that, for these flight conditions, the nose cone effects can be safely neglected to obtain a reasonable estimate of the value of the N factor and the corresponding frequency at the transition location.

CHAPTER 9

DNS Results for $M_\infty = 10$ Flat Plate

Commonly, in studies of boundary-layer instability over a flat plate, a local Reynolds number, R, is used. This Reynolds number is defined as

$$R = \frac{\rho_\infty u_\infty L}{\mu_\infty} \tag{9.1}$$

where L is the local length scale of the boundary-layer thickness and is defined as

$$L = \left(\frac{\mu_\infty x}{\rho_\infty u_\infty} \right)^{1/2}. \tag{9.2}$$

This local length scale is used here to nondimensionalize the growth rate. The frequency of a boundary-layer mode for LST, or a disturbance simulated in a DNS, is commonly nondimensionalized to obtain

$$F = \frac{2\pi f \mu_\infty}{\rho_\infty u_\infty^2} \tag{9.3}$$

where f is the dimensional frequency. Also the frequency may be nondimensionalized with a spatial component resulting in

$$\Omega = \frac{2\pi f L}{u} = RF. \tag{9.4}$$

Both nondimensionalizations for frequency will be used here.

For a DNS, it is required that the meanflow be perturbed in order to study the growth, or decay, of the perturbation. Here, the flow is perturbed with a suction/blowing slot at the plate surface. The equation for the mass flux of the slot is

$$\rho v \left(x,t\right)'_w = \epsilon_b \left(\rho u\right)_\infty \exp\left\{ -\frac{\left(t-\mu_b\right)^2}{2\sigma_b^2} \right\} \sin\left\{ \frac{2\pi \left(x - x_b\right)}{l_b} \right\} \tag{9.5}$$

where l_b is the length of the slot, x_b is the center of the slot measured from the leading edge of the flat plate, ϵ_b scales the function, μ_b shifts the gaussian component to avoid negative times, and σ_b adjusts the spectral content of the function. Notice the time dependent gaussian portion of the function. When transformed to frequency space, this yields a continuous range of frequencies with non-zero amplitudes making this particular approach for perturbing the meanflow an effective strategy when studying a wide range of frequencies.

The freestream conditions are from the previous LST studies of [MA91] and [Hud96] that investigated second-mode instability of a real-gas flow over a flat plate. The freestream conditions are given in Table 5.1. The freestream unit Reynolds number, Re_u, is 10.9×10^6 /m and the freestream stagnation enthalpy, $h_{o,\infty}$, is 5.9 MJ/kg.

A schematic of the DNS simulation is given in Fig. 9.1. The computational domain is bounded by the inlet, outlet, shock, and flat plate. For the DNS simulation, the meanflow is initially converged to a specified tolerance. This tolerance must be below the linear forcing of the blowing/suction slot, or numerical noise will contaminate the unsteady results. Next, the slot is activated, and a linear perturbation is introduced at the slot. This perturbation is then simulated as it travels throughout the meanflow.

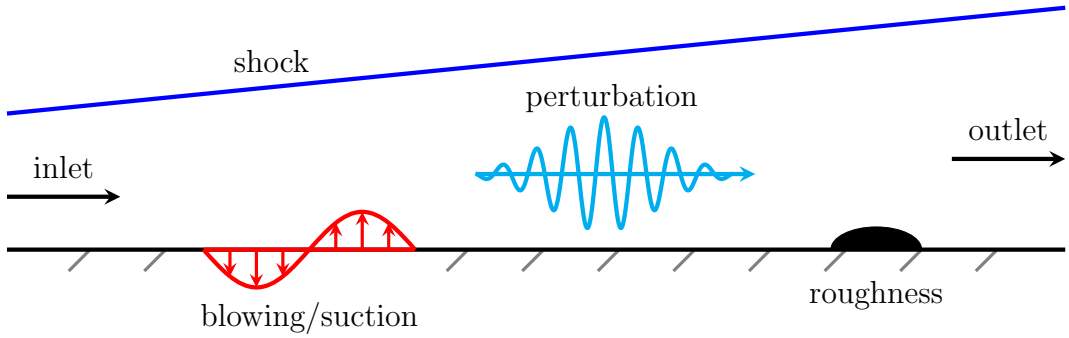

Figure 9.1: Schematic of the physical domain with the roughness location and blowing/suction slot.

Table 9.1: Case numbers for $M_\infty = 10$ flat plate DNSs.

Case Number	h/δ
8	0
9	25.0%
10	37.5%

In order to quantify roughness effects on the instability process, multiple cases are run for varying roughness heights. These cases are defined in Table 9.1 which shows that case 8 has no roughness element, while cases 9 and 10 have a roughness element of the same width but different height. Only the roughness height is varied as it was shown in [FWZ15] that varying the roughness height plays a much more significant role in second mode suppression than varying the width. The roughness elements have an elliptical shape defined by

$$\frac{(x - x_c)^2}{a^2} + \frac{y^2}{h^2} = 1 \tag{9.6}$$

where x_c is the center of the roughness element and $2a$ is the width. For this case, $x_c = 0.27$ m and $a = 2.55 \times 10^{-3}$ m.

Before analyzing the simulation results, a grid convergence study was performed to ensure that the computational grid was sufficiently dense to capture the relevant flow physics. The first grid used 642 by 241 points in the streamwise and wall-normal directions, respectively. The second grid was a double grid solution which used 1282 by 481 points. Case 9 was used as the test case for the grid convergence study. For both grids, the meanflow solution was converged within a specified tolerance and then a perturbation was simulated. Figure 9.2 shows the frequency spectrum of the wall-pressure perturbation directly behind the roughness at $x = 0.28$ m. There are only minimal differences between the

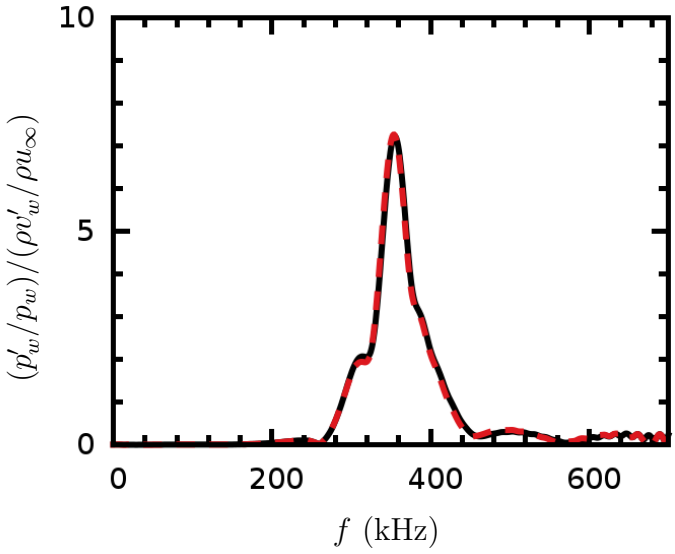

Figure 9.2: Comparison of single grid (642 by 241) results to double grid (1282 by 481) results for case 9. single grid - - , double grid — .

two simulations. The lack of any significant difference between the two separate results shows that the single grid result is grid converged.

9.1 Steady Flow Simulations for $M_\infty = 10$ Flat Plate

The first part of the direct numerical simulation is to simulate the time invariant meanflow. Figure 9.3 shows the meanflow pressure contours for cases 9 and 10. Initially, the roughness element compresses the incoming flow which is shown by the increase in pressure near $x = 0.26$ m to the center of the roughness element. This compression turns into a Mach wave which travels downstream. As the roughness height is increased, the strength of this Mach wave increases and will eventually become a shock wave. After this compression, there is a flow expansion on the leeward side of the roughness element resulting in a decreased pressure. Also, it can be seen that as the height of the roughness element is increased, its effects are present further upstream.

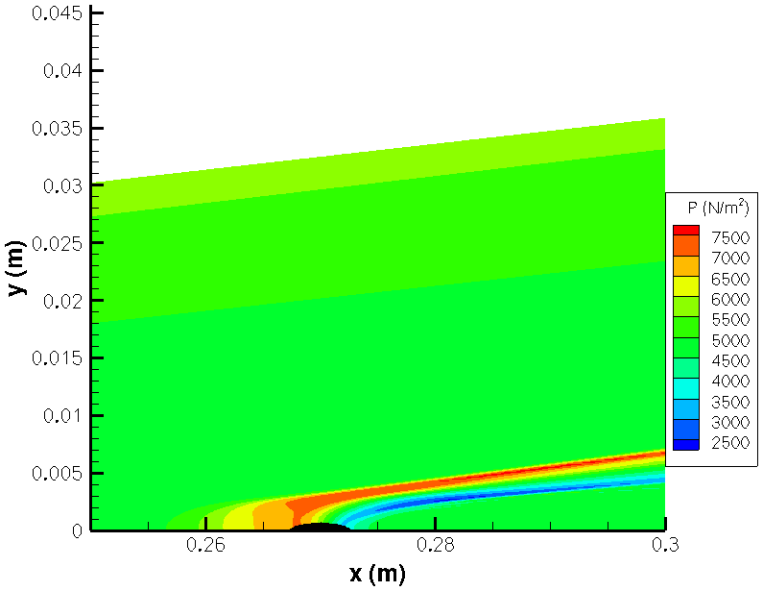

(a)

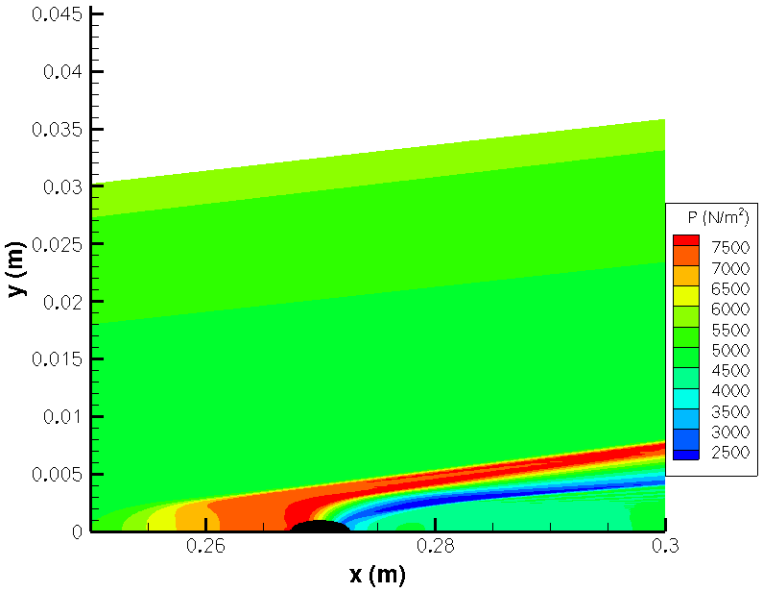

(b)

Figure 9.3: Meanflow solutions of pressure for (a) case 9 and (b) case 10.

Meanflow simulations are also shown in Fig. 9.4 for the translation-rotation temperature and $1 - T/T_V$ near the roughness element for cases 8 and 10. For case 8, the translation-rotation temperature contour remains nearly constant in the streamwise direction over the region shown. Similarly, contours of $1 - T/T_V$ remain constant in the streamwise direction over the region shown. For case 10, there is a noticeable increase in translation-rotation temperature as the flow reaches the bump due to the flow compression. After the bump, the flow expands and the temperature decreases. The maximum translation-rotation temperature at $x = 0.28$ m for case 10 is actually 20 K less than the maximum value for case 8. As the flow moves further downstream, the maximum temperature for case 10 approaches the value of case 8.

9.2 Unsteady Flow Simulations for $M_\infty = 10$ Flat Plate

Figure 9.5 shows the wall-normal mass flux imposed at the centerline ($x = x_b$) of the surface blowing/suction slot. For cases 8–10, $x_b = 0.15$ m ($R(x_b) = 1719$), $l_b = 0.002$ m, $\epsilon_b = 1 \times 10^{-4}$, $\mu_b = 3 \times 10^{-6}$, and $\sigma_b = 8 \times 10^{-7}$. These parameters were chosen to ensure that the perturbation is linear, as well as ensuring larger forcing amplitudes for the frequencies of interest. As the gaussian function has tails that approach zero at infinity, the function needs to be truncated while not strongly affecting the frequency content. Here, the function was truncated at $t = 6 \times 10^{-6}$ s without any adverse effects. Figure 9.5(b) shows the analytic Fourier transform, along with the discrete Fourier transform (DFT) obtained from the DNS results, at $x = x_b$. The two results lie directly on top of one another, as they should. Note that most of the spectral energy density is contained in the range $0 \leq f \leq 400$ kHz which contains the most unstable second mode.

Before analyzing the unsteady results, a comparison with previous findings for the same flow conditions is performed to show that the current findings are

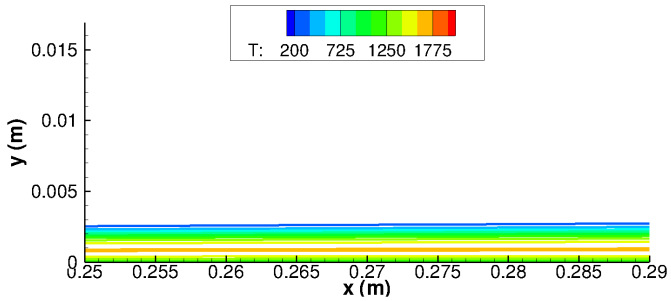

(a) case 8

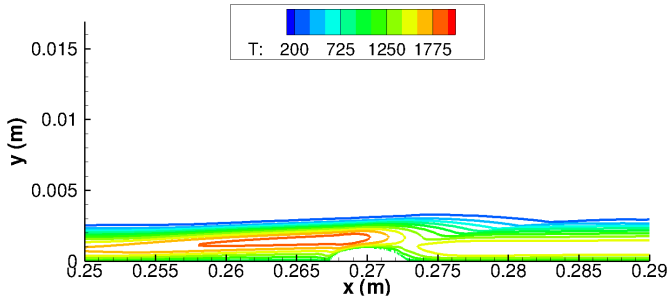

(b) case 10

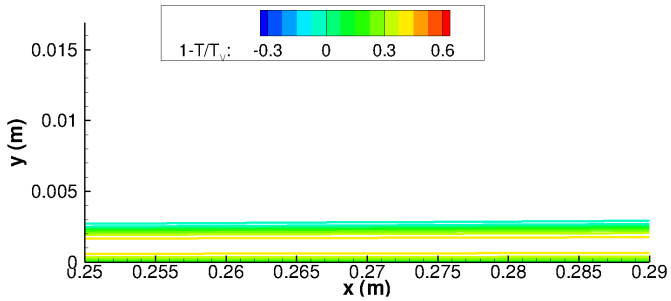

(c) case 8

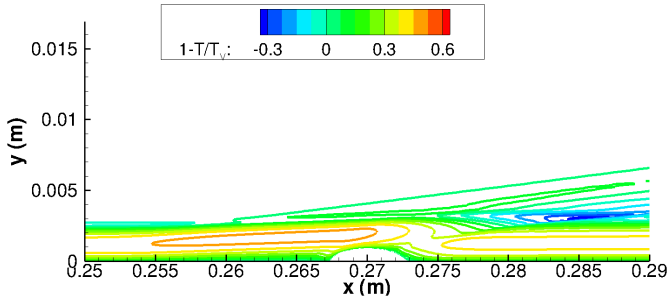

(d) case 10

Figure 9.4: Steady state solutions of (a–b) translation-rotation temperature and (c–d) $1 - T/T_V$.

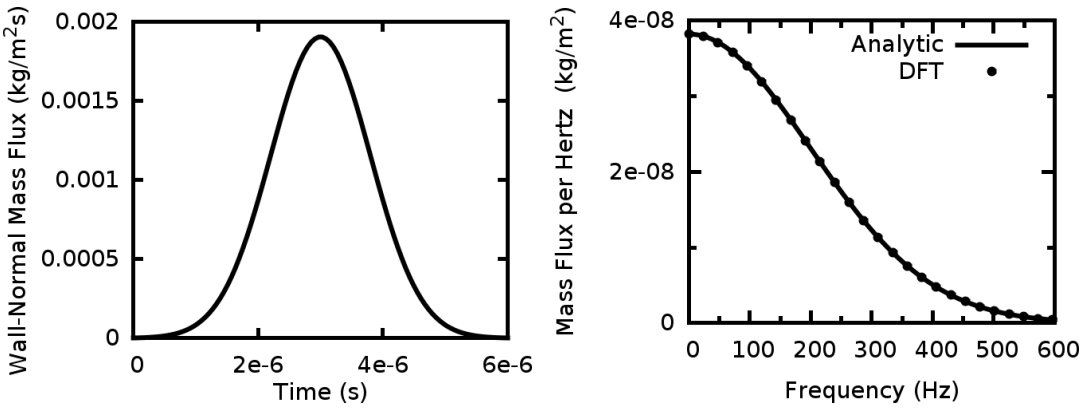

(a) (b)

Figure 9.5: The (a) mass flux imposed at $x = x_b$ and (b) comparison of the Fourier transform to the discrete Fourier transform obtained from DNS.

consistent with previous results. A comparison of the growth rate and phase velocity of the second mode to the previous results of [Hud96] is shown in Fig. 9.6. In [Hud96], the same thermochemical nonequilibrium model is used for solution of the meanflow except the reactions and reaction rates differ. Overall the growth rate compares quite well. The maximum amplification, as well as the frequency at maximum amplification, compare well. There is some difference in the phase velocity for $\Omega > 0.7$ and the reason for the small difference is unclear. Likely it is due to the differences in the gas model or perhaps small differences in the meanflow. Overall, the comparison between the two methods is adequate, showing that the current results follow previous findings.

When the blowing/suction slot is activated in a DNS, the disturbance is not a pure mode. As the disturbance travels downstream, some frequency components will grow and some will decay. Further, each frequency component can be composed of multiple modes that may individually grow or decay. As one mode begins to dominate for a single frequency component, i.e., its amplitude grows much larger than any other mode's amplitude, it is possible to achieve an accurate comparison for that mode between a DNS and LST calculations. Figure 9.7

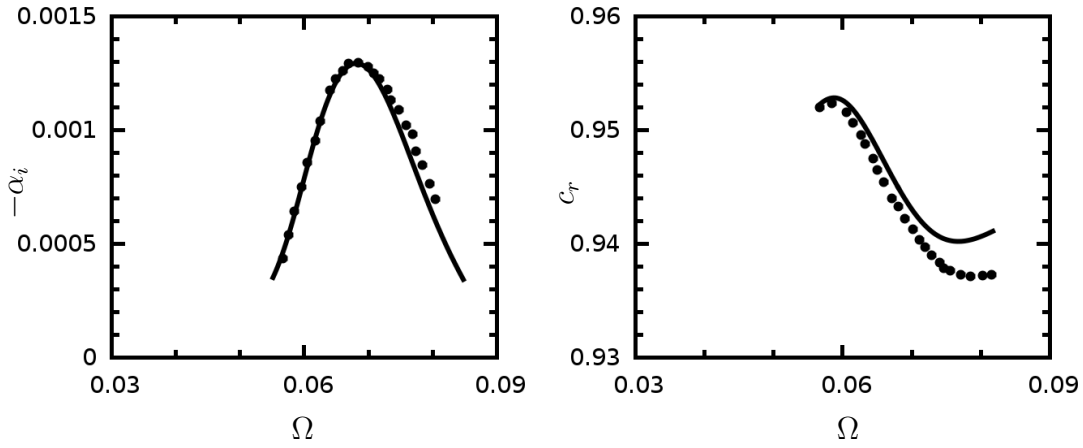

(a) (b)

Figure 9.6: Comparison at $R = 739.6$ of (a) growth rate and (b) phase velocity to [Hud96]. Current work —, and [Hud96] •.

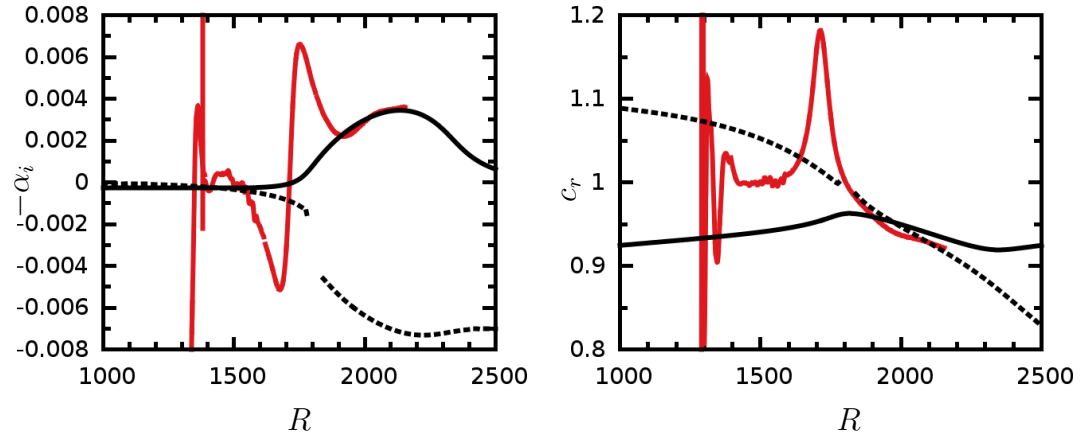

(a) (b)

Figure 9.7: Comparison of DNS (- -) at $F = 4.28 \times 10^{-5}$ for case 8 with mode S (—) and mode F (- -) obtained from LST.

shows a comparison of the growth rate and phase velocity obtained from a DNS to those obtained from LST for case 8. Near the blowing/suction slot ($R = 1719$), the DNS results do not match either mode F or mode S. However, near $R = 1900$, the DNS results match closely with mode S, or the second mode, predicted by LST. This shows that as the disturbance travels downstream, the second mode

begins to grow significantly and dominate the other boundary-layer modes at that frequency. Also, this shows that the disturbance created by the blowing/suction slot is developing into the second mode.

In the previous results of [DWZ13, FWZ13, FWZ14, FWZ15], it was found that for a fixed frequency, when a roughness element was placed upstream of the synchronization point in a hypersonic boundary layer, the second mode was destabilized. Conversely, when it was placed downstream of the synchronization point, the second mode was stabilized. It should be noted that the synchronization point referred to is obtained from the meanflow solution without any surface roughness. Here, that would refer to case 8. Therefore, for analysis of the DNS results, it is necessary to find the synchronization point of mode S and mode F using LST from the meanflow of case 8. Figure 9.8 shows the phase velocity and growth rate for mode S and mode F at R=1719. Recall that the roughness is located at R=1719. This figure is obtained by fixing the streamwise location and varying the frequency. To differentiate between the first discrete mode that originates from the fast acoustic spectrum and the second, the terminology "mode F I" is used to refer to the first and "mode F II" used for the second. Mode F I synchronizes with mode S at $\Omega = 0.085$, or $F = 4.94 \times 10^{-5}$. Therefore, it is expected that frequencies above $F = 4.94 \times 10^{-5}$ will be damped while frequencies below $F = 4.94 \times 10^{-5}$ will be amplified.

Figure 9.9 shows the wall-pressure perturbation for two fixed frequencies. The break in the lines of each plot for cases 9 and 10 is due to the surface roughness. The first frequency, $F = 3.43 \times 10^{-5}$, is below the frequency at the synchronization location so it is expected that it will be amplified compared to case 8. Each of the three cases start with the same pressure perturbation near $R = 1600$. As the perturbation approaches the roughness element, the wall-pressure perturbation increases wildly. After the roughness, there is some slight damping before the wall-pressure perturbation grows again and becomes larger than the perturbation

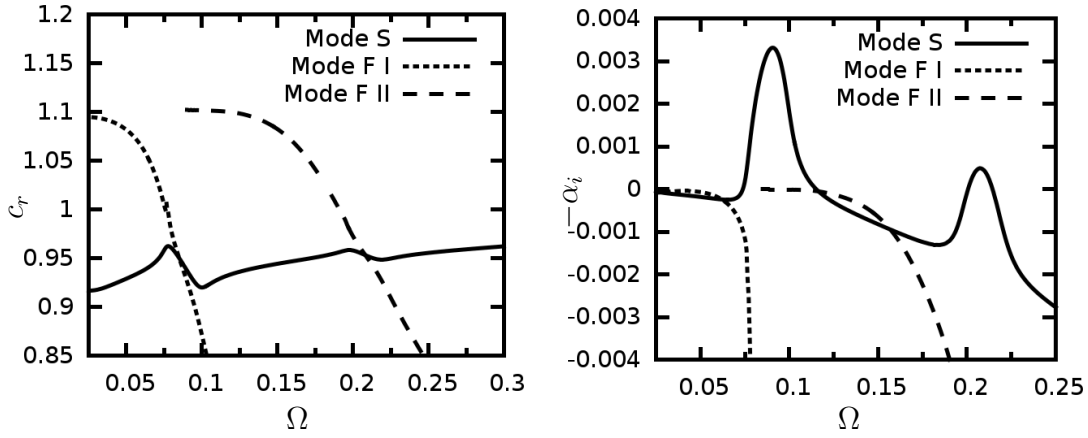

(a) (b)

Figure 9.8: Plot of (a) phase velocity and (b) growth rate at the fixed location $R = 1719$.

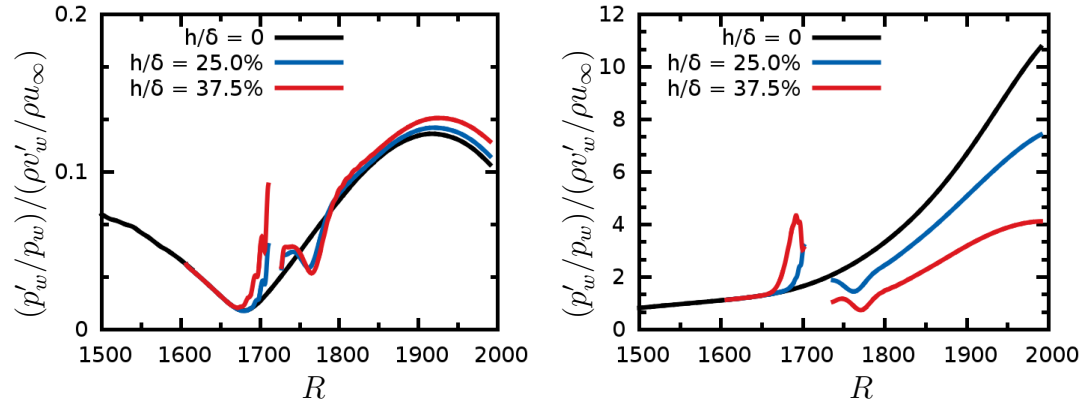

(a) $F = 3.43 \times 10^{-5}$ ($f = 200$ kHz) (b) $F = 5.14 \times 10^{-5}$ ($f = 300$ kHz)

Figure 9.9: Wall-pressure perturbation for cases 8–10 of a single frequency (a) below and (b) above the synchronization frequency.

for case 8. This growth is second mode growth. Recall from Fig. 9.8 that the growth in the DNS disturbance was similar to LST predictions of the growth rate and phase velocity of the second mode. Also note that, as the roughness height increases, the growth of the disturbance increases. These findings that a frequency below the synchronization frequency is amplified, and a larger roughness height

more strongly amplifies the second mode, correspond with the previous results of [DWZ13, FWZ13, FWZ14, FWZ15].

The second frequency, $F = 5.14 \times 10^{-5}$, is above the frequency at the synchronization location so it is expected that it will be damped when compared to case 8. Each of the three cases start with the same pressure perturbation near $R = 1600$. Similar to $F = 3.43 \times 10^{-5}$, as the perturbation approaches the roughness element, the wall-pressure perturbation increases wildly. After the roughness element, the wall-pressure perturbation stays damped for the remaining portion of the simulation. Also, as the roughness height is increased, the corresponding damping of the wall-pressure perturbation is decreased. These findings that a disturbance at a frequency below the synchronization frequency is damped, and a larger roughness height more strongly damps the second mode, correspond with the previous results of [DWZ13, FWZ13, FWZ14, FWZ15].

Similar to analyzing a single frequency along the flat plate, since the frequency content of the perturbation is continuous, it is possible to fix the streamwise location and visualize the frequency spectra. Figure 9.10 shows the wall-pressure perturbation spectra at two separate streamwise locations. The large amplitudes are due to the growth of the second-mode instability. The first location, $R = 1687$ is upstream of the roughness element. Notice that for both roughness cases the perturbation is amplified for almost the entire frequency range. Upstream of the roughness, the effects of the roughness are to amplify each frequency component. The second location, $R = 1985$, is downstream of the roughness element. Now the damping effect due to the roughness element is clear. The amplifying effect of the roughness on the second mode is slight at this streamwise location but still visible for case 10 at $F = 5 \times 10^{-5}$.

Overall, the results for the Mach 10 flat plate cases 8–10 of a real-gas flow were shown to be consistent with previous research for hypersonic flows with a perfect gas assumption. It was shown that a two-dimensional roughness element

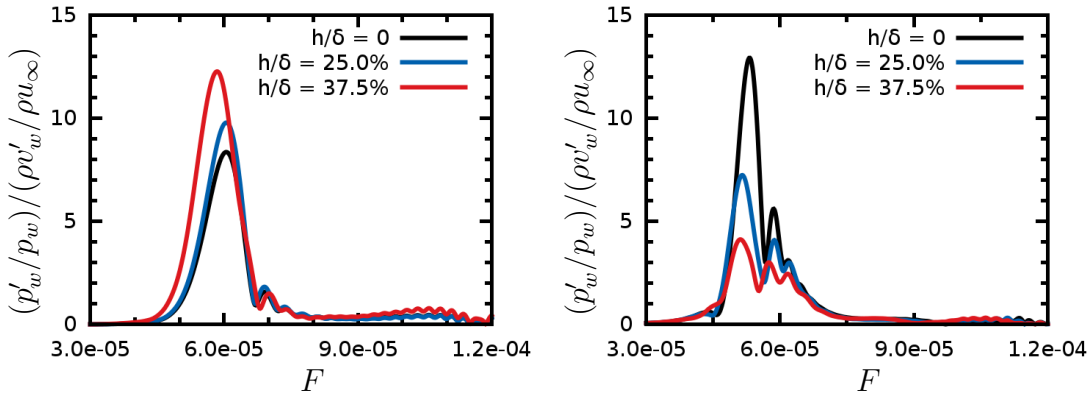

(a) $R = 1687$ ($x = 0.26$ m) (b) $R = 1985$ ($x = 0.36$ m)

Figure 9.10: Wall-pressure perturbation frequency spectra for cases 8–10 at a location (a) upstream and (b) downstream of the roughness element.

can suppress second-mode instability in a real gas. These results show that the idea of stabilizing a hypersonic boundary layer through use of two-dimensional roughness elements does extend to real gas flows.

CHAPTER 10

DNS Results for $M_\infty = 15$ Flat Plate

The freestream conditions are from the previous LST studies of [MA91] and [Hud96] for second-mode instability of a real-gas flow over a flat plate. They are given in Table 10.1. The freestream unit Reynolds number, Re_u, is 3.33×10^6 /m and the freestream stagnation enthalpy, $h_{o,\infty}$, is 32.6 MJ/kg. The boundary conditions at the flat plate are no-slip for each of the velocities, a constant wall temperature of $T_w = T_{V,w} = 1225$ K, and non-catalytic conditions for each of the chemical species.

Table 10.1: Freestream conditions for $M_\infty = 15$ flat plate.

Parameter	Value
M_∞	15.0
ρ_∞ [kg/m^3]	1.391×10^{-2}
p_∞ [N/m^2]	2812
c_{N_2}	0.78
c_{O_2}	0.22

A schematic of the DNS simulation is given in Fig. 10.1. The computational domain is bounded by the inlet, outlet, shock, and flat plate. For the DNS simulation, the meanflow is initially converged to a specified tolerance. This tolerance must be below the linear forcing of the blowing/suction slot, or numerical noise

will contaminate the unsteady results. Next, the slot is activated, and a linear perturbation is introduced at the slot. This perturbation is then simulated as it travels throughout the meanflow.

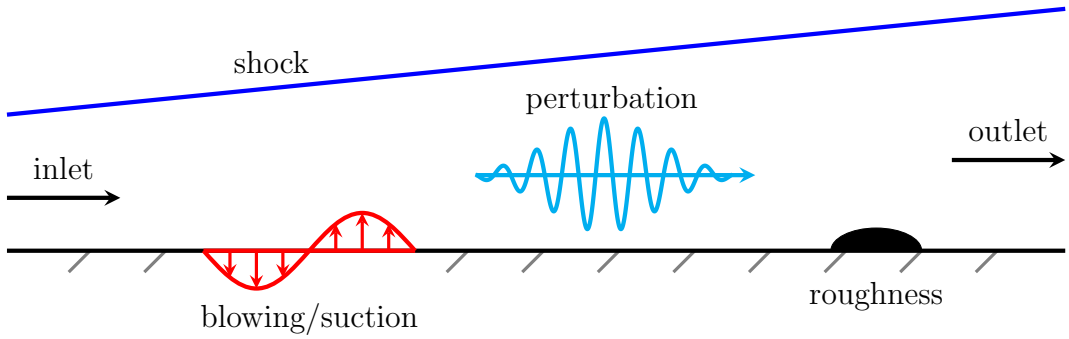

Figure 10.1: Schematic of the physical domain with the roughness location and blowing/suction slot.

In an attempt to quantify real gas and roughness effects in the instability process, multiple cases are run for varying gas models and roughness heights. These cases are defined in Table 10.2. The cases are a mix of varying roughness heights and either a real gas, or a perfect gas, model. The perfect gas model is obtained from the real gas model described in Ch. 2. For the case of a perfect gas, the source terms are turned off, the vibration energy is held constant, and the mass fractions are held to their freestream values. This is done so that the viscosity, thermal conductivity, etc., are calculated the exact same way for either the real, or perfect, gas.

Before analyzing the simulation results, a grid convergence study was performed to ensure that the computational grid was sufficiently dense to capture the relevant flow physics. The first grid used 962 by 241 points in the streamwise and wall-normal directions, respectively. The second grid was a double grid solution which used 1922 by 481 points. Case 12 was used as the test case for the grid convergence study. For both grids, the meanflow solution was converged within a specified tolerance and then a perturbation was simulated. Figure 10.2 shows

Table 10.2: Types of DNSs for $M_\infty = 15$ flat plate.

Case Number	h/δ	Gas Model
11	0	real gas
12	10%	real gas
13	20%	real gas
14	30%	real gas
15	0	perfect gas
16	10%	perfect gas
17	20%	perfect gas
18	30%	perfect gas

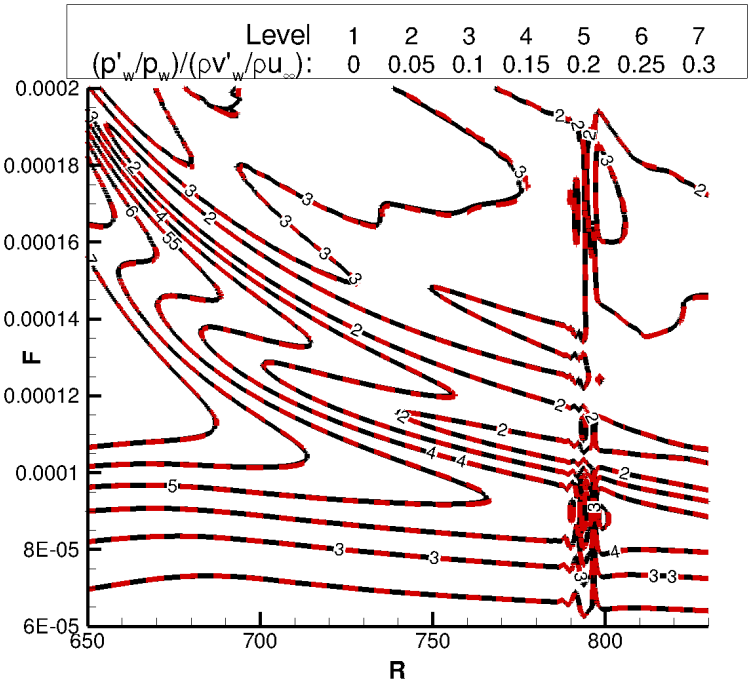

Figure 10.2: Comparison of single grid (962 by 241) results to double grid (1922 by 481) results for case 12. single grid - - , double grid —.

the frequency spectra of the wall-pressure perturbation over the region tested. There are only minimal differences between the two simulations. The lack of any significant difference between the two separate results shows that the single grid result is grid converged.

10.1 Steady Flow Simulations for $M_\infty = 15$ Flat Plate

The first step in the direct numerical simulation is to simulate the time invariant meanflow. Figure 10.3 shows the meanflow contours of the translation-rotation temperature and $1-T/T_V$ near the roughness element for cases 11 and 14. For case 11, the translation-rotation temperature contour remains nearly constant in the streamwise direction over the region shown. However, the vibration temperature is increasing and equilibrating with the translation-rotation temperature as the flow moves downstream. For case 14, the roughness element compresses the flow and causes a strong increase in translation-rotation temperature near $x = 0.185$ m. Behind the roughness, the maximum translation-rotation temperature is higher than case 11. Also, the vibration temperature is increased and moves closer to thermal equilibrium behind the roughness element. Overall, the roughness element serves to increase the translation-rotation temperature of the flow and move the vibration temperature closer to thermal equilibrium.

Figure 10.4 shows the meanflow contours of temperature for cases 15 and 18. Similar to the roughness element in a real gas flow, the roughness element in the perfect gas flow increases the temperature immediately upstream of the roughness. It also increases the maximum temperature in the boundary layer downstream of the roughness in the range $x \geq 0.2$ m. Overall, the temperature for the perfect gas flow is higher than that for a real gas. This makes sense as energy is input into chemical reactions, as well as higher energy modes, for the real gas flow which are not present in the perfect gas flow.

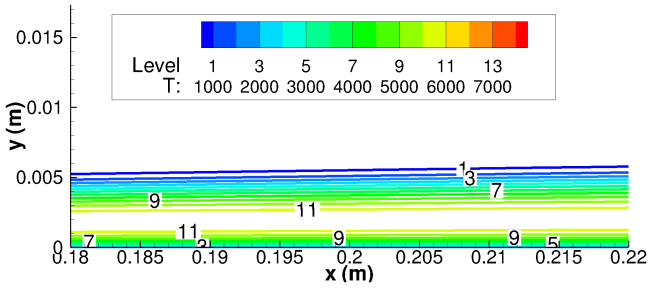

(a)

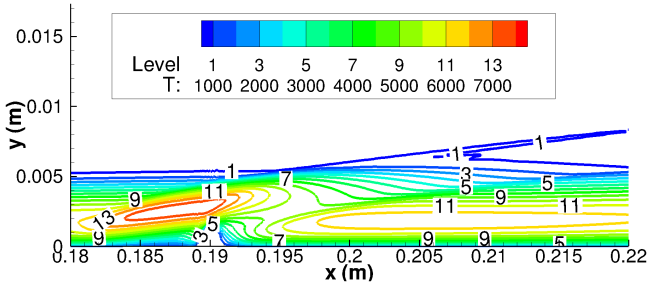

(b)

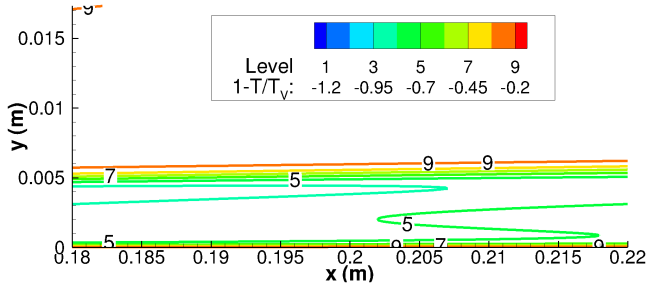

(c)

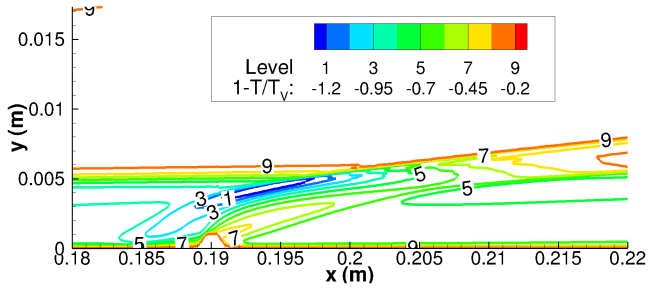

(d)

Figure 10.3: Meanflow contours of translation-rotation temperature for (a) case 11 and (b) case 14 along with contours of $1 - T/T_V$ for (c) case 11 and (d) case 14.

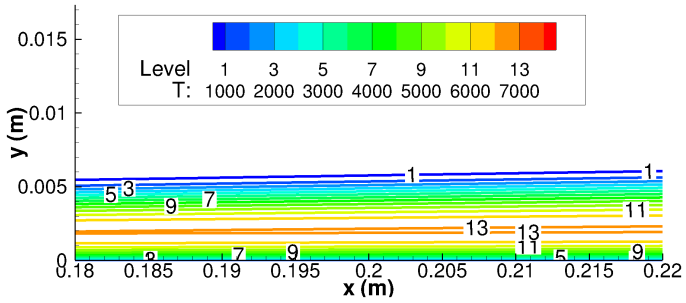

(a)

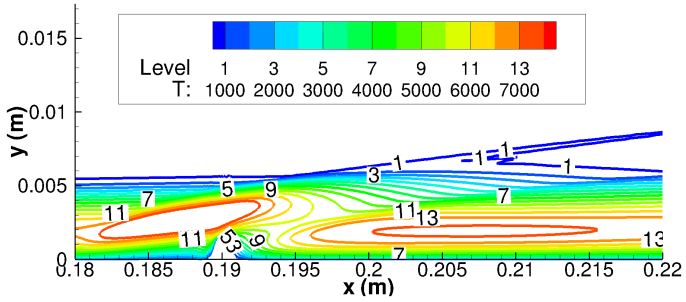

(b)

Figure 10.4: Meanflow contours of the temperature for (a) case 15 and (b) case 18.

Figure 10.5 gives a comparison of cases 11 and 14 with cases 15 and 18 at two separate streamwise locations. The first location—$x = 0.22$ m (R=856.0)—is 19.6δ downstream of the roughness element. Both temperatures have clearly increased for case 14 compared to case 11 with the maximum vibration temperature increasing nearly 600 K. Similarly, the temperature for case 18 has clearly increased when compared to case 15. The second location—$x = 0.37$ m (R=1110)—is 117.6δ downstream of the roughness element. The difference between the temperatures here is much less pronounced. Near the wall, there is little distinguishable difference between any of the profiles. There is some difference in the translation-rotation temperature for cases 11 and 14 where $y > 0.003$ m due mainly to boundary-layer thickening. For the vibration temperature, there is still an increase in the maximum value but it is not as pronounced as before. For cases

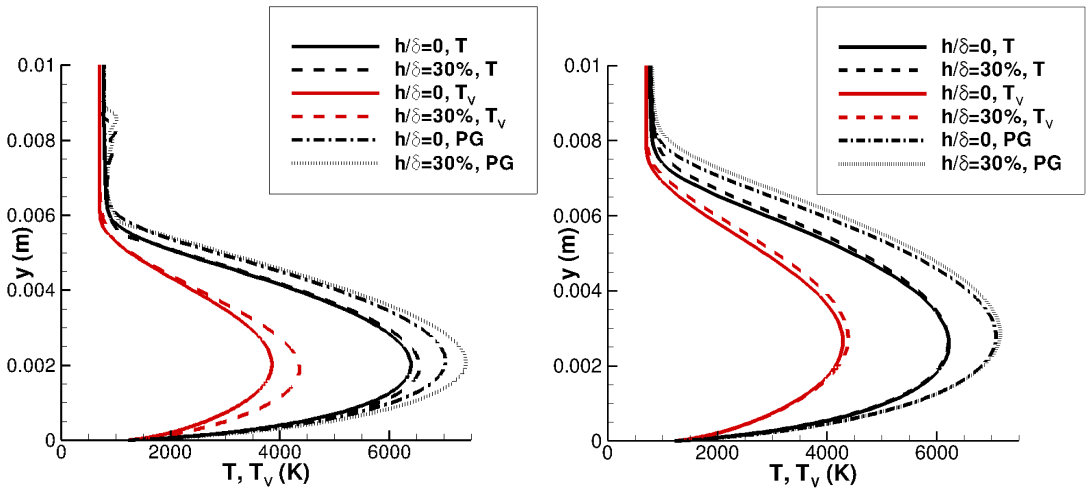

(a) (b)

Figure 10.5: Wall-normal profiles of temperatures at (a) $x = 0.22$ m ($R = 856.0$) and (b) $x = 0.37$ m ($R = 1110$).

15 and 18, there is also an increase in the maximum value, but again, it is not as pronounced as before. Overall, as the flow moves downstream, the roughness perturbed meanflow approaches the unperturbed meanflow with a slight shift due to boundary-layer thickening.

As the roughness element strongly increases the translation-rotation temperature, it is expected that this will have an effect on the chemical composition of the flow. The reaction this increase in temperature is likely to affect the most is the dissociation of oxygen. Figure 10.6 shows the contours of the mass fraction of atomic oxygen for cases 11 and 14. There is an increase in c_{O} for case 11 in the downstream direction, as well as for case 14. However, the increase in c_{O} for case 14 is much larger due to the increased temperatures created by the roughness element. As c_{O} increases, the flow moves closer to chemical equilibrium.

To compare the concentration of c_{O} between cases 11–14, Fig. 10.7 shows the wall-normal profiles of the mass fraction of atomic oxygen at two separate streamwise locations. For each case the roughness element increases the concentration of

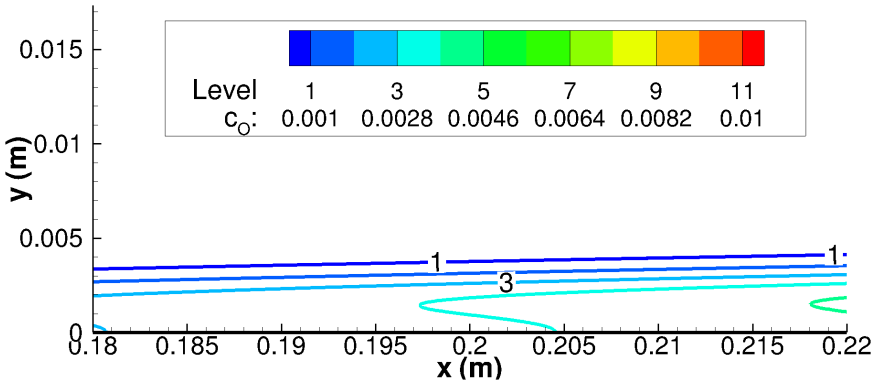

(a) case 11

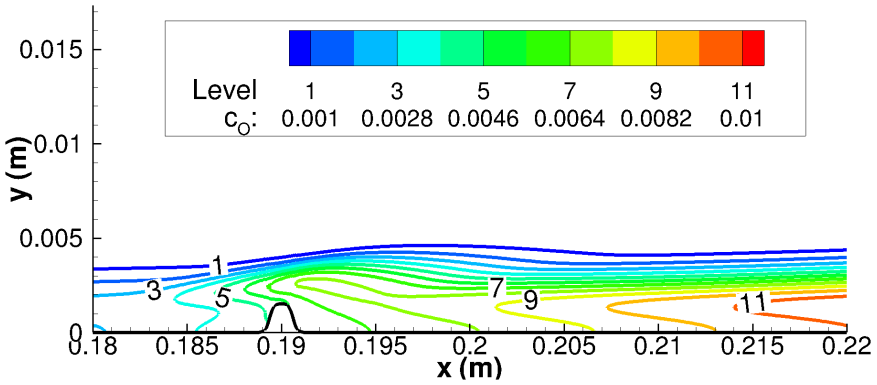

(b) case 14

Figure 10.6: Meanflow contours of the mass fraction of atomic oxygen.

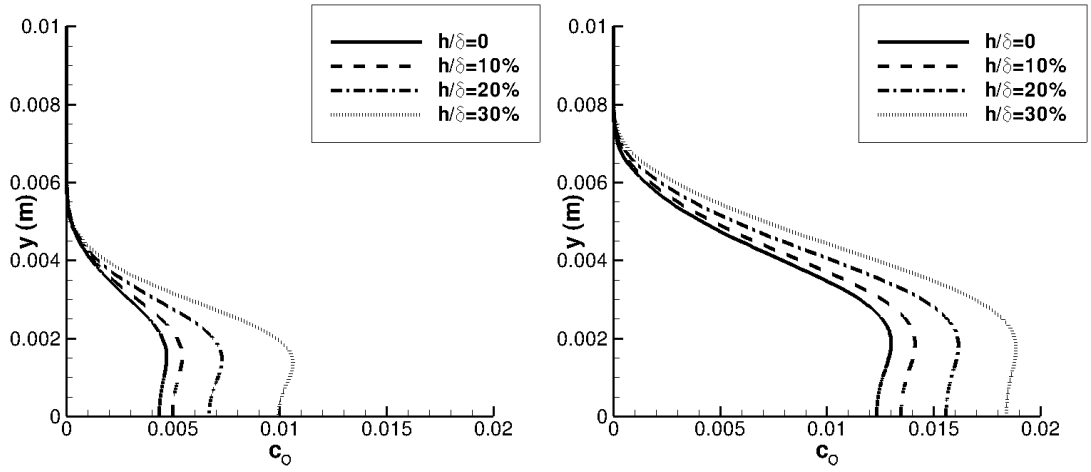

(a) (b)

Figure 10.7: Wall-normal profiles of the mass fraction of atomic oxygen (c_{O}) at (a) $x = 0.22$ m ($R = 856.0$) and (b) $x = 0.37$ m ($R = 1110$).

atomic oxygen with the largest roughness case creating the highest concentration of atomic oxygen. As the flow moves far downstream from the roughness element to $x = 0.37$ m, the concentration of atomic oxygen is still significantly larger for case 14 than case 11. This is unlike the temperatures which are approaching the same value.

A common question that naturally arises when studying the flow over a perturbed surface is, "how does the perturbation affect the surface heat transfer?" If the surface heat transfer induced by the perturbation is larger than the heat transfer obtained from a turbulent flow, then the purpose of delaying transition by judiciously placed surface roughness is partially defeated. Figure 10.8(a) shows the wall heat flux from case 2 with and without surface roughness. The two results begin to diverge near $R = 770$ where the roughness case actually has less heat transferred to the wall than the clean case. At the roughness, the wall heat flux for the roughness case is nearly 5 times larger than the clean case. However, this rise in heat flux is only over a small portion of the plate. Downstream of $R = 900$, the heat flux for the clean and roughness cases converges to the same value.

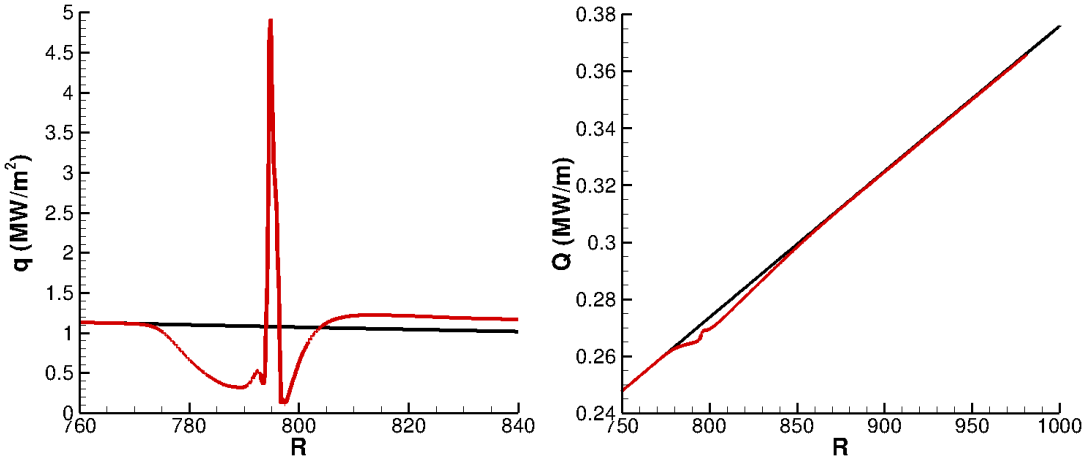

(a) (b)

Figure 10.8: Comparison of (a) wall heat flux and (b) total wall heat transfer for cases 11 and 14. Roughness at R=795.5. Case 11 —, Case 14 —.

Clearly, there is a difference in the local surface heat flux near the element, but how does this affect the total energy transferred to the vehicle surface? In Fig. 10.8(a), the total heat transferred to the vehicle is shown. The total heat transfer is obtained by integrating, along the body surface, the local surface heat flux. As the flat plate is infinite in the transverse direction, the result is given in units of power over length. It can be seen that the difference between the clean and perturbed surface is small. At $R = 1000$, the difference between the two is 0.04%. This small difference shows that, for a single roughness element, there is no significant change in the total heat transferred to the vehicle surface. To summarize, near the roughness there are strong local variations in the surface heat flux, however, the total heat transferred to the surface remains relatively unaffected when a single roughness element is added to the flat plate's surface.

10.2 Unsteady Flow Simulations for $M_\infty = 15$ Flat Plate

Figure 10.9 shows the wall-normal mass flux imposed at the centerline ($x = x_b$) of the surface blowing/suction slot. For cases 11–18, $x_b = 0.10$ m, $l_b = 0.002$ m, $\epsilon_b = 1 \times 10^{-6}$, $\mu_b = 3 \times 10^{-6}$, and $\sigma_b = 5 \times 10^{-7}$. These parameters were chosen to ensure that the perturbation is linear, as well as ensuring larger forcing amplitudes for the frequencies of interest. As the gaussian function has tails that approach zero at infinity, the function needs to be truncated while not strongly affecting the frequency content. Here, the function was truncated at $t = 6 \times 10^{-6}$ s without any adverse effects. Figure 10.9(b) shows the analytic Fourier transform, along with the discrete Fourier transform (DFT) obtained from the DNS results, at $x = x_b$. The two results lie directly on top of one another, as they should. Note that most of the spectral energy density is contained in the range $0 \leq f \leq 700$ kHz. This was done to more strongly force the frequencies near the second and third mode frequency ranges for the simulated domain.

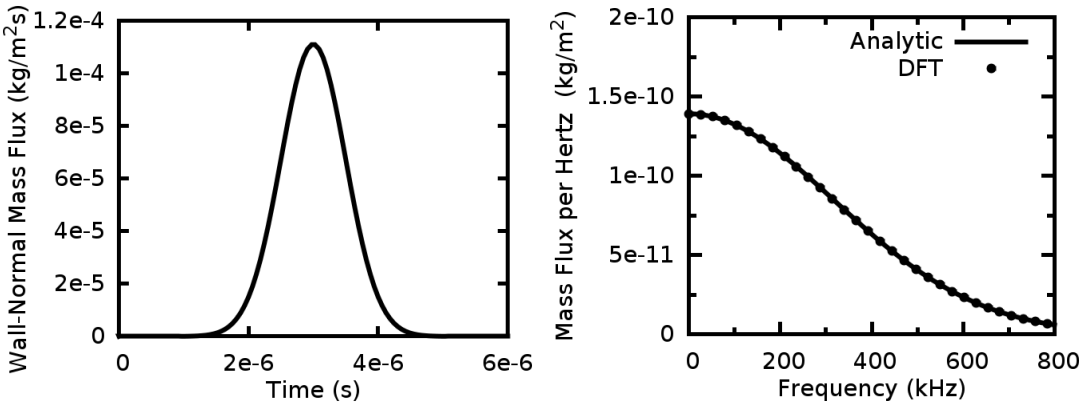

(a) (b)

Figure 10.9: The (a) mass flux imposed at $x = x_b$ and (b) comparison of the Fourier transform to the discrete Fourier transform obtained from DNS.

Before analyzing the unsteady results, a comparison with previous results for the same geometry and flow conditions is performed to show that the current find-

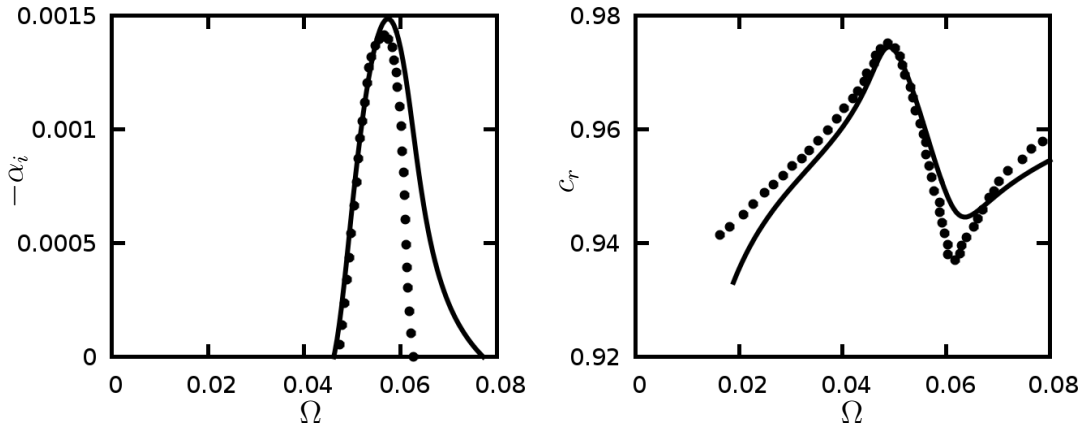

(a) (b)

Figure 10.10: Comparison at R=1000 of (a) growth rate and (b) phase velocity to [MA91]. Current work —, and [MA91] •.

ings are consistent with previous results. A comparison of the growth rate and phase velocity of the second mode to the previous results of [MA91] is shown in Fig. 10.10. In [MA91], a boundary layer solver is used to compute the meanflow which is modeled using an assumption of chemical equilibrium. This differs from the thermochemical nonequilibrium assumption used here and the shock-fitting method used to simulate the meanflow. Considering the differences, the two results match quite well. The maximum amplification, as well as the frequency at maximum amplification, compare well. There is some difference in the amplification rate near $0.06 < \Omega < 0.08$. However, this difference could be due to the different gas models used, or, the solution procedure of the meanflow. Similarly, the phase velocity compares well over the region of second mode instability. Away from the second-mode unstable region, near the tails of the plot, the differences are larger. Overall, considering the two different gas models and solution procedures, the comparison between the two methods is quite accurate. This shows that the current results are consistent with previous results for the same geometry and flow conditions.

Instantaneous snapshots of the translation-rotation and vibration temperatures for cases 11 and 14 are shown in Fig. 10.11. In Figs. 10.11(a) and 10.11(b) there is a Mach wave visible near $y = 0.001$ m. This Mach wave is due to the flow adjusting to the initial perturbation at the wall. It is about an order of magnitude larger than any other flow disturbance. The Mach wave is not visible in the vibration temperature plots because the induced perturbation from the Mach wave is too weak. Also, notice that the original Gaussian forcing has changed to a pattern that is clearly oscillatory. As the initial disturbance enters the boundary layer, it excites boundary-layer modes for different frequencies that grow and/or decay at different rates. These boundary-layer modes are oscillatory in nature thus creating the oscillatory structure in the figures.

Between the Mach wave and the wall, the largest perturbation amplitudes are found near the leading edge of the perturbation near $x = 0.2$ m. Moving upstream, the perturbation gradually decreases until it reaches far enough upstream where it decays to zero. Both temperatures have an oscillation in amplitude near the boundary-layer edge and the wall. The oscillation near the wall is much stronger for translation-rotation temperature than vibration temperature. These oscillations are characteristic of a second-mode wave in a hypersonic boundary-layer where the translation-rotation temperature eigenfunction has large amplitudes near the boundary-layer edge and wall. For Figs. 10.11(a) and 10.11(c), the oscillatory pattern is smooth and continuous. However, when the roughness is added to the meanflow as shown in Figs. 10.11(b) and 10.11(d), this pattern is adjusted. From 0.18 m $\leq x \leq$ 0.19 m, there is a squishing together of the high and low amplitudes as the disturbance moves into the compression region in front of the roughness element. Behind the element in the region 0.19 m $\leq x \leq$ 0.20 m, the low amplitude disturbance at the wall is stretched out and decreased in magnitude when compared to the flow with no roughness. Also, the high amplitude disturbance is pushed away from the wall.

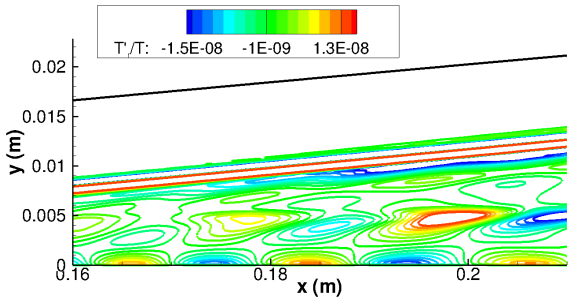

(a) case 11

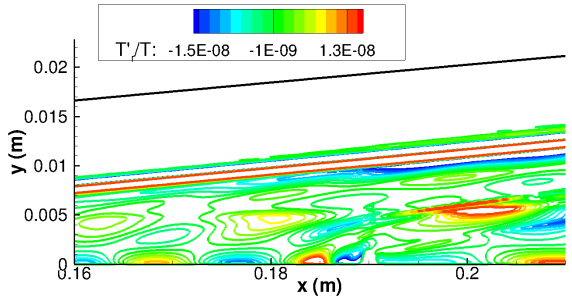

(b) case 14

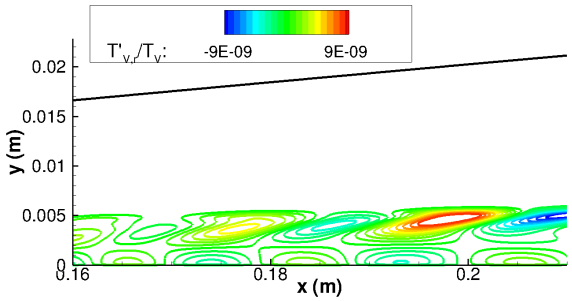

(c) case 11

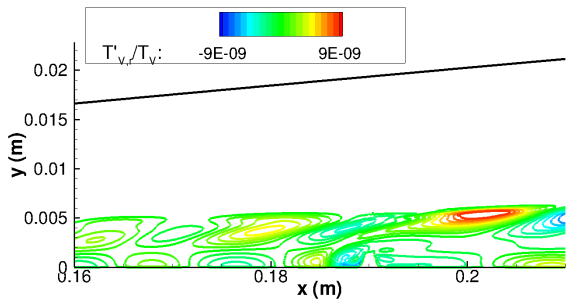

(d) case 14

Figure 10.11: Instantaneous translation-rotation temperature and vibration temperature perturbation from DNS.

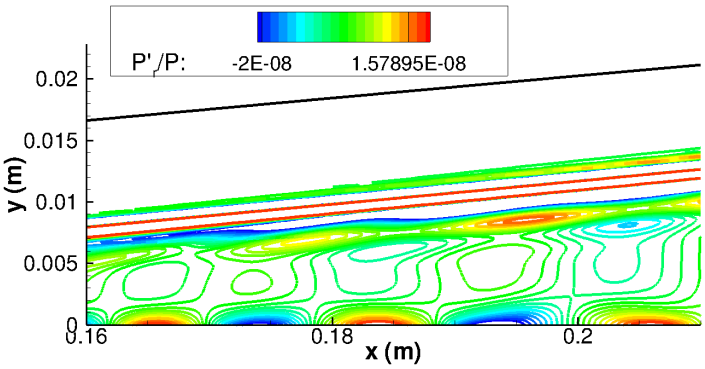

(a) case 11

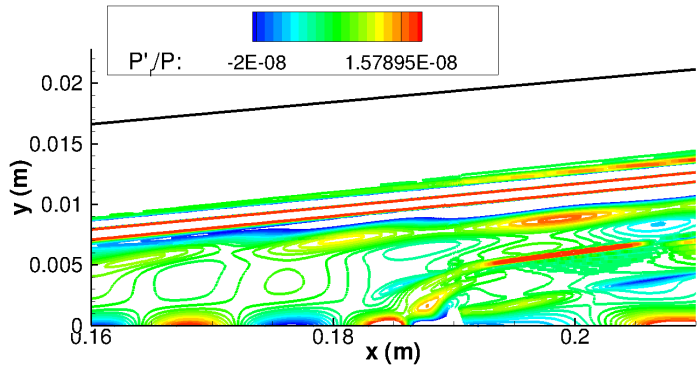

(b) case 14

Figure 10.12: Instantaneous pressure perturbation from DNS.

An instantaneous snapshot of the pressure perturbation is given in Fig. 10.12. Similar to the perturbation of translation-rotation temperature, there is a Mach wave near $y = 0.001$ m due to the flow adjusting to the initial gaussian forcing at $x = 0.10$ m. Towards the wall, the pressure perturbation is characteristic of a second-mode wave in a hypersonic boundary-layer with the largest amplitude found at the wall. Again, before the roughness, the disturbance seems to squish together where behind the roughness it seems to stretch out. Note how downstream of the roughness there are two more peaks in pressure where upstream of the roughness there is only one. This is due to the fact that after the roughness the pressure disturbance is traveling along the compression and expansion waves present in the meanflow.

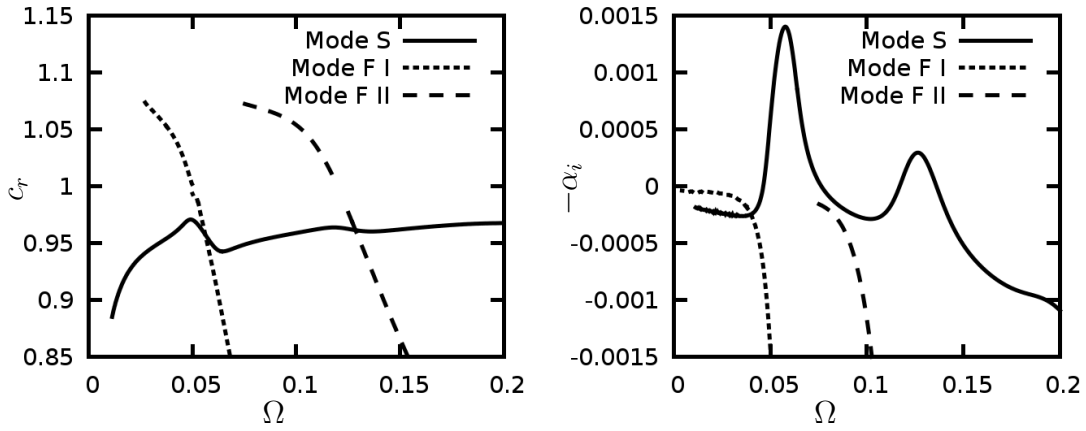

Figure 10.13: Plot of (a) phase velocity and (b) growth rate at the fixed location $R = 795.5$.

In order to determine the synchronization location of the fast (mode F) and slow (mode S) acoustic modes, the phase velocity and the growth rate of the modes were computed using LST and are shown in Fig. 10.13. This plot is found using the meanflow of case 11 and fixing the location while varying the frequency. The location corresponds to the center of the roughness element at x=0.19 m which corresponds to R=795.5. The synchronization location of mode F and mode S is loosely defined as the location where the phase velocities of the modes are equal rather than the more strict definition requiring both the real and imaginary parts of α to be equal. This occurs at $\Omega = 0.056$ which corresponds to the nondimensional frequency $F = 7.06 \times 10^{-5}$. Although it is not shown, the perfect gas synchronization frequency was found to be $\Omega = 0.055$ which corresponds to $F = 6.96 \times 10^{-5}$. Similarly, the synchronization location between mode S and the second discrete mode originating out of the fast acoustic spectrum (mode F II) can be found. This synchronization occurs at $\Omega = 0.128$ which corresponds to $F = 1.615 \times 10^{-4}$. There is no change in the synchronization frequency for the third mode in the perfect gas flow.

Figure 10.14 shows contour plots of wall-pressure perturbation for cases 11–14. These figures show the frequency range over which the second mode is unstable. Note that the roughness element for cases 12–14 is located at $R = 795.5$. For case 11 where there is no roughness element, the contours are smooth and ordered. There is a clear high amplitude region running across the figure from $F = 9\times10^{-5}$ at $R = 750$ to $F = 7 \times 10^{-5}$ at $R = 1100$. This high amplitude region is caused by second-mode growth. For the cases with roughness elements, the contours are less ordered and the clear region of second-mode growth changes. For each roughness case, there are wild oscillations in amplitude immediately upstream of the roughness element. These oscillations are not dependent on the frequency, rather each frequency experiences them. Near the region of second mode growth, these wild oscillations can lead to large amplitudes before the roughness element. However, behind the roughness element these oscillations are quickly damped. As the roughness element increases in height, the clearly defined second mode region in Fig. 10.14(a) slowly changes until in Fig. 10.14(d) where the second mode region looks like it is almost split into two separate horizontal sections. The frequency at which this splitting occurs corresponds roughly to the synchronization frequency which was found to be $F = 7.06 \times 10^{-5}$.

Figure 10.15 shows contour plots of wall-pressure perturbation over the third-mode frequency range for cases 11–14. These figures show the frequency range over which the third mode is unstable. Note that the roughness element for cases 12–14 is located at $R = 795.5$. For case 11 where there is no roughness element, the contours are more smooth and ordered. There is a clear high amplitude region running across the figure from $F = 1.8\times10^{-4}$ at $R = 750$ to $F = 1.2\times10^{-4}$ at $R = 1100$. This high amplitude region is caused by third-mode growth. The waviness seen in the contours of Fig. 10.15(a) for frequencies higher than $F = 1.8 \times 10^{-4}$ is due to modulation caused by multiple boundary layer modes all present in the boundary layer simultaneously. For the cases with roughness elements, the

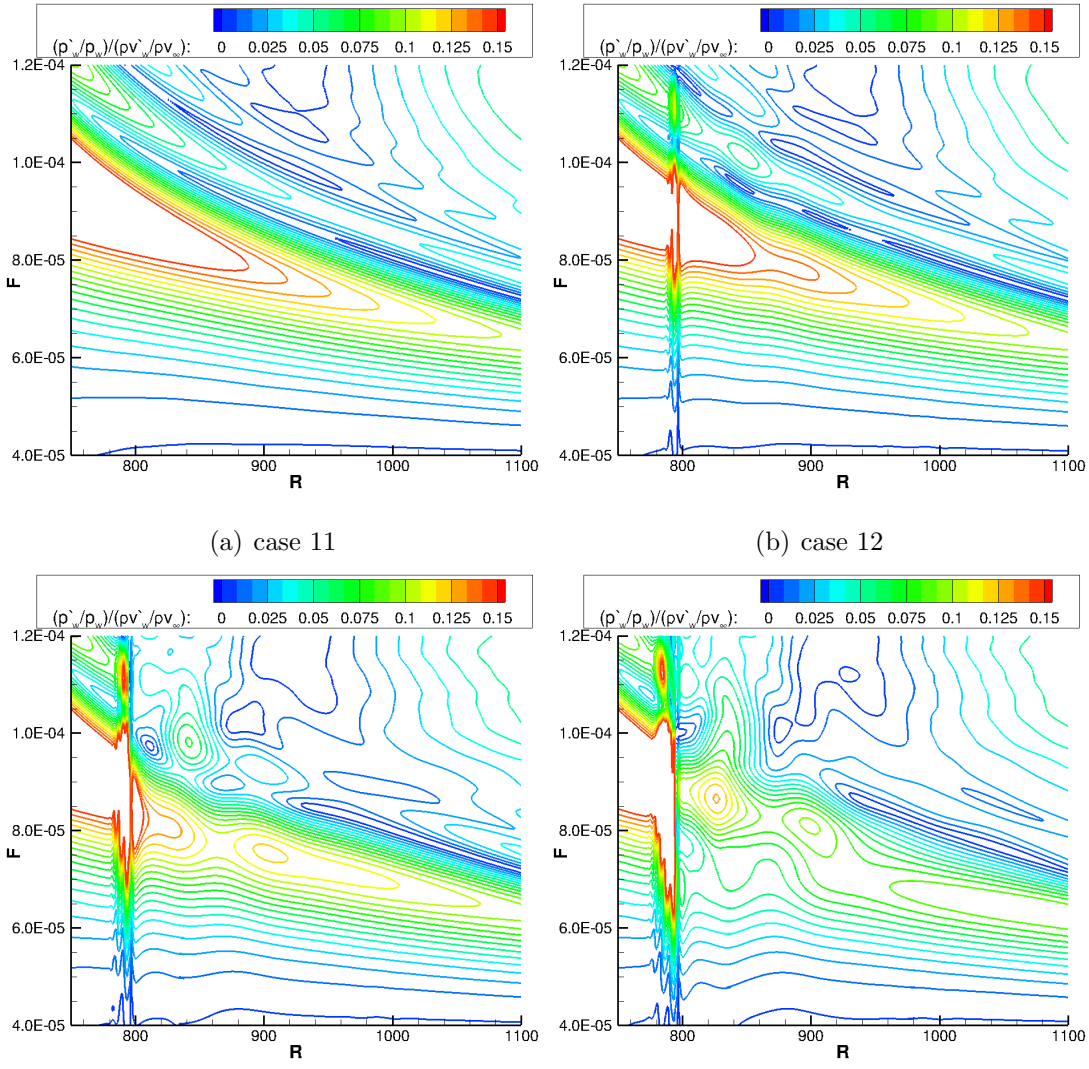

(a) case 11

(b) case 12

(c) case 13

(d) case 14

Figure 10.14: Contour plots of wall-pressure perturbation for the second mode.

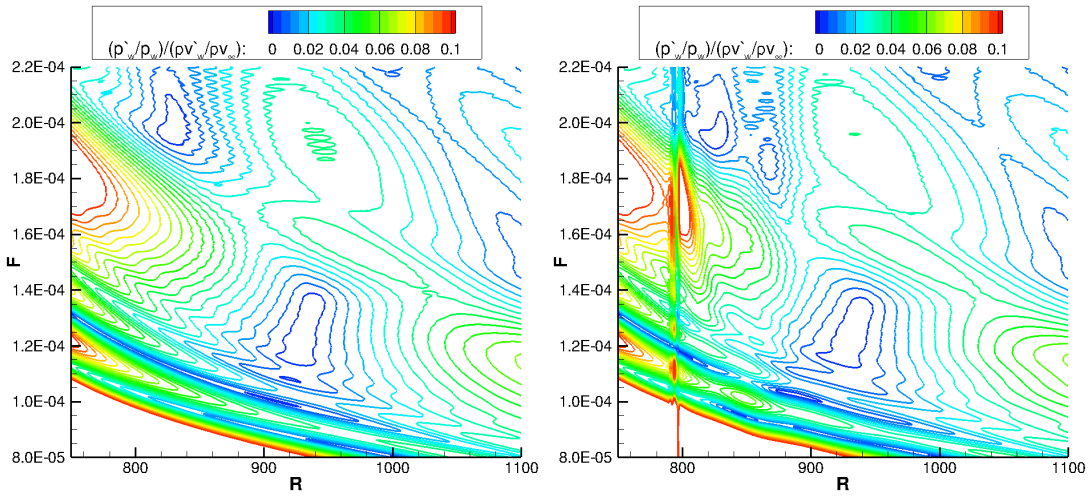

(a) case 11

(b) case 12

(c) case 13

(d) case 14

Figure 10.15: Contour plots of wall-pressure perturbation for the third mode.

contours are less ordered and the clear region of third-mode growth changes. For each roughness case, there are wild oscillations in amplitude immediately upstream of the roughness element. These oscillations are not dependent on the frequency, rather each frequency experiences them. Near the region of third-mode growth, these wild oscillations can lead to large amplitudes before the roughness element. However, behind the roughness element these oscillations are quickly damped. As the roughness element increases in height, the clearly defined third-mode region in Fig. 10.15(a) slowly changes until in Fig. 10.14(d) where the third-mode region looks like it is almost split into two separate horizontal sections. The frequency at which this splitting occurs corresponds roughly to the synchronization frequency of mode S and mode F II which was found to be $F = 1.615 \times 10^{-4}$.

Figure 10.16 shows the wall-pressure perturbation contours for cases 15 and 18. These are the ideal gas cases that correspond to the real gas cases 11 and 14. Qualitatively, the contour plots of the wall-pressure perturbation for the second mode are the same for each of the ideal gas cases. However, the amplitude for the ideal gas cases is slightly lower. Similarly, the contour plots of the wall-pressure perturbation for the third mode are the same for the ideal gas. However, there is no noticeable decrease in the amplitude of the third mode.

To analyze which frequencies are stabilized and/or destabilized by the roughness elements, Fig. 10.17 shows the wall-pressure perturbation for cases 11–14 of a single frequency below and above the synchronization frequency. The frequency below the synchronization frequency is destabilized for each of the cases with a roughness element when compared to the case without a roughness element. This destabilizing effect is rather small but it is noticeable. Also, the destabilizing effects increase as the roughness height increases. Conversely, the frequency above the synchronization frequency is stabilized for each of the cases with a roughness element. This stabilizing effect is rather weak for cases 12 and 13 and is much stronger for case 14. Clearly, for this frequency, the resultant damping due to

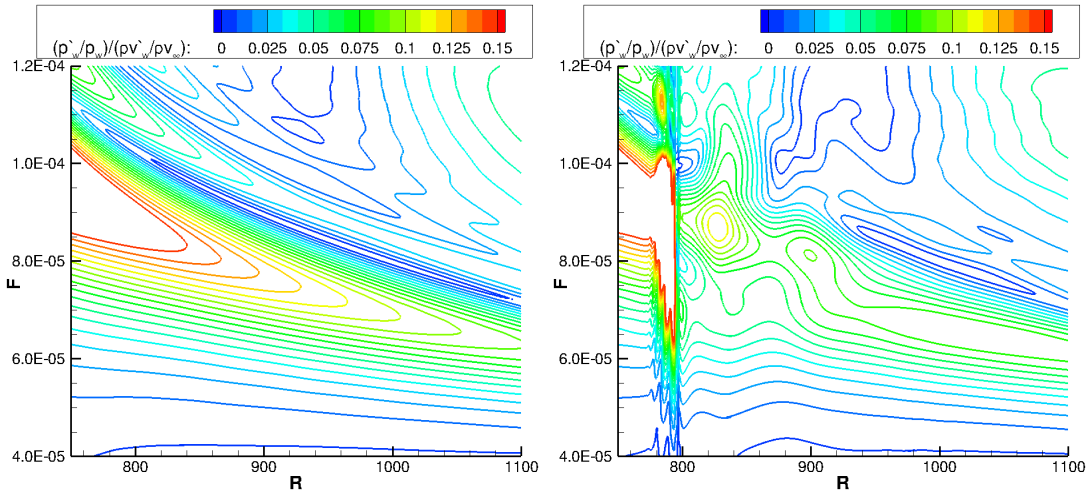

(a) case 15

(b) case 18

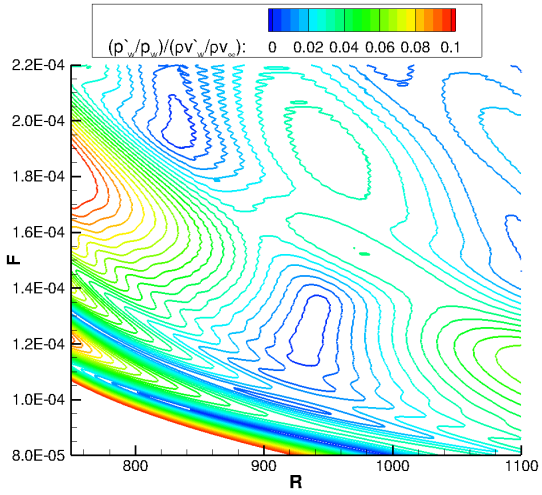

(c) case 15

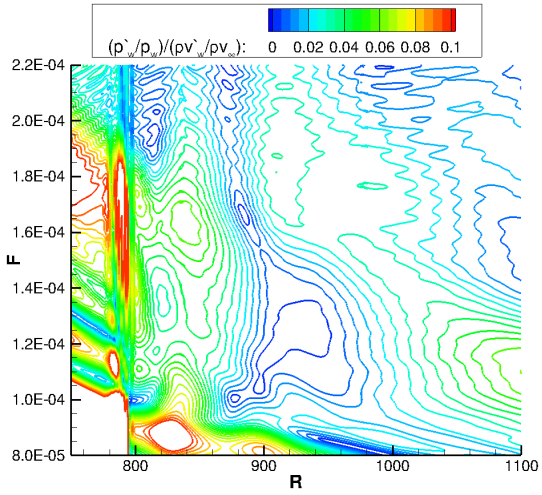

(d) case 18

Figure 10.16: Contour plots of wall-pressure perturbation for second and third modes of perfect gas cases.

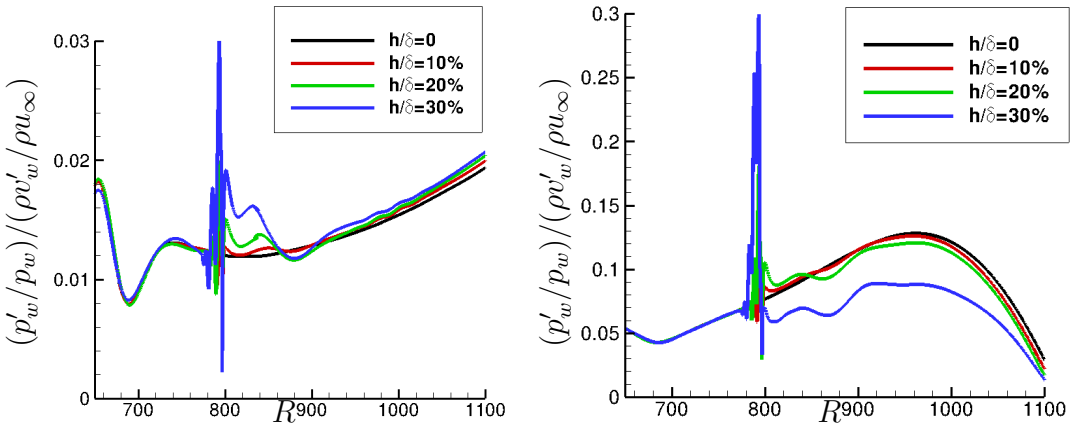

(a) $F = 4.73 \times 10^{-5}$ (b) $F = 7.09 \times 10^{-5}$

Figure 10.17: Wall-pressure perturbation for cases 11–14 of a single frequency (a) below and (b) above the synchronization frequency.

changing the roughness height is nonlinear. This is unlike the destabilizing effect shown in Fig. 10.17(a) where the resultant growth due to changing the roughness height is close to linear. These effects are most likely associated with the roughness height rather than the gas model as the perfect gas simulations show the exact same behavior.

Figure 10.18 shows the wall-pressure perturbation spectra near the frequency range of the second and third modes. The growth in the wall-pressure perturbation in Fig. 10.18(a) is due to the second mode and the growth in Fig. 10.18(b) is due to the third mode. From Fig. 10.18(a), it is seen that as the roughness height increases, the amplitude of the perturbation decreases and moves to a lower frequency. Also, similar to the single frequency results of Fig. 10.17(a), the decrease in amplitude is nonlinear. For Fig. 10.18(b), the results are less clear. While it seems that the roughness elements are damping the third mode, the damping is not as large as the second mode. Part of this is due to the fact that the growth rate of the third mode is about one third of the second mode's growth rate. With this small of a growth rate, the third mode is not clearly the dominant

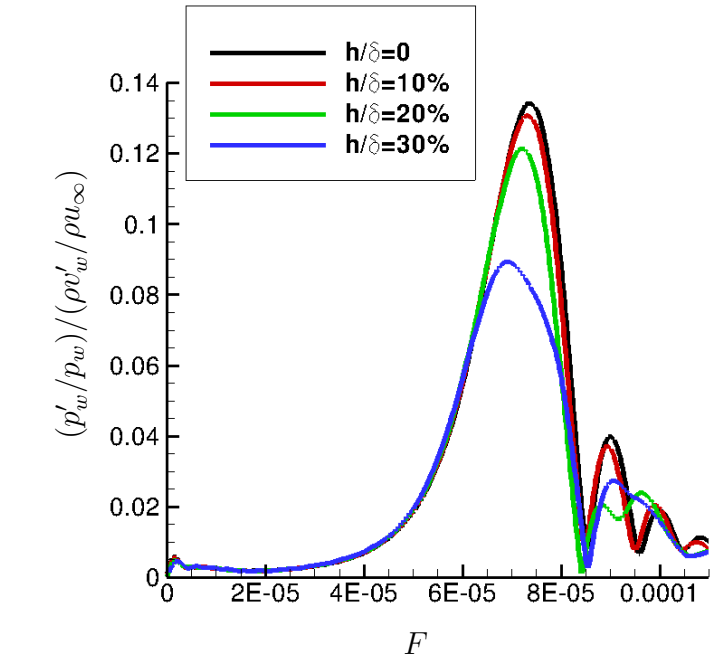

(a)

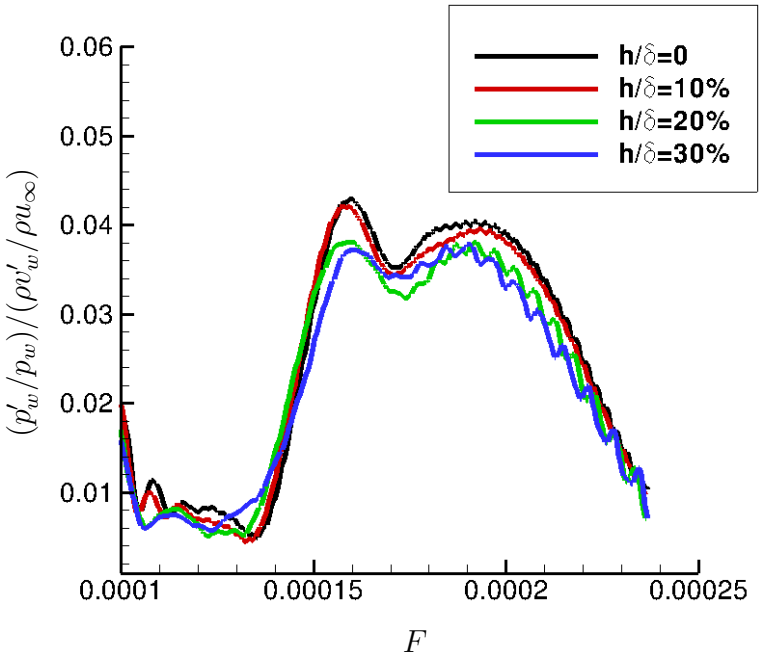

(b)

Figure 10.18: Wall-pressure perturbation for cases 11–14 at $R = 948$ over the frequency range of (a) the second mode and (b) the third mode.

instability mode over this frequency range. This is shown by the waviness in the wall-pressure perturbation. This waviness is not seen in Fig. 10.18(a) over the second mode frequency range.

The difference between the perfect gas and real gas cases at the frequencies $F = 4.73 \times 10^{-5}$ and $F = 7.09 \times 10^{-5}$ for the wall-pressure perturbation is shown in Fig. 10.19. It is interesting to note that either with or without a roughness element the ideal gas case has a larger amplitude at $R = 1100$ for $F = 4.73 \times 10^{-5}$. This is likely caused by the slightly thicker boundary layer for the perfect gas which causes the second-mode instability to move to a lower frequency range. However, this difference is minimal and the two gas models behave almost identically. For $F = 7.09 \times 10^{-5}$, the real gas perturbation is larger over the entire domain either with or without roughness.

Figure 10.20 shows a comparison of cases 11, 14, 15, and 18 at $R = 948$ for the second and third modes. The difference between cases 11 and 15, as well as the difference between cases 14 and 18, is the gas model. The difference between cases 11 and 14, as well as cases 15 and 18, is the roughness height. The percent difference of the maximum amplitude between cases 11 and 14 in Fig. 10.20(a) for the second mode is 40.0%. The percent difference of the maximum amplitude for the second mode between cases 15 and 18 is 34.9%. These differences are due solely to the damping effect of the roughness. Taking this information into account, it follows that the real-gas flow with a roughness element at $R = 948$ is damping the maximum second-mode instability 5.1% more than the corresponding perfect-gas flow. In other words, the real gas with roughness flow is more effective at damping the maximum second-mode instability than the corresponding perfect gas flow. There are a couple of possible explanations as to why the roughness element more effectively damps the second mode instability in the real-gas flow. Recall from Fig. 10.5(a) that the roughness element for case 14 significantly increases the vibration temperature moving it closer to equilibrium with the translation-rotation

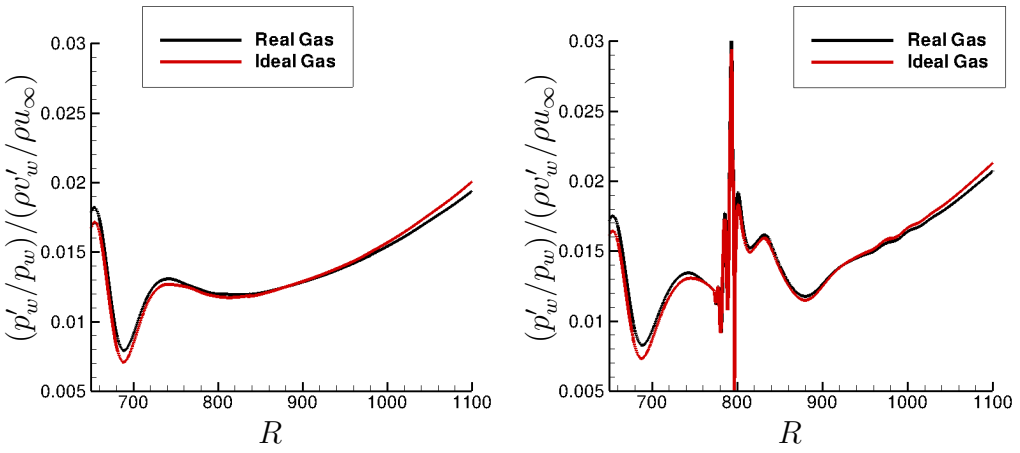

(a) $h/\delta = 0$, $F = 4.73 \times 10^{-5}$

(b) $h/\delta = 30\%$, $F = 4.73 \times 10^{-5}$

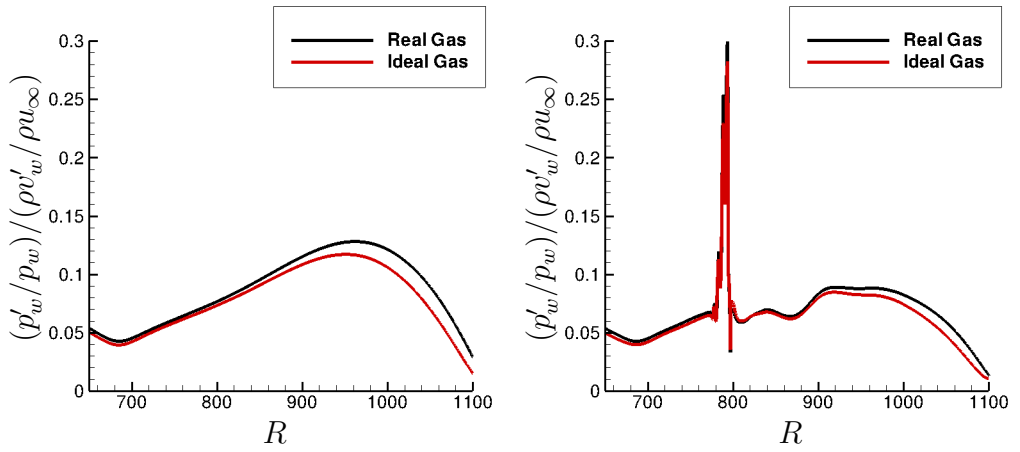

(c) $h/\delta = 0$, $F = 7.09 \times 10^{-5}$

(d) $h/\delta = 30\%$, $F = 7.09 \times 10^{-5}$

Figure 10.19: Comparison of the wall-pressure perturbation at two distinct frequencies.

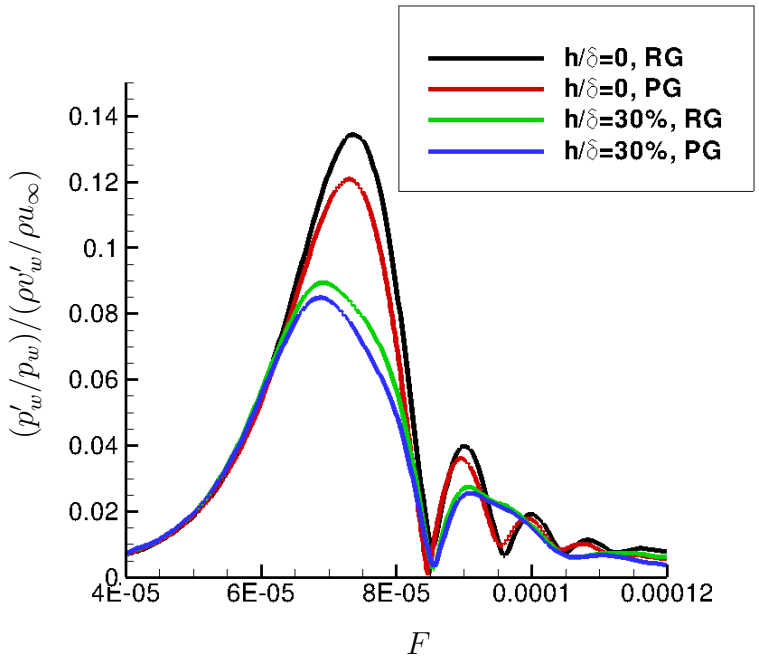

(a)

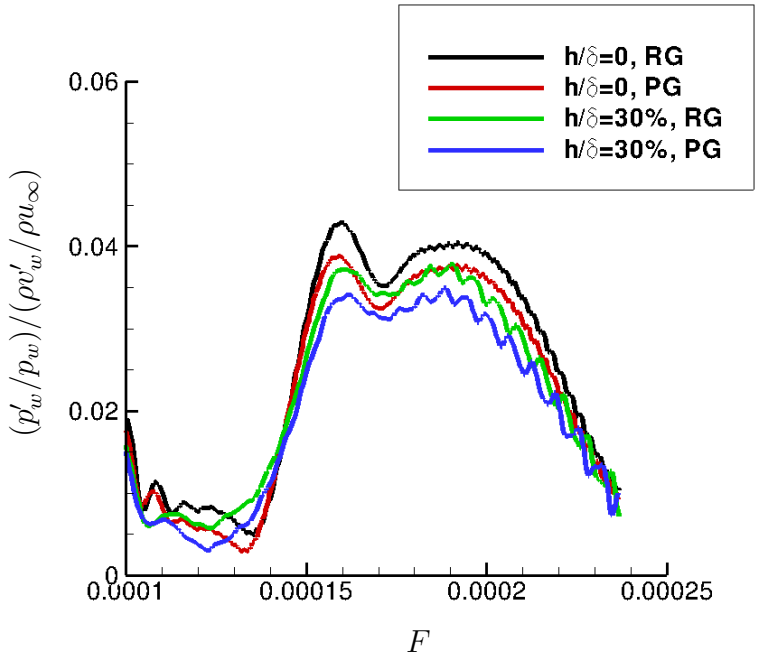

(b)

Figure 10.20: Comparison of the wall-pressure perturbation at $R = 948$ for cases 11, 14, 15, and 18 for (a) the second mode and (b) the third mode.

temperature. Also, recall from Fig. 10.6 that these increases in temperature cause oxygen in the real-gas flow to dissociate and form a larger amount of atomic oxygen. Both of these physical phenomena require a closer look to determine exactly what is responsible for the increased damping.

Recall from the discussion of Figs. 10.5(a) and 10.6 that the roughness element is moving the flow closer to thermal and chemical equilibrium. Also, in [Hud96] it was shown that an equilibrium flow, with the exact same flow conditions and geometry used in this work, had a more stable second mode than a corresponding thermochemical nonequilibrium flow. Therefore, for the geometry and flow conditions tested, it would seem that the roughness element serves to move the flow closer to thermal and chemical equilibrium which is stabilizing to the second mode. Note that this explanation applies to this case only, and is not generally applicable to all nonequilibrium flows. For example, in [Hud96] for a Mach 10 flow over a flat plate, the second mode instability was substantially damped by assuming a thermochemical nonequilibrium flow as compared to an equilibrium flow. It seems, for that situation, that the real-gas flow may damp the second mode less than the perfect gas flow as equilibrium would be destabilizing. Certainly, further test cases would be required to help elucidate these issues.

For the third mode region shown in Fig. 10.20(b), the results are different than the second mode. Both of the gas models damp the third mode the same amount and the stronger real gas stabilizing effects are not seen. The reasons for this are currently unclear. The third-mode instability may not be large enough to dominate other boundary-layer modes at the same frequency making the damping effects on only the third mode unclear. Also, it is possible that the third mode damping by surface roughness is truly unaffected by the gas model. Further study must be done to determine the cause.

CHAPTER 11

Summary and Future Work

11.1 Summary

The objectives of this research were to study the receptivity and instability of thermochemical nonequilibrium flows with: 1) the effects of surface ablation and 2) the effects of isolated two-dimensional surface roughness. To accomplish this, multiple flow configurations were analyzed using direct numerical simulation and linear stability theory.

To study the effects of surface ablation on boundary-layer receptivity and instability, a new high-order shock-fitting method for hypersonic flows with thermochemical nonequilibrium and graphite surface ablation was developed and validated. Also, a new linear stability theory code for thermochemical nonequilibrium flow with a linearized surface ablation model was developed and validated. An 11-species gas model without ionization was used for chemical nonequilibrium, and a two-temperature model was used for thermal nonequilibrium. The shock was treated using a shock-fitting formulation using the Rankine-Hugoniot jump conditions. The surface reactions simulated consisted of oxidation, recombination of atomic oxygen, and sublimation of C, C_2, and C_3.

Three cases with a spherical geometry were computed to validate the direct numerical simulation method. Two cases were taken from the PANT program with $M_\infty = 15.99$ where the shock-fitting results were compared to a code with similar gas and surface chemistry models. The third case was at $M_\infty = 5.84$, where

the shock-fitting results were compared to a code with different gas and surface chemistry models, as well as compared to corresponding experimental data. The two PANT cases showed that the shock-fitting method correctly simulated species mass concentrations in the flow, as well as translation-rotation and vibration temperatures. The comparison to the third case showed that the shock-fitting method was capable of accurately predicting surface mass flux due to graphite ablation. Overall, the new shock-fitting method compared well with established research codes.

Using the new validated high-order shock-fitting method, a direct numerical simulation was run for a 7 deg half angle blunt cone at Mach 15.99 to find how a real gas and graphite ablation affects boundary-layer receptivity and instability. Three separate cases were simulated in order to investigate real gas and graphite ablation effects. Fast acoustic freestream disturbances were used to perturb the steady base flow. The real gas simulation showed a strong second mode wave for the 525 kHz frequency. On the other hand, neither ideal gas simulation showed significant second mode growth for any of the simulated frequencies. Steady surface blowing was small and found to have a minimal effect for the simulated conditions. However, real-gas effects were found to significantly enhance boundary layer instability. The results show that real-gas effects for similar flow conditions should not be ignored.

The effects of surface ablation induced outgassing, in the absence of surface recession and roughness, on the instability of a real and ideal gas hypersonic boundary layer has been studied using linear stability theory. Before studying the instability physics, a new thermochemical nonequilibrium linear stability theory code with carbon species due to graphite ablation and a linearized surface model for graphite pseudo-ablation was developed and validated. The derivation of the linear stability theory coefficient matrices follows the work of Hudson. An eleven species gas model was used where five species model air and six more

species are used to model graphite ablation effects. A linearized surface model for graphite pseudo-ablation applicable to parallel and non-parallel flows was given. The derivative operators were discretized using Lagrange polynomials in physical space, where, for a five point stencil, the order of error was shown to be four. The code was then validated with results from a direct numerical simulation of flowfield disturbances over a blunt cone. The comparison of the eigenfunction amplitudes were good. As direct numerical simulation and linear stability theory are two dramatically different methods to analyze linear instabilities in a boundary layer, the good agreement obtained between the methods shows that they have been implemented correctly.

To study hypersonic boundary layer instability physics, multiple simulations were run for two separate geometries and freestream conditions. Five simulations were run for a 7 deg half angle blunt cone at Mach 15.99 and two simulations were run for a 5 deg half angle blunt cone at Mach 19.925. The meanflows, when applicable, had the same blowing and wall temperature profiles so that the effects of a real gas, blowing, and carbon species on hypersonic boundary-layer instability could be isolated and analyzed. N factors for different unstable frequencies and their corresponding growth rates were computed. For the first set of conditions, it was shown that changing the temperature perturbation boundary condition for an ablative flow has a strong effect on boundary-layer instability. For these freestream conditions, real gas effects are strongly destabilizing. The amplification rates are higher and the instability zones are longer for a real gas. The effects of carbon species on second-mode instability was slightly stabilizing when compared to a similar case with only five species air. Blowing was seen to be slightly destabilizing for a real gas but its effect was negligible on an ideal gas. As a consequence to these results, a real gas should be considered in transition prediction for vehicles with ablative surfaces. If a real gas was not considered, the estimated transition location may be severely overpredicted.

For the second set of conditions, inclusion of the ablating nose cone was shown to increase the region of second mode growth near the nose cone. Away from the nose cone, the second mode was relatively unaffected. It was shown that exclusion of the nose cone effects gives a reasonable estimate of the frequency that leads to transition and its N factor at transition for the given case.

To study the effects of two-dimensional surface roughness on suppression of the second mode in a thermochemical nonequilibrium flow, a new high-order shock-fitting direct simulation method for hypersonic flows with thermochemical non-equilibrium and arbitrary surface roughness was developed and validated. A set of five chemical species was used to model chemical nonequilibrium in air where a two-temperature model was used for thermal nonequilibrium. A cut-cell method was used to simulate arbitrary shaped surface roughness elements that cannot be simulated with a body conforming grid.

The cut-cell method validation was performed using a surface element that could be simulated with a body-fitted grid, or a cut-cell, grid. There was little noticeable difference in the wall-normal velocity and pressure contours between the two grid solutions. The percent difference in temperature profiles at three separate streamwise locations was less than 1% for each profile. Overall, the simulation of the flow on the cut-cell grid accurately compared to the simulation performed on the body-fitted grid, which showed that the implementation of the cut-cell method was valid.

Two separate meanflow conditions were used to study hypersonic boundary-layer instability in a real gas over a flat plate. For a Mach 10 flow, it was found that a roughness element placed downstream of the synchronization location of mode S and mode F stabilized the second mode. When the same roughness element was upstream of the synchronization location for a given frequency, the second mode was destabilized. These results are consistent with the results of previous researchers for a perfect gas.

For a Mach 15 flow, both real-gas and perfect-gas simulations were run with and without surface roughness. The real-gas flow with a roughness element resulted in a 40.0% reduction in the maximum amplitude of the second mode, where the perfect-gas flow with a roughness element resulted in a 34.9% reduction. The real-gas flow with a two-dimensional roughness element more effectively stabilized the second-mode instability when compared to a perfect-gas flow. Also, the third mode was found to be moderately stabilized by a roughness element for both a real-gas and a perfect-gas flow. The stronger stabilizing effect in a real gas was not visible for the third mode, instead, both gas models stabilized the third mode the same amount.

11.2 Future Work

For both DNS and LST codes, future work includes updating the gas phase chemistry models with up-to-date forward reaction rates and equilibrium constants. Also, a good next step would be to add a model for flow ionization.

For surface ablation, it would be useful to study how ablation affects boundary-layer transition on a shape similar to a reentry capsule, such as a sphere. The instabilities on blunt capsules that lead to transition, especially at an angle-of-attack, will likely be different than the second mode studied here.

To further understand how surface roughness affects second-mode instability in a real-gas boundary layer, it would be useful to use the new method described here to simulate a blunt geometry where real-gas effects are, in general, stronger. Specifically, it would be useful to use the Mach 10 flow conditions described here to study the flow over a blunted plate. The blunted plate should significantly alter the chemical composition of the flow, as compared to a perfect gas, hopefully revealing a more complete understanding of the effects on second-mode instability for a two-dimensional roughness element in a real-gas boundary layer.

APPENDIX A

Gas Model Constants

Constants for the gas model and surface chemistry model are given here. Constants for the forward rates in the dissociation reactions are given in Table A.1 and constants for the forward rates in the exchange reactions are given in Table A.2. The coefficients to compute the viscosity are given in Table A.3. The coefficients used to predict sublimation are given in Table A.4.

Table A.1: Dissociation reactions with corresponding forward reaction rate constants.

	Reaction	Partner	$C_f\left(\frac{\mathrm{m}^3}{\mathrm{mol\cdot s}}\right)$	η	θ_d (K)
1	$N_2+M \rightleftharpoons N+N+M$	all molecular species	3.70×10^{15}	-1.6	113200
		all atomic species	1.11×10^{16}	-1.6	113200
2	$O_2+M \rightleftharpoons O+O+M$	all molecular species	2.75×10^{13}	-1.0	59500
		all atomic species	8.25×10^{13}	-1.0	59500
3	$NO+M \rightleftharpoons N+O+M$	all molecular species	2.30×10^{11}	-0.5	75500
		all atomic species	4.60×10^{11}	-0.5	75500
4	$C_3+M \rightleftharpoons C_2+C+M$	all species	1.60×10^{10}	1.0	87480
5	$CO_2+M \rightleftharpoons CO+O+M$	all species	1.20×10^{5}	0.5	36850
6	$C_2+M \rightleftharpoons C+C+M$	all species	4.50×10^{12}	-1.0	70930
7	$CO+M \rightleftharpoons C+O+M$	all species	8.50×10^{13}	-1.0	129000
8	$CN+M \rightleftharpoons C+N+M$	all species	2.50×10^{8}	0.0	71000

* Reactions 1-3 from [Par85], 8 from [PHJ91], and 4-7 from [BL92].

Table A.2: Exchange reactions with corresponding forward reaction rate constants.

	Reaction	$C_f\left(\frac{\mathrm{m}^3}{\mathrm{mol\cdot s}}\right)$	η	θ_d (K)
9	$N_2+O \rightleftharpoons NO+N$	3.18×10^7	0.10	37700
10	$NO+O \rightleftharpoons N+O_2$	2.16×10^2	1.29	19220
11	$CO+O \rightleftharpoons C+O_2$	2.00×10^4	1.00	69500
12	$CN+O \rightleftharpoons NO+C$	1.60×10^7	0.10	14600
13	$CO_2+O \rightleftharpoons O_2+CO$	3.00×10^2	1.00	18210
14	$CO+C \rightleftharpoons C_2+O$	4.10×10^4	0.50	59790
15	$N_2+C \rightleftharpoons CN+N$	2.00×10^8	0.00	23200
16	$CN+C \rightleftharpoons C_2+N$	5.00×10^7	0.00	13000
17	$C_3+C \rightleftharpoons C_2+C_2$	1.70×10^3	1.50	19580
18	$CO+N \rightleftharpoons CN+O$	2.00×10^8	0.00	38600
19	$CO+N \rightleftharpoons NO+C$	9.00×10^{10}	-1.00	53200
20	$CO+CO \rightleftharpoons CO_2+C$	1.00×10^{-3}	2.00	72390
21	$C_2+CO \rightleftharpoons C_3+O$	1.20×10^7	0.00	43240
22	$CO+CO \rightleftharpoons C_2+O_2$	9.20×10^5	0.75	163300
23	$CO+NO \rightleftharpoons CO_2+N$	1.00×10^{-3}	2.00	20980
24	$N_2+O_2 \rightleftharpoons NO+NO$	6.69×10^3	-2.54	64639

* Reactions 9,10, and 24 are from [Par85], reactions 12, 16, and 18 from [PHJ91], and the remaining reactions are from [BL92].

Table A.3: Species viscosity coefficients.

species	A_s^μ	B_s^μ	C_s^μ
N_2	0.0268142	0.3177838	-11.3155513
O_2	0.0449290	-0.0826158	-9.2019475
NO	0.0436378	-0.0335511	-9.5767430
C_3	-0.0147000	0.8811000	-13.5051000
CO_2	-0.0195274	1.0478180	-14.3221200
C_2	-0.0031000	0.6920000	-12.6127000
CO	-0.0195274	1.0132950	-13.9787300
CN	-0.0025000	0.6810000	-12.4914000
N	0.0115572	0.6031679	-12.4327495
O	0.0203144	0.4294404	-11.6031403
C	-0.0001000	0.7928000	-13.4154000

Table A.4: Sublimation reaction probabilities and vapor pressure coefficients.

	α_s	P_s	Q_s
C	0.14	-85715	18.69
C_2	0.26	-98363	22.20
C_3	0.03	-93227	23.93

* α_s from [PM68] and P_s and Q_s [DMG68].

The elements of the Jacobian matrix ($\frac{\partial F_i}{\partial x_j}$) used to solve the nonlinear system of equations for the surface chemistry model at each grid point at the surface is given here. The derivatives have been discretized using a Lagrange polynomial as defined in Eq. (2.64).

$$\frac{\partial F_i}{\partial x_j} = \frac{1}{\rho}\left(\delta_{ij} - c_i\right)\left(\dot{m} - \rho D_i A_1\right) + c_i \sum_{l=1}^{ns} \frac{\partial \dot{m}_l}{\partial \rho_j} - \frac{\partial \dot{m}_i}{\partial \rho_j} - \left(D_i + \rho \frac{\partial D_i}{\partial \rho_j}\right) \sum_{Q=1}^{N} A_Q c_{i,Q},$$

$$i = 1, 2, \ldots, ns-1 \quad j = 1, 2, \ldots, ns \quad \text{(A.1)}$$

$$\frac{\partial F_i}{\partial x_j} = c_i \sum_{l=1}^{ns} \frac{\partial \dot{m}_l}{\partial T} - \rho \frac{\partial D_i}{\partial T} \sum_{Q=1}^{N} A_Q c_{i,Q} - \frac{\partial \dot{m}_i}{\partial T},$$

$$i = 1, 2, \ldots, ns-1 \quad j = ns+1 \quad \text{(A.2)}$$

$$\frac{\partial F_i}{\partial x_j} = -\frac{R}{M_j} T, \qquad i = ns \quad j = 1, 2, \ldots, ns \quad \text{(A.3)}$$

$$\frac{\partial F_i}{\partial x_j} = -\sum_{s=1}^{ns} \rho_s \frac{R}{M_s}, \qquad i = 1, 2, \ldots, ns-1 \quad j = ns+1 \quad \text{(A.4)}$$

$$\frac{\partial F_i}{\partial x_j} = \frac{\partial k}{\partial \rho_j} \sum_{Q=1}^{N} A_Q T_Q + \frac{\partial k_V}{\partial \rho_j} \sum_{Q=1}^{N} A_Q T_{V,Q} + \sum_{s=1}^{ns} h_s D_s \left(\sum_{Q=1}^{N} A_Q c_{s,Q}\right)$$
$$+ \rho \sum_{s=1}^{ns} h_s \frac{\partial D_s}{\partial \rho_j} \left(\sum_{Q=1}^{N} A_Q c_{s,Q}\right) + A_1 \sum_{s=1}^{ns} h_s D_s \left(\delta_{sj} - c_s\right) - \sum_{l=1}^{ns} \frac{\partial \dot{m}_l}{\partial \rho_j} \sum_{s=1}^{ns} c_s h_{s,o}$$
$$- \frac{\dot{m}}{\rho} \sum_{s=1}^{ns} \left(\delta_{sj} - c_s\right) h_{s,o} - \dot{m} \sum_{s=1}^{ns} c_s \frac{\partial h_{s,o}}{\partial \rho_j},$$

$$i = ns+1 \quad j = 1, 2, \ldots, ns \quad \text{(A.5)}$$

$$\frac{\partial F_i}{\partial x_j} = \frac{\partial k}{\partial T} \sum_{Q=1}^{N} A_Q T_Q + \frac{\partial k_V}{\partial T} \sum_{Q=1}^{N} A_Q T_{V,Q} + A_1 \left(k + k_V\right) + \rho \sum_{s=1}^{ns} \frac{\partial h_s}{\partial T} D_s \left(\sum_{Q=1}^{N} A_Q c_{s,Q}\right)$$
$$+ \rho \sum_{s=1}^{ns} h_s \frac{\partial D_s}{\partial T} \left(\sum_{Q=1}^{N} A_Q c_{s,Q}\right) - 4\sigma\epsilon T^3 - \sum_{l=1}^{ns} \frac{\partial \dot{m}_l}{\partial T} \sum_{s=1}^{ns} c_s h_{s,o} - \dot{m} \sum_{s=1}^{ns} c_s \frac{\partial h_{s,o}}{\partial T},$$

$$i = ns+1 \quad j = ns+1 \quad \text{(A.6)}$$

APPENDIX B

Complex Matrix Coefficients for LST

The nonzero elements of each complex matrix for the nonequilibrium linear stability theory perturbation equations are given along with the equation itself for reference. Here $\vec{\phi} = (\hat{\rho}_1, \hat{\rho}_2, \ldots, \hat{\rho}_{ns}, \hat{u}, \hat{v}, \hat{w}, \hat{T}, \hat{T}_v)^T$, δ_{ij} is the Kronecker delta and all i and j subscripts run from $1, 2, \ldots, ns$ where ns is the number of species. The bars on the steady state variables have been dropped for simplicity. Grid transformation effects are included yielding

$$\alpha_0 = \frac{\alpha}{h_1}$$
$$\beta_0 = \frac{\beta}{h_3}$$
$$m_{11} = \frac{1}{h_1}\frac{\partial h_1}{\partial y}$$
$$m_{13} = \frac{1}{h_1 h_3}\frac{\partial h_3}{\partial x}$$
$$m_{33} = \frac{1}{h_3}\frac{\partial h_3}{\partial y}.$$

$$\left(\mathbf{A}\frac{d^2}{dy^2} + \mathbf{B}\frac{d}{dy} + \mathbf{C}\right)\vec{\phi} = \vec{0}$$

$$A_{ij} = D_i\left(c_i - \delta_{ij}\right)$$

$$A_{ns+1,ns+1} = 1$$

$$A_{ns+2,ns+2} = 1$$

$$A_{ns+3,ns+3} = 1$$

$$A_{ns+4,j} = \sum_{s=1}^{ns} h_s D_s c_s - h_j D_j$$

$$A_{ns+4,ns+4} = -k$$

$$A_{ns+4,ns+5} = -k_V$$

$$A_{ns+5,j} = \sum_{s=1}^{ns} e_{vs} D_s c_s - e_{vj} D_j$$

$$A_{ns+5,ns+5} = -k_V$$

$$B_{ij} = -\left[\rho \frac{d}{dy}\left(\frac{D_i}{\rho}\right) + \left(m_{11} + m_{33}\right) D_i\right] \delta_{ij} + \rho \frac{d}{dy}\left(D_i \frac{c_i}{\rho}\right)$$

$$+ \left(c_i \frac{d\rho}{dy} - \frac{d\rho_i}{dy}\right) \frac{\partial D_i}{\partial \rho_j} + \left(m_{11} + m_{33}\right) D_i c_i$$

$$B_{i,ns+2} = \rho_i$$

$$B_{i,ns+4} = \left(c_i \frac{d\rho}{dy} - \frac{d\rho_i}{dy}\right) \frac{\partial D_i}{\partial T}$$

$$B_{ns+1,j} = \frac{1}{\mu} \frac{\partial \mu}{\partial \rho_j} \left(\frac{du}{dy} - u m_{11}\right)$$

$$B_{ns+1,ns+1} = \frac{1}{\mu} \frac{d\mu}{dy} + m_{11} + m_{33}$$

$$B_{ns+1,ns+2} = \alpha_0 \left(i \frac{1}{3}\right)$$

$$B_{ns+1,ns+4} = \frac{1}{\mu} \frac{\partial \mu}{\partial T} \left(\frac{du}{dy} - u m_{11}\right)$$

$$B_{ns+2,j} = -\frac{3}{4\mu} \frac{R}{M_j} T - \frac{1}{2} \frac{u}{\mu} m_{13} \frac{\partial \mu}{\partial \rho_j}$$

$$B_{ns+2,ns+1} = \alpha_0 \left(\frac{1}{4} i\right) + \frac{1}{4} m_{13}$$

$$B_{ns+2,ns+2} = \frac{1}{\mu} \frac{d\mu}{dy} + m_{11} + m_{33}$$

$$B_{ns+2,ns+3} = \frac{1}{4} \beta_0 i$$

$$B_{ns+2,ns+4} = -\frac{3}{4\mu} \frac{P}{T} - \frac{1}{2} \frac{u}{\mu} m_{13} \frac{\partial \mu}{\partial T}$$

$$B_{ns+3,ns+2} = \frac{1}{3} \beta_0 i$$

$$B_{ns+3,ns+3} = \frac{1}{\mu} \frac{d\mu}{dy} + m_{11} + m_{33}$$

$$B_{ns+4,j} = -\frac{dT}{dy} \frac{\partial k}{\partial \rho_j} - \frac{dT_V}{dy} \frac{\partial k_V}{\partial \rho_j} + \rho \frac{d}{dy} \left[\frac{1}{\rho} \left(\sum_{s=1}^{ns} h_s D_s c_s - h_j D_j\right)\right]$$

$$+ \sum_{s=1}^{ns} h_s \left(c_s \frac{d\rho}{dy} - \frac{d\rho_s}{dy}\right) \frac{\partial D_s}{\partial \rho_j} + \left(m_{11} + m_{33}\right) \left(\sum_{s=1}^{ns} h_s D_s c_s - h_j D_j\right)$$

$$B_{ns+4,ns+1} = 2\mu \left(u m_{11} - \frac{du}{dy}\right)$$

$$B_{ns+4,ns+2} = P + T\sum_{s=1}^{ns}\rho_s c_{v,s} + \sum_{s=1}^{ns}\rho_s e_{vs} + \sum_{s=1}^{ns}\rho_s h_s^o + \tfrac{4}{3}\mu u m_{13}$$

$$B_{ns+4,ns+4} = -\tfrac{dT}{dy}\tfrac{\partial k}{\partial T} - \tfrac{dk}{dy} - \tfrac{dT_V}{dy}\tfrac{\partial k_V}{\partial T} + \sum_{s=1}^{ns} h_s\left(c_s\tfrac{d\rho}{dy} - \tfrac{d\rho_s}{dy}\right)\tfrac{\partial D_s}{\partial T}$$

$$-\left(m_{11}+m_{33}\right)k + \sum_{s=1}^{ns} D_s\left(c_s\tfrac{d\rho}{dy} - \tfrac{d\rho_s}{dy}\right)\left(c_{v,s} + \tfrac{R}{M_s}\right)$$

$$B_{ns+4,ns+5} = -\tfrac{dT_V}{dy}\tfrac{\partial k_V}{\partial T_V} - \tfrac{dk_V}{dy} + \sum_{s=1}^{ns} D_s\left(c_s\tfrac{d\rho}{dy} - \tfrac{d\rho_s}{dy}\right)\tfrac{\partial e_{vs}}{\partial T_V} - \left(m_{11}+m_{33}\right)k_V$$

$$B_{ns+5,j} = -\tfrac{dT_V}{dy}\tfrac{\partial k_V}{\partial \rho_j} + \rho\tfrac{d}{dy}\left[\tfrac{1}{\rho}\left(\sum_{s=1}^{ns} e_{vs}D_s c_s - e_{vj}D_j\right)\right]$$

$$+\sum_{s=1}^{ns} e_{vs}\left(c_s\tfrac{d\rho}{dy} - \tfrac{d\rho_s}{dy}\right)\tfrac{\partial D_s}{\partial \rho_j} + \left(m_{11}+m_{33}\right)\left(\sum_{s=1}^{ns} e_{vs}D_s c_s - e_{vj}D_j\right)$$

$$B_{ns+5,ns+2} = \sum_{s=1}^{ns}\rho_s e_{vs}$$

$$B_{ns+5,ns+4} = -\tfrac{dT_V}{dy}\tfrac{\partial k_V}{\partial T} + \sum_{s=1}^{ns} e_{vs}\left(c_s\tfrac{d\rho}{dy} - \tfrac{d\rho_s}{dy}\right)\tfrac{\partial D_s}{\partial T}$$

$$B_{ns+5,ns+5} = -\tfrac{dk_V}{dy} - \tfrac{dT_V}{dy}\tfrac{\partial k_V}{\partial T_V} + \sum_{s=1}^{ns} D_s\left(c_s\tfrac{d\rho}{dy} - \tfrac{d\rho_s}{dy}\right)\tfrac{\partial e_{vs}}{\partial T_V} - \left(m_{11}+m_{33}\right)k_V$$

$$C_{ij} = \Big[i\left(\alpha_0 u - \omega - m_{13}\alpha_0 D_i\right) + D_i\left(\alpha_0^2+\beta_0^2\right) + \tfrac{d}{dy}\left(\tfrac{D_i}{\rho}\tfrac{d\rho}{dy}\right) + m_{13}u$$

$$+\left(m_{11}+m_{33}\right)\tfrac{D_i}{\rho}\tfrac{d\rho}{dy}\Big]\delta_{ij} + i\alpha_0 m_{13}D_i c_i - \tfrac{d}{dy}\left(D_i\tfrac{c_i}{\rho}\tfrac{d\rho}{dy}\right) - D_i c_i\left(\alpha_0^2+\beta_0^2\right) -$$

$$\tfrac{\partial \omega_i}{\partial \rho_j} + \tfrac{d}{dy}\left[\left(c_i\tfrac{d\rho}{dy} - \tfrac{d\rho_i}{dy}\right)\tfrac{\partial D_i}{\partial \rho_j}\right] + \left(m_{11}+m_{33}\right)\left[\left(c_i\tfrac{d\rho}{dy} - \tfrac{d\rho_i}{dy}\right)\tfrac{\partial D_i}{\partial \rho_j} - D_i\tfrac{c_i}{\rho}\tfrac{d\rho}{dy}\right]$$

$$C_{i,ns+1} = \alpha_0\left(i\rho_i\right) + m_{13}\rho_i$$

$$C_{i,ns+2} = \tfrac{d\rho_i}{dy} + \left(m_{11}+m_{33}\right)\rho_i$$

$$C_{i,ns+3} = i\beta_0\rho_i$$

$$C_{i,ns+4} = -\tfrac{\partial \omega_i}{\partial T} + \tfrac{d}{dy}\left[\left(c_i\tfrac{d\rho}{dy} - \tfrac{d\rho_i}{dy}\right)\tfrac{\partial D_i}{\partial T}\right] + \left(m_{11}+m_{33}\right)\left(c_i\tfrac{d\rho}{dy} - \tfrac{d\rho_i}{dy}\right)\tfrac{\partial D_i}{\partial T}$$

$$C_{i,ns+5} = -\tfrac{\partial \omega_i}{\partial T_v}$$

$$C_{ns+1,j} = \tfrac{1}{\mu}\tfrac{d}{dy}\left(\tfrac{du}{dy}\tfrac{\partial \mu}{\partial \rho_j}\right) - \alpha_0\left(i\tfrac{1}{\mu}\tfrac{R}{M_j}T\right) - \tfrac{d}{dy}\left(\tfrac{\partial \mu}{\partial \rho_j}\right)\tfrac{u}{\mu}m_{11}$$

$$+\tfrac{\partial \mu}{\partial \rho_j}\left[-i\alpha_0\tfrac{2}{3}\tfrac{u}{\mu}m_{13} + \left(m_{11}+m_{33}\right)\tfrac{1}{\mu}\tfrac{du}{dy} - \tfrac{u}{\mu}\left(m_{11}^2 + m_{11}m_{33} + \tfrac{4}{3}m_{13}^2\right)\right]$$

$$C_{ns+1,ns+1} = i\left(\tfrac{\omega\rho}{\mu}\right) - \beta_0^2 - \tfrac{4}{3}\alpha_0^2 + \alpha_0 i\left(\tfrac{4}{3}m_{13} - \tfrac{\rho u}{\mu}\right)$$

$$-m_{11}\left(\frac{1}{\mu}\frac{\partial\mu}{\partial y}+m_{11}+m_{33}\right)-\frac{4}{3}m_{13}^2$$

$$C_{ns+1,ns+2}=\alpha_0 i\left(\frac{7}{3}m_{11}+\frac{1}{3}m_{33}+\frac{1}{\mu}\frac{d\mu}{dy}\right)-\frac{\rho}{\mu}\left(um_{11}+\frac{du}{dy}\right)$$

$$-\frac{4}{3}m_{13}m_{33}+2m_{13}m_{11}$$

$$C_{ns+1,ns+3}=-\alpha_0\left(\frac{1}{3}\beta_0\right)-i\frac{7}{3}\beta_0 m_{13}$$

$$C_{ns+1,ns+4}=\frac{1}{\mu}\frac{d}{dy}\left(\frac{du}{dy}\frac{\partial\mu}{\partial T}\right)-\alpha_0 i\left(\frac{1}{\mu}\frac{P}{T}\right)-\frac{d}{dy}\left(\frac{\partial\mu}{\partial T}\right)\frac{u}{\mu}m_{11}$$

$$+\frac{\partial\mu}{\partial T}\left[-i\alpha_0\frac{2}{3}\frac{u}{\mu}m_{13}+\left(m_{11}+m_{33}\right)\frac{1}{\mu}\frac{du}{dy}-\frac{u}{\mu}\left(m_{11}^2+m_{11}m_{33}+\frac{4}{3}m_{13}^2\right)\right]$$

$$C_{ns+2,j}=-\frac{3}{4\mu}\frac{R}{M_j}\frac{dT}{dy}+\frac{3}{4}m_{11}\frac{u^2}{\mu}+\alpha_0 i\left(\frac{du}{dy}-m_{11}u\right)\frac{3}{4\mu}\frac{\partial\mu}{\partial\rho_j}-\frac{1}{2}\frac{u}{\mu}m_{13}\frac{d}{dy}\left(\frac{\partial\mu}{\partial\rho_j}\right)$$

$$+\frac{\partial\mu}{\partial\rho_j}\frac{m_{13}}{\mu}\left(\frac{1}{4}\frac{du}{dy}-\frac{1}{4}m_{11}u-m_{33}u\right)$$

$$C_{ns+2,ns+1}=-\alpha_0 i\left(\frac{1}{2\mu}\frac{d\mu}{dy}+\frac{7}{4}m_{11}\right)+\frac{3}{2}m_{11}\frac{\rho u}{\mu}-m_{13}\left(\frac{1}{4}m_{11}+m_{33}+\frac{1}{2\mu}\frac{d\mu}{dy}\right)$$

$$C_{ns+2,ns+2}=i\frac{3}{4\mu}\omega\rho-\frac{3}{4}\left(\alpha_0^2+\beta_0^2\right)+\alpha_0 i\left(\frac{3}{4}m_{13}-\frac{3}{4\mu}\rho u\right)$$

$$-\frac{1}{2\mu}\frac{d\mu}{dy}\left(m_{11}+m_{33}\right)-m_{11}^2-m_{33}^2$$

$$C_{ns+2,ns+3}=-i\beta_0\left(\frac{1}{2\mu}\frac{d\mu}{dy}+\frac{7}{4}m_{33}\right)$$

$$C_{ns+2,ns+4}=-\frac{3}{4\mu}\frac{d}{dy}\left(\frac{P}{T}\right)+\alpha_0 i\left(\frac{du}{dy}-m_{11}u\right)\frac{3}{4\mu}\frac{\partial\mu}{\partial T}-\frac{1}{2}\frac{u}{\mu}m_{13}\frac{d}{dy}\left(\frac{\partial\mu}{\partial T}\right)$$

$$+\frac{\partial\mu}{\partial T}\frac{m_{13}}{\mu}\left(\frac{1}{4}\frac{du}{dy}-\frac{1}{4}m_{11}u-m_{33}u\right)$$

$$C_{ns+3,j}=i\frac{\beta_0}{\mu}\left(\frac{4}{3}um_{13}\frac{\partial\mu}{\partial\rho_j}-\frac{R}{M_j}T\right)$$

$$C_{ns+3,ns+1}=-\alpha_0\left(\frac{1}{3}\beta_0\right)+i\frac{7}{3}\beta_0 m_{13}$$

$$C_{ns+3,ns+2}=i\beta_0\left(\frac{1}{\mu}\frac{d\mu}{dy}+\frac{7}{3}m_{33}+\frac{1}{3}m_{11}\right)$$

$$C_{ns+3,ns+3}=i\frac{\rho\omega}{\mu}-\frac{4}{3}\beta_0^2-\alpha_0^2-\alpha_0 i\left(\frac{\rho u}{\mu}-m_{13}\right)-\frac{\rho u}{\mu}m_{13}-m_{13}^2-\frac{1}{\mu}\frac{d\mu}{dy}m_{33}-$$

$$m_{33}^2-m_{11}m_{33}$$

$$C_{ns+3,ns+4}=i\frac{\beta_0}{\mu}\left(\frac{4}{3}um_{13}\frac{\partial\mu}{\partial T}-\frac{P}{T}\right)$$

$$C_{ns+4,j}=i\alpha_0\left[u\left(Tc_{v,j}+e_{vj}+h_j^o\right)+m_{13}\left(\sum_{s=1}^{ns}h_sD_sc_s-h_jD_j\right)\right]$$

$$-i\omega\left(Tc_{v,j}+e_{vj}+h_j^o\right)-\frac{d}{dy}\left(\frac{dT}{dy}\frac{\partial k}{\partial\rho_j}\right)-\frac{d}{dy}\left(\frac{dT_V}{dy}\frac{\partial k_V}{\partial\rho_j}\right)+\frac{d}{dy}\left(D_jh_j\frac{1}{\rho}\frac{d\rho}{dy}\right)+$$

$$\frac{\partial\mu}{\partial\rho_j}\left[-\left(\frac{du}{dy}\right)^2+2u\frac{du}{dy}m_{11}-\frac{4}{3}u^2m_{13}-u^2m_{11}^2\right]-\sum_{s=1}^{ns}h_sD_sc_s\left(\alpha_0^2+\beta_0^2\right)+$$
$$h_jD_j\left(\alpha_0^2+\beta_0^2\right)-\sum_{s=1}^{ns}\frac{d}{dy}\left(h_sD_s\frac{c_s}{\rho}\frac{d\rho}{dy}\right)+\sum_{s=1}^{ns}\frac{d}{dy}\left(h_s\left(c_s\frac{d\rho}{dy}-\frac{d\rho_s}{dy}\right)\frac{\partial D_s}{\partial\rho_j}\right)+$$
$$(m_{11}+m_{33})\left[\sum_{s=1}^{ns}h_s\left(c_s\frac{d\rho}{dy}-\frac{d\rho_s}{dy}\right)\frac{\partial D_s}{\partial\rho_j}+\frac{1}{\rho}\frac{d\rho}{dy}\left(h_jD_j-\sum_{s=1}^{ns}h_sD_sc_s\right)\right.$$
$$\left.-\frac{dT}{dy}\frac{\partial k}{\partial\rho_j}-\frac{dT_V}{dy}\frac{\partial k_V}{\partial\rho_j}\right]+m_{13}u\left(Tc_{v,j}+e_{vj}+h_j^o+\frac{R}{M_j}T\right)$$
$$C_{ns+4,ns+1}=i\alpha_0\left(p+T\sum_{s=1}^{ns}\rho_sc_{v,s}+\sum_{s=1}^{ns}\rho_se_{vs}+\sum_{s=1}^{ns}\rho_sh_s^o+\frac{4}{3}\mu um_{13}\right)+$$
$$m_{13}\left(p+T\sum_{s=1}^{ns}\rho_sc_{v,s}+\sum_{s=1}^{ns}\rho_se_{vs}+\sum_{s=1}^{ns}\rho_sh_s^o\right)$$
$$+2\mu\left(\frac{du}{dy}m_{11}-\frac{4}{3}um_{13}^2-um_{11}^2\right)$$
$$C_{ns+4,ns+2}=i\alpha_0\left[2\mu\left(um_{11}-\frac{du}{dy}\right)\right]+\frac{d}{dy}\left(\sum_{s=1}^{ns}\rho_sc_{v,s}T\right)+\sum_{s=1}^{ns}\frac{d}{dy}\left(\rho_se_{vs}\right)+$$
$$\sum_{s=1}^{ns}\frac{d\rho_s}{dy}h_s^o+(m_{11}+m_{33})\left(p+T\sum_{s=1}^{ns}\rho_sc_{v,s}+\sum_{s=1}^{ns}\rho_se_{vs}+\sum_{s=1}^{ns}\rho_sh_s^o\right)$$
$$+\frac{4}{3}\mu um_{13}\left(m_{11}-2m_{33}\right)$$
$$C_{ns+4,ns+3}=i\beta_0\left(p+T\sum_{s=1}^{ns}\rho_sc_{v,s}+\sum_{s=1}^{ns}\rho_se_{vs}+\sum_{s=1}^{ns}\rho_sh_s^o-\frac{8}{3}\mu um_{13}\right)$$
$$C_{ns+4,ns+4}=-i\omega\sum_{s=1}^{ns}\rho_sc_{v,s}+i\alpha_0\left(u\sum_{s=1}^{ns}\rho_sc_{v,s}-m_{13}k\right)$$
$$+m_{13}u\left(\sum_{s=1}^{ns}\rho_sc_{v,s}+\frac{p}{T}\right)+k\left(\alpha_0^2+\beta_0^2\right)-\frac{d}{dy}\left(\frac{dT}{dy}\frac{\partial k}{\partial T}\right)-\frac{d}{dy}\left(\frac{dT_V}{dy}\frac{\partial k_V}{\partial T}\right)+$$
$$\frac{\partial\mu}{\partial T}\left[2u\frac{du}{dy}m_{11}-\left(\frac{du}{dy}\right)^2-u^2m_{11}^2-\frac{4}{3}u^2m_{13}\right]$$
$$+\sum_{s=1}^{ns}\frac{d}{dy}\left(h_s\left(c_s\frac{d\rho}{dy}-\frac{d\rho_s}{dy}\right)\frac{\partial D_s}{\partial T}\right)+\sum_{s=1}^{ns}\left(c_{v,s}+\frac{R}{M_s}\right)\frac{d}{dy}\left(D_s\left(c_s\frac{d\rho}{dy}-\frac{d\rho_s}{dy}\right)\right)+$$
$$(m_{11}+m_{33})\left[\sum_{s=1}^{ns}h_s\left(c_s\frac{d\rho}{dy}-\frac{d\rho_s}{dy}\right)\frac{\partial D_s}{\partial T}+\sum_{s=1}^{ns}\left(c_{v,s}+\frac{R}{M_s}\right)D_s\left(c_s\frac{d\rho}{dy}-\frac{d\rho_s}{dy}\right)\right.$$
$$\left.-\frac{dT}{dy}\frac{\partial k}{\partial T}-\frac{dT_V}{dy}\frac{\partial k_V}{\partial T}\right]$$
$$C_{ns+4,ns+5}=-i\omega\sum_{s=1}^{ns}\rho_s\frac{\partial e_{vs}}{\partial T_V}+i\alpha_0\left(u\sum_{s=1}^{ns}\rho_s\frac{\partial e_{vs}}{\partial T_V}-m_{13}k_V\right)$$
$$+m_{13}u\sum_{s=1}^{ns}\rho_s\frac{\partial e_{vs}}{\partial T_V}+k_V\left(\alpha_0^2+\beta_0^2\right)-\frac{d}{dy}\left(\frac{dT_V}{dy}\frac{\partial k_V}{\partial T_V}\right)$$

$$+\sum_{s=1}^{ns}\frac{d}{dy}\left(D_s\left(c_s\frac{d\rho}{dy}-\frac{d\rho_s}{dy}\right)\frac{\partial e_{vs}}{\partial T_V}\right)$$
$$+(m_{11}+m_{33})\left[\sum_{s=1}^{ns}D_s\left(c_s\frac{d\rho}{dy}-\frac{d\rho_s}{dy}\right)\frac{\partial e_{vs}}{\partial T_v}-\frac{dT_V}{dy}\frac{\partial k_V}{\partial T_V}\right]$$
$$C_{ns+5,j}=i\left[\alpha_0 u e_{vj}-\omega e_{vj}+m_{13}\alpha_0\left(\sum_{s=1}^{ns}e_{vs}D_s c_s-e_{vj}D_j\right)\right]$$
$$-\frac{d}{dy}\left(\frac{dT_V}{dy}\frac{\partial k_V}{\partial\rho_j}\right)-\frac{\partial Q_{TV}}{\partial\rho_j}-\sum_{s=1}^{ns}e_{vs}\frac{\partial\omega_s}{\partial\rho_j}+\left(e_{vj}D_j-\sum_{s=1}^{ns}e_{vs}D_s c_s\right)\left(\alpha_0^2+\beta_0^2\right)+$$
$$\frac{d}{dy}\left(e_{vj}D_j\frac{1}{\rho}\frac{d\rho}{dy}\right)-\sum_{s=1}^{ns}\frac{d}{dy}\left(e_{vs}D_s\frac{c_s}{\rho}\frac{d\rho}{dy}\right)+\sum_{s=1}^{ns}\frac{d}{dy}\left(e_{vs}\left(c_s\frac{d\rho}{dy}-\frac{d\rho_s}{dy}\right)\frac{\partial D_s}{\partial\rho_j}\right)+$$
$$m_{13}u e_{vj}+(m_{11}+m_{33})$$
$$\left(e_{vj}D_j\frac{d\rho}{dy}\frac{1}{\rho}-\sum_{s=1}^{ns}e_{vs}D_s\frac{d\rho}{dy}\frac{c_s}{\rho}-\frac{dT_V}{dy}\frac{\partial k_V}{\partial\rho_j}+\sum_{s=1}^{ns}e_{vs}\left(c_s\frac{d\rho}{dy}-\frac{d\rho_s}{dy}\right)\frac{\partial D_s}{\partial\rho_j}\right)$$
$$C_{ns+5,ns+1}=i\alpha_0\sum_{s=1}^{ns}\rho_s e_{vs}+m_{13}\sum_{s=1}^{ns}\rho_s e_{vs}$$
$$C_{ns+5,ns+2}=\frac{d}{dy}\left(\sum_{s=1}^{ns}\rho_s e_{vs}\right)+(m_{11}+m_{33})\sum_{s=1}^{ns}\rho_s e_{vs}$$
$$C_{ns+5,ns+3}=i\beta_0\sum_{s=1}^{ns}\rho_s e_{vs}$$
$$C_{ns+5,ns+4}=-\frac{d}{dy}\left(\frac{dT_v}{dy}\frac{\partial k_V}{\partial T}\right)-\frac{\partial Q_{TV}}{\partial T}-\sum_{s=1}^{ns}e_{vs}\frac{\partial\omega_s}{\partial T}$$
$$+\sum_{s=1}^{ns}\frac{d}{dy}\left(e_{vs}\left(c_s\frac{d\rho}{dy}-\frac{d\rho_s}{dy}\right)\frac{\partial D_s}{\partial T}\right)$$
$$+(m_{11}+m_{33})\left[\sum_{s=1}^{ns}e_{vs}\left(c_s\frac{d\rho}{dy}-\frac{d\rho_s}{dy}\right)\frac{\partial D_s}{\partial T}-\frac{dT_V}{dy}\frac{\partial k_V}{\partial T}\right]$$
$$C_{ns+5,ns+5}=i\left(\alpha_0 u\sum_{s=1}^{ns}\rho_s\frac{\partial e_{vs}}{\partial T_V}-\omega\sum_{s=1}^{ns}\rho_s\frac{\partial e_{vs}}{\partial T_V}-m_{13}\alpha_0 k_V\right)$$
$$+k_V\left(\alpha_0^2+\beta_0^2\right)-\frac{d}{dy}\left(\frac{dT_V}{dy}\frac{\partial k_V}{\partial T_V}\right)-\frac{\partial Q_{TV}}{\partial T_V}-\sum_{s=1}^{ns}e_{vs}\frac{\partial\omega_s}{\partial T_V}-\sum_{s=1}^{ns}\omega_s\frac{\partial e_{vs}}{\partial T_V}$$
$$+\sum_{s=1}^{ns}\frac{d}{dy}\left(D_s\left(c_s\frac{d\rho}{dy}-\frac{d\rho_s}{dy}\right)\frac{\partial e_{vs}}{\partial T_V}\right)+m_{13}u\sum_{s=1}^{ns}\rho_s\frac{\partial e_{vs}}{\partial T_V}$$
$$+(m_{11}+m_{33})\left[\sum_{s=1}^{ns}D_s\left(c_s\frac{d\rho}{dy}-\frac{d\rho_s}{dy}\right)\frac{\partial e_{vs}}{\partial T_V}-\frac{dT_v}{dy}\frac{\partial k_V}{\partial T_V}\right]$$

APPENDIX C

Partial Derivatives

Partial derivatives are required in solution of the surface chemistry boundary conditions, as well as in LST. The partial derivatives used in these methods are given here.

Chemical Source Term Partial Derivatives

For the chemical source terms

$$\omega_s' = \sum_{r=1}^{ns} \frac{\partial \omega_s}{\partial \rho_r} \rho_r' + \frac{\partial \omega_s}{\partial T} T' + \frac{\partial \omega_s}{\partial T_V} T_V'. \tag{C.1}$$

A generic partial derivative of the chemical source term may be written as

$$\frac{\partial \omega_s}{\partial x} = M_s \left(\sum_c \frac{\partial R_c}{\partial x} \right) \tag{C.2}$$

where each of the reactions R_c for the given chemical source term are included, and x is either ρ_s, T, or T_V.

For each of the dissociation reactions,

$$\begin{aligned} \frac{\partial R_c}{\partial \rho_r} = \sum_{s=1}^{ns} \Bigg[& -k_{f,c,s} \left(\frac{\rho_c}{M_c} \frac{\delta_{sr}}{M_s} + \frac{\rho_s}{M_s} \frac{\delta_{cr}}{M_c} \right) \\ & + k_{b,c,s} \left(\frac{\rho_{p_1}}{M_{p_1}} \frac{\rho_{p_2}}{M_{p_2}} \frac{\delta_{sr}}{M_s} + \frac{\rho_{p_1}}{M_{p_1}} \frac{\rho_s}{M_s} \frac{\delta_{p_2 r}}{M_{p_2}} + \frac{\rho_{p_2}}{M_{p_2}} \frac{\rho_s}{M_s} \frac{\delta_{p_1 r}}{M_{p_1}} \right) \Bigg] \end{aligned} \tag{C.3}$$

$$\frac{\partial R_c}{\partial T} = \sum_{s=1}^{ns} \left[-\frac{\rho_c}{M_c} \frac{\rho_s}{M_s} \frac{\partial k_{f,c,s}}{\partial T} + \frac{\rho_{p_1}}{M_{p_1}} \frac{\rho_{p_2}}{M_{p_2}} \frac{\rho_s}{M_s} \frac{\partial k_{b,c,s}}{\partial T} \right] \tag{C.4}$$

$$\frac{\partial R_c}{\partial T_V} = \sum_{s=1}^{ns} -\frac{\rho_c}{M_c} \frac{\rho_s}{M_s} \frac{\partial k_{f,c,s}}{\partial T_V} \tag{C.5}$$

where for reactions 1–3

$$\frac{\partial k_{f,c,s}}{\partial T} = \frac{k_{f,c,s}}{2T}\left(\eta_{f,c,s} + \frac{\theta_{f,c,s}}{(TT_V)^{1/2}}\right) \tag{C.6}$$

$$\frac{\partial k_{f,c,s}}{\partial T_V} = \frac{k_{f,c,s}}{2T_V}\left(\eta_{f,c,s} + \frac{\theta_{f,c,s}}{(TT_V)^{1/2}}\right) \tag{C.7}$$

$$\frac{\partial k_{b,c,s}}{\partial T} = \frac{k_{b,c,s}}{T}\left(\eta_{f,c,s} + \frac{\theta_{f,c,s}}{T} - \frac{A_{1c}}{Z} + A_{3c} + A_{4c}Z + 2A_{5c}Z^2\right) \tag{C.8}$$

and for reactions 4–8

$$\frac{\partial k_{f,c,s}}{\partial T} = \frac{k_{f,c,s}}{T}\left(\eta_{f,c,s} + \frac{\theta_{f,c,s}}{T}\right) \tag{C.9}$$

$$\frac{\partial k_{f,c,s}}{\partial T_V} = 0 \tag{C.10}$$

$$\frac{\partial k_{b,c,s}}{\partial T} = \frac{k_{b,c,s}}{T}\left[\eta_{f,c,s} + \frac{\theta_{f,c,s}}{T} + \Delta n + T\frac{\partial}{\partial T}\left(\frac{G^{p_1}}{RT} + \frac{G^{p_2}}{RT} - \frac{G^{r_1}}{RT} - \frac{G^{r_2}}{RT}\right)\right] \tag{C.11}$$

where

$$T\frac{\partial}{\partial T}\left(\frac{G^o}{RT}\right) = -a_1 - \frac{a_2}{2}T - \frac{a_3}{3}T^2 - \frac{a_4}{4}T^3 - \frac{a_5}{5}T^4 - \frac{a_6}{T}. \tag{C.12}$$

Similarly, for each of the exchange reactions,

$$\frac{\partial R_c}{\partial \rho_r} = -k_{f,c}\left(\frac{\rho_{r_1}}{M_{r_1}}\frac{\delta_{r_2 r}}{M_{r_2}} + \frac{\rho_{r_2}}{M_{r_2}}\frac{\delta_{r_1 r}}{M_{r_1}}\right) + k_{b,c}\left(\frac{\rho_{p_1}}{M_{p_1}}\frac{\delta_{p_2 r}}{M_{p_2}} + \frac{\rho_{p_2}}{M_{p_2}}\frac{\delta_{p_1 r}}{M_{p_1}}\right) \tag{C.13}$$

$$\frac{\partial R_c}{\partial T} = -\frac{\rho_{r_1}}{M_{r_1}}\frac{\rho_{r_2}}{M_{r_2}}\frac{\partial k_{f,c}}{\partial T} + \frac{\rho_{p_1}}{M_{p_1}}\frac{\rho_{p_2}}{M_{p_2}}\frac{\partial k_{b,c}}{\partial T} \tag{C.14}$$

$$\frac{\partial R_c}{\partial T_V} = 0 \tag{C.15}$$

$$\frac{\partial k_{f,c}}{\partial T} = \frac{k_{f,c}}{T}\left(\eta_{f,c} + \frac{\theta_{f,c}}{T}\right) \tag{C.16}$$

where for reactions 9,10

$$\frac{\partial k_{b,c}}{\partial T} = \frac{k_{b,c}}{T}\left(\eta_{f,c} + \frac{\theta_{f,c}}{T} - \frac{A_{1c}}{Z} + A_{3c} + A_{4c}Z + 2A_{5c}Z^2\right) \tag{C.17}$$

and for each of the remaining exchange reactions

$$\frac{\partial k_{b,c}}{\partial T} = \frac{k_{b,c}}{T}\left[\eta_{f,c} + \frac{\theta_{f,c}}{T} + \Delta n + T\frac{\partial}{\partial T}\left(\frac{G^{p_1}}{RT} + \frac{G^{p_2}}{RT} - \frac{G^{r_1}}{RT} - \frac{G^{r_2}}{RT}\right)\right]. \tag{C.18}$$

Transport Properties

$$\frac{\partial \mu}{\partial \rho_s} = \sum_{r=1}^{ns} \frac{\mu_r}{\phi_r} \left(\frac{\partial X_r}{\partial \rho_s} - \frac{X_r}{\phi_r} \frac{\partial \phi_r}{\partial \rho_s} \right) \tag{C.19}$$

$$\frac{\partial X_r}{\partial \rho_s} = \frac{1}{M_r} \left(\sum_{n=1}^{ns} \frac{\rho_n}{M_n} \right)^{-1} \left[\delta_{sr} - \frac{\rho_r}{M_s} \left(\sum_{n=1}^{ns} \frac{\rho_n}{M_n} \right)^{-1} \right] \tag{C.20}$$

$$\frac{\partial \phi_r}{\partial \rho_s} = \sum_{n=1}^{ns} \left[\left(8 \left(1 + \frac{M_r}{M_n} \right) \right)^{1/2} \right]^{-1} \left[1 + \left(\frac{M_n}{M_r} \right)^{1/4} \left(\frac{\mu_r}{\mu_n} \right)^{1/2} \right]^2 \frac{\partial X_n}{\partial \rho_s} \tag{C.21}$$

$$\frac{\partial \mu}{\partial T} = \sum_{r=1}^{ns} \frac{X_r}{\phi_r} \left(\frac{\partial \mu_r}{\partial T} - \frac{\mu_r}{\phi_r} \frac{\partial \phi_r}{\partial T} \right) \tag{C.22}$$

$$\frac{\partial \mu_r}{\partial T} = \frac{\mu_r}{T} \left(2A_r \ln T + B_r \right) \tag{C.23}$$

$$\frac{\partial \phi_r}{\partial T} = \sum_{s=1}^{ns} X_s \left[\sqrt{8 \left(1 + \frac{M_r}{M_s} \right)} \right]^{-1} \left[1 + \left(\frac{M_s}{M_r} \right)^{1/4} \sqrt{\frac{\mu_r}{\mu_s}} \right] \left(\frac{M_s}{M_r} \right)^{1/4} \left(\frac{\mu_r}{\mu_s} \right)^{1/2} \left(\frac{1}{\mu_r} \frac{\partial \mu_r}{\partial T} - \frac{1}{\mu_s} \frac{\partial \mu_s}{\partial T} \right) \tag{C.24}$$

$$\frac{\partial D_r}{\partial \rho_s} = \frac{2}{\rho} \left(\frac{\partial \mu}{\partial \rho_s} - \frac{\mu}{\rho} \right) \tag{C.25}$$

$$\frac{\partial D}{\partial T} = \frac{2}{\rho} \frac{\partial \mu}{\partial T} \tag{C.26}$$

$$\frac{\partial k}{\partial \rho_s} = \sum_{r=1}^{ns} \frac{k_r}{\phi_r} \left(\frac{\partial X_r}{\partial \rho_s} - \frac{X_r}{\phi_r} \frac{\partial \phi_r}{\partial \rho_s} \right) \tag{C.27}$$

$$\frac{\partial k}{\partial T} = \sum_{r=1}^{ns} \left(\frac{5}{2} c_{v,tr,r} + c_{v,rot,r} \right) \frac{X_r}{\phi_r} \left(\frac{\partial \mu_r}{\partial T} - \frac{\mu_r}{\phi_r} \frac{\partial \phi_r}{\partial T} \right) \tag{C.28}$$

$$\frac{\partial k_V}{\partial \rho_s} = \sum_{r=1}^{nms} \frac{k_{v,r}}{\phi_r} \left(\frac{\partial X_r}{\partial \rho_s} - \frac{X_r}{\phi_r} \frac{\partial \phi_r}{\partial \rho_s} \right) \tag{C.29}$$

$$\frac{\partial k_V}{\partial T} = \sum_{r=1}^{nms} \frac{de_{v,r}}{dT_V} \frac{X_r}{\phi_r} \left(\frac{\partial \mu_r}{\partial T} - \frac{\mu_r}{\phi_r} \frac{\partial \phi_r}{\partial T} \right) \tag{C.30}$$

$$\frac{\partial k_V}{\partial T_V} = \sum_{s=1}^{nms} \frac{X_s}{\phi_s} \mu_s \frac{d^2 e_{v,s}}{dT_V^2} \tag{C.31}$$

$$\frac{d^2 e_{v,s}}{dT_V^2} = \frac{R}{M_s} \left(\frac{\theta_{v,s}}{T_V} \right)^2 \frac{\exp\left(\theta_{v,s}/T_V\right)}{T_V \left(\exp\left(\theta_{v,s}/T_V\right) - 1 \right)^2} \left[2 \frac{\theta_{v,s}}{T_V} \frac{\exp\left(\theta_{v,s}/T_V\right)}{\exp\left(\theta_{v,s}/T_V\right) - 1} - 2 - \frac{\theta_{v,s}}{T_V} \right] \tag{C.32}$$

Vibration-Translation Source Term

$$\frac{\partial Q_{T-V}}{\partial \rho_s} = \frac{e_{v,s}\left(T\right) - e_{v,s}\left(T_V\right)}{\tau_s} - \sum_{r=1}^{nms} \rho_r \frac{e_{v,r}\left(T\right) - e_{v,r}\left(T_V\right)}{\tau_r^2} \frac{\partial \tau_r}{\partial \rho_s} \tag{C.33}$$

$$\frac{\partial \tau_r}{\partial \rho_s} = \frac{\tau_r}{M_s \sum\limits_{n=1}^{ns} \rho_n / M_n} \left(1 - \frac{\tau_r}{\tau_{rs}}\right) - \tau_r \frac{TR}{pM_s} \tag{C.34}$$

$$\frac{\partial Q_{T-V}}{\partial T} = \sum_{s=1}^{nms} \frac{\rho_s}{\tau_s} \left(\frac{\partial e_{v,s}\left(T\right)}{\partial T} - \frac{e_{v,s}\left(T\right) - e_{v,s}\left(T_V\right)}{\tau_s} \frac{\partial \tau_s}{\partial T} \right) \tag{C.35}$$

$$\frac{\partial e_{v,s}\left(T\right)}{\partial T} = \frac{R}{M_s} \exp\left(\theta_{v,s}/T\right) \left(\frac{\theta_{v,s}/T}{\exp\left(\theta_{v,s}/T\right) - 1} \right)^2 \tag{C.36}$$

$$\frac{\partial \tau_s}{\partial T} = \frac{-\tau_s^2}{\sum\limits_{n=1}^{ns} \rho_n / M_n} \left[\frac{T^{-4/3}}{3} \sum_{r=1}^{ns} \frac{\rho_r A_{sr}}{M_r \tau_{sr}} + \left(\frac{R}{p} \sum_{n=1}^{ns} \frac{\rho_n}{M_n} \right) \left(\sum_{r=1}^{ns} \frac{\rho_r}{M_r \tau_{sr}} \right) \right] \tag{C.37}$$

$$\frac{\partial Q_{T-V}}{\partial T_V} = -\sum_{s=1}^{nms} \frac{\rho_s}{\tau_s} \frac{\partial e_{v,s}\left(T_V\right)}{\partial T_V} \tag{C.38}$$

Chemical Production Terms

Derivatives of the chemical production terms are required to set the surface conditions for ablation, as well as to set the perturbation conditions at the surface in the linearized ablation model. The derivatives of the sublimation terms with respect to wall temperature are

$$\frac{\partial \dot{m}_{C_3}}{\partial T} = -\frac{\dot{m}_{C_3}}{2T} - \alpha_{C_3} \sqrt{\frac{M_{C_3}}{2\pi RT}} \left(p_{v,C_3} \frac{P_{C_3}}{T^2} \right) \tag{C.39}$$

$$\frac{\partial \dot{m}_{C_2}}{\partial T} = -\frac{\dot{m}_{C_2}}{2T} - \alpha_{C_2} \sqrt{\frac{M_{C_2}}{2\pi RT}} \left(p_{v,C_2} \frac{P_{C_2}}{T^2} \right) \tag{C.40}$$

$$\frac{\partial \dot{m}_{C}}{\partial T} = -\frac{\dot{m}_{C}}{2T} - \alpha_{C} \sqrt{\frac{M_{C}}{2\pi RT}} \left(p_{v,C} \frac{P_{C}}{T^2} \right). \tag{C.41}$$

Since each of the partial pressures in Eqs. (2.51)–(2.53) are taken at the first grid point away from the surface, the chemical production terms due to sublimation are only a function of the wall temperature.

The remaining partial derivatives of the chemical production terms are

$$\frac{\partial \dot{m}_{O_2}}{\partial \rho_{O_2}} = -k_1 \tag{C.42}$$

$$\frac{\partial \dot{m}_{O_2}}{\partial \rho_O} = k_3 \tag{C.43}$$

$$\frac{\partial \dot{m}_{O_2}}{\partial T} = -\rho_{O_2}\frac{\partial k_1}{\partial T} + \rho_O \frac{\partial k_3}{\partial T} \tag{C.44}$$

$$\frac{\partial \dot{m}_{CO}}{\partial \rho_{O_2}} = \frac{M_{CO}}{M_{O_2}} k_1 \tag{C.45}$$

$$\frac{\partial \dot{m}_{CO}}{\partial \rho_O} = \frac{M_{CO}}{M_O} k_2 \tag{C.46}$$

$$\frac{\partial \dot{m}_{CO}}{\partial T} = \rho_{O_2}\frac{M_{CO}}{M_{O_2}}\frac{\partial k_1}{\partial T} + \rho_O \frac{M_{CO}}{M_O}\frac{\partial k_2}{\partial T} \tag{C.47}$$

$$\frac{\partial \dot{m}_O}{\partial \rho_{O_2}} = \frac{1}{2} k_1 \tag{C.48}$$

$$\frac{\partial \dot{m}_O}{\partial \rho_O} = -k_2 - k_3 \tag{C.49}$$

$$\frac{\partial \dot{m}_O}{\partial T} = \rho_{O_2}\frac{1}{2}\frac{\partial k_1}{\partial T} - \rho_O \left(\frac{\partial k_2}{\partial T} + \frac{\partial k_3}{\partial T}\right) \tag{C.50}$$

where

$$\frac{\partial k_1}{\partial T} = \frac{k_1}{2T}\left(1 + \frac{2T}{\alpha_1}\frac{\partial \alpha_1}{\partial T}\right) \tag{C.51}$$

$$\frac{\partial k_2}{\partial T} = \frac{k_2}{2T}\left(1 + \frac{2320}{T}\right) \tag{C.52}$$

$$\frac{\partial k_3}{\partial T} = \frac{k_3}{2T}\left(1 + \frac{2320}{T}\right) \tag{C.53}$$

and

$$\frac{\partial \alpha_1}{\partial T} = \frac{14.5\exp\left(-1450/T\right) + 2.6\alpha_1 \exp\left(13000/T\right)}{T^2\left[1 + 2\times 10^{-4}\exp\left(13000/T\right)\right]}. \tag{C.54}$$

Conservative to Nonconservative Jacobian

When treating the source term implicitly, a nonlinear solver is required. The nonlinear solver requires the derivative $\partial W/\partial U$ to obtain a solution. However, the derivatives of the source terms were given in terms of the nonconservative variables, rather than the conserved variables. It is possible to take derivatives of

source terms, transport properties, etc., with respect to the conserved variables. However, that complicated task can be easily avoided noting that

$$\frac{\partial W}{\partial U} = \frac{\partial V}{\partial U}\frac{\partial W}{\partial V} \tag{C.55}$$

where

$$V = (\rho_1, \rho_2, \ldots, \rho_{ns}, u_1, u_2, u_3, T, T_V)^T . \tag{C.56}$$

The resulting Jacobian is

$$\frac{\partial V}{\partial U} = \begin{bmatrix} 1 & 0 & \cdots & 0 & 0 & 0 & 0 & 0 & 0 \\ 0 & 1 & \cdots & 0 & 0 & 0 & 0 & 0 & 0 \\ \vdots & \vdots & \ddots & \vdots & 0 & 0 & 0 & 0 & 0 \\ 0 & 0 & \cdots & 1 & 0 & 0 & 0 & 0 & 0 \\ -\frac{u_1}{\rho} & -\frac{u_1}{\rho} & \cdots & -\frac{u_1}{\rho} & \frac{1}{\rho} & 0 & 0 & 0 & 0 \\ -\frac{u_2}{\rho} & -\frac{u_2}{\rho} & \cdots & -\frac{u_2}{\rho} & 0 & \frac{1}{\rho} & 0 & 0 & 0 \\ -\frac{u_3}{\rho} & -\frac{u_3}{\rho} & \cdots & -\frac{u_3}{\rho} & 0 & 0 & \frac{1}{\rho} & 0 & 0 \\ \frac{\partial T}{\partial \rho_1} & \frac{\partial T}{\partial \rho_2} & \cdots & \frac{\partial T}{\partial \rho_{ns}} & \frac{-u_1}{\kappa} & \frac{-u_2}{\kappa} & \frac{-u_3}{\kappa} & \frac{1}{\kappa} & \frac{-1}{\kappa} \\ \frac{\partial T_V}{\partial \rho_1} & \frac{\partial T_V}{\partial \rho_2} & \cdots & \frac{\partial T_V}{\partial \rho_{ns}} & 0 & 0 & 0 & 0 & \frac{\partial T_V}{\partial \rho e_v} \end{bmatrix} \tag{C.57}$$

where

$$\frac{\partial T}{\partial \rho_s} = \frac{\frac{u_i u_i}{2} - h_s^o - T c_{v,s}}{\sum_{r=1}^{ns} \rho_r c_{v,r}} \tag{C.58}$$

$$\kappa = \sum_{s=1}^{ns} \rho_s c_{v,s} \tag{C.59}$$

$$\frac{\partial T_V}{\partial \rho_1} = e_{v,s}\frac{\partial T_V}{\partial \rho e_v} \tag{C.60}$$

$$\frac{\partial T_V}{\partial \rho e_v} = \frac{1}{\sum_{s=1}^{nms} \rho_s \frac{\partial e_{v,s}}{\partial T_V}}. \tag{C.61}$$

APPENDIX D

Cut-Cell Derivative Coefficients

The third-order coefficients for a first-order derivative near a boundary using the cut-cell method are given. The inviscid coefficients are given in Table D.1 and the viscous coefficients are given in Table D.2.

Table D.1: Finite-difference coefficients for inviscid terms at irregular points.

	$a^+_{j,1}$	$a^+_{j,2}$	$a^+_{j,3}$	$a^+_{j,4}$	$a^+_{j,5}$	$a^+_{j,6}$
j=2	$\frac{-2}{\sigma(\sigma+1)(\sigma+2)}$	$\frac{2-3\sigma}{2\sigma}$	$\frac{2\sigma}{\sigma+1}$	$\frac{-\sigma}{2(2+\sigma)}$	0	0
j=3	$\frac{1}{\sigma(1+\sigma)(2+\sigma)}$	$\frac{-\sigma-1}{2\sigma}$	$\frac{1}{1+\sigma}$	$\frac{\sigma+1}{2(2+\sigma)}$	0	0
j=4	$\frac{-2}{\sigma(\sigma+1)(\sigma+2)(\sigma+3)}$	$\frac{2+\sigma}{6\sigma}$	$\frac{-2-\sigma}{\sigma+1}$	$\frac{4+\sigma}{2(2+\sigma)}$	$\frac{2+\sigma}{3(3+\sigma)}$	0
	$a^-_{j,1}$	$a^-_{j,2}$	$a^-_{j,3}$	$a^-_{j,4}$	$a^-_{j,5}$	$a^-_{j,6}$
j=2	0	$-\frac{11}{6}$	3	$-\frac{3}{2}$	$\frac{1}{3}$	0
j=3	0	$-\frac{1}{3}$	$-\frac{1}{2}$	1	$-\frac{1}{6}$	0
j=4	0	$\frac{1}{12}$	$-\frac{2}{3}$	0	$\frac{2}{3}$	$-\frac{1}{12}$

Table D.2: Finite-difference coefficients for viscous terms at irregular points.

	$a_{j,1}$	$a_{j,2}$	$a_{j,3}$	$a_{j,4}$	$a_{j,5}$	$a_{j,6}$
j=1	$\frac{-2(2\sigma+3)\left(\sigma^2+3\sigma+1\right)}{\sigma(\sigma+1)(\sigma+2)(\sigma+3)}$	$\frac{(\sigma+1)(\sigma+2)(\sigma+3)}{6\sigma}$	$\frac{-\sigma(\sigma+2)(\sigma+3)}{2(\sigma+1)}$	$\frac{\sigma(\sigma+1)(\sigma+3)}{2(\sigma+2)}$	$\frac{-\sigma(\sigma+1)(\sigma+2)}{6(\sigma+3)}$	0
j=2	$\frac{-6}{\sigma(\sigma+1)(\sigma+2)(\sigma+3)}$	$\frac{6-11\sigma}{6\sigma}$	$\frac{3\sigma}{\sigma+1}$	$\frac{-3\sigma}{2(\sigma+2)}$	$\frac{\sigma}{3(\sigma+3)}$	0
j=3	$\frac{2}{\sigma(\sigma+1)(\sigma+2)(\sigma+3)}$	$\frac{-\sigma-1}{3\sigma}$	$\frac{1-\sigma}{2(\sigma+1)}$	$\frac{\sigma+1}{\sigma+2}$	$\frac{-\sigma-1}{6(\sigma+3)}$	0
j=4	$\frac{-4}{\sigma(\sigma+1)(\sigma+2)(\sigma+3)(\sigma+4)}$	$\frac{\sigma+2}{12\sigma}$	$\frac{-2(\sigma+2)}{3(\sigma+1)}$	$\frac{1}{2+\sigma}$	$\frac{2(\sigma+2)}{3(\sigma+3)}$	$\frac{-\sigma-2}{12(\sigma+4)}$

References

[AAB13] A. Anna, H. Alkandry, and I. Boyd. "Computational Modeling of Gas-Surface Interactions for High-Enthalpy Reacting Flows." *AIAA paper 2013-0187*, 2013.

[ABB99] E. Anderson, Z. Bai, C. Bischof, S. Blackford, J. Demmel, J. Dongarra, J. Du Croz, A. Greenbaum, S. Hammarling, A. McKenney, and D. Sorensen. *LAPACK Users' Guide*. Society for Industrial and Applied Mathematics, Philadelphia, PA, third edition, 1999.

[AH97] P. Adam and H. Hornung. "Enthalpy Effects on Hypervelocity Boundary-Layer Transition: Ground Test and Flight Data." *Journal of Spacecraft and Rockets*, **34**(5):614–619, 1997.

[Bak77] R. Baker. "Graphite Sublimation Chemistry Nonequilibrium Effects." *AIAA Journal*, **15**(10):1391–1397, 1977.

[BC06] J. Bertin and R. Cummings. "Critical Hypersonic Aerothermodynamic Phenomena." *Annual Review of Fluid Mechanics*, **38**:129–157, 2006.

[BCM13] D. Bountin, T. Chimitov, A. Maslov, A. Novikov, I. Egorov, A. Fedorov, and S. Utyuzhnikov. "Stabilization of a Hypersonic Boundary Layer Using a Wavy Surface." *AIAA Journal*, **51**(5):1203–1210, 2013.

[BJE71] F. Blottner, M. Johnson, and M. Ellis. "Chemically Reacting Gas Viscous Flow Program for Multi-Component Gas Mixtures." SC-RR-70-754, Sandia National Laboratories, 1971.

[BL92] B. Bhutta and C. Lewis. "Low-to-High Altitude Predictions of Three-Dimensional Ablative Reentry Flowfields." *AIAA 92-0366*, 1992.

[Can90] G. Candler. "Computation of Thermo-Chemical Nonequilibrium Martian Atmospheric Entry Flow." *AIAA 90-1695*, 1990.

[Cha04] C-L. Chang. "Langley Stability and Transition Analysis Code (LASTRAC) Version 1.2 User Manual." NASA TM-2004-213233, NASA, 2004.

[CM05a] Y.-K. Chen and F. Milos. "Navier-Stokes Solutions with Finite Rate Ablation for Planetary Mission Earth Reentries." *Journal of Spacecraft and Rockets*, **42**(6):961–970, 2005.

[CM05b] Y.-K. Chen and F. Milos. "Three-Dimensional Ablation and Thermal Response Simulation System." *AIAA paper 2005-5064*, 2005.

[CN10] O. Cabrit and F. Nicoud. "Direct numerical simulation of a reacting turbulent channel flow with thermo-chemical ablation." *Journal of Turbulence*, **11**:1–33, 2010.

[CRH71] H. Carter, J. Raper, W. Hinson, and W. Morris. "Basic Measurements from a Turbulent-Heating Flight Experiment on a 5° Half-Angle Cone at Mach 20 (Reentry F)." NASA TM X-2308, NASA, 1971.

[CVM97] C. Chang, H. Vinh, and M. Malik. "Hypersonic Boundary-Layer Stability with Chemical Reactions using PSE." *AIAA 1997-2012*, 1997.

[DM11] D. Driver and M. MacLean. "Improved Predictions of PICA Recession in Arc Jet Shear Tests." *AIAA paper 2011-141*, 2011.

[DMG68] T. Dolton, R. Maurer, and H. Goldstein. "Thermodynamic Performance of Carbon in Hyperthermal Environments." *AIAA 68-754*, 1968.

[DWZ10] L. Duan, X. Wang, and X. Zhong. "A high-order cut-cell method for numerical simulation of hypersonic boundary-layer instability with surface roughness." *Journal of Computational Physics*, **229**(19):7207–7237, 2010.

[DWZ13] L. Duan, X. Wang, and X. Zhong. "Stabilization of a Mach 5.92 Boundary Layer by Two-Dimensional Finite-Height Roughness." *AIAA Journal*, **51**(1):266–270, 2013.

[Fed11] A. Fedorov. "Transition and Stability of High-Speed Boundary Layers." *Annual Review of Fluid Mechanics*, **43**:79–95, 2011.

[Fuj06] K. Fujii. "Experiment of the Two-Dimensional Roughness Effect on Hypersonic Boundary-Layer Transition." *Journal of Spacecraft and Rockets*, **43**(4):731–738, 2006.

[FWH15] K. Fong, X. Wang, Y. Huang, X. Zhong, G. McKiernan, R. Fisher, and S. Schneider. "Second Mode Suppression in Hypersonic Boundary Layer by Roughness: Design and Experiments." to appear in *AIAA Journal*, 2015.

[FWZ13] K. Fong, X. Wang, and X. Zhong. "Stabilization of Hypersonic Boundary Layer by 2-D Surface Roughness." *AIAA 2013-2985*, 2013.

[FWZ14] K. Fong, X. Wang, and X. Zhong. "Numerical simulation of roughness effect on the stability of a hypersonic boundary layer." *Computers & Fluids*, **96**(13):350–367, 2014.

[FWZ15] K. Fong, X. Wang, and X. Zhong. "Parametric Study on Stabilization of Hypersonic Boundary-Layer Waves Using 2-D Surface Roughness." *AIAA 2015-0837*, 2015.

[GLS90] R. Gupta, K. Lee, and K. Sutton. "Viscous-Shock-Layer Solutions with Coupled Radiation and Ablation Injection for Earth Entry." *AIAA 90-1697*, 1990.

[GMI10] S. Ghaffari, O. Marxen, G. Iaccarino, and E. Shaqfeh. "Numerical Simulations of Hypersonic Boundary-layer Instability with Wall Blowing." *AIAA 2010-706*, 2010.

[Gre14] P. Greene. *Numerical Simulations of High-Speed Flows Over Complex Geometries*. PhD thesis, University of California Los Angeles, 2014.

[HCC97] M. Hudson, N. Chokani, and G. Candler. "Linear Stability of Hypersonic Flow in Thermochemical Nonequilibrium." *AIAA Journal*, **35**(6):958–964, 1997.

[How71] F. Howard. "Thermal Analysis Methods and Basic Heat-Transfer Data for a Turbulent Heating Flight Experiment at Mach 20 (Reentry F)." TM X-2282, NASA, 1971.

[HS64] P. Holloway and J. Sterrett. "Effect of Controlled Surface Roughness on Boundary-Layer Transition and Heat Transfer at Mach Numbers of 4.8 and 6.0." TN-D-2054, NASA, 1964.

[Hud96] M. Hudson. *Linear Stability Theory of Hypersonic, Chemically Reacting Viscous Flow*. PhD thesis, North Carolina State University, 1996.

[JC05] H. Johnson and G. Candler. "Hypersonic Boundary Layer Stability Analysis Using PSE-Chem." *AIAA 2005-5023*, 2005.

[JGC09] H. Johnson, J. Gronvall, and G. Candler. "Reacting Hypersonic Boundary Layer Stability with Blowing and Suction." *AIAA 2009-938*, 2009.

[Joh00] H. Johnson. *Thermochemical Interactions in Hypersonic Boundary Layer Stability*. PhD thesis, University of Minnesota, 2000.

[JSC98] H. Johnson, T. Seipp, and G. Candler. "Numerical study of hypersonic reacting boundary layer transition on cones." *Physics of Fluids*, **10**(10):2676–2685, 1998.

[JSW72] C. Johnson, P. Stainback, K. Wicker, and L. Bony. "Boundary-Layer Edge Conditions and Transition Reynolds Number Data for a Flight Test at Mach 20 (Reentry F)." NASA TM X-2584, NASA, 1972.

[Kaa78] G. Kaattari. "Effects of Mass Addition on Blunt-Body Boundary Layer Transition and Heat Transfer." NASA-TP-1139, NASA, Jan. 1978.

[KC93] J. Keenan and G. Candler. "Simulation of Ablation in Earth Atmospheric Entry." *AIAA 93-2789*, 1993.

[KC94] J. Keenan and G. Candler. "Simulation of Graphite Sublimation and Oxidation under Re-Entry Conditions." *AIAA 94-2083*, 1994.

[Kee94] J. Keenan. *Thermo-chemical Ablation of Heat Shields Under Earth Re-entry Conditions*. PhD thesis, North Carolina State University, 1994.

[KUT12] J. Klentzman, E. Ulker, and A. Tumin. "Projection of the Solution of the Linearized Navier-Stokes Equations in Reacting High Speed Boundary Layers onto Discrete Modes." *AIAA 2012-3149*, 2012.

[LCC11] F. Li, M. Choudhari, C. Chang, and J. White. "Boundary Layer Transition over Blunt Hypersonic Vehicles Including Effects of Ablation-Induced Out-Gassing." *AIAA 2011-3303*, 2011.

[Lee85] J. Lee. "Basic Governing Equations for the Flight Regimes of Aeroassisted Orbital Transfer Vehicles." In H. F. Nelson, editor, *Thermal Design of Aeroassisted Orbital Transfer Vehicles*, volume 96, pp. 3–53. AIAA, New York, 1985.

[Lin08] T. Lin. "Influence of Laminar Boundary-Layer Transition on Entry Vehicle Design." *Journal of Spacecraft and Rockets*, **45**(2):165–175, 2008.

[LSO94] T. Lin, L. Sproul, and M. Olmos. "An Aerothermal Model for Ablating Heatshields." *AIAA paper 1994-247*, 1994.

[MA91] M. Malik and E. Anderson. "Real gas effects on hypersonic boundary-layer stability." *Physics of Fluids A: Fluid Dynamics*, **803**(3):803–821, 1991.

[Mac84] L. Mack. "Boundary Layer Linear Stability Theory." AGARD report No. 709, 1984.

[Mal89] M. Malik. "Prediction and Control of Transition in Supersonic and Hypersonic Boundary Layers." *AIAA Journal*, **27**(11):1487–1493, 1989.

[Mal90] M. Malik. "Numerical Methods for Hypersonic Boundary Layer Stability." *Journal of Computational Physics*, **86**(2):376–413, 1990.

[Mal03] M. Malik. "Hypersonic Flight Transition Data Analysis Using Parabolized Stability Equations with Chemistry Effects." *Journal of Spacecraft and Rockets*, **40**(3):332–344, 2003.

[MHE63] B. McBride, S. Heimel, J. Ehlers, and S. Gordon. "Thermodynamic Properties to 6000° for 210 Substances Involving the First 18 Elements." NASA SP-3001, NASA, 1963.

[MS91] M. Malik and R. Spall. "On the stability of compressible flow past axisymmetric bodies." *Journal of Fluid Mechanics*, **228**:443–463, 1991.

[MW63] R. Millikan and D. White. "Systematics of Vibrational Relaxation." *Journal of Chemical Physics*, **39**(12):3209–3213, 1963.

[MZ03a] Y. Ma and X. Zhong. "Receptivity of a Supersonic Boundary Layer Over a Flat Plate. Part 1. Wave Structures and Interactions." *Journal of Fluid Mechanics*, **488**:31–78, 2003.

[MZ03b] Y. Ma and X. Zhong. "Receptivity of a supersonic boundary layer over a flat plate. Part 1. Wave structures and interactions." *Journal of Fluid Mechanics*, **488**:31–78, 2003.

[MZ03c] Y. Ma and X. Zhong. "Receptivity of a Supersonic Boundary Layer Over a Flat Plate. Part 2. Receptivity to Free-stream Sound." *Journal of Fluid Mechanics*, **488**:79–121, 2003.

[MZ04] Y. Ma and X. Zhong. "Receptivity to Freestream Disturbances of a Mach 10 Nonequilibrium Reacting Oxygen Flow over a Flat Plate." *AIAA paper 2004-0256*, 2004.

[MZ05] Y. Ma and X. Zhong. "Receptivity of a Supersonic Boundary Layer Over a Flat Plate. Part 3. Effects of Different Types of Free-stream Disturbances." *Journal of Fluid Mechanics*, **532**:63–109, 2005.

[MZ13] C. Mortensen and X. Zhong. "Numerical Simulation of Graphite Ablation Induced Outgassing Effects on Hypersonic Boundary Layer Receptivity over a Cone Frustum." *AIAA paper 2013-0522*, 2013.

[MZ14] C. Mortensen and X. Zhong. "Simulation of Second-Mode Instability in a Real-Gas Hypersonic Flow with Graphite Ablation." *AIAA Journal*, **52**(8):1632–1652, 2014.

[Par76] C. Park. "Effects of Atomic Oxygen on Graphite Ablation." *AIAA Journal*, **14**(11):1640–1642, 1976.

[Par83] C. Park. "Stagnation-Point Ablation of Carbonaceous Flat Disks-Part I: Theory." *AIAA Journal*, **21**(11):1588–1594, 1983.

[Par85] C. Park. "On Convergence of Computation of Chemically Reacting Flows." *AIAA 85-0247*, 1985.

[Par90] C. Park. *Nonequilibrium Hypersonic Aerothermodynamics*. John Wiley & Sons Inc., New York, 1990.

[Par93] C. Park. "Review of Chemical-Kinetic Problems of Future NASA Missions, I: Earth Entries." *Journal of Thermophysics and Heat Transfer*, **7**(3):385–398, 1993.

[Par05] C. Park. "Calculation of Stagnation-Point Heating Rates Associated with Stardust Vehicle." *AIAA 2005-190*, 2005.

[PB06] C. Park and D. Bogdanoff. "Shock-Tube Measurements of Nitridation Coefficient of Solid Carbon." *Journal of Thermophysics and Heat Transfer*, **20**(3):487–492, 2006.

[PHJ91] C. Park, J. Howe, R. Jaffe, and G. Candler. "Chemical-Kinetic Problems of Future NASA Missions." *AIAA 91-0464*, 1991.

[PM68] H. Palmer and S. Mordecai. *Chemistry and Physics of Carbon*. Marcel Dekker, Inc., NY, 1968.

[Pot95] R. Potts. "Application of Integral Methods to Ablation Charring Erosion, A Review." *Journal of Spacecraft and Rockets*, **32**(2):200–209, 1995.

[PPW10] A. Prakash, N. Parsons, X. Wang, and X. Zhong. "High-order Shock-fitting Methods for Hypersonic Flow with Chemical and Thermal Nonequilibrium." *AIAA 2010-4997*, 2010.

[PPW11] A. Prakash, N. Parsons, X. Wang, and X. Zhong. "High-order Shock-fitting Methods for Direct Numerical Simulation of Hypersonic Flow with Chemical and Thermal Nonequilibrium." *Journal of Computational Physics*, **230**(23):8474–8507, 2011.

[PZK10] N. Parsons, X. Zhong, J. Kim, and J. Eldredge. "Numerical Study of Hypersonic Receptivity with Thermochemical Non-Equilibrium on a Blunt Cone." *AIAA paper 2010-4446*, 2010.

[Res08] E. Reshotko. "Transition Issues for Atmospheric Entry." *Journal of Spacecraft and Rockets*, **45**:161–164, 2008.

[Sch33] H. Schlichting. "Zur Entstehung der Turbulenz bei der Plattenstromung." *Nachrichten von der Gesellschaft der Wissenschaften zu Göttingen, Mathematisch-Physikalische KI. II*, pp. 182–208, 1933.

[Sch08] S. Schneider. "Effects of Roughness on Hypersonic Boundary-Layer Transition." *Journal of Spacecraft and Rockets*, **45**(2):193–209, 2008.

[Sch10] S. Schneider. "Hypersonic Boundary-Layer Transition with Ablation and Blowing." *Journal of Spacecraft and Rockets*, **47**(2):225–237, 2010.

[SCM00] S. Sepka, Y.-K. Chen, J. Marschall, and R. Copeland. "Experimental Investigation of Surface Reactions in Carbon Monoxide and Oxygen Mixtures." *Journal of Thermophysics and Heat Transfer*, **14**(1):45–52, 2000.

[SFA08] T. Suzuki, K. Fujita, K. Ando, and T. Sakai. "Experimental Study of Graphite Ablation in Nitrogen Flow." *Journal of Thermophysics and Heat Transfer*, **22**(3):382–389, 2008.

[SFP74] A. Shimizu, J. Ferrell, and C. Powars. "Interim Report Passive Nosetip Technology (PANT) Program. Volume XII. Nosetip Transition and Shape Change Tests in the AFFDL 50 MW RENT Arc–Data Report." SAMSO-TR-74-86, Air Force Space and Missile Systems Orgainization, April 1974.

[SN70] M. Sherman and T. Nakamura. "Flight Test Measurements of Boundary-Layer Transition on a Nonablating 22-Degree Cone." *Journal of Spacecraft and Rockets*, **7**(2):137–142, 1970.

[SR94] G. Stuckert and H. Reed. "Linear Disturbances in Hypersonic, Chemically Reacting Shock Layers." *AIAA Journal*, **32**(7):1384–1393, 1994.

[SRK02] W. Saric, H. Reed, and E. Kerschen. "Boundary-Layer Receptivity to Freestream Disturbances." *Annual Review of Fluid Mechanics*, **34**:291–319, 2002.

[SS48] G. Schubauer and H. Skramstad. "Laminar-boundary-layer Oscillations and Transition on a Flat Plate." Technical report, NACA Report No. 909, 1948.

[STD84] K. Stetson, E. Thompson, J. Donaldson, and L. Siler. "Laminar Boundary Layer Stability Experiments on a Cone at Mach 8, Part 2: Blunt Cone." *AIAA 84-0006*, 1984.

[Ste06] C. Stemmer. "Transition Investifation on Hypersonic Flat-Plate Boundary Layers Flows with Chemical and Thermal Non-Equilibrium." In *Sixth IUTAM Symposium on Laminar-Turbulent Transition*, pp. 363–368. Springer, 2006.

[Ste09] C. Stemmer. "Instability of high Mach number flows in the presence of high-temperature gas effects." In *Seventh IUTAM Symposium on Laminar-Turbulent Transition*, pp. 391–396. Springer, 2009.

[Stu91] G. Stuckert. *Linear Stability Theory of Hypersonic, Chemically Reacting Viscous Flows*. PhD thesis, Arizona State University, 1991.

[Tol29] W. Tollmien. "Über die Entstehung der Turbulenz. 1. Mitteilung." *Nachrichten von der Gesellschaft der Wissenschaften zu Göttingen, Mathematisch-Physikalische KI. II*, pp. 21–44, 1929.

[Tum03] A. Tumin. "Multimode decomposition of spatially growing perturbations in a two-dimenstional boundary layer." *Physics of Fluids*, **15**(9), 2003.

[TZC15] Q. Tang, Y. Zhu, X. Chen, and C. Lee. "Development of second-mode instability in a Mach 6 flat plate boundary layer with two-dimensional roughness." *Physics of Fluids*, **27**(6), 2015.

[Ung67] E. Ungar. "Ablation Thermal Protection Systems." *Science*, **158**(3802):740–744, November 1967.

[Wil50] C. Wilke. "A Viscosity Equation for Gas Mixtures." *The Journal of Chemical Physics*, **18**(4):517–519, 1950.

[Wil80] J. Williamson. "Low-Storage Runge-Kutta Schemes." *Journal of Computational Physics*, **35**(1):48–56, 1980.

[Woo75] M. Wool. "Final Summary Report Passive Nosetip Technology (PANT) Program." SAMSO-TR-75-250, SAMSO/RSSE, June 1975.

[ZA99] S. Zhluktov and T. Abe. "Viscous Shock-Layer Simulation of Airflow Past Ablating Blunt Body with Carbon Surface." *Journal of Thermophysics and Heat Transfer*, **13**(1):50–59, 1999.

[Zho98] X. Zhong. "High-Order Finite-Difference Schemes for Numerical Simulation of Hypersonic Boundary-Layer Transition." *Journal of Computational Physics*, **144**(2):662–709, 1998.

[ZTW04] E. Zoby, R. Thompson, and K. Wurster. "Aeroheating Design Issues for Reusable Launch Vehicles – A Perspective." *AIAA paper 2004-2535*, 2004.

[ZW12] X. Zhong and X. Wang. "Direct Numerical Simulation on the Receptivity, Instability, and Transition of Hypersonic Boundary Layers." *Annual Review of Fluid Mechanics*, **44**:527–561, 2012.